

Ministry of Education and Science of the Russian Federation  
Saint Petersburg National Research University of Information  
Technologies, Mechanics, and Optics

***NANOSYSTEMS:***  
***PHYSICS, CHEMISTRY, MATHEMATICS***

**2015, volume 6(3)**

**Наносистемы: физика, химия, математика**

**2015, том 6, № 3**



# NANOSYSTEMS:

PHYSICS, CHEMISTRY, MATHEMATICS

## ADVISORY BOARD MEMBERS

**Chairman:** V.N. Vasiliev (*St. Petersburg, Russia*),  
V.M. Ievlev (*Voronezh*), P.S. Kop'ev (*St. Petersburg, Russia*),  
V.N. Parmon (*Novosibirsk*), A.I. Rusanov (*St. Petersburg, Russia*).

## EDITORIAL BOARD

**Editor-in-Chief:** N.F. Morozov (*St. Petersburg, Russia*)  
**Deputy Editor-in-Chief:** I.Yu. Popov (*St. Petersburg, Russia*)

### Section Co-Editors:

Physics – V.M. Uzdin (*St. Petersburg, Russia*),  
Chemistry, material science – V.V. Gusarov (*St. Petersburg, Russia*),  
Mathematics – I.Yu. Popov (*St. Petersburg, Russia*).

### Editorial Board Members:

V.M. Adamyan (*Odessa, Ukraine*); O.V. Al'myasheva (*St. Petersburg, Russia*);  
A.P. Alodjants (*Vladimir, Russia*); S. Bechta (*Stockholm, Sweden*); J. Behrndt (*Graz, Austria*);  
M.B. Belonenko (*Volgograd, Russia*); V.G. Bepalov (*St. Petersburg, Russia*); J. Brasche  
(*Clausthal, Germany*); A. Chatterjee (*Hyderabad, India*); S.A. Chivilikhin (*St. Petersburg,  
Russia*); A.V. Chizhov (*Dubna, Russia*); A.N. Enyashin (*Ekaterinburg, Russia*), P.P. Fedorov  
(*Moscow, Russia*); E.A. Gudilin (*Moscow, Russia*); V.K. Ivanov (*Moscow, Russia*),  
H. Jónsson (*Reykjavik, Iceland*); A.A. Kiselev (*Madison, USA*); Yu.S. Kivshar (*Canberra,  
Australia*); S.A. Kozlov (*St. Petersburg, Russia*); P.A. Kurasov (*Stockholm, Sweden*);  
A.V. Lukashin (*Moscow, Russia*); V.A. Margulis (*Saransk, Russia*); I.V. Melikhov (*Moscow,  
Russia*); G.P. Miroshnichenko (*St. Petersburg, Russia*); I.Ya. Mittova (*Voronezh, Russia*);  
H. Neidhardt (*Berlin, Germany*); K. Pankrashkin (*Orsay, France*); B.S. Pavlov (*Auckland,  
New Zealand*); A.V. Ragulya (*Kiev, Ukraine*); V. Rajendran (*Tamil Nadu, India*);  
A.A. Rempel (*Ekaterinburg, Russia*); V.Ya. Rudyak (*Novosibirsk, Russia*); D Shoikhet  
(*Karmiel, Israel*); P Stovicek (*Prague, Czech Republic*); V.M. Talanov (*Novocherkassk,  
Russia*); A.Ya. Vul' (*St. Petersburg, Russia*); V.A. Zagrebnov (*Marseille, France*).

### Editors:

I.V. Blinova; A.I. Popov; A.I. Trifanov; E.S. Trifanova (*St. Petersburg, Russia*),  
R. Simoneaux (*Philadelphia, Pennsylvania, USA*).

**Address:** University ITMO, Kronverkskiy pr., 49, St. Petersburg 197101, Russia.

**Phone:** +7(812)232-67-65, **Journal site:** <http://nanojournal.ifmo.ru/>,

**E-mail:** [popov1955@gmail.com](mailto:popov1955@gmail.com)

## AIM AND SCOPE

The scope of the journal includes all areas of nano-sciences. Papers devoted to basic problems of physics, chemistry, material science and mathematics inspired by nanosystems investigations are welcomed. Both theoretical and experimental works concerning the properties and behavior of nanosystems, problems of its creation and application, mathematical methods of nanosystem studies are considered.

The journal publishes scientific reviews (up to 30 journal pages), research papers (up to 15 pages) and letters (up to 5 pages). All manuscripts are peer-reviewed. Authors are informed about the referee opinion and the Editorial decision.

# Content

## MATHEMATICS

P. Kurasov, A. Serio

**Topological damping of Aharonov-Bohm effect: quantum graphs and vertex conditions** 309

## PHYSICS

B. Assfour, S. Leoni

**Storage and separation of CO<sub>2</sub> and CH<sub>4</sub> in boron imidazolate frameworks: a theoretical study from Monte Carlo simulation** 320

S.V. Dzyubanenko, V.D. Lukyanov

**Modeling of the kinetics of reactive diffusion of gallium in copper particles** 332

Yu.S. Kivshar

**From metamaterials to metasurfaces and metadevices** 346

V.L. Kulinskii, D.Yu. Panchenko

**Localized states near the Abrikosov vortex core in type-II superconductors within zero-range potential model** 353

V.M. Pugachev, K.A. Dativ, A.S. Valnyukova,  
M.V. Ananyeva, A.V. Kalenskii

**Synthesis of copper nanoparticles for use in an optical initiation system** 361

V. Rudyak, A. Belkin

**Statistical mechanics of transport processes of fluids under confined conditions** 366

E.F.Sheka, I. Natkaniec, V. Mel'nikov, K. Druzbecki

**Neutron scattering from graphene oxide paper and thermally exfoliated reduced graphene oxide** 378

V.V. Zubkov, V.M. Samsonov, I.V. Grinev, I.V. Popov

**Classical density functional approach to adsorption of hydrogen in carbon materials** 394

## **CHEMISTRY AND MATERIAL SCIENCE**

- N.E. Kochkina, O.A. Skobeleva, Yu.V. Khokhlova  
**Synthesis of silver nanoparticles in DMSO solutions of starch: a comparative investigation of native and soluble starches** 405
- I.V. Melikhov, O.V. Alekseeva, V.N. Rudin,  
E.D. Kozlovskaya, A.V. Noskov  
**Morphological memory of polymeric bodies** 412
- I.Ya. Mittova, V.F. Kostryukov  
**Chemostimulating effect of mixture and separate evaporation of manganese (IV) oxide compositions with lead (II) oxide and vanadium (V) oxide on GaAs thermal oxidation** 424
- K.N. Semenov, N.A. Charykov, O.S. Manyakina, A.V. Fedorov,  
V.A. Keskinov, K.V. Ivanova, O.V. Rakhimova, D.G. Letenko,  
V.A. Nikitin, N.A. Kulenova, Z. Akhmetvalieva, M.S. Gutenev  
**Mass transport properties of water soluble light fullerene tris-malonate  $C_{60}[=C(COOH)_2]_3$  in aqueous solutions** 435
- M.V. Talanov, V.B. Shirokov, V.M. Talanov  
**Atomic order and metallic nanoclusters in  $Na_4Ir_3O_8$**  442
- Information for authors** 451

# Topological damping of Aharonov-Bohm effect: quantum graphs and vertex conditions

P. Kurasov and A. Serio

Department of Mathematics, Stockholm University,  
106 91 Stockholm, Sweden

kurasov@math.su.se

**PACS 02.30.Tb, 03.65.Vf, 05.60.Gg DOI 10.17586/2220-8054-2015-6-3-309-319**

The magnetic Schrödinger operator was studied on a figure 8-shaped graph. It is shown that for specially chosen vertex conditions, the spectrum of the magnetic operator is independent of the flux through one of the loops, provided the flux through the other loop is zero. Topological reasons for this effect are explained.

**Keywords:** Quantum graphs, Magnetic field, Trace formula.

*Received: 2 April 2015*

## 1. Introduction

Transport of quantum particles in nanostructures can be described by Schrödinger equation on metric graphs, also known as *quantum graphs*. The spectral theory of quantum graphs is a hot topic in modern mathematical physics and many interesting properties have been observed and described, see for example recent monographs on the subject [2, 9, 12]. Propagation of particles in such structures is described by certain matching conditions at the vertices and by electric and magnetic potentials on the edges. The vertex conditions reflect the topology of the graph, connecting together limiting values of functions at one particular vertex. Transport along the edges is governed by the electric potential and is reminiscent of the one-dimensional Schrödinger equation. The magnetic potential plays a role only if the underlying graph contains cycles and the flux of the magnetic field through the cycles is not multiple of  $2\pi$  [4, 8]. Such dependence of the spectrum on the magnetic fluxes is usually understood as the Aharonov-Bohm effect, which goes back to [1]. The intuition behind Aharonov-Bohm effect is that a charged particle going around cycles ‘feels’ the magnetic field inside the cycles. If magnetic flux is a multiple of  $2\pi$ , then the magnetic potential can be removed and therefore does not influence the spectrum.

In the current article, we consider a figure 8-shaped graph with magnetic Schrödinger operator. Our intuition, based on Aharonov-Bohm effect, tells us that the spectrum depends on the magnetic field fluxes through the two loops; explicit calculations support this prediction. On the other hand, it is discovered that if one of the fluxes is zero, then the spectrum might be independent of the flux through the other loop. This fact appears surprising, since no difference to the original Aharonov-Bohm setting can easily be seen. We use trace formula connecting the spectrum of the operator to the set of periodic orbits on the underlying metric graph. It appears that only the orbits going around the loops with nontrivial flux in opposite directions, and therefore not feeling the flux, contribute to the trace formula. We call this observation the topological damping of the Aharonov-Bohm effect and discuss how to obtain other graphs exhibiting the same property.

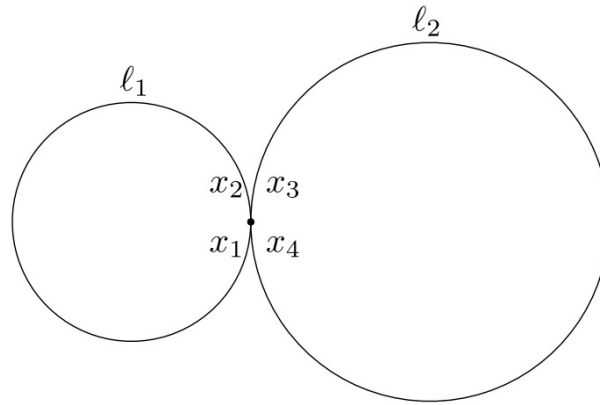


FIG. 1. The figure 8-shaped graph

The article is organized as follows: we first define the graph and the operator and calculate the spectrum explicitly. In the last section the trace formula is considered and the reason for the topological damping is explained. The role of vertex conditions is illuminated.

## 2. Getting started

Let us consider the metric figure 8-shaped graph  $\Gamma_\infty$  formed by two edges  $E_1 = [x_1, x_2]$  and  $E_2 = [x_3, x_4]$ , joined together at one vertex  $V = \{x_1, x_2, x_3, x_4\}$ .

We study the magnetic Schrödinger operator on  $\Gamma_\infty$ :

$$L = \left( i \frac{d}{dx} + a(x) \right)^2, \quad (1)$$

with zero electric potential and arbitrary integrable real magnetic potential  $a$ . To make the operator self-adjoint, we assume vertex matching conditions of the form:

$$i(S - \mathbf{I})\vec{u} = (S + \mathbf{I})\partial\vec{u}, \quad (2)$$

where  $\vec{u}$  and  $\partial\vec{u}$  are the vectors of all limit values of the function and its normal extended derivatives at the vertex  $V$ :

$$\vec{u} = \begin{pmatrix} u(x_1) \\ u(x_2) \\ u(x_3) \\ u(x_4) \end{pmatrix}, \quad \partial\vec{u} = \begin{pmatrix} u'(x_1) - ia(x_1)u(x_1) \\ -(u'(x_2) - ia(x_2)u(x_2)) \\ u'(x_3) - ia(x_3)u(x_3) \\ -(u'(x_4) - ia(x_4)u(x_4)) \end{pmatrix}.$$

The matrix  $S$  is unitary and is used to parametrize all possible matching conditions making the operator  $L$  self-adjoint in  $L_2(\Gamma_\infty)$  when defined on all functions from the Sobolev space  $W_2^2(\Gamma \setminus V)$  satisfying (2).

The spectrum of the operator  $L$  is purely discrete and consists of eigenvalues accumulating towards  $+\infty$ . The eigenvalues can be calculated by solving the eigenvalue equation:

$$\left( i \frac{d}{dx} + a(x) \right)^2 \psi(x) = \lambda \psi(x), \quad (3)$$

on each of the intervals and substituting the solution into the vertex conditions (2). Our main interest is the dependence of the spectrum upon the magnetic potential  $a$ . The first elementary observation is that magnetic potential can be eliminated on each of the edges,

but not globally, leading to new vertex conditions that depend on the integrals of the magnetic potential along the two loops:

$$\phi_j = \int_{x_{2j-1}}^{x_{2j}} a(x)dx, \quad j = 1, 2. \tag{4}$$

It appears that that particular form of the magnetic potential does not play any role. The following transformation:

$$U_a : u(x) \mapsto \exp \left( -i \int_{x_{2j-1}}^x a(y)dy \right) u(x), \tag{5}$$

maps the operator  $L$  into the operator  $\mathbf{L} = U_a L U_a^{-1}$  given by the same differential expression but with zero magnetic potential:

$$\mathbf{L} = -\frac{d^2}{dx^2}, \tag{6}$$

on the set of functions from  $W_2^2(\Gamma \setminus V)$  satisfying vertex conditions:

$$i(S^{\phi_1, \phi_2} - \mathbf{I})\vec{u} = (S^{\phi_1, \phi_2} + \mathbf{I})\partial_n \vec{u}, \tag{7}$$

which are obtained from (2) by substituting the matrix  $S$  with:

$$S^{\phi_1, \phi_2} = DSD^{-1}, \quad D = \begin{pmatrix} 1 & 0 & 0 & 0 \\ 0 & e^{-i\phi_1} & 0 & 0 \\ 0 & 0 & 1 & 0 \\ 0 & 0 & 0 & e^{-i\phi_2} \end{pmatrix}, \tag{8}$$

and the vector of extended derivatives  $\partial \vec{u}$  – with the vector of normal derivatives

$$\partial_n \vec{u} = \begin{pmatrix} u'(x_1) \\ -u'(x_2) \\ u'(x_3) \\ -u'(x_4) \end{pmatrix}.$$

The integrals  $\phi_j$  can be interpreted as fluxes of the magnetic field through the corresponding loops.

In general, the spectrum of the operator  $\mathbf{L}$  depends on the fluxes, but it might happen that only the sum of the fluxes counts. For example, if  $S = \begin{pmatrix} 0 & 0 & 0 & 1 \\ 0 & 0 & 1 & 0 \\ 0 & 1 & 0 & 0 \\ 1 & 0 & 0 & 0 \end{pmatrix}$ , then

the graph  $\Gamma_\infty$  is equivalent to the loop of length  $\mathcal{L} = x_2 - x_1 + x_4 - x_3$  and the spectrum obviously depends on the sum of the of the fluxes  $\phi_1 + \phi_2$ . This case is not interesting, since the anomalous behavior of the spectrum is due to the choice of the vertex conditions that do not respect the geometry of the graph; the vertex  $V$  can be divided into two vertices,  $V_1 = \{x_1, x_4\}$  and  $V_2 = \{x_2, x_3\}$  and the vertex conditions separately connect the boundary values corresponding to the two new vertices. Such boundary conditions do not correspond to the figure 8-shaped graph, but rather to the loop graph.

Another degenerate example is when  $S = \begin{pmatrix} 0 & 1 & 0 & 0 \\ 1 & 0 & 0 & 0 \\ 0 & 0 & 0 & 1 \\ 0 & 0 & 1 & 0 \end{pmatrix}$ . In this case, every

second eigenvalue depends only on  $\phi_1$  and all other – only on  $\phi_2$ . The vertex conditions connect together the pairs of end points  $(x_1, x_2)$  and  $(x_3, x_4)$  separately. The corresponding metric graph is not  $\Gamma_\infty$ , but rather two separate loops formed by the two edges. This case is not interesting for us either.

In what follows, we study the magnetic Schrödinger operator corresponding to the vertex conditions given by the following vertex scattering matrix:

$$S = \begin{pmatrix} 0 & 0 & \alpha & \beta \\ 0 & 0 & -\beta & \alpha \\ \alpha & -\beta & 0 & 0 \\ \beta & \alpha & 0 & 0 \end{pmatrix}, \quad \alpha, \beta \in \mathbb{R}, \quad \alpha^2 + \beta^2 = 1. \quad (9)$$

This unitary matrix connects together boundary values at all four end points and therefore is properly connecting. One may visualize this by the following picture, where all possible scattering processes are indicated by curves. It will be shown that interesting effects can

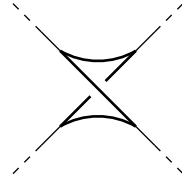


FIG. 2. Visual representation of the connections given by the vertex conditions with  $S$  given by (9): the curves indicate possible passages.

be observed if the probabilities of these passages are equal, which corresponds to the choice  $\alpha = \beta = 1/\sqrt{2}$ :

$$S = \begin{pmatrix} 0 & 0 & \frac{1}{\sqrt{2}} & \frac{1}{\sqrt{2}} \\ 0 & 0 & -\frac{1}{\sqrt{2}} & \frac{1}{\sqrt{2}} \\ \frac{1}{\sqrt{2}} & -\frac{1}{\sqrt{2}} & 0 & 0 \\ \frac{1}{\sqrt{2}} & \frac{1}{\sqrt{2}} & 0 & 0 \end{pmatrix}. \quad (10)$$

### 3. Explicit calculation of the spectrum.

Our immediate goal is to derive the equation describing the spectrum of the operator  $\mathbf{L}$ , depending on the fluxes  $\phi_1$  and  $\phi_2$  and parameters  $\alpha$  and  $\beta$ . All nonzero eigenvalues of  $\mathbf{L}$  can be calculated using the vertex and edge scattering matrices [3, 5, 6, 7, 10]. The matrix  $S$ , and therefore the matrix  $S^{\phi_1, \phi_2} = DSD^{-1}$ , appearing in the vertex conditions is not only unitary, but also Hermitian. It follows that the corresponding vertex scattering

matrix  $S_v$  does not depend on the energy and coincides with  $S^{\phi_1, \phi_2}$ :

$$S_v \equiv S^{\phi_1, \phi_2} = \begin{pmatrix} 0 & 0 & \alpha & e^{i\phi_2}\beta \\ 0 & 0 & -e^{-i\phi_1}\beta & e^{-i(\phi_1-\phi_2)}\alpha \\ \alpha & -e^{i\phi_1}\beta & 0 & 0 \\ e^{-i\phi_2}\beta & e^{i(\phi_1-\phi_2)}\alpha & 0 & 0 \end{pmatrix}. \quad (11)$$

The differential operator on the edges does not contain any electric or magnetic potential, hence the plane waves penetrate the edges without any reflection but with the addition of extra phases. The corresponding edge scattering matrix is

$$S_e = \begin{pmatrix} 0 & e^{ik\ell_1} & 0 & 0 \\ e^{ik\ell_1} & 0 & 0 & 0 \\ 0 & 0 & 0 & e^{ik\ell_2} \\ 0 & 0 & e^{ik\ell_2} & 0 \end{pmatrix}, \quad (12)$$

where  $\ell_j = x_{2j} - x_{2j-1}$ ,  $j = 1, 2$  are the lengths of the edges. Then, all nonzero eigenvalues are given by the solutions of the equation:

$$\det(S_e(k)S_v - \mathbb{I}) = 0, \quad (13)$$

which is equivalent to:

$$\det \begin{pmatrix} -1 & 0 & -e^{ik\ell_1}e^{-i\phi_1}\beta & e^{ik\ell_1}e^{-i(\phi_1-\phi_2)}\alpha \\ 0 & -1 & e^{ik\ell_1}\alpha & e^{ik\ell_1}e^{i\phi_2}\beta \\ e^{ik\ell_2}e^{-i\phi_2}\beta & e^{ik\ell_2}e^{i(\phi_1-\phi_2)}\alpha & -1 & 0 \\ e^{ik\ell_2}\alpha & -e^{ik\ell_2}e^{i\phi_1}\beta & 0 & -1 \end{pmatrix} = 0, \quad (14)$$

$$\Leftrightarrow 1 + (\alpha^2 + \beta^2)^2 e^{2ik(\ell_1+\ell_2)} + 2(\cos(\phi_1 + \phi_2)\beta^2 - \cos(\phi_1 - \phi_2)\alpha^2) e^{ik(\ell_1+\ell_2)} = 0. \quad (15)$$

Taking into account that  $\alpha^2 + \beta^2 = 1$  and  $e^{ik(\ell_1+\ell_2)} \neq 0$ , we arrive at the following secular equation:

$$\cos k(\ell_1 + \ell_2) = \alpha^2 \cos(\phi_1 - \phi_2) - \beta^2 \cos(\phi_1 + \phi_2). \quad (16)$$

The right hand side of this equation is a constant between  $-1$  and  $1$  and hence, solutions to the equation form two periodic in  $k$  sequences. The corresponding eigenvalues,  $\lambda = k^2$ , in general, depend on both magnetic fluxes  $\phi_1$  and  $\phi_2$ .

An interesting phenomenon occurs if one choses  $\alpha = \beta = 1/\sqrt{2}$ , *i.e.* the matrix  $\mathbf{S}$  given by (10). The secular equation (16) takes the form:

$$\begin{aligned} \cos k(\ell_1 + \ell_2) &= \frac{\cos(\phi_1 - \phi_2) - \cos(\phi_1 + \phi_2)}{2} \\ &= \sin \phi_1 \sin \phi_2. \end{aligned} \quad (17)$$

It follows, that if one of the magnetic fluxes is an integer multiple of  $\pi$ , then the spectrum is independent of the other flux. This is a trivial consequence of the secular equation (17), but we are interested in having an intuitive explanation of this phenomena. The Aharonov-Bohm effect tells us that the spectrum of a system, like the magnetic Schrödinger operator on  $\Gamma_\infty$  should depend on the magnetic fluxes. This dependence is damped only in very special cases. Why is it so special when one of the fluxes is zero? An explicit answer to this question is given in the following section. We use the trace formula connecting the spectrum of a quantum graph to the set of periodic orbits on the underlying metric graph.

In what follows, we are interested in this special case, when one of the fluxes is zero. Without loss of generality, we may assume that  $\phi_1 = 0$ .

First, let us determine whether  $\lambda = 0$  is an eigenvalue of the operator  $\mathbf{L}$  or not. The value of  $k = 0$  is a solution to the secular equation only if  $\sin \phi_1 \sin \phi_2 = 1$ . If one of the fluxes is zero, then  $k = 0$  is not a solution to the secular equation. It follows that the so-called *algebraic multiplicity*<sup>1</sup>  $m_a(0)$  [10, 6] of the zero eigenvalue is zero.

Let us turn to calculation of the spectral multiplicity  $m_s(0)$  – the number of linearly independent solutions to the equation  $\mathbf{L}\psi = 0$ . In order to emphasize that only the lengths of the edges are important, we parameterize the edges as follows:

$$[x_1, x_2] = [0, \ell_1], \quad [x_3, x_4] = [0, \ell_2].$$

All solutions to the differential equation are then given by:

$$\psi(x) = \begin{cases} a_1 x + b_1 & \text{if } x \in [x_1, x_2], \\ a_2 x + b_2 & \text{if } x \in [x_3, x_4]. \end{cases} \quad (18)$$

Then, at the endpoints, we have:

$$\vec{\psi} = \begin{pmatrix} b_1 \\ a_1 \ell_1 + b_1 \\ b_2 \\ a_2 \ell_2 + b_2 \end{pmatrix}, \quad \partial_n \vec{\psi} = \begin{pmatrix} a_1 \\ -a_1 \\ a_2 \\ -a_2 \end{pmatrix}. \quad (19)$$

The matrix  $\mathbf{S}^{\phi_1, \phi_2}$  is unitary and Hermitian, hence its eigenvalues are just  $\pm 1$ . Therefore, the vertex conditions (7) are satisfied if and only if both the left and right hand sides are equal to zero:

$$\begin{pmatrix} -\frac{1}{2} & 0 & \frac{1}{2\sqrt{2}} & \frac{e^{-i\phi_2}}{2\sqrt{2}} \\ 0 & -\frac{1}{2} & -\frac{1}{2\sqrt{2}} & \frac{e^{i\phi_1-i\phi_2}}{2\sqrt{2}} \\ \frac{1}{2\sqrt{2}} & -\frac{e^{-i\phi_1}}{2\sqrt{2}} & -\frac{1}{2} & 0 \\ \frac{e^{i\phi_2}}{2\sqrt{2}} & \frac{e^{-i\phi_1+i\phi_2}}{2\sqrt{2}} & 0 & -\frac{1}{2} \end{pmatrix} \begin{pmatrix} a_1 \\ -a_1 \\ a_2 \\ -a_2 \end{pmatrix} = 0, \quad (20)$$

$$\begin{pmatrix} \frac{1}{2} & 0 & \frac{1}{2\sqrt{2}} & \frac{e^{-i\phi_2}}{2\sqrt{2}} \\ 0 & \frac{1}{2} & -\frac{1}{2\sqrt{2}} & \frac{e^{i\phi_1-i\phi_2}}{2\sqrt{2}} \\ \frac{1}{2\sqrt{2}} & -\frac{e^{-i\phi_1}}{2\sqrt{2}} & \frac{1}{2} & 0 \\ \frac{e^{i\phi_2}}{2\sqrt{2}} & \frac{e^{-i\phi_1+i\phi_2}}{2\sqrt{2}} & 0 & \frac{1}{2} \end{pmatrix} \begin{pmatrix} b_1 \\ a_1 \ell_1 + b_1 \\ b_2 \\ a_2 \ell_2 + b_2 \end{pmatrix} = 0. \quad (21)$$

We omit tedious computations and give just a sketch. From the first equation, we obtain  $a_1 = a_2 = 0$ , then plugging this result into the second equation we obtain  $b_1 = b_2 = 0$  for any values of  $\phi_2$ . This proves that  $\lambda = 0$  is not an eigenvalue and hence the spectral multiplicity (as well as the algebraic multiplicity) is zero in this case.

<sup>1</sup>The algebraic multiplicity is the order of zero in the secular equation.

In summary, the spectrum of the magnetic Schrödinger operator on  $\Gamma_\infty$  is given by the solutions of the secular equation:

$$\cos k\mathcal{L} = 0, \quad \mathcal{L} = \ell_1 + \ell_2, \tag{22}$$

provided one of the magnetic fluxes is zero.

#### 4. Topological reasons for damping

We have seen that in the case  $\phi_1 = 0$  the spectrum does not depend on the flux  $\phi_2$  – the Aharonov-Bohm effect is damped which contradicts our intuition. The main goal of this section is to explain that this effect has a topological explanation. We are going to use trace formula (see [3, 5, 10, 6, 13]) connecting the spectrum of a quantum graph to the set of periodic orbits on the metric graph. It will be shown that orbits that "feel" the magnetic flux  $\phi_2$  give zero total contribution into the trace formula.

Under a periodic orbit, we understand any oriented closed path on the graph  $\Gamma_\infty$ , which is allowed to turn back at vertices only. Paths having opposite directions are considered to be different. The trace formula for the Laplace operator on a metric graph can be written as [3, 5, 10, 6, 13]:

$$\begin{aligned} u(k) &:= 2m_s(0)\delta(k) + \sum_{k_n \neq 0} (\delta(k - k_n) + \delta(k + k_n)) \\ &= (2m_s(0) - m_a(0))\delta(k) + \frac{\mathcal{L}}{\pi} + \frac{1}{\pi} \sum_{p \in \mathcal{P}} l(\text{prim}(p))S_v(p) \cos kl(p), \end{aligned} \tag{23}$$

where

- $\mathcal{L} = \ell_1 + \ell_2$  is the total length of the graph,
- $m_s(0)$  is the (spectral) multiplicity of the eigenvalue zero;
- $m_a(0)$  is the algebraic multiplicity of the eigenvalue zero – the order of zero given by the secular equation (16);
- $p$  is a closed path on  $\Gamma$ ;
- $\mathcal{P}$  is the set of closed paths;
- $l(p)$  is the length of the closed path  $p$ ;
- $\text{prim}(p)$  is one of the primitive paths for  $p$ ;
- $S_v(p)$  is the product of all vertex scattering coefficients along the path  $p$ .

This formula was proven for the Laplace operator with standard vertex conditions (assuming that the functions are continuous and the sum of normal derivatives is zero), but just the same proof holds in the case where the vertex conditions are described by vertex scattering matrices which are independent of the energy [11]. In the considered case, the vertex scattering matrices  $S_v$  are Hermitian, and therefore, independent of the energy.

The fluxes  $\phi_1$  and  $\phi_2$  are contained in the products  $S_v(p)$ , since the entries of  $S_v \equiv S^{\phi_1, \phi_2}$  depend on the fluxes (see formula (11)). Therefore, it is natural to expect that the left side of the equation also depends on the fluxes. Conversely, the left side in (23) is determined by the spectrum of  $\mathbf{L}$ , which in the case  $\phi_1 = 0$ , is independent of  $\phi_2$ . More precisely, the spectrum is determined by  $\cos k\mathcal{L} = 0$  (we have already shown that  $\lambda = 0$  is not an eigenvalue in this case,  $m_s(0) = 0$ ):

$$k_n = \frac{\pi}{2\mathcal{L}} + \frac{\pi}{\mathcal{L}}n, \quad n = 0, 1, 2, 3, \dots \tag{24}$$

Then, the left side of the trace formula can be written as:

$$\begin{aligned} u(k) &= \sum_{k_n \neq 0} (\delta(k - k_n) + \delta(k + k_n)) \\ &= \sum_{n \in \mathbb{Z}} \delta\left(k - \left(\frac{\pi}{2\mathcal{L}} + \frac{\pi}{\mathcal{L}}n\right)\right) \\ &= \sum_{m \in \mathbb{Z}} \delta\left(k - \frac{\pi}{2\mathcal{L}}m\right) - \sum_{m \in \mathbb{Z}} \delta\left(k - \frac{\pi}{\mathcal{L}}m\right). \end{aligned}$$

We use now the Poisson summation formula:

$$\sum_{n \in \mathbb{Z}} \delta(x - Tn) = \frac{1}{T} \sum_{m \in \mathbb{Z}} e^{-i2\pi \frac{m}{T}x},$$

and rewrite the last expression as follows:

$$u(k) = \sum_{n \in \mathbb{Z}} \delta\left(k - \left(\frac{\pi}{2\mathcal{L}} + \frac{\pi}{\mathcal{L}}n\right)\right) = \frac{2\mathcal{L}}{\pi} \sum_{m \in \mathbb{Z}} e^{-i4\mathcal{L}mk} - \frac{\mathcal{L}}{\pi} \sum_{m \in \mathbb{Z}} e^{-i2\mathcal{L}mk}. \tag{25}$$

This formula represents the distribution  $u(k)$  as a formal exponential series. This series is independent of  $\phi_2$ , while the series on the right side of (23) formally contains  $\phi_2$ , since  $S_v(p)$  depends on the second flux. Let us examine the series over all periodic orbits in more detail in order to understand the reason why all terms containing  $\phi_2$  cancel. It appears that the cause is mostly topological.

The algebraic multiplicity of the eigenvalue zero is zero  $m_a = 0$  ( $k = 0$  is not a solution to  $\cos k\mathcal{L} = 0$ ) and the right hand side of trace formula can be written as:

$$u(k) = \frac{\mathcal{L}}{\pi} + \frac{1}{\pi} \sum_{p \in \mathcal{P}} l(\text{prim}(p)) S_v(p) \cos kl(p).$$

Let us first note that the sum in the trace formula contains contributions from the paths that go around the left and right loops an equal number of times. This is due to the fact that the coefficients 12, 21, 34 and 43 in the vertex scattering matrix are zero:

$$(S_v)_{12} = (S_v)_{21} = (S_v)_{34} = (S_v)_{43} = 0.$$

Therefore, the length of each path with nontrivial  $S_v(p)$  is an integer multiple of the total length  $\mathcal{L} := \ell_1 + \ell_2$ .

The sum over all paths is taken over all closed paths and  $l(\text{prim } p)$  is the length of the corresponding primitive path. It will be convenient for us to distinguish paths with different starting edges – the first edges the path comes across. Then, the sum  $\sum_{p \in \mathcal{P}} l(\text{prim}(p)) S_v(p) \cos kl(p)$  can be written as two sums – over the paths that go around the left loop first and over the paths that go around the right loop first:

$$\begin{aligned} u(k) &= \frac{\mathcal{L}}{\pi} + \frac{1}{\pi} \sum_{p \in \mathcal{P}} l(\text{prim}(p)) S_v(p) \cos kl(p) \\ &= \frac{\mathcal{L}}{\pi} + \frac{\ell_1}{\pi} \sum_{p \in \mathbb{P}_l} S_v(p) \cos kl(p) + \frac{\ell_2}{\pi} \sum_{p \in \mathbb{P}_r} S_v(p) \cos kl(p), \end{aligned} \tag{26}$$

where  $\mathbb{P}_{l,r}$  denote the sets of paths where paths with different starting edges are considered different. The lower indices  $l$  and  $r$  indicate whether the path goes around the left or the right loop first. Each of the two sums can be treated in a similar fashion.

Let us first consider the series  $\sum_{p \in \mathbb{P}_l} S_v(p) \cos kl(p)$  over all paths starting by going into the left edge. After going around the left loop, the path should go around the right

loop and then again around the left one: the left and right loops appear one after another. Every such path can be uniquely parameterized by a series of indices  $\nu_j = \pm$ , indicating whether the path goes around the left or right path in the positive (+) (clockwise following the orientation of the edges) or negative (-) (counterclockwise) direction. All odd indices correspond to the left loop, all even - to the right loop. The number of signs is even, which reflects the fact that every such path goes around the left and right loops equal number of times. For example the path indicated on Fig. 3 is parameterized as (+, -, +, +).

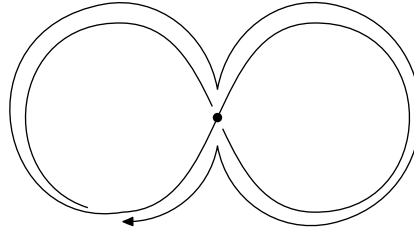


FIG. 3. A path of length  $2(l_1 + l_2)$ .

Let us turn to the calculation of the coefficients  $S_v(p)$ . The path indicated on Fig. 3 has coefficient  $S_v(p)$  equal to:

$$\begin{aligned} S_v(p) &= (S_v)_{14}(S_v)_{32}(S_v)_{13}(S_v)_{42} \\ &= e^{i\phi_2} \beta \cdot (-e^{-i\phi_1} \beta) \cdot \alpha \cdot e^{i(\phi_1 - \phi_2)} \alpha \\ &= -e^{2i\phi_1} \alpha^2 \beta^2 = \frac{-1}{4} e^{i2\phi_1}. \end{aligned}$$

One may calculate the same product using the original vertex scattering matrix (10), but taking into account that each time when the path goes along the left or right loop, the product gains the phase coefficient  $e^{\pm i\phi_1}$  or  $e^{\pm i\phi_2}$ , respectively. The sign corresponds to positive or negative direction. Each time when the path crosses the middle vertex,  $S_v(p)$  gets an extra term  $\pm \frac{1}{\sqrt{2}}$ . Note that only coefficients corresponding to the transitions  $2 \rightarrow 3$  and  $3 \rightarrow 2$  have a minus sign; all other coefficients are positive:

$$S_v(p) = \underbrace{e^{i\phi_1}}_{\substack{\text{left loop} \\ \text{positive}}} \underbrace{\frac{1}{\sqrt{2}}}_{2 \rightarrow 4} \underbrace{e^{-i\phi_2}}_{\substack{\text{right loop} \\ \text{negative}}} \underbrace{\frac{1}{\sqrt{2}}}_{3 \rightarrow 1} \underbrace{e^{i\phi_1}}_{\substack{\text{left loop} \\ \text{positive}}} \underbrace{\frac{-1}{\sqrt{2}}}_{2 \rightarrow 3} \underbrace{e^{i\phi_2}}_{\substack{\text{right loop} \\ \text{positive}}} \underbrace{\frac{1}{\sqrt{2}}}_{4 \rightarrow 1} = \frac{-1}{4} e^{i2\phi_1}.$$

It will be convenient to see the product  $S_v(p)$  corresponding to the path  $(\nu_1, \nu_2, \dots, \nu_{2n})$  divided into three factors

- the product of all phase factors

$$e^{i \sum_{j=1}^n \nu_{2j-1} \phi_1} \cdot e^{i \sum_{j=1}^n \nu_{2j} \phi_2},$$

- the product of absolute values of scattering coefficients

$$\left( \frac{1}{\sqrt{2}} \right)^{2n} = \frac{1}{2^n};$$

- the product of sign factors  $\pm 1$ .

Our next claim is that only paths that every second time go around the right loop in a different direction give a contribution into the trace formula. Consider the path  $p'$  that contains the sequence  $(\dots, \underbrace{+}_{2m}, \underbrace{+}_{2m+1}, \underbrace{+}_{2m+2} \dots)$ . Then, the contribution from the path  $p''$  obtained from  $p'$  by reversing the edge with the number  $2m + 1$ , *i.e.* given by  $(\dots, \underbrace{+}_{2m}, \underbrace{-}_{2m+1}, \underbrace{+}_{2m+2} \dots)$ , cancels the contribution from  $p'$ . Really, the phase contributions from  $p'$  and  $p''$  are the same, the absolute values are also the same, while the product of signs for  $p'$  contains  $(-1) \times 1$  corresponding to transitions  $3 \rightarrow 2$  and  $1 \rightarrow 4$ , in contrast to the product  $1 \times 1$  appearing in the product for  $p''$  (corresponds to the transitions  $3 \rightarrow 1$  and  $2 \rightarrow 4$ , all other coefficients are the same). Similarly contributions from the paths given by  $(\dots, \underbrace{-}_{2m}, \underbrace{-}_{2m+1}, \underbrace{-}_{2m+2} \dots)$  and  $(\dots, \underbrace{-}_{2m}, \underbrace{+}_{2m+1}, \underbrace{-}_{2m+2} \dots)$  cancel each other.

We now assume that the path  $p'$  contains the sequence  $(\dots, \underbrace{+}_{2m}, \underbrace{+}_{2m+1}, \underbrace{-}_{2m+2} \dots)$ , then the contribution from  $p''$  corresponding to  $(\dots, \underbrace{+}_{2m}, \underbrace{-}_{2m+1}, \underbrace{-}_{2m+2} \dots)$  is just the same. It follows that only the paths of the form  $(\nu_1, +, \nu_3, -, \nu_5, +, \nu_7, -, \dots)$  and  $(\nu_1, -, \nu_3, +, \nu_5, -, \nu_7, +, \dots)$  survive in the series. Every such path has a discrete length (the number of edges it comes across) being multiple of 4. The phase contribution from such paths is zero, since we assumed  $\phi_1 = 0$ . It follows that the sum over the periodic paths starting with the left loop does not depend on  $\phi_2$ . A similar result holds for the other sum, explaining the reason why the spectrum of the magnetic Schrödinger operator on  $\Gamma_\infty$  does not depend on  $\phi_2$ , provided  $\phi_1 = 0$ .

Let us continue to calculate the sum over the periodic orbits. We have seen that only orbits of lengths  $2n\mathcal{L}$  (discrete length  $4n$ ) make a contribution to the series. Consider, for example, the orbits of length  $2\mathcal{L}$ . Only the orbits of the form  $(\nu_1, +, \nu_3, -)$  and  $(\nu_1, -, \nu_3, +)$  give nonzero contributions. The phase contribution is  $e^{i0} = 1$ . The absolute value contribution is  $\left(\frac{1}{\sqrt{2}}\right)^4 = \frac{1}{4}$ . The sign contribution is  $-1$ . Together, there are  $4 \times 2$  such orbits, since the signs  $\nu_1, \nu_3$  can be chosen freely. So, the total contribution to the series is:  $-\ell_1 2 \cos k2\mathcal{L}$ .

Similarly, contribution from the orbits of length  $2n\mathcal{L}$  is  $\ell_1 2(-1)^n \cos k2\mathcal{L}n$ . Taking into account contribution from the paths from  $\mathbb{P}_r$  (starting by first going around the right loop), we obtain the following expression:

$$\begin{aligned} u(k) &= \frac{\mathcal{L}}{\pi} + \frac{1}{\pi} \underbrace{(\ell_1 + \ell_2)}_{=\mathcal{L}} \sum_{n=1}^{\infty} 2(-1)^n \cos k2\mathcal{L}n \\ &= \frac{\mathcal{L}}{\pi} + \frac{\mathcal{L}}{\pi} \left( \sum_{m=1}^{\infty} (2e^{ik4\mathcal{L}m} - e^{ik2\mathcal{L}m}) + \sum_{m=1}^{\infty} (2e^{-ik4\mathcal{L}m} - e^{-ik2\mathcal{L}m}) \right) \\ &= \frac{2\mathcal{L}}{\pi} \sum_{m \in \mathbb{Z}} e^{-ik4\mathcal{L}m} - \frac{\mathcal{L}}{\pi} \sum_{m \in \mathbb{Z}} e^{-ik2\mathcal{L}m}, \end{aligned}$$

which coincides with the expression (25) obtained using the left hand side of trace formula (23).

The performed calculations show why the Aharonov-Bohm effect is not present if one of the fluxes is zero: contributions from the periodic orbits going with non-zero flux cancel each other. Conversely, if one of the fluxes is not zero, then the spectrum depends

on the other flux, as can be seen from equation (16). Similar results hold even if one of the fluxes is an integer multiple of  $\pi$ . It is not so difficult to propose different examples of graphs, where similar effects are observed. Trace formulae, together with our explicit calculations, provide a methodology to construct such graphs.

## 5. Acknowledgements

The work of PK was partially supported by the Swedish Research Council (Grant D0497301) and ZiF-Zentrum für interdisziplinäre Forschung, Bielefeld (Cooperation Group Discrete and continuous models in the theory of networks). The authors would like to thank Muhammad Usman for careful reading of the manuscript.

## References

- [1] Y. Aharonov, D. Bohm. Significance of electromagnetic potentials in quantum theory. *Phys. Rev.*, 1959, **115**, P. 485–491.
- [2] G. Berkolaiko, P. Kuchment. *Introduction to quantum graphs*. Mathematical Surveys and Monographs, Amer. Math. Soc., 2013, **186** Providence, RI.
- [3] B. Gutkin and U. Smilansky. Can one hear the shape of a graph? *J. Phys. A*, 2001, **34**, P. 6061–6068.
- [4] V. Kostrykin, R. Schrader. Quantum wires with magnetic fluxes, Dedicated to Rudolf Haag. *Comm. Math. Phys.*, 2003, **237** (1–2), P. 161–179.
- [5] T. Kottos and U. Smilansky. Periodic orbit theory and spectral statistics for quantum graphs. *Ann. Physics*, 1999, **274** (1), P. 76–124.
- [6] P. Kurasov. Graph Laplacians and topology. *Arkiv för Matematik*, 2008, **46**, P. 95–111.
- [7] P. Kurasov. Schrödinger operators on graphs and geometry. I. Essentially bounded potentials. *J. Funct. Anal.*, 2008, **254** (4), P. 934–953.
- [8] P. Kurasov. Inverse problems for Aharonov-Bohm rings. *Math. Proc. Cambridge Philos. Soc.*, 2010, **148** (2), P. 331–362.
- [9] P. Kurasov. Quantum graphs: spectral theory and inverse problems. To appear in Birkhäuser.
- [10] P. Kurasov and M. Nowaczyk. Inverse spectral problem for quantum graphs. *J. Phys. A*, 2005, **38** (22), P. 4901–4915.
- [11] P. Kurasov and M. Nowaczyk. Geometric properties of quantum graphs and vertex scattering matrices. *Opuscula Math.*, 2010, **30** (3), P. 295–309.
- [12] O. Post. *Spectral analysis on graph-like spaces*. Lecture Notes in Mathematics, 2012, **2039**, 431 p.
- [13] J.-P. Roth. Le spectre du laplacien sur un graphe. *Theorie du potentiel, Lecture Notes in Math.*, 1984, **1096**, P. 521–539 [in French].

# Storage and separation of CO<sub>2</sub> and CH<sub>4</sub> in boron imidazolate frameworks: a theoretical study from Monte Carlo simulation

B. Assfour\*<sup>1,2</sup>, S. Leoni<sup>1</sup>

<sup>1</sup>Institut für Physikalische Chemie, Technische Universität Dresden,  
01062 Dresden, Germany

<sup>2</sup>Department of Chemistry, Atomic Energy Commission, P.O. Box 6091, Damascus, Syria  
cscientific@aec.org.sy

PACS 87.15.ag

DOI 10.17586/2220-8054-2015-6-3-320-331

In this work, the storage of pure CO<sub>2</sub> and CH<sub>4</sub> gases and separation of their binary mixture in new type of nanostructured materials called boron imidazolate frameworks (BIFs) have been investigated using atomistic simulation to provide information for material selection in adsorbent designs. Adsorption isotherms and adsorption selectivities were computed using grand canonical Monte Carlo (GCMC). Our results showed that BIFs exhibit significantly higher selectivities for separation of CO<sub>2</sub> from CH<sub>4</sub> compared to other widely studied metal organic framework (MOF) materials.

**Keywords:** Adsorption, MOFs, BIFs, Gas Separation and Selectivity.

*Received: 3 March 2015*

*Revised: 30 March 2015*

## 1. Introduction

The continued combustion of fossil fuel causes a rapid increase in the concentration of carbon dioxide (CO<sub>2</sub>) in earth's atmosphere, which is believed to be responsible for global warming and climate change [1]. In order to avoid CO<sub>2</sub> from reaching the atmosphere, the capture of CO<sub>2</sub> and the utilization of a clean energy source are prominent. Methane, the primary component of natural gas, is an appealing energy source. Compared to gasoline, methane provides much more energy because of its higher hydrogen-to-carbon ratio, and has much lower CO<sub>2</sub> emissions [2]. However, the practical storage of methane in automobiles is still a prime challenge. According to U.S. Department of Energy (DOE) requirements, the storage capacity of material-based adsorbed methane should exceed 180 cm<sup>3</sup> (STP). cm<sup>-3</sup> at 298 K and 35 bar for practical on-board methane storage, where cm<sup>3</sup> (STP).cm<sup>-3</sup> means standard temperature and pressure equivalent volume of methane per volume of the adsorbent material. In term of energy density, this is equivalent to methane compressed at 250 bar and room temperature [3].

In parallel to the environmentally friendly fuel research, a large amount of work has been focused on the development of novel techniques for the separation, capture, and storage of CO<sub>2</sub>. The former is a key step in carbon sequestration for the prevention of global warming. Furthermore, CO<sub>2</sub> is an impurity in natural gas, biogas and syngas [4]. Its presence will reduce the overall energy content of gas streams. Therefore, beside the storage of pure CO<sub>2</sub> and CH<sub>4</sub> components, it is of large importance to separate their mixtures. One promising method for separation of CO<sub>2</sub> from its mixtures is adsorption separation by nanoporous materials. Among the potential adsorbent candidates (i.e. zeolites, activated carbon and

so on) [5,6], metal organic frameworks (MOFs) have emerged as a front-runner. MOFs are ultra-porous crystalline materials that are able to trap and store voluminous amounts of gas molecules (i.e. CH<sub>4</sub>, H<sub>2</sub>, N<sub>2</sub> and CO<sub>2</sub>) [7]. The fact that the structure of MOFs can be tailored and chemically functionalized to selectively adsorb specific gas in a mixture gives them an enormous advantage over other nanoporous materials. Furthermore, MOFs have a versatile ability to store and release gases with fast kinetics and high reversibility over multiple cycles.

Boron imidazolate frameworks (BIFs) [8], a novel subclass of MOFs, are considered as promising materials for hydrogen storage applications [9]. Unlike the zinc imidazolate system (ZIFs), BIFs contain light chemical elements (i.e. Li and B) as framework vertices linked by different imidazolate ligands (im). The coordinatively unsaturated centers presented in BIFs have been shown to be favorable for enhancing gas uptake capacity [10]. Recently, Yang *et al.* have prepared novel neutral boron-imidazolate-framework (BIF-35) based on the assembly of tetradentate B(im)<sub>4</sub> ligands and (CdBr) units, illustrating the ability to include a much wider variety of metal ions than traditional tetrahedral metal centers in order to produce new BIFs [11].

In contrast to the extensive studies on other MOFs, investigations of BIFs are rather limited. Zheng and co-workers integrated metal carboxylates and boron imidazolates to prepare a novel family of BIFs called MC-BIFs [12]. Amongst these materials, MC-BIF-2H exhibits extraordinary volumetric capacity for storing CO<sub>2</sub> (81 L/L at 273 K and ambient pressure), comparable to that previously reported for a highly porous ZIF-69 (83 L/L) [13]. Zhang *et al.* developed a new strategy for the design of zeolite-type MOFs. They successfully synthesized the first interrupted zeolite A (4-connected tetrahedral framework) with a 3-connected network denoted as BIF-20. The initial H<sub>2</sub> uptake of BIF-20 is remarkably high. However, The CO<sub>2</sub> uptake capacity (34.8 cm<sup>3</sup>/g under ambient condition) is comparable to that reported for other ZIFs [14]. Wang *et al.* synthesized new set of BIFs with ACO and ABW topologies. The ACO-type material shows interesting gas selectivity of CO<sub>2</sub> over N<sub>2</sub> and CH<sub>4</sub> [15]. Recently, Zang and co-workers [16] reported highly porous *ctn*-type BIF material with high CO<sub>2</sub> storage capacity (104.3 cm<sup>3</sup>/g at 273 K). Moreover, this material presents high selectivity for the adsorption of CO<sub>2</sub> over CH<sub>4</sub> at ambient conditions. Jayaramulu *et al.* have synthesized a new three-dimensional boron based MOF, and made use of it as a precursor to produce a borocarbonitride (BC<sub>4</sub>N). Besides having an unusual coral-like morphology, BC<sub>4</sub>N has a high BET surface area (988 m<sup>2</sup>/g) and exhibits significant CO<sub>2</sub> and H<sub>2</sub> uptake [17].

Complementary to experimental studies, a number of computational investigations of gas adsorption in various types of nanoporous compounds have been reported. Most of these studies investigated the chemical structure, network topology, and porosity effects on the adsorption properties of the materials [18-20].

In this paper, we extend our previous work on BIFs by using molecular modeling to examine CO<sub>2</sub> storage and separation (relative to CH<sub>4</sub>) in series of BIFs with different topologies. The results of this work may provide useful information for unlocking the potential of these materials in storage and separation applications and help the design of new adsorbents with improved properties by studying the effect of topology on CO<sub>2</sub> adsorption. The crystal structures of these materials are shown in Fig 1. For a description of topology symbols, see the Database of Zeolite Structures, <http://www.iza-structure.org/databases/>.

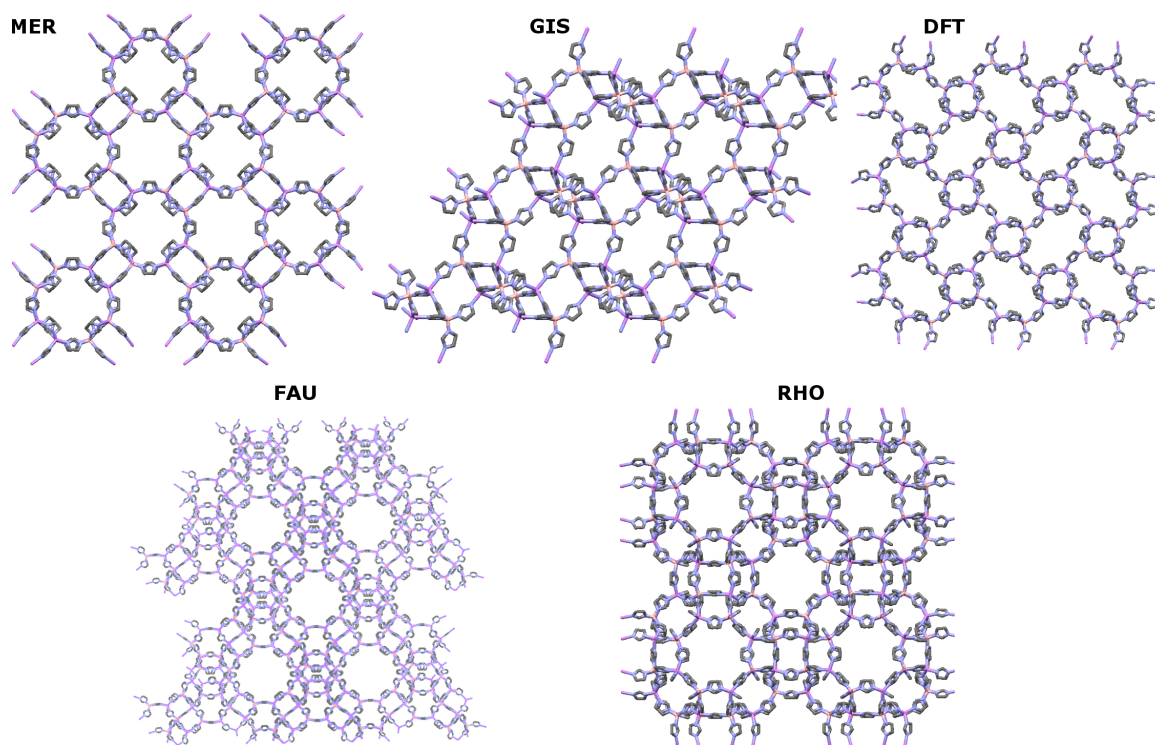


FIG. 1. Crystal structures of the MOFs studied in this work. The structures are not drawn to scale. B: pink, C: grey, N: blue, Li: cyan. Hydrogen atoms are omitted for clarity

## 2. Model

The methane and carbon dioxide adsorption and separation in BIF structures were simulated with the grand canonical Monte-Carlo (GCMC) method using the multipurpose simulation code MUSIC [21]. The code MUSIC was successfully used to simulate the adsorption of different gases, such as  $\text{CH}_4$ ,  $\text{CO}_2$  and  $\text{H}_2$ , on a variety of nanoporous materials [22-26]. In the grand canonical ensemble, the chemical potential, temperature and volume are constant. The chemical potential was converted to fugacity using Peng–Robinson equation of state [27]. The intermolecular interactions were modeled by the Lennard-Jones pair potential between all sites to represent van der Waals interactions. A methane molecule is modeled as united atom, where potential parameters are taken from Goodbody *et al.* [28]. The carbon dioxide molecule is modeled using TraPPE force field [29]. In this model, the  $\text{CO}_2$  is treated as three-site linear molecule, where the C–O bond measures 1.16 Å. This model can reproduce the experimental gas-phase quadrupole moment of carbon dioxide by placing partial charges on C (+0.70  $e$ ) and O (−0.35  $e$ ) atoms. The potential parameters of BIF atoms were taken from the universal force field (UFF) of Rappe *et al.* [30], which has been widely used to study the adsorption of different gases on nanoporous materials [23, 31-33]. Lorentz-Berthelot mixing rules were used to calculate mixed Lennard-Jones parameters. The electrostatic interactions between  $\text{CO}_2$  molecules and the BIF structure were accounted for by placing point charges on each atom. The Bader partitioning scheme was performed on electronic density with the program Dgrid [34] to calculate the charge on individual atoms. The electronic density was calculated with the all-electron, full-potential local orbital (FPLO) minimal basis method [35]. The FPLO method does not have any atomic (or muffin-tin) spheres so that the whole space is treated in a uniform manner. The atomic

charges were calculated for zni topology, and kept permanent from structure to structure. The Ewald summation technique is used to calculate the electrostatic interactions.

The simulation box, representing each BIF structure, contains 8 (2×2×2) unit cells. Adsorbents were treated as rigid with atom positions taken from Ref [36]. The periodic boundary conditions were employed in all dimensions to mimic the crystalline periodicity. Interactions beyond 13 Å were neglected. Each simulation point consisted of 5×10<sup>6</sup> Monte-Carlo steps to reach equilibrium followed by an extra 5×10<sup>6</sup> steps to take the statistical average.

GCMC simulation delivers the absolute amount adsorbed ( $N_{abs}$ ), whereas experiments give the excess amount of adsorption ( $N_{ex}$ ). In order to make the comparison, the excess amount should be converted into absolute as:

$$N_{ex} = N_{abs} - \rho_p V_{free} \quad (1)$$

where  $\rho_p$  is the density of the bulk phase [37], and  $V_{free}$  is the available pore volume per unit cell of the sorbent estimated using a non-adsorbing species (helium) as a probe [23, 25, 26].

The accessible surface area was calculated by “rolling” a probe molecule with a diameter equal to the Lennard–Jones parameter for N<sub>2</sub> (3.681 Å) over the framework’s surface as described in Ref [38]. Calculation of the isosteric heat of adsorption ( $Q_{st}$ ) at zero coverage was performed through the fluctuations over the internal energy and from fluctuations of number of particles in the system by considering a very low pressure. These calculations are reported in more detail elsewhere [39].

In adsorption-based separation process, a good indication of the ability for separation is the adsorption selectivity for different components in gas mixture. The adsorption selectivity of component  $i$  relative to component  $j$  is defined by:

$$S = \frac{x_i/x_j}{y_i/y_j} \quad (2)$$

where  $x_i$  and  $x_j$  are the molar fractions of component  $i$  and  $j$  in adsorbed phase and  $y_i$  and  $y_j$  are the molar fractions in the gas phase.

### 3. Results and discussion

#### 3.1. Adsorption of pure components of CH<sub>4</sub> and CO<sub>2</sub>

Table 1 gives the density, pore volume and accessible surface area for all five BIFs as well as the initial isosteric heats of adsorption for pure CO<sub>2</sub> and CH<sub>4</sub> in each material. All materials provide moderate surface area and low density, indicating that they may be promising candidates for gas storage applications [2]. The material with FAU topology has the lowest density (0.492 g/cm<sup>3</sup>) as well as the highest surface area (2773 m<sup>2</sup>/g), which is higher than that of zeolites, porous silica and lower than some MOFs [40] or COFs [25]. As is the case for most CH<sub>4</sub> sorbents, the  $Q_{st}$  is in the range of 12–18 kJ.mol<sup>-1</sup> [41–46]. However, for MOFs exhibiting very high methane uptake, such as PCN-14 [47], the  $Q_{st}$  is much larger (15–30 kJ.mol<sup>-1</sup>), which is known to be responsible for the exceptionally high methane uptake at low pressure.

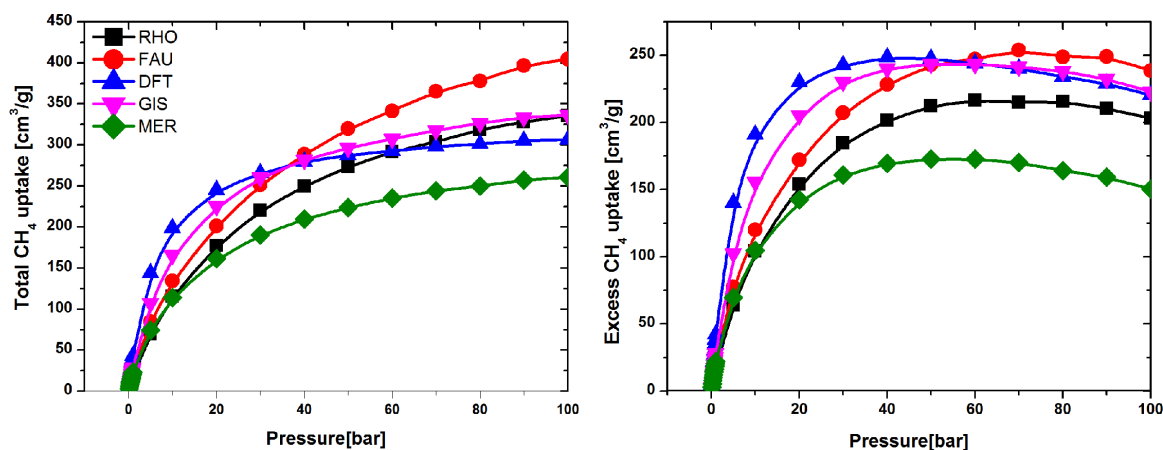
In the given material, the  $Q_{st}$  of CO<sub>2</sub> is larger than that of CH<sub>4</sub>, indicating that CO<sub>2</sub> is more strongly adsorbed. Consequently, BIFs show more affinity toward CO<sub>2</sub> at lower pressures. This is expected because the CO<sub>2</sub> molecule has a greater interaction with the adsorbent than CH<sub>4</sub> because it contains three interaction sites plus the role of electrostatic

TABLE 1. Summary of calculated properties of different BIFs

Material	density (g/cm <sup>3</sup> )	pore vol- ume (cm <sup>3</sup> /g)	accessible surface area for N <sub>2</sub>	Initial $Q_{st}$ for CH <sub>4</sub> (kJ/mol)	Initial $Q_{st}$ for CO <sub>2</sub> (kJ/mol)
RHO	0.566	1.11	2654	12.15	38.52
FAU	0.492	1.41	2773	14.61	36.55
DFT	0.730	0.74	1686	17.33	49.93
GIS	0.627	0.97	2625	13.11	36.11
MER	0.635	0.95	2613	12.57	37.72

interactions, which is expected to be enhanced compared to other MOFs due to the asymmetries in the metal sites. The  $Q_{st}$  is in the range of 36–50 kJ.mol<sup>-1</sup> higher than those for other MOFs, i.e. UiO-68(Zr) (20 kJ.mol<sup>-1</sup>) [48], MOF-5 (34 kJ.mol<sup>-1</sup>) [49], CPO-27. (38–43 kJ mol<sup>-1</sup>) [44]. For both CO<sub>2</sub> and CH<sub>4</sub>, The  $Q_{st}$  is the largest in DFT. This is probably due to the lower porosity.

The predicted gravimetric methane uptakes in selected BIFs at 298 K are shown in Figure 2. As expected, all materials show type I for total and excess isotherms, with profiles that depend on the material. The material with DFT topology shows the highest excess uptake almost all over the pressure range. Its saturation uptake is calculated to be 248 cm<sup>3</sup>/g at 40 bar, which is close to 252 cm<sup>3</sup>/g (290 K, 35 bar) for PCN-14, which holds the current record for methane storage [47]. Although, recently Peng *et al.* [50] discovered that packed HKUST-1 exhibits a room-temperature volumetric methane uptake that exceeds any value reported to date. The material with FAU topology shows a slightly higher saturation gravimetric uptake (254 cm<sup>3</sup>/g) but at higher saturation pressure (70 bar). The total uptake that a material can store is more relevant to the practicability of using CH<sub>4</sub> as a fuel. In terms of total methane uptake, the best material at 100 bar is the one with FAU topology, with 405 cm<sup>3</sup>/g followed by GIS and RHO (336 cm<sup>3</sup>/g) and DFT (306 cm<sup>3</sup>/g) respectively.

FIG. 2. Excess and total gravimetric CH<sub>4</sub> uptake in BIFs

Concerning the volumetric uptake (Figure 3), we see that all BIFs materials do not reach the DOE target in a total volumetric uptake basis at 35 bar. However, we predict that materials with FAU and RHO topologies perform nicely, having uptakes of 200 and

190 v(STP)/v at 100 bar, respectively, suggesting that they could be suitable for practical applications of methane storage.

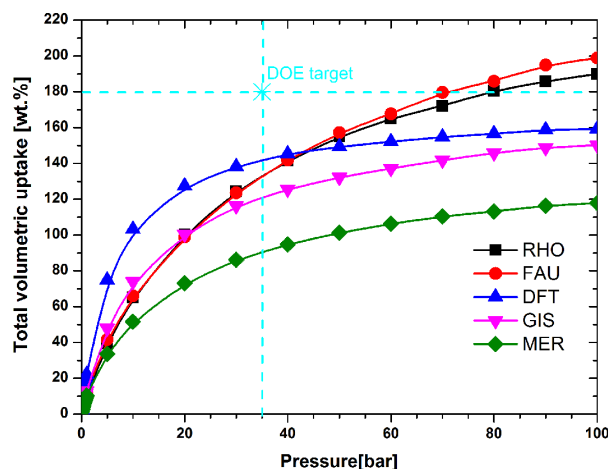


FIG. 3. Total volumetric CH<sub>4</sub> uptake in BIFs

High and low pressure CO<sub>2</sub> isotherms for all five BIFs were calculated and are presented in Figure 4. Unlike the CH<sub>4</sub> isotherm, CO<sub>2</sub> isotherms show dramatic steps, similar to those reported for CO<sub>2</sub> in other MOFs [32, 51-53] indicating a very high affinity for CO<sub>2</sub> gas. Compared with other porous materials [22, 54], BIFs reach their saturation uptakes at relatively low pressures (around 10 bar). The material with FAU topology shows the highest excess and total uptake (figure 4) almost over the entire pressure range. The total CO<sub>2</sub> storage capacity for FAU at 50 bar reaches the value of 450 mg.g<sup>-1</sup>. Such value is significantly lower than those reported for other recently synthesized materials such as MOF-200 (2400 mg.g<sup>-1</sup>) and NU-100 (2315 mg.g<sup>-1</sup>). This is due to very large pore volumes provided by these materials, where the amounts of CO<sub>2</sub> uptake are directly related to the total pore volume [54]. However, BIFs present very high CO<sub>2</sub> capacities at low pressure range (left panel of figure 4). For instance the calculated excess capacity of FUA at 1 bar (298 mg.g<sup>-1</sup>) is almost three times higher than that reported for NU-100 (110 mg.g<sup>-1</sup>) under the same conditions [22] and more than 50% greater than that of ZIF-69 (130 mg.g<sup>-1</sup>) at 273 K, which makes this type of materials very promising candidates for CO<sub>2</sub> capture, especially at low pressures.

### 3.2. Adsorption of CO<sub>2</sub>/CH<sub>4</sub> mixture

In this section, the CO<sub>2</sub> selectivity for CO<sub>2</sub>/CH<sub>4</sub> mixtures with different pressures at room temperature is discussed. Figure 5 shows the adsorption isotherms for an equimolar mixture of CH<sub>4</sub>/CO<sub>2</sub> in BIFs as a function of pressure. We find that in all BIFs, CO<sub>2</sub> is more readily adsorbed than CH<sub>4</sub> at low pressures (below 10 bar). This is due to stronger interaction with structures as explained above. However, at high pressures, the number of CH<sub>4</sub> molecules adsorbed per unit cell increases exponentially and CH<sub>4</sub> become more favorably adsorbed.

Figure 5 (right bottom) illustrates the effect of pressure on the CO<sub>2</sub> selectivity at room temperature for five BIFs. It shows that selectivities for CO<sub>2</sub> are different between BIFs at low pressures with the order RHO > FAU > GIS > DFT > MER. It can be seen that selectivities decrease exponentially along with rising pressure and become close at pressures

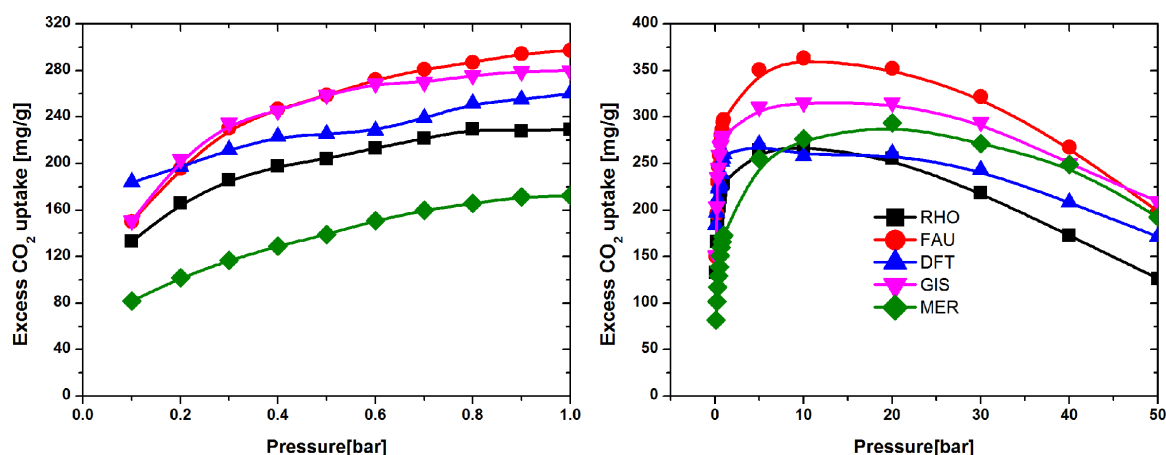


FIG. 4. Low (left) and high (right) excess gravimetric CO<sub>2</sub> uptake in BIFs

higher than 1.0 bar. Therefore, we conclude that the topology of BIFs plays the main role on the CO<sub>2</sub> selectivity rather than pressure.

Keskin studied the adsorption selectivities of ZIF type materials for equimolar CO<sub>2</sub>/CH<sub>4</sub> mixture [55]. Results showed that adsorption selectivities of ZIFs are better than those of IRMOFs due to their smaller pore sizes and better confinement of CO<sub>2</sub> molecules. In contrast to BIFs, the selectivities for ZIFs increase with pressure. ZIF-3 (DFT topology) provides the best selectivity with 5 at 0.1 bar and up to 12 at 50 bar, whereas, for BIFs, RHO has the maximum selectivity with 50 at 0.1 bar down to almost 0 at 50 bar. Therefore, in sources such as flue gas, where the typical anticipated partial pressure of CO<sub>2</sub> is about 0.1 bar [56], BIFs outperform ZIFs and related MOFs because of their suitable pore sizes. However, at high pressures MOFs are better for CO<sub>2</sub> capture because of their larger pore sizes. This makes BIFs very promising candidates for CO<sub>2</sub> separation at low pressures.

#### 4. Preferential adsorption sites

To understand the adsorption mechanism for CH<sub>4</sub> and CO<sub>2</sub> on BIFs, preferential adsorption sites were investigated. Since the picture of adsorption sites for all BIFs is similar, we choose DFT BIF as a representative. Figure 6 shows equilibrium snapshots of adsorbed CH<sub>4</sub>/CO<sub>2</sub> mixture in the simulation unit cell at three different pressures, 0.1, 1.0, and 10 bar. It is clear that CO<sub>2</sub> molecules preferentially adsorb in the small pores formed by imidazole linkers (figure 7 (a)), while CH<sub>4</sub> molecules cannot enter the small pores because their sizes are smaller than the kinetic diameter of CH<sub>4</sub>. Therefore CH<sub>4</sub> molecules are accommodated in the large pore. With increasing pressure, the CO<sub>2</sub> molecules also adsorb in large pores near to the polar centers in the framework because the electrostatic contribution of CO<sub>2</sub> is larger than that of CH<sub>4</sub> (figure 7 (b)). At higher pressures, the adsorption sites are saturated and the electrostatic interaction decreases to a negligible value. Therefore, CO<sub>2</sub> molecules are no longer favorable and together with CH<sub>4</sub> molecules, fill in the free space in the pores far from the charge centers. This behavior explains the large uptake of CO<sub>2</sub> at low pressure.

Generally, in separation processes, the differences in electronic properties and size of molecules are used. However, the relatively small difference in kinetic diameters between CO<sub>2</sub> (3.30 Å) and CH<sub>4</sub> (3.76 Å) makes separation based solely on molecule size a very difficult task. Therefore, many MOFs with unsaturated metal sites were synthesized to enhance adsorption of quadrupolar CO<sub>2</sub> over non-quadrupolar CH<sub>4</sub> and to make the separation beneficial. Bae *et al.* [57] found that incorporation of Li cations into MOFs, by either chemical reduction

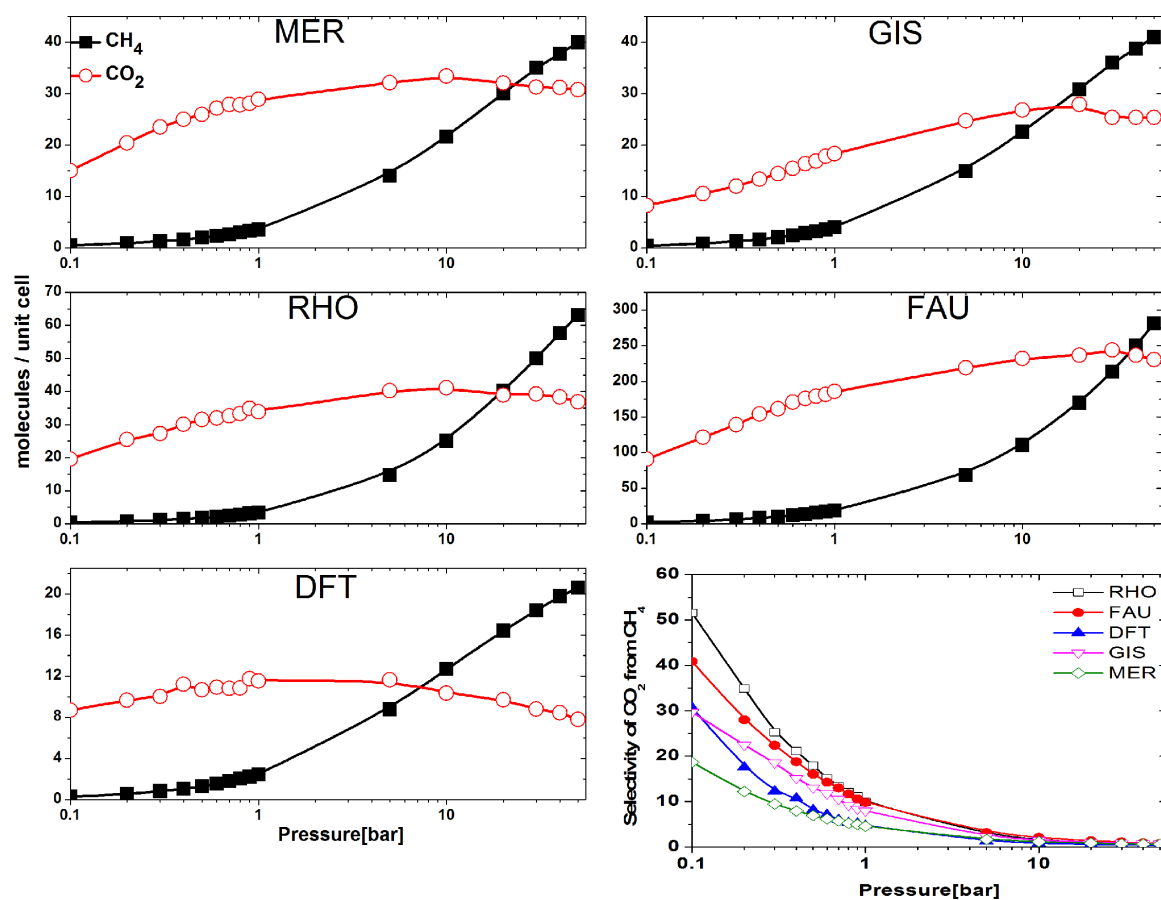


FIG. 5. Equimolar mixture adsorption isotherms of CH<sub>4</sub>/CO<sub>2</sub> in five BIFs. Adsorption selectivity of BIFs for CO<sub>2</sub>/CH<sub>4</sub> mixture at room temperature (right bottom)

or cation exchange, significantly improved the CO<sub>2</sub>/CH<sub>4</sub> selectivity. In case of BIFs both effects are presented, the unsaturated metal sites and optimal pore size. This may explain the large CO<sub>2</sub> uptake at low pressure relative to other MOFs.

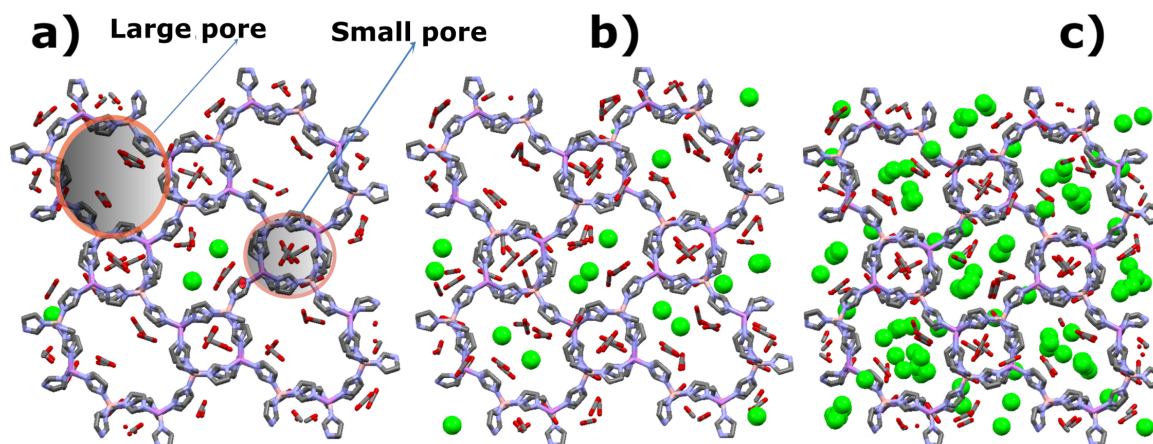


FIG. 6. Snapshots of mixture of CO<sub>2</sub> and CH<sub>4</sub> in DFT for low ((a) 0.1 bar), normal ((b) 1 bar), and intermediate ((c) 10 bar) loading. CH<sub>4</sub> molecules are represented in green

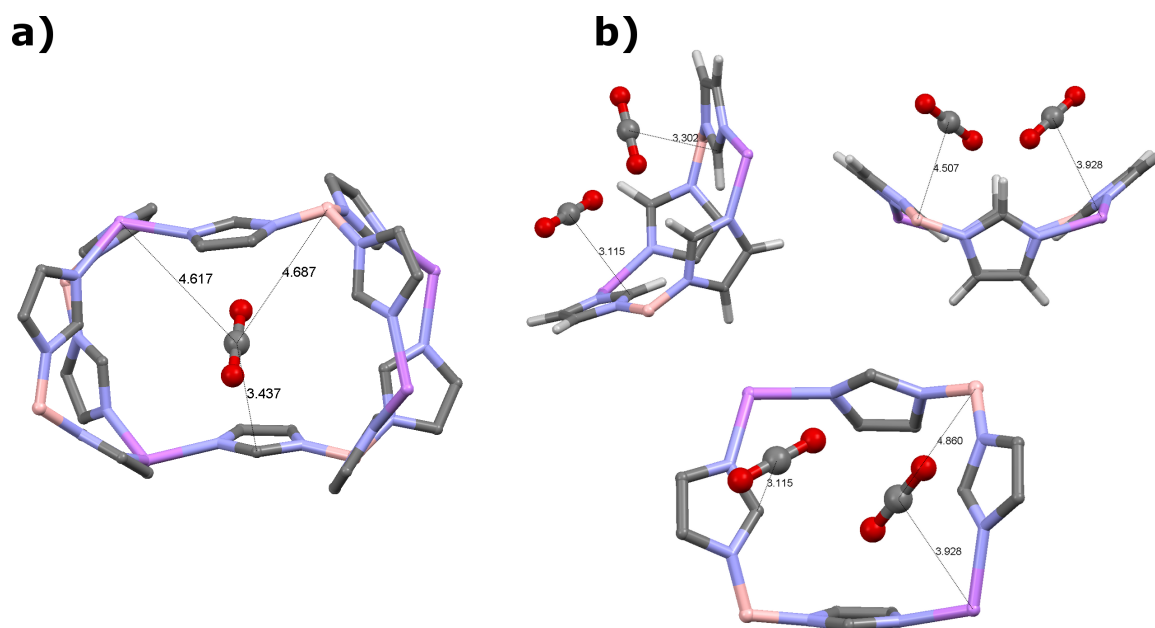


FIG. 7. CO<sub>2</sub> adsorption site in the small (a) and in the large cage (b). Distances are reported in angstroms

## 5. Conclusions

We have used computational modeling to study the storage and separation of CO<sub>2</sub> and CH<sub>4</sub> in a new class of porous materials known as BIFs. Our results show that BIFs could be suitable for practical applications of methane storage, particularly from a gravimetric point of view. We have also established that BIFs are highly selective for the absorption of CO<sub>2</sub> at low pressures as compared to other MOFs. Such high selectivities are believed to be the result of both appropriate pore sizes and unsaturated metal sites, which are known to significantly influence the CO<sub>2</sub> uptake capacity. The results of this work will provide guidelines for the optimum choice of BIF materials to be used in gas storage and separation applications.

## Acknowledgments

The author is highly grateful to *Prof. Dr. I.othman* and *Dr. Z.ajji* for giving the opportunity and help performing this work.

## References

- [1] Haszeldine R.S. Carbon Capture and Storage. How Green Can Black Be? *Science*, 2009, **325**(5948), P. 1647-52.
- [2] Duren T., Sarkisov L., Yaghi O.M., Snurr R.Q. Design of new materials for methane storage. *Langmuir*, 2004, **20**(7), P. 2683-9.
- [3] Wegrzyn J., Gurevich M. *Appl Energy*, 1996, **55**, P. 71.
- [4] Singh D., Croiset E., Douglas P.L., Douglas M.A. Techno-economic study of CO<sub>2</sub> capture from an existing coal-fired power plant: MEA scrubbing vs. O<sub>2</sub>/CO<sub>2</sub> recycle combustion. *Energy Conversion and Management*, 2003, **44**(19), P. 3073-91.
- [5] D'Alessandro D.M., Smit B., Long J.R. Carbon Dioxide Capture: Prospects for New Materials. *Angewandte Chemie International Edition*, 2010, **49**(35), P. 6058-82.
- [6] Mulgundmath V.P., Tezel F.H., Saatcioglu T., Golden T.C. Adsorption and separation of CO<sub>2</sub>/N<sub>2</sub> and CO<sub>2</sub>/CH<sub>4</sub> by 13X zeolite. *The Canadian Journal of Chemical Engineering*, 2012, **90**(3), P. 730-8.

- [7] Furukawa H., Cordova K.E., O’Keeffe M., Yaghi O.M. The Chemistry and Applications of Metal-Organic Frameworks. *Science*, 2013, **341**(6149).
- [8] Zhang H., Wu T., Zhou C., Chen S.M., Feng P.Y., Bu X.H.. Zeolitic Boron Imidazolate Frameworks. *Angewandte Chemie-International Edition*, 2009, **48**(14), P. 2542-5.
- [9] Baburin I.A., Assfour B., Seifert G., Leoni S. Polymorphs of lithium-boron imidazolates: energy landscape and hydrogen storage properties. *Dalton Transactions*, 2011, **40**(15), P. 3796-8.
- [10] Horike S., Shimomura S., Kitagawa S. Soft porous crystals. *Nature Chem.*, 2009, **1**, P. 695-704.
- [11] Yang E., Wang L., Zhang J. A luminescent neutral cadmium(ii)-boron(iii)-imidazolate framework with sql net. *CrystEngComm.*, 2014, **16**(14), P. 2889-91.
- [12] Zheng S., Wu T., Zhang J., Chow M., Nieto R.A., Feng P., et al. Porous Metal Carboxylate Boron Imidazolate Frameworks. *Angewandte Chemie International Edition*, 2010, **49**(31), P. 5362-6.
- [13] Banerjee R., Phan A., Wang B., Knobler C., Furukawa H., O’Keeffe M., et al. High-throughput synthesis of zeolitic imidazolate frameworks and application to CO<sub>2</sub> capture. *Science*, 2008, **319**(5865), P. 939-43.
- [14] Zhang H.-X., Wang F., Yang H., Tan Y.-X., Zhang J., Bu X. Interrupted Zeolite LTA and ATN-Type Boron Imidazolate Frameworks. *Journal of the American Chemical Society*, 2011, **133**(31), P. 11884-7.
- [15] Wang F., Shu Y.-B., Bu X., Zhang J. Zeolitic Boron Imidazolate Frameworks with 4-Connected Octahedral Metal Centers. *Chemistry – A European Journal*, 2012, **18**(38), P. 11876-9.
- [16] Zhang H.-X., Fu H.-R., Li H.-Y., Zhang J., Bu X. Porous ctn-Type Boron Imidazolate Framework for Gas Storage and Separation. *Chemistry – A European Journal*, 2013, **19**(35), P. 11527-30.
- [17] Jayaramulu K., Kumar N., Hazra A., Maji T.K., Rao C.N.R. A Nanoporous Borocarbonitride (BC<sub>4</sub>N) with Novel Properties Derived from a Boron-Imidazolate-Based Metal–Organic Framework. *Chemistry – A European Journal*, 2013, **19**(22), P. 6966-70.
- [18] Fischer M., Bell R.G. Interaction of hydrogen and carbon dioxide with sod-type zeolitic imidazolate frameworks: A periodic DFT-D study. *Cryst. Eng. Comm.*, 2014, **16**(10), P. 1934-49.
- [19] Mellot-Draznieks C., Kerkeni B. Exploring the interplay between ligand and topology in zeolitic imidazolate frameworks with computational chemistry. *Molecular Simulation*, 2013, **40**(1-3), P. 25-32.
- [20] Galvelis R., Slater B., Cheetham A.K., Mellot-Draznieks C. Comparison of the relative stability of zinc and lithium-boron zeolitic imidazolate frameworks. *Cryst. Eng. Comm.*, 2012, **14**(2), P. 374-8.
- [21] Gupta A., Chempath S., Sanborn M.J., Clark L.A., Snurr R.Q. Object-oriented programming paradigms for molecular modeling. *Mol Simul.*, 2003, **29**(1), P. 29-46.
- [22] Farha O.K., Özgür Yazaydın A., Eryazici I., Malliakas C.D., Hauser B.G., Kanatzidis M.G., et al. De novo synthesis of a metal–organic framework material featuring ultrahigh surface area and gas storage capacities. *Nat Chem.*, 2010, **2**(11), P. 944-8.
- [23] Assfour B., Seifert G. Hydrogen storage in 1D nanotube-like channels metal-organic frameworks: Effects of free volume and heat of adsorption on hydrogen uptake. *International Journal of Hydrogen Energy*, 2009, **34**(19), P. 8135-43.
- [24] Bae Y.-S., Snurr R.Q. Optimal isosteric heat of adsorption for hydrogen storage and delivery using metal-organic frameworks. *Microporous and Mesoporous Materials*, 2010, **132**(1-2), P. 300-3.
- [25] Assfour B., Seifert G. Adsorption of hydrogen in covalent organic frameworks: Comparison of simulations and experiments. *Microporous and Mesoporous Materials*, 2010, **133**(1-3), P. 59-65.
- [26] Assfour B., Leoni S., Yurchenko S., Seifert G. Hydrogen storage in zeolite imidazolate frameworks. A multiscale theoretical investigation. *International Journal of Hydrogen Energy*, 2011, **36**(10), P. 6005-13.
- [27] Peng D.-Y., Robinson D.B. A New Two-Constant Equation of State. *Industrial & Engineering Chemistry Fundamentals*, 1976, **15**(1), P. 59-64.
- [28] Goodbody S.J., Watanabe K., MacGowan D., Walton J.P.R.B., Quirke N. Molecular simulation of methane and butane in silicalite. *Journal of the Chemical Society, Faraday Transactions*, 1991, **87**(13), P. 1951-8.
- [29] Potoff J.J., Siepmann J.I. Vapor–liquid equilibria of mixtures containing alkanes, carbon dioxide, and nitrogen. *AIChE Journal*, 2001, **47**(7), P. 1676-82.
- [30] Casewit C.J., Colwell K.S., Rappe A.K. Application of a universal force field to organic molecules. *Journal of the American Chemical Society*, 1992, **114**(25), P. 10035-46.
- [31] Keskin S., Sholl D.S. Assessment of a Metal-Organic Framework Membrane for Gas Separations Using Atomically Detailed Calculations: CO<sub>2</sub>, CH<sub>4</sub>, N-2, H-2 Mixtures in MOF-5. *Industrial & Engineering Chemistry Research*, 2009, **48**(2), P. 914-22.

- [32] Liu D.H., Zheng C.C., Yang Q.Y., Zhong C.L. Understanding the Adsorption and Diffusion of Carbon Dioxide in Zeolitic Imidazolate Frameworks: A Molecular Simulation Study. *Journal of Physical Chemistry C*, 2009, **113**(12), P. 5004-9.
- [33] Morris W., He N., Ray K.G., Klonowski P., Furukawa H., Daniels I.N., et al. A Combined Experimental-Computational Study on the Effect of Topology on Carbon Dioxide Adsorption in Zeolitic Imidazolate Frameworks. *The Journal of Physical Chemistry C*, 2012, **116**(45), P. 24084-90.
- [34] Kohout M. DGrid. 4.5 ed. Radebeul 2009.
- [35] Koepernik K., Eschrig H. Full-potential nonorthogonal local-orbital minimum-basis band-structure scheme. *Physical Review B*, 1999, **59**(3), P. 1743-57.
- [36] Baburin I.A., Assfour B., Seifert G., Leoni S. Polymorphs of lithium-boron imidazolates: energy landscape and hydrogen storage properties. *Dalton Transactions*, 2011.
- [37] Webbook N.C. Available from: <http://webbook.nist.gov/chemistry/fluid/>.
- [38] Düren T., Millange F., Ferey G., Walton K.S., Snurr R.Q. Calculating geometric surface areas as a characterization tool for metal-organic frameworks. *Journal of Physical Chemistry C*, 2007, **111**, P. 15350-6.
- [39] Nicholson D., Parsonage, N.G. *Computer Simulation and the Statistical Mechanics of Adsorption*. Academic, editor. San Diego, 1982.
- [40] Farha O.K., Eryazici I., Jeong N.C., Hauser B.G., Wilmer C.E., Sarjeant A.A., et al. Metal-Organic Framework Materials with Ultrahigh Surface Areas: Is the Sky the Limit? *Journal of the American Chemical Society*, 2012, **134**(36), P. 15016-21.
- [41] Zhou W., Wu H., Hartman M.R., Yildirim T. Hydrogen and Methane Adsorption in Metal-Organic Frameworks: A High-Pressure Volumetric Study. *The Journal of Physical Chemistry C*, 2007, **111**(44), P. 16131-7.
- [42] Wu H., Zhou W., Yildirim T. Methane Sorption in Nanoporous Metal-Organic Frameworks and First-Order Phase Transition of Confined Methane. *The Journal of Physical Chemistry C*, 2009, **113**(7), P. 3029-35.
- [43] Furukawa H., Yaghi O.M. Storage of Hydrogen, Methane, and Carbon Dioxide in Highly Porous Covalent Organic Frameworks for Clean Energy Applications. *Journal of the American Chemical Society*, 2009, **131**(25), P. 8875-83.
- [44] Dietzel P.D.C., Besikiotis V., Blom R. Application of metal-organic frameworks with coordinatively unsaturated metal sites in storage and separation of methane and carbon dioxide. *Journal of Materials Chemistry*, 2009, **19**(39), P. 7362-70.
- [45] Guo Z., Wu H., Srinivas G., Zhou Y., Xiang S., Chen Z., et al. A Metal-Organic Framework with Optimized Open Metal Sites and Pore Spaces for High Methane Storage at Room Temperature. *Angewandte Chemie International Edition*, 2011, **50**(14), P. 3178-81.
- [46] Duan X., Yu J., Cai J., He Y., Wu C., Zhou W., et al. A microporous metal-organic framework of a rare sty topology for high CH<sub>4</sub> storage at room temperature. *Chemical Communications*, 2013, **49**(20), P. 2043-5.
- [47] Ma S., Sun D., Simmons J.M., Collier C.D., Yuan D., Zhou H.-C. Metal-Organic Framework from an Anthracene Derivative Containing Nanoscopic Cages Exhibiting High Methane Uptake. *Journal of the American Chemical Society*, 2007, **130**(3), P. 1012-6.
- [48] Yang Q., Guillerm V., Ragon F., Wiersum A.D., Llewellyn P.L., Zhong C., et al. CH<sub>4</sub> storage and CO<sub>2</sub> capture in highly porous zirconium oxide based metal-organic frameworks. *Chemical Communications*, 2012, **48**(79), P. 9831-3.
- [49] Zhao Z., Li Z., Lin Y.S. Adsorption and Diffusion of Carbon Dioxide on Metal-Organic Framework (MOF-5). *Industrial & Engineering Chemistry Research*, 2009, **48**(22), P. 10015-20.
- [50] Peng Y., Krungleviciute V., Eryazici I., Hupp J.T., Farha O.K., Yildirim T. Methane Storage in Metal-Organic Frameworks: Current Records, Surprise Findings, and Challenges. *Journal of the American Chemical Society*, 2013, **135**(32), P. 11887-94.
- [51] Walton K.S., Millward A.R., Dubbeldam D., Frost H., Low J.J., Yaghi O.M., et al. Understanding inflections and steps in carbon dioxide adsorption isotherms in metal-organic frameworks. *Journal of the American Chemical Society*, 2008, **130**(2), P. 406.
- [52] Li D., Kaneko K. Hydrogen bond-regulated microporous nature of copper complexassembled microcrystals. *Chem Phys Lett.*, 2001, **335**, P. 50-56.

- [53] Bourrelly S., Llewellyn P.L., Serre C., Millange F., Loiseau T., Férey G. Different adsorption behaviors of methane and carbon dioxide in the isotypic nanoporous metal terephthalates MIL-53 and MIL-47. *Journal of the American Chemical Society*, 2005, **127**(39), P. 13519-21.
- [54] Furukawa H., Ko N., Go Y.B., Aratani N., Choi S.B., Choi E., et al. Ultrahigh Porosity in Metal-Organic Frameworks. *Science*, 2010, **329**(5990), P. 424-8.
- [55] Keskin S. Atomistic Simulations for Adsorption, Diffusion, and Separation of Gas Mixtures in Zeolite Imidazolate Frameworks. *The Journal of Physical Chemistry C*, 2010, **115**(3), P. 800-7.
- [56] Yazaydın A.Ö. Screening of metal-organic frameworks for carbon dioxide capture from flue gas using a combined experimental and modeling approach. *J Am Chem Soc.*, 2009, **131**, P. 18198-9.
- [57] Bae Y.-S., Hauser B.G., Farha O.K., Hupp J.T., Snurr R.Q. Enhancement of CO<sub>2</sub>/CH<sub>4</sub> selectivity in metal-organic frameworks containing lithium cations. *Microporous and Mesoporous Materials*, 2011, **141**(1-3), P. 231-5.

# Modeling of the kinetics of reactive diffusion of gallium in copper particles

S. V. Dzyubanenko<sup>1,2</sup>, V. D. Lukyanov<sup>1,2</sup>

<sup>1</sup>ITMO University, 49 Kronverkskiy, St. Petersburg, 197101, Russia

<sup>2</sup>JSC Avangard, St. Petersburg, Russia

lukyanovvd@rambler.ru

PACS 02.30.Hq; 66.30.-h

DOI 10.17586/2220-8054-2015-6-3-332-345

The results of experimental studies for the formation kinetics of an intermetallic compound in the diffusion of gallium in copper are discussed. The mathematical model for the experimental study made it possible to calculate the diffusion coefficient of gallium in copper. A mathematical model for the kinetics of intermetallic compound formation at the reactive diffusion of gallium in a copper particle allows one to estimate the solidification time for diffusion-curing paste-based solder consisting of molten gallium and copper powder.

**Keywords:** reactive diffusion, solder, gallium, copper, intermetallic, kinetics.

*Received:* 2 December 2014

*Revised:* 18 December 2014

## 1. Introduction

Currently, new composite nanostructure materials are being actively introduced in many production areas. The relevance of these materials above all depends on their outstanding mechanical properties. These materials are also actively used in microelectronics.

When assembling electronic equipment, diffusion-curing paste-based solder (DCPS) based on gallium is used; such alloys allow the combining of strength and vacuum density, inherent to solder joints and with the ability of adhesives to cure at ambient temperatures [1–4]. We propose to use the available solder with copper powder filler when preparing diffusion-curing paste-based solder [5, 6]. The optimum composition of DCPS components, as a result of reactive diffusion of gallium into the particles of copper, provides the formation of an homogeneous copper intermetallic compound  $\text{CuGa}_2$ , which has fast (10 – 60 hours) solidity and possesses high operating temperature (up to 1000 °C), which allows the utilization of the product in harsh environments [7–11].

One of the main process parameters characterizing practical properties of paste-based solder is their solidification time,  $T_*$ . The small diameter of the copper powder particle (5 – 30 microns) prevents experimental investigation of homogeneous DCPS formation kinetics and in particular, prevents us from estimating the end time for reactive diffusion of interacting components and homogeneous intermetallic formation. In the experiments, another observed factor,  $T_0$  was under investigation; this factor characterizes an important property of paste-based solder, the formation time of a monolithic DCPS mass that does break into fragments when applying pressure of about 3 kg/mm<sup>2</sup>. The load value was selected on the base of the operating conditions for products where DCPS was used. For the studied DCPS composition at the operating temperature (85 ± 5)°C, it was deduced from experiments that  $T_0 = 16.5 \pm 0.5$  hour. Let us set a challenge for the mathematical modeling of reactive diffusion of gallium in the copper particles: to evaluate the solidification time of DCPS  $T_*$  and to match this figure with  $T_0$  time.

## 2. Experimental study of reactive diffusion of gallium in the copper particles and experimental data analysis

To justify the choice of mathematical model, an experimental study of gallium and copper reactive diffusion has been carried out. The study of the diffusion layer was carried out on samples of copper metal wire with 3 mm diameter, incubated for various times ranging from several hours up to seven days at  $85 \pm 5$  °C with gallium fusion. After incubation, gallium surplus was removed by means of washing in 2-propanol and distilled water. Wire samples were cut with the help of a slow-precision cutting machine. To form the electron-microscope image of cross-sections, we used signals of secondary and backscattered electrons, allowing us to obtain morphological and compositional contrast, respectively, which depended on the element or phase composition of the sample. Specification of the ultimate sample composition was carried out by means of electron probe microanalysis (EPMA), which is based on comparison of X-ray spectra of the analyzed sample and standards of known composition. The sensitivity of the method is  $\sim 0.1$  wt. %.

Figure 1 shows a photograph of the section of a cylindrical wire cross-section with intermetallic layer and Fig. 2 shows the results of combined SEM and X-ray microanalysis studies of gallium  $\mu$  and copper  $1 - \mu$  mass content distribution in this section  $\mu = M/(M + M_1)$ , where  $M$  and  $M_1$  are the mass of gallium and copper in unit volume.

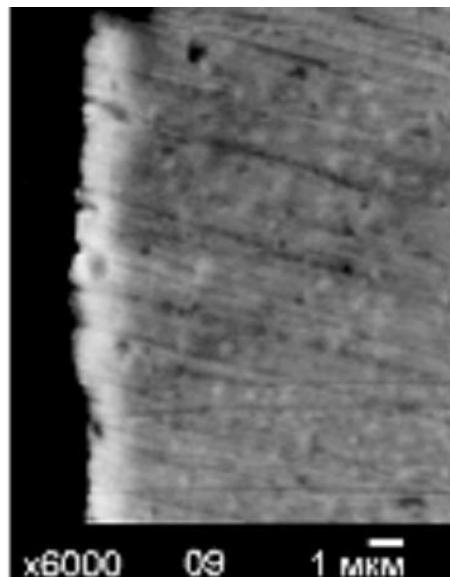


FIG. 1. cross-section of cylindrical wire (light area is a zone of an intermetalli formation)

It becomes clear from the analysis of the experimental data that after bringing gallium and copper in contact in the first short period of time, the duration of which is about 10 – 20 minutes, the diffusion of gallium into copper without intermetallic formation takes place. At the same time, copper is partially displaced from the gallium particle. Taking into account gallium liquid phase, having its surplus and taking into account the possibility of gallium intermixing, we believe that the concentration of gallium here remains unchanged. After reaching the critical mass of gallium fraction  $\mu_* = 0.63$  on the surface of the particle, intermetallic formation begins to take place [1]. The diffusion of gallium through formed intermetallic compound leads to a moving of the intermetallic compound boundaries deeper into copper. Distribution of gallium, bound in intermetallic compound and freely diffusing through it, depends on the distance from the surface of the copper particles and has a linear relationship at Fig. 2 that is typical

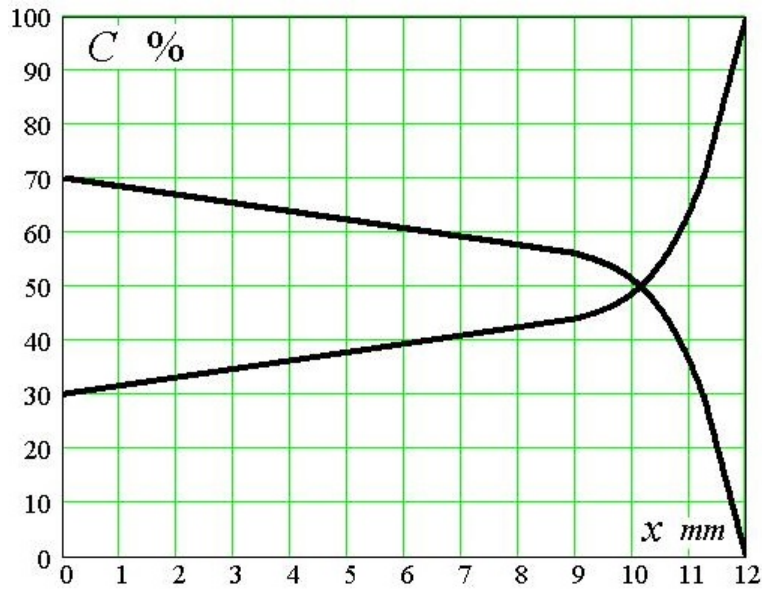


FIG. 2. Experimental data on the distribution of concentration of DCPS components, depending on the distance of gallium penetration into the copper (curve 1 – concentration of Ga, curve 2 – concentration of Cu)

for a stationary diffusion process. This may be because the speed of intermetallic compound boundaries moving deeper into the particle is much less than the speed set by the concentration distribution of gallium in copper.

### 3. Determination of diffusion coefficient of gallium in the intermetallic $\text{CuGa}_2$

Copper particles with particle form and dimensions of 3 – 4 mm were used in the experiment. All diffusion processes occur only near the surface of the particle; penetration depth was 150 – 200  $\mu\text{m}$ . Therefore, by means of mathematical modeling, we are solving initial-boundary one-dimensional, by Cartesian coordinate, non-stationary problem for the diffusion equation of gallium into the half-space filled with copper.

### 4. Mathematical modeling of one-dimensional reactive diffusion of liquid gallium in copper

Suppose at a moment of time,  $t = 0$ , the half-space  $x < 0$  is filled with liquid gallium and the half-space  $x > 0$  is filled with solid copper. For a while, there is a diffusion process of gallium in copper, which leads to the appearance of free gallium in the half-space  $x > 0$ . The experiments showed that the duration of this process is small, less than an hour. From a certain moment, an intermetallic  $\text{CuGa}_2$  component is starting to be formed in copper from the surface and goes deeper. This time  $t$  is supposed to be the initial ( $t = 0$ ) and the count shall be carried out starting from it.

The distribution of gallium in copper shall be described by the task at the point  $x$  at a point in time,  $t$ , concentration value of gallium in copper  $C = C(x, t)$ , which is a dimensionless value that is equal to the mass of gallium  $M$  in the volume  $V_0$ , normalized to the bulk density of gallium  $\rho$ :  $C = M/\rho V_0$ , if we consider that  $M = \rho V$ , where  $V$  is the value of the volume occupied by gallium, the concentration of gallium is the volume fraction of gallium in unit volume  $V_0$ ,  $C = V/V_0$ .

When measuring the concentration  $C$ , we consider the gallium that comprises the intermetallic compound – its concentration is  $C_*$ , and the gallium that continues to diffuse through the intermetallic [1,3]. The critical concentration of gallium  $C_*$  in formation of intermetallic compound is evaluated through a critical mass fraction  $\mu_*$ :  $C_* = \frac{\mu_*\rho_1}{(1-\mu_*)\rho + \mu_*\rho_1}$ , where  $\rho_1$  is the density of copper. If we consider that  $\rho = 5910 \text{ kg/m}^3$ ,  $\rho_1 = 8920 \pm 10 \text{ kg/m}^3$ ,  $\mu_* = 0.63 \pm 0.02$ , then  $C_* = 0.76 \pm 0.02$ .

The thickness of intermetallic compound grows with the time; its leading edge has  $x = \xi$  coordinate.

The diffusion process of gallium into the intermetallic compound with  $0 < x < \xi$  is described by the second Fick's law [1, 12, 13]:

$$\frac{\partial C}{\partial t} = D \frac{\partial^2 C}{\partial x^2}, \quad (1)$$

where  $D$  is the diffusion coefficient of gallium into the intermetallic compound.

Equation (1) shall be solved with the initial condition  $C_1(x, 0) = 0$  and boundary conditions:

with  $x = 0$ :

$$-D \frac{\partial C}{\partial x}(0, t) = \alpha (C_0 - C(0, t)), \quad (2)$$

where  $\alpha$  is the coefficient of diffusion permeability of gallium into the intermetallic compound,  $C_0 = 1$  the concentration of gallium in the half-space  $x < 0$ ;

with  $x = \xi$ :

$$C_1(\xi, t) = C_*. \quad (3)$$

This boundary condition defines the condition for the formation of the intermetallic compound at its front.

If we consider the case  $\alpha \rightarrow +\infty$  – full penetration of gallium into intermetallic, then condition (2) leads to the boundary condition:

$$C(0, t) = C_0. \quad (4)$$

The movement of the intermetallic front  $\xi = \xi(t)$  with  $t > 0$  is given by differential equation:

$$C_* \frac{d\xi}{dt} = -D \frac{\partial C_1(\xi - 0, t)}{\partial x}, \quad (5)$$

which is obtained by equating the amount of gallium  $dm_1(t) = C_* d\xi$  at the unit area of intermetallic front of gallium and the quantity of gallium flowing through a unit area per unit time

$$dm_2(t) = -D \frac{\partial C_1(\xi - 0, t)}{\partial x} dt.$$

The differential equation (5) we solve with the initial condition

$$\xi(0) = 0. \quad (6)$$

Analysis of the experimental curves (Fig. 2) shows that the distribution of concentration of gallium in the intermetallic layer is close to stationary when in equation (1) the value  $\partial C / \partial t$  can be neglected and the equation becomes  $d^2 C / dx^2 = 0$ . The general solution of this equation is a linear function along the  $x$  coordinate.

The approximate solution of equation (1) by Leibenson [14, 15] we are looking for in a ‘quasi-static’ form when there is a linear dependence on  $x$  coordinate with coefficients that depend on time as a parameter:

$$C(x, t) = A(t)x + B(t) \left( 1 - \frac{x}{\xi(t)} \right). \quad (7)$$

Using boundary conditions (4) and (5), we shall express functions  $A(t)$  and  $B(t)$  through the unknown function :

$$A(t) = \frac{C_*}{\xi(t)}, \quad B(t) = \frac{\alpha\xi(t)C_0 + DC_*}{\alpha\xi(t) + D}. \quad (8)$$

For the  $\xi(t)$  function, we shall obtain the differential equation of the first order, if we substitute the representation (7), taking into account formula (8):

$$C_* \frac{d\xi}{dt} = \alpha D \frac{C_0 - C_*}{\alpha\xi + D}. \quad (9)$$

A particular solution of differential equation (9), satisfying initial condition (6) has the form:

$$t = \frac{C_*}{C_0 - C_*} \left( \frac{1}{2D} \xi^2 + \frac{1}{\alpha} \xi \right). \quad (10)$$

An ultimate situation of complete penetration, when  $\alpha \rightarrow +\infty$  we get a particular solution:

$$t = \frac{C_*}{2D(C_0 - C_*)} \xi^2, \quad (11)$$

or after the solution relative to the intermetallic front coordinate, we shall get the famous [2] law of displacement of the front of the phase transition:

$$\xi = \sqrt{2D \left( \frac{C_0}{C_*} - 1 \right) t}. \quad (12)$$

Comparing the theoretical dependences (11) and (12) shows that counting of final permeability at the boundary of liquid gallium and copper leads to a change in the coordinate position of the intermetallic, depending on the time in comparison with the case of full penetrability. The main difference we have in the initial stage of the diffusion process, for example, the speed of front moving in the initial time at full permeability is infinite, in case of finite permeability, this speed is finite.

## 5. Calculation of diffusion coefficient of gallium in the intermetallic

Consideration of mutual leakage at the border of liquid gallium and copper allows one, from the range of particular solutions (11) and (12), to hypothesize that the experimental data for the dependence of penetration depth  $\xi = \xi(t)$ , shown in Fig. 3 with the help of dots have to be approximated by a quadratic function of the form in the case of finite permeability [16],

$$t = a\xi^2 + b\xi \quad (13)$$

or in the case of complete penetration:

$$t = a\xi^2. \quad (14)$$

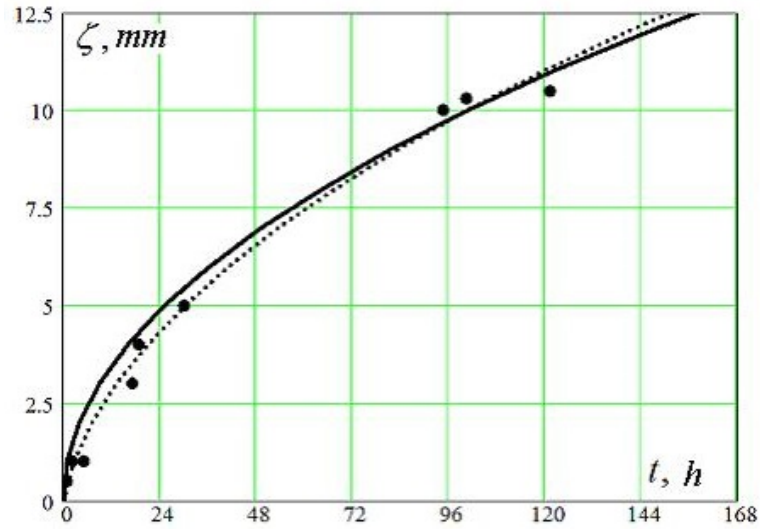


FIG. 3. Dependence of the intermetallic layer depth on the time of sample exposure in gallium. The dots show the experimental data, the dotted line is the dependence diagram (10), continuous line – the dependence diagram (11).

We shall find coefficients in these solutions, using the least-squares method.

Calculations on the data from Fig. 3 give the following values for the coefficients:

– for dependence of type (13) –  $a = 48.09$ ,  $b = 123.8$ ;

– for dependence of type (14) –  $a = 61 \pm 1$ .

Comparison of the dependence diagrams in Fig. 3 and numerical values of diffusion coefficients in the case of finite permeability ( $\alpha < +\infty$ ) and full permeability ( $\alpha \rightarrow +\infty$ ) shows that account of final permeability is essential for the initial stage of the process; with the large time and deep penetration of intermetallic it can be limited to the case of full permeation.

Comparing formulas (13) and (16) leads to the equation:

$$\frac{C_*}{2D(C_0 - C_*)} = a,$$

to calculate the diffusion coefficient of gallium in intermetallic:

$$D = \frac{C_*}{2a(C_0 - C_*)}.$$

Value  $C_* = 0.76 \pm 0.02$  [4], we have  $D = 1.38 \pm 0.12 \text{ mm}^2/\text{h}$ .

## 6. Reactive diffusion of molten gallium in copper particle

Let assume that copper particle of radius  $R$  is put into molten gallium. Reactive diffusion of gallium into the copper particle begins. Assuming spherical symmetry of the process, we have the formation of a spherical layer of the intermetallic, starting from the surface of the copper particle and going deeper into the particle.

Let the radius of the copper particle, in which gallium has not penetrated, be  $\zeta$ . We assume that the steady-state diffusion of gallium into the copper particle is described by the equation of diffusion for gallium concentration in copper  $C = C(r, t)$  at a moment of time  $t$  at the point with  $r$  coordinate of spherical coordinate system, the benchmark of which is located in the center of the copper particle and that in the absence of concentration of spherical angles has the following form:

$$\frac{d^2C}{dr^2} + \frac{2}{r} \frac{dC}{dr} = 0, \quad (15)$$

with  $\zeta < r < R$ .

The boundary condition on the surface of the copper particle with  $r = R$  setting a condition of full permeability of gallium into copper:

$$C(R, t) = C_0(t), \quad (16)$$

where  $C_0(t)$  function determines the law of concentration variation of gallium outside a copper particle.

At the intermetallic front with  $r = \zeta$ , gallium concentrations equals  $C_*$ , ensuring the condition of intermetallic formation:

$$C(\zeta, t) = C_*. \quad (17)$$

The equation of intermetallic front motion determines the law of front coordinates variation in time  $\zeta = \zeta(t)$  and has with  $r = \zeta$  and  $t > 0$  the following form:

$$C_* \frac{d\zeta}{dt} = -D \frac{\partial C}{\partial r}(\zeta, t), \quad (18)$$

with initial condition:

$$\zeta(0) = R. \quad (19)$$

The general solution of differential equation (15),

$$C(r) = B - \frac{A}{r}. \quad (20)$$

The approximate solution of diffusion equation, according to solutions (20) after the method of Leibenson [14, 15] will be found in the 'quasi-static' form:

$$C(r, t) = B(t) - \frac{A(t)}{r}. \quad (21)$$

Satisfying the boundary conditions (16) and (17), we obtain a system of algebraic linear equations in order to express the functions  $A(t)$  and  $B(t)$  through coordinates of mobile front of the intermetallic compound  $\zeta = \zeta(t)$ :

$$\begin{cases} B(t) - \frac{A(t)}{R} = C_0(t), \\ B(t) - \frac{A(t)}{\zeta(t)} = C_*. \end{cases} \quad (22)$$

From this system of equations we obtain:

$$A(t) = \frac{R(C_0(t) - C_*)\zeta(t)}{R - \zeta(t)}, \quad B(t) = \frac{RC_0(t) - C_*\zeta(t)}{R - \zeta(t)}. \quad (23)$$

Substitution of formula (21) for the distribution of the gallium concentration in the copper particle, taking into account the obtained formulas (23) into the equation of intermetallic front motion (18) leads to a differential equation of intermetallic boundary motion at the counter reactive diffusion of liquid gallium in the copper particle:

$$\frac{d\zeta}{dt} = -\frac{D}{C_*} \frac{(C_0(t) - C_*)}{(R - \zeta(t))\zeta(t)}. \quad (24)$$

To solve the differential equation (24) with separable variables it is necessary to set the law of concentration variation  $C_0(t)$ .

### 7. The time of completion of counter reactive diffusion in the copper particle with an unlimited quantity of molten gallium

Let us assume that the copper particle is surrounded by such an amount of gallium that its diffusion into copper and repression of copper from the particle does not change the concentration of gallium ( $C_0(t) = 1$ ) in the ambient space of the particle. The differential equation (24) in this case has the form:

$$C_* \frac{d\zeta}{dt} = -D \frac{(1 - C_*) R}{\zeta(t)(R - \zeta(t))}. \quad (25)$$

Analysis of the right side of the differential equation shows that with  $\zeta \rightarrow R - 0$  and  $\zeta \rightarrow 0 + 0$  the intermetallic front moving speed is striving to  $+\infty$  that indicates inapplicability of the obtained equation in these cases. To simulate the diffusion process in these two cases, instead of (16) one must use the boundary conditions with the final permeability of the form (3).

Integration of the equation (25) with initial condition (19) gives the particular integral:

$$t = \frac{C_* R^2}{(1 - C_*) D} \left( \frac{1}{6} - \frac{\zeta^2}{2R^2} + \frac{\zeta^3}{3R^3} \right). \quad (26)$$

The diffusion process is over, if the front reaches the center of the particle and the copper particle becomes intermetallic. The time of diffusion completion,  $t_*$ , shall be calculated if we add the value  $\zeta = 0$  into the solution (26) and we get:

$$t_* = \frac{C_* R^2}{6(1 - C_*) D}. \quad (27)$$

This time increases quadratically with increase of the radius of the copper particle and is inversely proportional, depending on the diffusion coefficient,  $D$ .

### 8. Ratio of the components required to produce intermetallic $\text{Ga}_2\text{Cu}$

We are carrying out mixing of molten gallium with  $M$  mass and copper powder with  $M_1$  mass in a vessel. The condition for full use of the components in order to form an intermetallic has the form:

$$\mu_* = \frac{M}{M + M_1}. \quad (28)$$

We assume that the copper powder consists of  $N$  identical spherical particles with radius  $R$ , the amount of which is which we uniformly distribute in gallium.

Using formula  $M_1 = \rho_1 V_1 N$ , where  $\rho_1$  is the copper density, we shall calculate the number of copper particles  $N = M_1 / \rho_1 V_1$ . For every copper particle, there is such an amount of gallium, which occupies a volume of  $V = M / \rho N$ .

Let's divide the mixture of substances into  $N$  cubes, the side length of which equals  $2H$  and the volume is  $V_0 = 8H^3$ . Each cube falls at exactly one particle of copper. We have the correlation between the volumes  $V_0 = V + V_1$ .

Let's place all the gallium, which occupies the volume  $V$  nearby this particle in a certain equivalent spherical layer, having the same volume. The radius of the spherical layer varies from  $R$  to  $R_0$ , where  $R$  is the radius of the particle;  $R_0$  is the outer radius of spherical layer.

From the conditions of intermetallic formation, with this amount of gallium and copper, we shall find the ratio between  $R$  and  $R_0$ .

For the volume of spherical layer filled with gallium, we have  $V = 4\pi(R_0^3 - R^3)/3$ . We shall use formula (28), which can be written as:

$$\mu_* = \frac{\rho V}{\rho V + \rho_1 V_1}.$$

After elementary transformations for the ratio of the radii, we shall obtain

$$\frac{R_0}{R} = \sqrt[3]{1 + \frac{\rho_2}{\rho_1} \cdot \frac{\mu}{1 - \mu}},$$

or the same radii ratio expressed in terms of the critical concentration of gallium  $C_*$

$$\frac{R_0}{R} = \frac{1}{\sqrt[3]{1 - C_*}}. \quad (29)$$

Such ratio of radii of the outer spherical layer and of the copper particle filled with gallium, when a complete intermetallic formation without any surplus takes place, one may call 'intermetallic'  $\text{Ga}_2\text{Cu}$ .

## 9. Counter reactive diffusion with limited number of gallium

We observe the copper particle of radius  $R$  covered with spherical layer of gallium, external radius of this layer equal to  $R_0$ .

When the diffusion of the surrounding gallium in copper particle at a moment of time  $t$  has a concentration distribution of the form (26) established, functions  $A(t)$  and  $B(t)$  comprising this formula are given by formula (28).

Using the law of perdurability, we shall find a relation between two unknown quantities,  $\zeta(t)$  and  $C_0(t)$ .

To do this, we shall calculate the amount of gallium  $\Delta M = \Delta M(t)$  that left the spherical layer and diffused into the copper particle:

$$\Delta M = \frac{4}{3}\pi (R_0^3 - R^3) (1 - C_0(t)) \rho. \quad (30)$$

We shall calculate the same amount of gallium that comes into the copper particle, having the formula for gallium concentration distribution (21). To do this, we integrate the distribution of gallium concentration on the spherical layer  $T$ , occupied by intermetallic:

$$\Delta M(t) = \rho \iiint_T C dV = 4\pi\rho \int_{\zeta(t)}^R C_1(t, r) r^2 dr = 4\pi\rho \left( B(t) \frac{(R^3 - \zeta^3(t))}{3} - A(t) \frac{(R^2 - \zeta^2(t))}{2} \right). \quad (31)$$

Equating the right sides of formulas (30) and (31), taking into account formula (23), we obtain a linear equation for the unknown quantity  $C_0(t)$ :

$$\begin{aligned} & \frac{4}{3}\pi (R_0^3 - R^3) (1 - C_0(t)) = \\ & = 4\pi \left( \frac{C_0(t)R - C_*\zeta(t)}{R - \zeta(t)} \cdot \frac{(R^3 - \zeta^3(t))}{3} - \frac{(C_0(t) - C_*)\zeta(t)}{R - \zeta(t)} \cdot \frac{(R^2 - \zeta^2(t))}{2} \right). \end{aligned}$$

The solution of the equation, relative to the function  $C_0(t)$ , leads to correlation, containing the desired function

$$C_0(t) = C_* + \frac{R_0^3(1 - C_*) - R^3 + C_*\zeta^3(t)}{R_0^3 - 0.5R\zeta(t)(R + \zeta(t))}. \quad (32)$$

### 10. Completion time of counter reactive diffusion in copper particle with ‘intermetallic’ ratio of gallium and copper

Let us consider the process of DCPS formation that is completed by full conversion of copper and gallium into intermetallic. Here, we have the formula (29), from which we have the equality  $R_0^3(1 - C_*) - R^3 = 0$  and formula (32) shall be transformed as:

$$C_0(t) = C_* + \frac{C_*\zeta^3(t)}{R_0^3 - 0.5R\zeta(t)(R + \zeta(t))}. \quad (33)$$

The equation of front motion of intermetallic formation (24) in view of the above formula (33) for  $C_0(t)$  function has the following form:

$$\frac{d\zeta}{dt} = -\frac{D\zeta^2(t)}{(R - \zeta(t))(R_0^3 - 0.5R\zeta(t)(R + \zeta(t)))}.$$

For the particular solutions of these differential equations with multiple variables with the initial condition (19) we have:

$$t = t(\zeta) = \frac{R^2}{D} \left( \frac{R^2 - \zeta^2}{4R^2} + \left( \frac{1}{2} + \frac{R_0^3}{R^3} \right) \ln \frac{\zeta}{R} + \frac{R_0^3}{R^3} \cdot \frac{R - \zeta}{\zeta} \right). \quad (34)$$

Note that the function  $t = t(\zeta)$  with  $0 < \zeta \leq R$  is monotonic and has backward  $0 < \zeta \leq R$ .

### 11. Analysis and comparison of the results for mathematical modeling of counter reactive diffusion kinetics of gallium in copper

The time  $t$  dependence diagram on the penetration depth into the copper particle of intermetallic front  $h = h(t) = 1 - \zeta(t)$  is shown on Fig. 4 by a solid line. Subsequent calculations were carried out for a particle of  $5 \mu\text{m}$  radius, with a value of  $C_* = 0.76$  when, according to formula (29) for the radius of the equivalent particle we have  $R_0 = 1.609R$ ,  $D = 1.38 \pm 0.12 \mu\text{m}^2/\text{h}$ .

For comparison, Fig. 4 shows a diagram of dependence on the depth of penetration into the copper particle at an unlimited quantity of gallium around it (dashed line). When constructing this graph, the function inverse to the function of  $\zeta = \zeta(t)$  was used, that defined the formula (26).

The dotted line at Fig. 4 shows the dependence of the depth of penetration into the copper intermetallic front  $h = \xi(t)$  in the 2D problem, here, the function  $\xi(t)$  is given by the formula (12).

Figure 5 is a diagram of dependence  $C_0 = C_0(\zeta(t))$ ; when specifying this dependence, we use formula (33) and find the dependence  $\zeta = \zeta(t)$ . This dependence shows the change

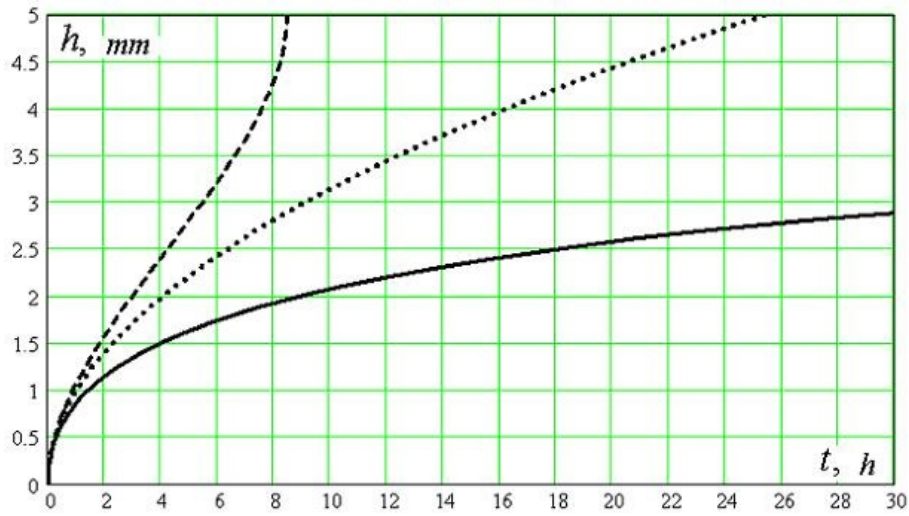


FIG. 4. The time  $t$  dependence of the relative depth of intermetallic front penetration into the copper particle. The solid line is the ‘intermetallic’ structure of gallium around the copper particle; the dotted line is an unlimited quantity of gallium around the copper particle, the dashed line – for a plane copper-gallium boundary

of gallium concentration in time in the spherical layer around the copper particle. When constructing this graph, parametric function  $C_0 = C_0(\zeta(t))$  solution is used,  $\zeta$  acts as a parameter value, and the functions are defined by formulas (33) and (34):

$$\begin{cases} t = t(\zeta), \\ C_0 = C_0(\zeta). \end{cases}$$

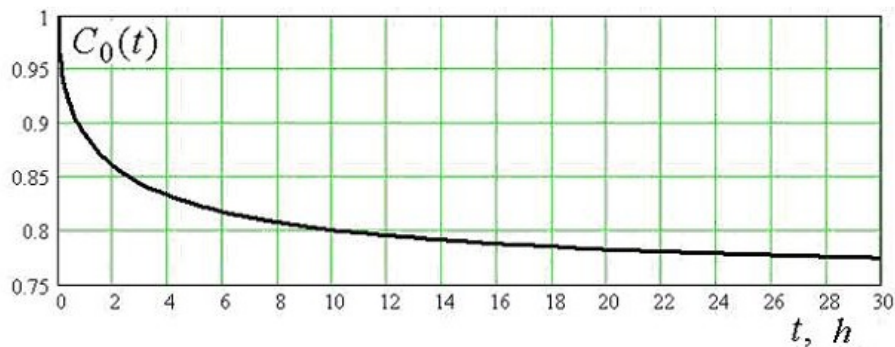


FIG. 5. The time  $t$  dependence of the normalized concentration of gallium in the spherical layer  $C_0(t)$

For distribution of the concentration of gallium in copper particle at the moment of time  $t = t_0$  we have:

$$C(r, t_0) = \frac{C_0(\zeta_0) - C_*\zeta_0}{R - \zeta_0} - \frac{(C_0(\zeta_0) - C_*)\zeta_0}{(R - \zeta_0)r},$$

with  $\zeta_0 < r < R$ ,  $\zeta_0 = \zeta(t_0)$ . The graph of function  $C = C(r, t_0)$  at some points of time are shown in Fig. 6.

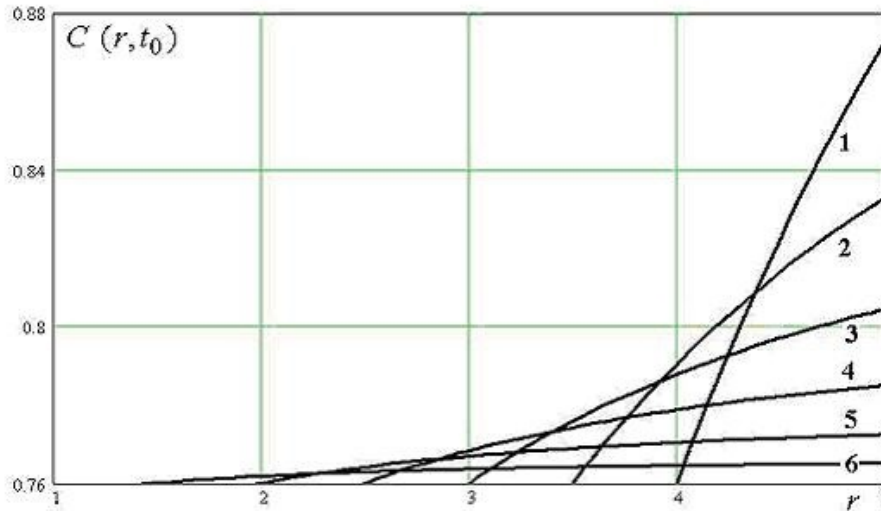


FIG. 6. Distribution of the normalized gallium concentration  $C(r, t_0)$  in the copper particle at different values of dimensionless time  $t_0$ . (Curve 1:  $t_0 = 1.5$  hours, curve 2:  $t_0 = 4.0$  hours, and the curve 3:  $t_0 = 9.0$  hours, curve 4:  $t_0 = 18.0$  hours; curve 5:  $t_0 = 35.0$  hours, curve 6:  $t_0 = 70.0$  hours)

## 12. Evaluation of DCPS formation time

Analysis of the dependences shown in Fig. 4 allows us to estimate the time of intermetallic formation in two cases: in the 2D problem and in case with an unlimited amount of gallium. If we consider that the radius of the copper particle was chosen to be 5 microns, the time of process completion in case of an unlimited quantity of gallium round the copper particle equals to  $T_1 = 8.5$  hours. This time is considerably smaller than the time = 26 hours – the time of entry into the intermetallic front at the 2D problem to the depth of  $5 \mu\text{m}$ . This is due to the fact that during diffusion process, while penetrating deeper into the particle, gallium flux density is increased by reducing the area of the sphere, separating the intermetallic from the copper particle. In the 2D problem, the section that is separating the intermetallic from the copper has a permanent area.

In the case of ‘intermetallic’ composition, the time of complete conversion of the components into intermetallic compound equals to infinity. Let’s determine the value  $T$  – the time of practical completion of reactive diffusion or the DCPS formation time to be the time, at which the volume fraction of the intermetallic compound formed throughout the volume of the paste-based solder, equals to some critical value.

By the time  $T$ , the depth of penetration of intermetallic front  $h(T)$  and the amount of formed intermetallic:

$$v = v(T) = V (1 - (1 - \alpha(T))^3), \quad (35)$$

where  $\alpha(T)$  – the proportion of penetration depth at  $R$  radius,  $\alpha = \alpha(T) = h(T)/R$ . Concentration of gallium in the spherical layer around the copper particle reaches  $C_0(T) > C_*$ . Concentration of copper in this layer equals  $1 - C_0(T)$ . This concentration of copper is not enough for intermetallic to be formed in the whole layer, as it is required by  $1 - C_*$  concentration. We shall calculate volume, where this amount of copper will be enough for intermetallic formation:

$$v_1 = \frac{1 - C_0(T)}{1 - C_*}(V_0 - V). \quad (36)$$

Let us calculate the volume fraction of the intermetallic compound  $v + v_1$  in  $V_0$  volume that is the volume of the particle, containing all the gallium and copper particles:  $(v + v_1)/V_0$ . The required time  $T$  is determined from the equation  $(v + v_1)/V_0 = \gamma$ , using the formulas (29), (35) and (36) it takes the form:

$$(1 - (1 - \alpha)^3)(1 - C_*) + (1 - C_0(T))\frac{C_*}{1 - C_*} = \gamma.$$

The value we shall find using the given experimental result: DCPS formation time is 16 hours. From Fig. 4 and 5 we shall find the values of  $\alpha(16) \approx 0.50 \pm 0.03$  and  $C_0(16) = 0.78 \pm 0.02$ . Taking into account these values and having the value  $C_* = 0.76$ , we shall calculate the value  $\gamma \approx 0.90 \pm 0.02$ .

Thus, the time for which 90 % of paste turns into intermetallic is understood to be the time of DCPS formation.

### 13. Conclusion

1. An experimental study of the kinetics of reactive diffusion of gallium and copper has been carried out. The experimental and analytical method for determination of the diffusion coefficient of gallium into intermetallic has been proposed; this method allowed us to determine the gallium diffusion coefficient into the intermetallic after building a mathematical model. It was shown that account of final permeability of gallium into copper insignificantly affects the kinetics of the diffusion process, except for a short initial period of time.
2. A theoretical study of the reactive diffusion kinetics of gallium in the copper particle was also done. The differential equation of intermetallic front moving in the copper particle was obtained, on condition of spherical symmetry and arbitrary law of gallium concentration change in the ambient space of the particle.
3. Analytical solutions for the differential equations of intermetallic front moving in the copper particle at a constant concentration of gallium in the space surrounding the particle have been found.
4. An analytical solution for the differential equation of intermetallic front moving in the copper particle, when a limited amount of 'intermetallic' gallium is near. This solution simulates the kinetics of formation of diffusion-curing paste-based solder.
5. A study of constructed analytical solutions has been carried out, which allowed understanding of the reactive diffusion kinetics of gallium and copper microparticles. Taking into account the results of the pilot study, the concept of diffusion-curing paste-based solder formation has been introduced.

### References

- [1] Lashko N.F., Lashko S.V. *Soldering of metals*. Mechanical engineering, Moscow, 1988, 326 p.
- [2] Petrova A.P. *Heat-resistant glues*. Chemistry, Moscow, 1977, 200 p.
- [3] Lashko S.V., Grishin V.L. Solders with gallium. *Instrumentation making*, 1965, **3**, P. 6–11.
- [4] Grzhimalsky L.L. *Gallic solders*. Leningrad: Knowledge, 1974.
- [5] MacKay C.A. Amalgams as alternative bonding materials. *Soldering & Surface Mount Technology*, 1990, **2**, P. 21–25.
- [6] Baldwin D.F. Amalgams As Alternative Microelectronic Interconnect Materials. *Sensors in Electronic Packaging*, 1995, **2**, P. 55–63.

- [7] Bhattacharya S.K. A low temperature processable ternary gallium alloy for via filling application in micro-electronic packaging. *Journal of Materials Science: Materials in Electronics*, 2000, **11**, P. 653–656.
- [8] Janssen Y. Differential thermal analysis and solution growth of intermetallic compounds. *Journal of Crystal Growth*, 2005, **285**, P. 670–680.
- [9] Deng Yue-Guang. Corrosion development between liquid gallium and four typical metal substrates used in chip cooling device. *Appl. Phys. A*, 2009, **95** (3), P. 907–915.
- [10] Sommadossi S. Diffusion soldering using a gallium metallic paste as solder alloy: study of the phase formation systematic. *Journal of Materials Science*, 2007, **42**, P. 9707–9712.
- [11] Dzyubanenko S. Gallium Amalgam Solder as a Bonding Material for SAW Devices. *Proceeding of “XIII International Conference for Young Researches ‘Wave Electronics and Its Applications in the Information and Telecommunication Systems’*. Saint-Petersburg, June 2010, Saint-Petersburg State University of Aerospace Instrumentation, 2010, P. 34.
- [12] Bugakov V.Z. *Diffusion in metals and alloys*. Moskow, GITTL, 1949, 122 p.
- [13] Tikhonov A.N., Samarsky A.A. *Equations of mathematical physics*. Science, Moskow, 1977, 734 p.
- [14] Leybenzon L.S. *Handbook of oil-field mechanics*. Moskow – Leningrad: ONTI NKTP USSR, 1934, 196 p.
- [15] Luikov A.V. *Heat conductivity theory*. Moskow, The Higher school, 1966, 600 p.
- [16] Lukyanov V.D. Relationship plurality approximation. *Nanosystems: Physics, Chemistry, Mathematics*, 2014, **5** (3), P. 384–390.

## From metamaterials to metasurfaces and metadevices

Yu. S. Kivshar<sup>1,2</sup>

<sup>1</sup>Nonlinear Physics Center, Australian National University,  
Canberra ACT 0200, Australia

<sup>2</sup>ITMO University, St. Petersburg 197101, Russia

Yuri.Kivshar@anu.edu.au

PACS 81.05.Xj, 78.67.Pt, 73.20.Mf

DOI 10.17586/2220-8054-2015-6-3-346-352

Metamaterials are artificial electromagnetic media that are structured on the subwavelength scale. Such structures were initially suggested for achieving the negative index of refraction, but later they became a paradigm for engineering electromagnetic space and controlling propagation of waves through the transformation optics and optically-induced magnetic response. The research agenda is now shifting towards tunable, switchable, nonlinear and sensing functionalities of metamaterials and their applications, and it involves the fields of metasurfaces and metadevices, with the recent demonstrations of breakthrough results with light-controlled metamaterials, nonlinear metamaterials, and tunable metasurfaces for MRI applications. Here, we briefly discuss the basic concepts of this rapidly growing research field, highlighting the recent developments in the physics of metamaterials, subwavelength nanophotonics, and graphene-based photonics.

**Keywords:** metamaterial, metasurface, metadevices, optical magnetism, graphene.

*Received:* 15 March 2015

*Revised:* 18 March 2015

### 1. What are metamaterials?

It is well known that the response of any material to applied electromagnetic radiation can be characterized by two electromagnetic parameters, magnetic *permeability* and electric *permittivity*. These two physical characteristics are combined in a product to define the square of a *refractive index*, which measures how fast the material transmits light and how light is bent on entering the material — the higher the refractive index, the slower the propagation and the stronger the deflection. However, a material whose permeability and permittivity become *simultaneously negative*, termed as a *left-handed material*, would also allow the propagation of electromagnetic waves with many unusual properties [1–5].

In a left-handed material, the Poynting vector of a wave is anti-parallel to the wave vector and, therefore, the basic feature of light is reversed; that is, light wave propagates in the opposite direction to the energy flow. This leads to some very interesting effects such as the reversal of the Doppler shift for radiation, and the reversal of Cherenkov radiation. In addition, one of the most basic principles of optics, Snell's law, is 'reversed' at the interface of a left-handed medium with a normal right-handed material, so that the electromagnetic waves experience *negative refraction*, and this property can be employed for flat-lens focusing [1,4].

The creation of novel composite materials demonstrating the left-handed properties at telecommunication and visible frequencies required the development of novel concepts and novel nanofabrication techniques. Many theoretical concepts that have been suggested so far are based around nanofabricated composites. One example is metal nanowires and *nanowire plasmonic materials*, where nanowires arranged into parallel pairs can act as a left-handed material with the effective magnetic permeability and dielectric permittivity that are both negative in the visible

and near-infrared spectral ranges [6]. Various composites, based on metallic and dielectric nanostructures that have macroscopic negative refraction and act as left-handed materials, have recently been suggested and developed [7–10] (see Fig. 1).

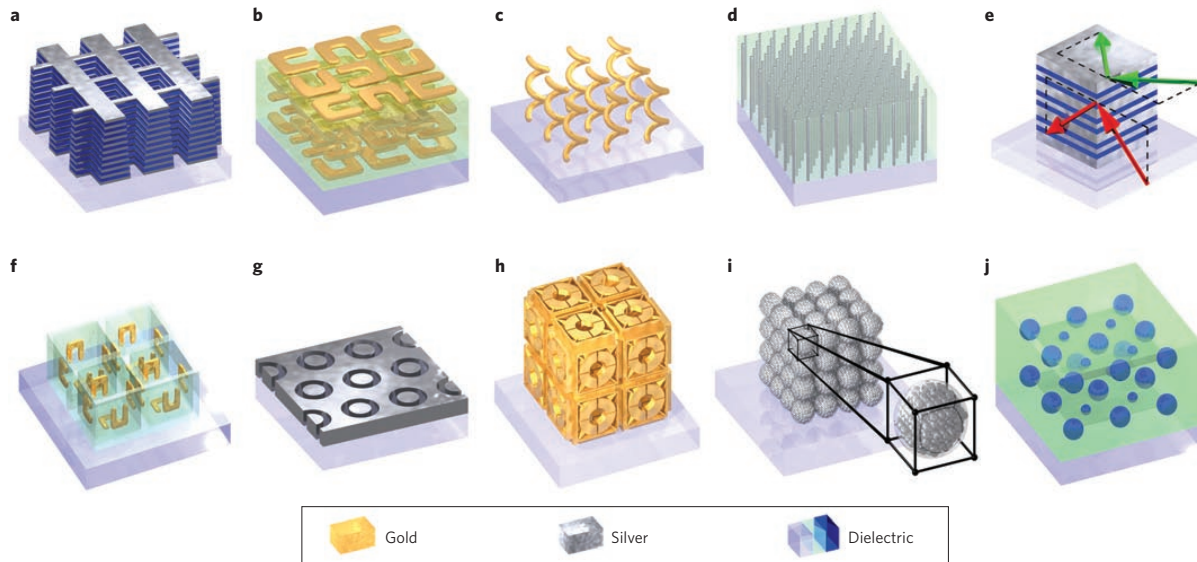


FIG. 1. Examples of metamaterial structures fabricated through composition and periodic repetition of metallic and dielectric elements – ‘meta-atoms’ or ‘meta-molecules’ (adopted from Ref. [10])

Over the last 10 years, the field of metamaterials has developed as a novel approach for engineering the electromagnetic response of passive micro- and nanostructured materials by engaging resonance excitations, such as localized plasmonic modes and Mie-like resonances. Remarkable results have been achieved including negative-index media that refract light in the opposite direction from that of conventional materials, chiral materials that rotate the polarization state of light hundreds of thousands of times more strongly than natural optical crystals, and structured thin films with remarkably strong dispersion that can slow light. A list of only few such remarkable highlights demonstrated with metamaterials during last 10 years includes: optical magnetism, negative index of refraction, invisibility cloaking, optical circuit components, improved imaging. A few example of nanostructured metamaterials are presented in Fig. 2.

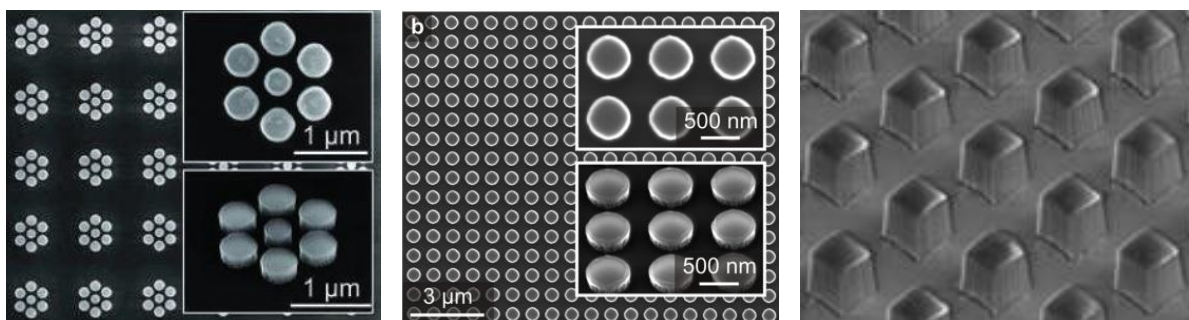


FIG. 2. Examples of metasurfaces with optically resonant electric and magnetic response: nanoantenna oligomers, regular arrays of silicon nanoparticles, and magnetic metamaterial mirrors

## 2. Nonlinear and magnetoelastic metamaterials

The physics of nonlinear metamaterials originates from an idea to design subwavelength structures having any desired nonlinear response properties [11–13]. Starting from the initial theoretical proposal for the enhancement of nonlinear properties of metamaterials, many nonlinear phenomena with metamaterials were investigated, both theoretically and experimentally. Recent studies cover several topics of magnetoelastic and tunable nonlinear metamaterials for THz and microwave applications.

As emphasized above, the advent of metamaterials provides novel methodologies for controlling light-matter interaction. With proper design and fabrication of the metamaterial units, – the so-called meta-atoms and meta-molecules, exotic properties unavailable with natural materials can be realized. These studies have inspired many unconventional ideas in optics and photonics, promising various ultra-compact and highly efficient metadevices [14]. Today, an important direction in the development of metadevices is achieving dynamic control over their exotic properties. This can be done by including nonlinear or tunable elements into passive metamaterials, such as liquid crystals; alternatively, one can design meta-molecules with deformable structures. For example, mechanical tuning is now widely used in THz metamaterials. We have recently proposed a post-processing approach for mechanical tuning of the electromagnetic properties of metamaterials, which may be used in applications which require precise engineering of metamaterial resonances.

Structural tuning shows advantages in modulation contrast and the ability to manipulate meta-molecules individually. However, deformation based on static electric or magnetic forces is not so straightforward for optical metamaterials with sub-micrometer features. To solve this problem, our research team introduced the concept of magnetoelastic metamaterials [13], where the meta-molecules can be deformed by the resonance-enhanced electromagnetic force. Importantly, this is a scalable solution of ‘light controls light’ concept over a wide frequency range, and the interaction between electromagnetic resonance and structural dynamics can demonstrate novel effects beyond a simple modulation of parameters.

To achieve strong electromagnetic-to-elastic interaction, we have introduced an optimized design by exploiting the torsional deformation of chiral meta-molecules. We have demonstrated giant bistable effect and dynamic nonlinear optical activity due to a self-oscillation effect. An important breakthrough we made recently is the prediction and observation of a spontaneous chiral symmetry breaking effect (see Fig. 3) in a metamaterial composed of enantiomeric torsional meta-molecules, i.e. chiral meta-molecules with opposite handedness. In such a scenario, the initial configuration of the system is achiral due to chiral symmetry. However, due to the intermolecular electromagnetic interaction, the system stability changes, and such symmetry can be broken spontaneously when the incident power exceeds a certain threshold value, which further leads to an abrupt nonlinear polarization change and mode splitting. The predicted effect is an artificial achiral-chiral phase transition and it was successfully demonstrated in a microwave experiment. As shown in the figure, the single resonance under chiral symmetry configuration splits into two new resonances in the power regime of broken symmetry.

Our studies provide a novel paradigm to achieve artificial nonlinear and phase transition effects in metamaterials via electromagnetic-elastic coupling. The realization of these effects at infrared and optical frequencies can greatly enrich the functionalities of future meta-devices.

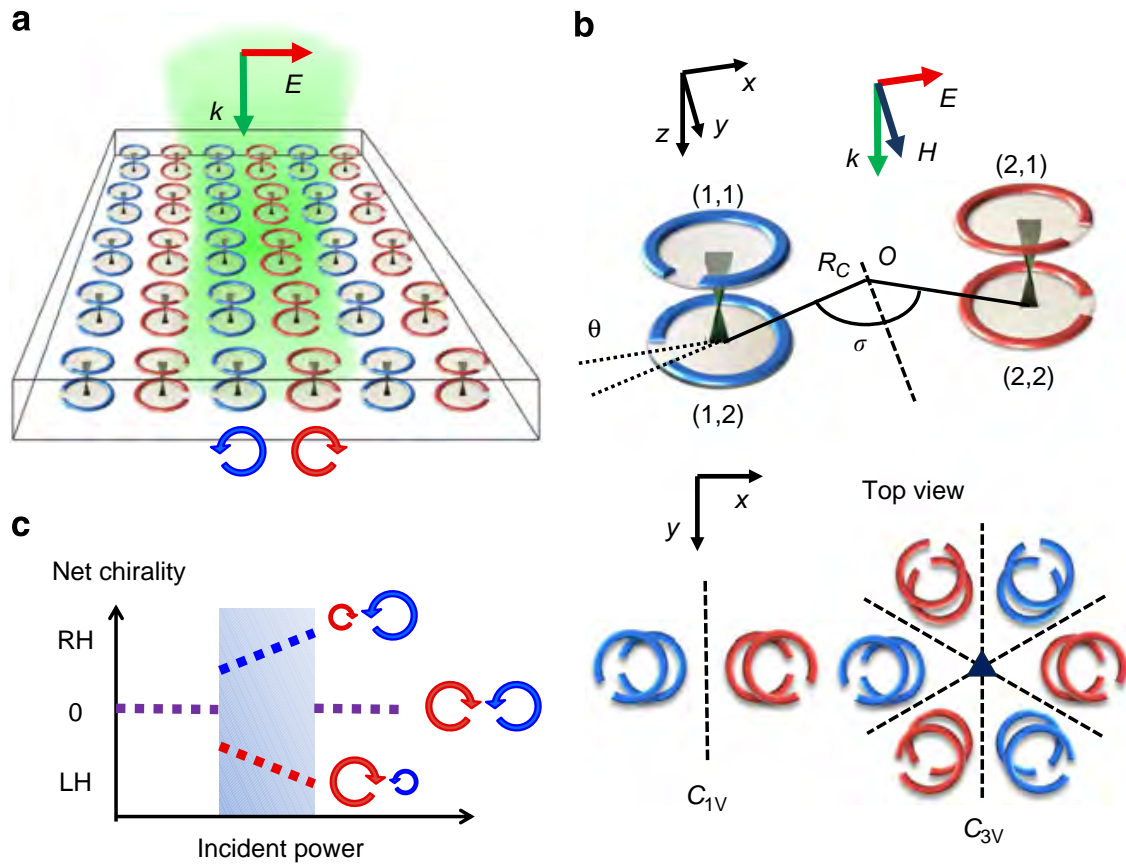


FIG. 3. Schematics of torsional metamaterial enantiomers and spontaneous chiral symmetry breaking [14]. (a) Conceptual layout of torsional metamaterials with chiral symmetry. Each meta-molecule consists of two coaxial twisted meta-atoms connected elastically, and meta-molecules with right and left handedness are plotted in blue and red colours, respectively. The green-shaded region represents the incident electromagnetic waves, and the responses of enantiomers are denoted by circular arrows. (b) Configurations of enantiomeric meta-molecules. Shown are the displacement vector between a meta-molecule and the rotation centre  $O$  and the rotation angle. The dashed lines are the axes of mirror symmetry. (c) Schematic showing the phase transition of net chirality of the system when the incident power changes. In the shaded regime, spontaneous chiral symmetry breaking occurs and the net chirality can fall into either the left-handed or the right-handed regime [15].

### 3. Metasurfaces and graphene physics

*Optical metasurfaces* are thin-layer subwavelength patterned structures which interact strongly with light, and they became a logical extension of the metamaterials concept with regards to its practical applications. In addition, we now observe the emergence of a new paradigm of *metadevices*, defined as devices having unique and useful functionalities realized by structuring the functional matter on the subwavelength scale.

One of the important directions in the physics of metasurfaces is the use of *graphene* as a component of metadevices. Graphene is a two-dimensional array of carbon atoms arranged in a honeycomb lattice, which has remarkable electronic and optical properties. Recently, its

unique optical properties have generated significant interest in the research community, revealing its great potential for applications in photonics and optoelectronics. The optical response of graphene is characterized by a surface conductivity which is determined by the chemical potential. For photon energies below a certain level, defined by a chemical potential, graphene exhibits a metal-like conductivity. In this regime, similar to metals, graphene can support transverse magnetic (TM) electromagnetic surface plasmon polaritons, and they represent coupled state of the electromagnetic field and electrons. For the range of frequencies above the chemical potential, graphene has dielectric characteristics and it supports transverse electric (TE) surface waves. The study of plasmonic effects in graphene structures has attracted a special interest from the nanoplasmonics research community due to novel functionalities delivered by such systems, including the strong confinement of electromagnetic waves by a graphene layer and tunability of graphene properties through doping or electrostatic gating. Currently, graphene plasmonics is a rapidly growing new field of physics which utilizes concepts of conventional metal plasmonics combined with the unique electronic and optical properties of graphene. Being guided by a graphene monolayer, TM-polarized plasmons with subwavelength localization have an extremely short wavelength, and that is why their excitation is rather challenging. Nevertheless, recent experiments have provided evidence for the existence of such plasmons by means of the scattering near-field microscopy and the nanoimaging.

More recent studies include the analysis of both linear and nonlinear effects in graphene structures, including the nonlinear propagation and switching of light in two coupled layers of graphene (see Fig. 3(a)), demonstrating that this simple double-layer structure can operate as an efficient optical coupler for both continuous plasmon polaritons and for subwavelength spatial solitons. Multi-layer graphene structures were shown to be capable of increasing the plasmon wavelength, thus increasing plasmon propagation length (see Figs. 4(b,c)) and also predicting the existence of plasmon solitons in graphene (see Figs. 4(d-g)).

#### 4. Towards metadevices

The ever-increasing demand for faster information transfer and processing drives efforts to remove the bottleneck between fiber-based optical telecommunication networks and electronic data handling and routing, improving data storage and developing parallel data processing operating in a compact space. Fulfilment of these tasks will require strong and fast nonlinearities for switching between different lights, and much improved control of the electromagnetic properties of matter with external stimuli, such as electric signals. Many of these functionalities may be greatly enhanced by hybridizing functional matter with metamaterials and graphene, by exploiting the nonlinearity of the metamaterial framework itself, and by taking advantage of the changing balance of forces in systems with building blocks smaller than the wavelength of light. This leads to the concept of *metadevices*, a logical extension of the metamaterial paradigm, where interactions are nonlinear and responses are dynamic. We envision that a future platform for highly integrated electromagnetic signal processing and distribution will emerge which will combine nonlinear, memory and switchable functionalities with transformation optics' ability to guide light via the engineered electromagnetic space, using metamaterials with spatially variable parameters.

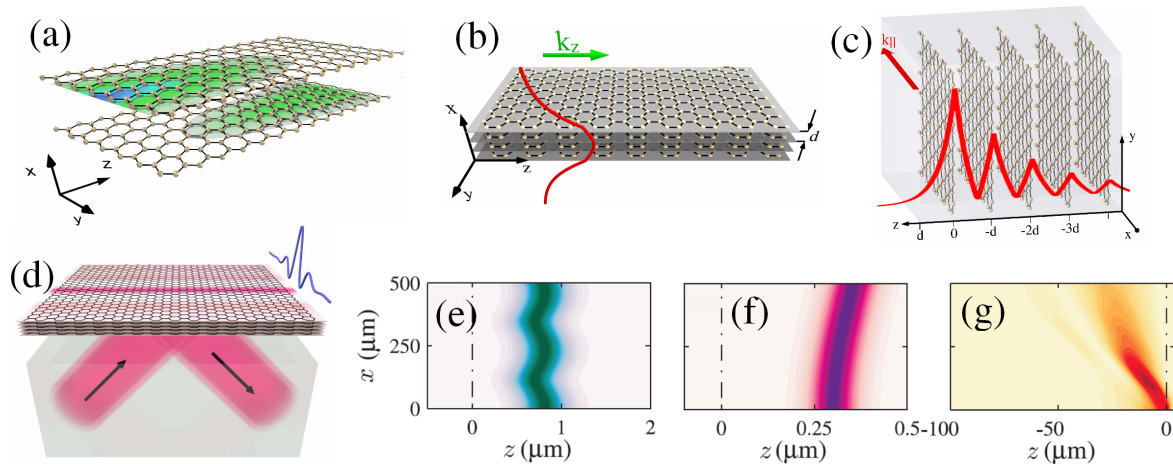


FIG. 4. Examples of linear and nonlinear waveguiding graphene structures [16, 17]: (a) Nonlinear graphene coupler composed of two layers of graphene where light can tunnel from one layer to the other; (b) Multilayer graphene waveguide supporting different types of TM and TE polarized surface waves-plasmon polaritons; (c) Optical Tamm states localized at the surface of multilayer graphene stack; (d) Schematics of the excitation of a dissipative plasmon soliton by an incoming laser light in a multi-layer graphene waveguide; (e-g) various regimes of the soliton propagation along an interface separating linear and nonlinear dielectric materials covered with a graphene layer: wobbling, deflection, and diffraction, respectively.

## 5. Summary and outlook

Future technologies will demand a huge increase in photonic integration and energy efficiency, far surpassing that of bulk optical components and silicon photonics. Such an integration can be achieved by embedding the data-processing and waveguiding functionalities at the material's level, creating *a new paradigm of metadevices*. It is now believed that robust and reliable metadevices will allow photonics to compete with electronics not only in telecommunication systems, but also at the level of consumer products such as mobile phones or automobiles. The main challenges in achieving this vision will be in developing cost-efficient fabrication and device integration technologies.

## References

- [1] V.G. Veselago. The electrodynamics of substances with simultaneously negative values of  $\epsilon$  and  $\mu$ . *Sov. Phys. Usp.*, 1968, **10**, P. 509.
- [2] R.A. Shelby, D.R. Smith, S. Schultz. Experimental Verification of a Negative Index of Refraction. *Science*, 2001, **292**, P. 77.
- [3] D.R. Smith, W. J. Padilla, et al. Composite medium with simultaneously negative permeability and permittivity. *Phys. Rev. Lett.*, 2000, **84**, P. 4184.
- [4] J.B. Pendry. Negative Refraction Makes a Perfect Lens. *Phys. Rev. Lett.*, 2000, **85**, P. 3966.
- [5] D.R. Smith, J.B. Pendry. Reversing Light with Negative Refraction. *Phys. Today*, 2004, **57** (6), P. 37.
- [6] V.M. Shalaev. Optical negative-index metamaterials. *Nature Photonics*, 2007, **1**, P. 41–48.
- [7] S. Linden, C. Enkrich, et al. Magnetic response of metamaterials at 100 terahertz. *Science*, 2004, **306**, P. 1351.
- [8] T.J. Yen, W.J. Padilla, et al. Terahertz magnetic response from artificial materials. *Science*, 2004, **303**, P. 1494.
- [9] A.N. Grigorenko, A.K. Geim, et al. Nanofabricated media with negative permeability at visible frequencies. *Nature*, 2005, **438**, P. 335.

- [10] C. Soukoulis, M. Wegener. Past achievements and future challenges in the development of three-dimensional photonic metamaterials. *Nature Photonics*, 2011, **5**, P. 523.
- [11] A.A. Zharov, I.V. Shadrivov, Yu.S. Kivshar. Nonlinear properties of left-handed metamaterials. *Phys. Rev. Lett.*, 2003, **91**, P. 037401.
- [12] M. Lapine, I.V. Shadrivov, Yu.S. Kivshar. Nonlinear metamaterials. *Rev. Mod. Phys.*, 2014, **86**, P. 1093.
- [13] I.V. Shadrivov, M. Lapine, Yu.S. Kivshar (Eds). *Nonlinear, Active, and Tunable Metamaterials*. Springer-Verlag, Berlin, 2015, 324 p.
- [14] N.I. Zheludev, Yu.S. Kivshar. From metamaterials to metadevices. *Nature Materials*, 2012, **11**, P. 917.
- [15] M. Liu, D.A. Powell, et al. Spontaneous chiral symmetry breaking in metamaterials. *Nature Communications*, 2014, **5**, P. 4441.
- [16] D.A. Smirnova, A.V. Gorbach, et al. Nonlinear switching with a graphene coupler. *Phys. Rev. B*, 2013, **88**, P. 045443.
- [17] D.A. Smirnova, I.V. Shadrivov, A.I. Smirnov, Yu.S. Kivshar. Dissipative plasmon-solitons in multilayer graphene. *Laser Photonics Rev.*, 2014, **8**, P. 291–296.

# Localized states near the Abrikosov vortex core in type-II superconductors within zero-range potential model

V. L. Kulinskii, D. Yu. Panchenko

Department of Theoretical Physics, Odessa National University, Dvoryanskaya 2, 65082  
Odessa, Ukraine

kulinskij@onu.edu.ua, dpanchenko@onu.edu.ua

PACS 74.25.Jb, 74.25.Ha

DOI 10.17586/2220-8054-2015-6-3-353-360

We propose to treat the lowest bound states near the Abrikosov vortex core in type-II superconductors on the basis of the self-adjoint extension of the Hamiltonian of Aharonov-Bohm type with the localized magnetic flux. It is shown that the Hamiltonian for the excitations near the vortex core can be treated in terms of the generalized zero-range potential method when the magnetic field penetration depth  $\delta$  is much greater than the coherence length  $\xi$  i.e. in the limit  $\varkappa = \delta/\xi \gg 1$ . In addition, it is shown that in this limit it is the singular behavior of  $d\Delta/dr|_{r=0}$  and not the details of the order parameter  $\Delta(\mathbf{r})$  profile that is important. In support of the proposed model, we reproduce the spectrum of the Caroli-de Gennes-Matricon states and provide direct comparison with the numerical calculations of Hayashi, N. *et al.* [Phys. Rev. Lett. **80**, p. 2921 (1998)]. In contrast to the empirical formula for the energy of the ground state in Hayashi, N. we use no fitting parameter. The parameters for the boundary conditions are determined in a self-consistent manner with Caroli-de Gennes-Matricon formula.

**Keywords:** Abrikosov vortex; bound states; zero-range potential.

*Received: 18 February 2015*

## Introduction

Understanding the electronic structure of the vortex core in superconductors and the spectrum of excitations in its vicinity are important for the technology of the superconducting materials, as the low temperature limit of their spectrum is known to determine their static and dynamic properties. In the seminal work of [1], the existence of bounded states localized near the vortex core was predicted. A striking feature of the Caroli-de Gennes-Matricon (CdGM) solution is that the energy spectrum similar to the Landau levels with the effective region of localization is on the order of the vortex core radius  $\xi_1$ . This radius corresponds to the effective field of the order's upper critical limit  $H_{c2} \simeq \varkappa \gg 1$  [2]; that is, the field above which the superconductivity is destroyed. The appearance of the effective magnetic field of order  $H_{c2}$  is due to coherent Andreev reflection from the Cooper pair condensate which is spatially characterized by the spatial profile of the order parameter (the amplitude of the wave function of superconducting condensate)  $\Delta(\mathbf{r})$  [3]. Also, the spectrum of the lowest bound states does not essentially depend on the specific spatial profile of the order parameter  $\Delta(r)$ . In fact, the linear dependence these states' energies on the angular momentum quantum number  $\mu$  is determined by the limiting slope parameter  $d\Delta/dr|_{r=0}$ . Self-consistent treatment in [4] showed that this slope parameter diverges in the quantum limit  $T \rightarrow 0$ . Shrinking of the core region leads to a reduction in the number of bound states [5, 6]. The singular behavior of the order parameter is expected from the

general reasonings about the gapless character of the fermionic excitations [7]. According to [7], the structure of  $\Delta(\mathbf{r})$  can be even more complex and is characterized by additional scale  $\xi_1 \lesssim \xi_{BCS} = \xi_0/\pi$ , where  $\xi_0 = v_F/\Delta_\infty^*$ , which separates the regions at the point where the jump of the derivative of the order parameter occurs. The quantity  $\xi_1$  also determines the distance where the supercurrent density reaches its maximum [8, 9]. So, we treat the distance  $\xi_1$  as another characteristic length scale of the vortex core. Thus, the structure of the vortex core is far from trivial even in the limit  $\kappa \rightarrow \infty$  due to singularities caused by both the point-like structure of the defect and the spatial distribution of  $\Delta(r)$ . As a result, the electronic structure of the vortex core and the behavior of the order parameter are strongly correlated in the limit  $T \rightarrow 0$  [8].

The aim of this paper is to propose a model Hamiltonian to describe the lowest bound state for conventional s-wave superconductors of the CdGM branch which is explicitly based on the singular behavior of the slope  $d\Delta(\mathbf{r})/dr|_{r \rightarrow 0}$  in the quantum limit. The independence of the spectrum from the specific spatial profile of the order parameter  $\Delta(\mathbf{r})$  follows directly. The concept is based on the results from [10, 11], where the self-adjoint extensions for the Aharonov-Bohm (AB) Hamiltonian were studied. The key parameter is the fraction of the flux quantum  $\Phi_{core}$  localized within the core. It should be noted that the standard AB effect for the Abrikosov vortex was considered for the scattering states and had little impact on the CdGM bound states [12]. From this point of view, the important result of [11] is that boundary conditions exist such that there is a bound state in the vicinity of the localized magnetic flux. This state is qualitatively different from the bound state in the potential well because it is caused in essence by the localized magnetic flux. This grounds the possibility of the treatment of the lowest bound states of the Bogolubov-de Gennes Hamiltonian with the help of self-adjoint extensions for AB Hamiltonian. Thus, we give physical interpretation for the nonstandard boundary conditions (or equivalently the self-adjoint extensions) for the AB Hamiltonian.

The structure of paper is as follows. In Section 1, we consider the relation between the BdG Hamiltonian for the quasiparticle excitations and the self-adjoint extension of the Aharonov-Bohm (AB) Hamiltonian. We show that these Hamiltonians are equivalent for the low lying energy states localized near the vortex core. In Section 2, we use the above result to study the dependence of the bound state energy on the relevant parameters and show how this can be used to explain the results of [5] in our approach. In the conclusion, the summary of the results is given and some problems for the further studies are listed.

## 1. The Hamiltonian reduction for the low lying bound states

Theoretical investigations of the quasiparticle spectrum around the vortex structure in the clean limit at low temperatures is based on the Bogoliubov-de Gennes Hamiltonian (BdGH) [1]:

$$\hat{H} = \sigma_z \left\{ \left( \hat{\mathbf{p}} - \sigma_z \frac{e}{c} \mathbf{A} - \frac{1}{2} \sigma_z \nabla \theta \right)^2 - E_F \right\} + \sigma_x \Delta(r) \quad (1)$$

where  $E_F$  is the Fermi energy, the vector potential  $\mathbf{A}$  of the applied magnetic field of the order's lower critical field  $H_{c1}$ , that is, the lowest field at which formation of vortices in a type-II superconductor becomes thermodynamically favorable while the gradient term is for the magnetic field localized in the vortex. The order parameter  $\Delta(\mathbf{r})$  has obvious asymptotic

---

\* $\hbar = 1$ ,  $m = 1/2$  in this work.

behavior:

$$\Delta(r) = \begin{cases} 0 & \text{if } r \rightarrow 0 \\ \Delta_\infty & \text{if } r \rightarrow \infty \end{cases} \quad (2)$$

and should be determined consistently. To find the spectrum for (1), some specific model for  $\Delta(r)$  can be used. Commonly,  $\Delta(r)$  is taken in the form (see [12–14]):

$$\Delta(r) = \Delta_\infty \tanh \frac{r}{\xi_0}. \quad (3)$$

At the low temperature limit, because of Kramer-Pesch anomaly [15], the increase of  $\Delta(r)$  to the asymptotic value  $\Delta_\infty$  occurs at a distance  $\xi_1$ , much smaller than  $\xi_0$ , namely  $\xi_1 \simeq k_F^{-1}$  [16]:

$$\Delta(r) = \Delta_\infty \frac{r}{\xi_1} + \dots \quad (4)$$

$$\frac{E_\mu}{\Delta_\infty} = \frac{2\mu}{k_F} \left. \frac{d\Delta(r)/\Delta_\infty}{dr} \right|_{r=0} \begin{cases} \xrightarrow{\text{Caroli et al. [1]}} \frac{2\mu}{k_F \xi_0} \quad \text{or} \quad \frac{2\mu}{k_F \xi_1} \\ \xrightarrow{\text{Kramer\&Pesch [4]}} \frac{2\mu}{k_F \xi_0} \ln \left[ \frac{\xi_0}{2\xi_1} \right], \quad \xi_1 \ll \xi_0 \end{cases} \quad (5)$$

due to presence of two length scales  $\xi_1$  and  $\xi_0$ .

It is natural that for the materials with  $\varkappa \gg 1$ , the vortex can be considered as a point-like singularity due to the localized magnetic flux, similar to the situation of the AB Hamiltonian. As has been said above, the appearance of the bound state is due to reflection of the excitation from the Bose condensate of Cooper pairs which is equivalent to the effective magnetic field of the order  $H_{c2} \propto \varkappa$ . Therefore we can interchange the  $\Delta$ -potential term in the Hamiltonian (1) by the field of the localized magnetic flux:

$$\mathbf{A}(r) = \frac{\Phi_{core}}{2\pi r} \mathbf{e}_\theta. \quad (6)$$

The parameter  $\alpha = \{\Phi_{core}/\Phi_0\}$  is the fraction of the magnetic flux corresponding to the region of the localization of the size  $\xi_1$ . Here the magnetic flux quantum  $\Phi_0 = 2\pi c/e$  corresponds to the excitation with charge  $e$ . The total flux of the Abrikosov vortex is  $\Phi_0/2$  so that  $\alpha < 1/2$ . Also we will use the dimensionless variables  $\tilde{r} = r/\xi_0$ . Thus, the Hamiltonian (1) can be reduced to a much simpler one:

$$\hat{H} = \hat{H}_\alpha^{(AB)} - E_F, \quad (7)$$

where  $\hat{H}_\alpha^{(AB)}$  is the self-adjoint extension for the AB Hamiltonian

$$H_{AB} = \hat{\mathbf{p}}^2 + \frac{(\alpha + 1/2)^2}{r^2}. \quad (8)$$

The divergence of the slope  $d(\Delta/\Delta_\infty)/dr$  at  $r \rightarrow 0$  can be treated correctly via the introduction of a dimensionless parameter  $\xi_1 d(\Delta/\Delta_\infty)/dr|_{r=0}$ . The latter determines the

energy of the bound states [1, 15]. It can be shown that  $2\mu\Delta_\infty/(k_F\xi_0)$  is similar to the energy spectrum of the Landau levels. The effective region of localization is on the order of the vortex core radius  $\xi_1$ , which corresponds to the effective field of order  $H_{c2}$ . Taking into consideration that  $\Delta_\infty = v_F/\xi_0$  and  $\xi_{GL}/\xi_{BCS} = \pi \xi_{GL}/\xi_0 \approx 0.74$  [17], for  $T/T_c \ll 1/(k_F\xi_0)$  at  $k_F\xi_0 > 1$  where  $\xi_{GL}$  is the Ginzburg-Landau coherence length and is as follows:

$$\xi_{GL} = \frac{1}{2\pi} \sqrt{\frac{\Phi_0}{H_{eff}}} = \frac{1}{\sqrt{\pi\omega_H}} \sqrt{\frac{H}{H_{eff}}} \quad \text{with} \quad H_{eff} = \frac{H_{c2}}{\pi}, \quad \omega_H = \frac{2eH}{c} \quad (9)$$

and therefore

$$E_\mu = 2\mu \frac{\Delta_\infty}{k_F\xi_0} = \frac{4\mu}{\xi_0^2} \approx 2\mu \frac{\omega_H}{\pi} \frac{H_{eff}}{H}. \quad (10)$$

Also considering that in the quantum limit the size of the vortex core  $\xi_1 < \xi_0$  [4], then the magnetic flux which is localized in the vortex core is defined as  $\Phi_{core} = 2\pi \xi_1^2 H_{eff}/\pi = 2\xi_1^2 H_{eff}$ . This choice of  $H = H_{eff}/\pi$  corresponds to the Landau levels from Eq. (10). It is easy to show that  $\alpha$  has the form:

$$\alpha = \frac{\Phi_{core}}{\Phi_0} = \frac{1}{2} \left( \frac{\xi_1}{\pi \xi_{GL}} \right)^2 \simeq \left( \frac{\xi_1}{\xi_0} \right)^2. \quad (11)$$

Note that parameter  $\alpha$  can be measured experimentally [8].

Thus, the inner structure of the vortex is encoded into the parameters of the proper boundary conditions for (8). The parameters of these conditions are related to the physical parameters of the limit  $\xi_1 \rightarrow 0$  such as  $k_F\xi_1$  and  $\xi_1/\xi_0$  (note that  $\delta_L \gg \xi_0$  corresponds to  $\varkappa \rightarrow \infty$ ) when the slope of the order parameter  $\Delta$  becomes singular.

It should be noted that the quadratic dependence  $\alpha$  on  $\xi_1/\xi_0$  is due to the assumption of effective magnetic field homogeneity within the core while taking the singular limit. In general, some scaling behavior can be expected  $\alpha \propto (\xi_1/\xi_0)^\nu$ . To estimate the value of  $\alpha$  for real materials and to check the scaling dependence, we use the experimental data of [5] for superconductors in which  $1 < k_F\xi_0 < 16$ . This way, it is possible to find the dependence of  $\alpha$  on the ratio  $\xi_1/\xi_0$ . In the quantum limit, the value  $\xi_1/\xi_0$  lies in the 0.1 – 0.7 interval. Based on the experimental data of [5], we can plot on a logarithmic scale the dependence  $\xi_1/\xi_0$  of  $k_F\xi_0$  in the quantum limit for different values of  $k_F\xi_0$ . This dependence is shown in Fig. 1 and is approximated by the formula:

$$\ln \xi_1/\xi_0 = \ln 3/4 - 0.72 \ln k_F\xi_0, \quad (12)$$

which leads to:

$$\alpha = \frac{1}{2(0.74)^2} \left( \frac{3}{4(k_F\xi_0)^{0.72}} \right)^2 \approx \frac{1}{2(k_F\xi_0)^{1.44}} < \frac{1}{2}. \quad (13)$$

For example, in the quantum limit for the *YBCO*-superconductor ( $k_F\xi_0 \sim 4$  with  $T_c = 90\text{ K}$  [18]) we get  $\alpha \sim 0.1$ . It is natural that for  $k_F\xi_0 \gg 1$  the parameter  $\alpha$  vanishes. Now, we use the general results of [11] on spectrum of the model Hamiltonian of AB type (8).

## 2. Bound states for the model Hamiltonian

The nontrivial spectrum in extended AB problem is determined by the radial part of the AB Hamiltonian in the cylindrical coordinates:

$$-\frac{d^2}{d\tilde{r}^2} - \frac{1}{\tilde{r}} \frac{d}{d\tilde{r}} + (\alpha + \mu)^2 \frac{1}{\tilde{r}^2}. \quad (14)$$

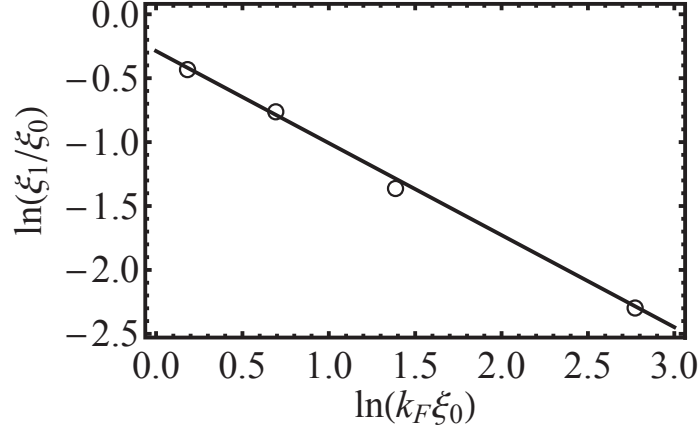


FIG. 1. The log-log plot for dependence  $\xi_1/\xi_0$  on  $k_F \xi_0$ . The points represent the data from [5].

According to the theory of self-adjoint extensions, for the AB Hamiltonian, there is generally a 4-parameter set of boundary conditions for each  $\alpha$  value [11]. But, if one requires that the Hamiltonian commutes with the angular momentum operator then this can be reduced to only 2 parameters [19]. In our case,  $\mu = 1/2$ , there is only a one-parameter set of boundary conditions for each value of  $\alpha$ :

$$\Phi_1 = b \Phi_2, \quad (15)$$

where

$$\Phi_1(\psi) := \lim_{r \rightarrow 0} r^D \int_0^{2\pi} \psi(r, \theta) e^{i\theta/2} d\theta / 2\pi \quad (16)$$

$$\Phi_2(\psi) := \lim_{r \rightarrow 0} r^{-D} \left[ \int_0^{2\pi} \psi(r, \theta) e^{i\theta/2} d\theta / 2\pi - r^{-D} \Phi_1(\psi) \right] \quad (17)$$

$$D = 1/2 + \alpha$$

and  $b$  is the corresponding parameter of the boundary condition. The energy of the ground state is

$$\frac{E_0(\alpha)}{\Delta_\infty} = \frac{2}{k_F \xi_0} \left( -\frac{b \Gamma(1/2 - \alpha)}{\Gamma(3/2 + \alpha)} \right)^{-2/(1+2\alpha)}. \quad (18)$$

Note that both  $\alpha$  and  $\mu$  parameters enter the Hamiltonian (14) in the same way. We need to determine the slope of the dispersion law of (5) using (18) at  $\Delta_\infty$  fixed. To do this, we take into account that the eigenvalues of (14) depend on the combination  $\alpha + \mu$ . Therefore if the gap  $\Delta_\infty$  is fixed, then:

$$\partial(E_0(\alpha))/\partial \alpha|_{\alpha=0} = - \partial(E_\mu)/\partial \mu|_{\mu=0}. \quad (19)$$

From Eq. (18) we obtain:

$$\left. \frac{\partial E_0(\alpha)/\Delta_\infty}{\partial \alpha} \right|_{\alpha=0} = \frac{2(1 - \gamma + \ln(-\frac{b}{2}))}{k_F \xi_0 b^2}, \quad (20)$$

but, according to (5):

$$\left. \frac{\partial E_\mu/\Delta_\infty}{\partial \mu} \right|_{\mu=0} = \frac{2}{k_F} \left. \frac{d \Delta(r)/\Delta_\infty}{dr} \right|_{r=0} = \frac{2}{k_F \xi_{BCS}} = \frac{2\pi}{k_F \xi_0}, \quad (21)$$

where  $\gamma$  is the Euler's constant and  $\lim_{r \rightarrow 0} \Delta(r) = \Delta_\infty r / \xi_{BCS}$ . This choice of  $\xi = \xi_{BCS}$  corresponds to the Landau levels with magnetic field of  $H_{eff}$  from Eq. (10). Comparing Eq. (20) and Eq. (21) we obtain the equation for the parameter  $b$ :

$$\frac{(\gamma - 1 - \ln(-\frac{b}{2}))}{b^2} = \pi, \quad (22)$$

which has the solution:

$$b = -\sqrt{\frac{W(8e^{2\gamma-2\pi})}{2\pi}} \approx -0.53, \quad (23)$$

where  $W$  is the Lambert  $W$ -function.

### 2.1. Comparison with numerical calculations

Self-consistent numerical solution of the Bogoliubov-de Gennes equations in the quantum limit for a clean  $s$ -wave superconductor was performed in [5]. There, it was shown that the shrinking of the core region leads to a reduction in the number of bound-quasiparticle state energy levels. For large  $k_F \xi_0$  values, the energy of the ground state ( $\mu = 1/2$ ) was fitted by the empirical expression (we use the notations of [5]):

$$\frac{E_{1/2}}{\Delta_\infty} = \frac{\ln(k_F \xi_0 / 0.3)}{2k_F \xi_0}. \quad (24)$$

Now, using Eq. (13) and Eq. (23) it is possible to obtain the corresponding asymptotic for the from Eq. (18). For  $k_F \xi_0 \gg 1$ , we get the following asymptotic behavior:

$$\frac{E_0(\alpha)}{\Delta_\infty} = \frac{\pi}{k_F \xi_0 W(8e^{2\gamma-2\pi})} + \alpha \frac{2\pi}{k_F \xi_0} + O(\alpha^2) \underset{\alpha \rightarrow 0}{\approx} \frac{1.75}{k_F \xi_0}. \quad (25)$$

Such behavior is due to the fact that  $\alpha \rightarrow 0$  the energy  $E_0(\alpha)$  tends to the CdGM ground

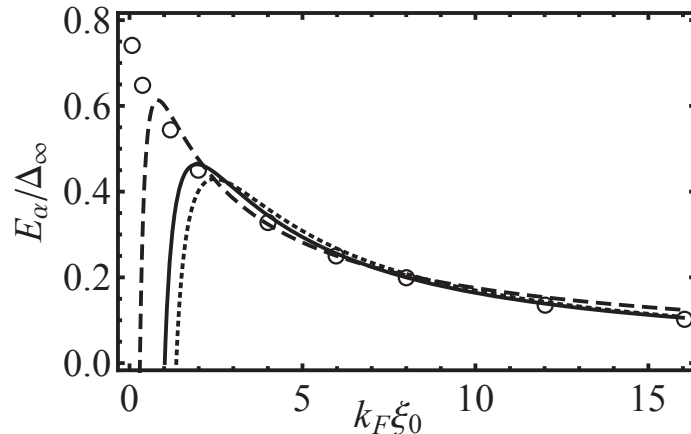


FIG. 2. The energy of ground state  $E_0/\Delta_\infty$  as a function of  $k_F \xi_0$ . The solid curve shows the result of Eq. (18) at  $b$  given by Eq. (23). The dashed line shows Eq. (24), the dotted line is the dependence of  $E_0(\alpha)/\Delta_\infty$  on  $k_F \xi_0$  for  $\alpha \simeq (k_F \xi_0)^{-2}$ . The open circles correspond to the numerical calculations of [5].

state. In Fig. 2 the comparison of our result with that of Hayashi N., *et. al.* [5] is shown. Note that the asymptotic behavior (25) of the ground state energy differs from the empirical result of Hayashi N., *et. al.* (24) and has better agreement for large values  $k_F\xi_0$ . Additionally, no fitting parameter was not used.

## Conclusion

The main result of this paper is twofold. First, we have shown that the Kramer-Pesch anomaly for the order parameter slope  $d\Delta(r)/dr$  in the core of the Abrikosov vortex can be described via non-standard boundary conditions for the Aaharonov-Bohm Hamiltonian. In such a manner, the well-known fact that CdGM spectrum is determined by the limiting slope of the order parameter  $d\Delta(r)/dr$  acquires natural explanation. The analytical expression for the ground state energy  $E_0$  as a function of the vortex core radius  $\xi_0$  is obtained and shows good correspondence with known results derived from the numerical solution of BdG equations.

The second issue is that the non-standard boundary conditions for the Aaharonov-Bohm Hamiltonian with the localized magnetic flux can be interpreted in physical terms as the Hamiltonian for the low-lying excitations near the Abrikosov vortex. This gives the possibility of using this approach for a more complicated situation, for example, a vortex pinned by the cylindrical defects [20].

## Acknowledgements

The authors thank Prof. Vadim Adamyan for clarifying discussions. This work was partially supported by MES of Ukraine, Grant no. 0115U003208.

## References

- [1] Caroli C., de Gennes P.G., Matricon J. Bound Fermion states on a vortex line in a type II superconductor. *Physics Letters*, 1964, **9**, **4**, P. 307–309. [http://dx.doi.org/10.1016/0031-9163\(64\)90375-0](http://dx.doi.org/10.1016/0031-9163(64)90375-0)
- [2] Bardeen J., Kümmel R., Jacobs A.E., Tewordt L. Structure of Vortex Lines in Pure Superconductors. *Phys. Rev.*, 1969, **187**(2), P. 556–569. <http://dx.doi.org/10.1103/PhysRev.187.556>
- [3] Rainer D., Sauls J.A., Waxman D. Current carried by bound states of a superconducting vortex. *Phys. Rev. B*, 1996, **54**(14), P. 10094–100106. <http://dx.doi.org/10.1103/PhysRevB.54.10094>
- [4] Kramer L., Pesch W. Core structure and low-energy spectrum of isolated vortex lines in clean superconductors at  $T \ll T_c$ . *Zeitschrift fur Physik A Hadrons and Nuclei*, 1974, **269**(1), P. 59–64. <http://dx.doi.org/10.1007/BF01668869>
- [5] Hayashi N., Isoshima T., Ichioka M., Machida K. Low-Lying Quasiparticle Excitations around a Vortex Core in Quantum Limit. *Phys. Rev. Lett.*, 1998, **80**(13), P. 2921–2924. <http://dx.doi.org/10.1103/PhysRevLett.80.2921>
- [6] Kato M., Maki K. Quasi-Particle Spectrum around a Single Vortex in Superconductors s-Wave Case. *Progress of Theoretical Physics*, 2000, **103**(5), P. 867–879. <http://dx.doi.org/10.1143/PTP.103.867>
- [7] Volovik G.E. Vortex Core Anomaly from the Gapless Fermions in the Core. *Pis'ma Zh. Eksp. Teor. Fiz.*, 1993, **58**(6), P. 455–460. [http://www.jetpletters.ac.ru/ps/1189/article\\_17952.shtml](http://www.jetpletters.ac.ru/ps/1189/article_17952.shtml)
- [8] Sonier J.E., Brewer J.H., Kiefl R.F.  $\mu$ SR studies of the vortex state in type-II superconductors. *Rev. Mod. Phys.*, 2000, **72**(3), P. 769–811. <http://dx.doi.org/10.1103/RevModPhys.72.769>
- [9] Sonier J.E. Investigations of the core structure of magnetic vortices in type-II superconductors using muon spin rotation. *Journal of Physics: Condensed Matter*, 2004, **16**(40), P. S4499–S4513. <http://dx.doi.org/10.1088/0953-8984/16/40/006>
- [10] Adami R., Teta A., On the Aharonov-Bohm Hamiltonian. *Letters in Mathematical Physics*, 1998, **43**(1), P. 43–54. <http://dx.doi.org/10.1023/A:1007330512611>
- [11] Dabrowski L., Štoviček P. Aharonov-Bohm effect with  $\delta$ -type interaction. *Journal of Mathematical Physics*, 1998, **39**(1), P. 47–62. <http://dx.doi.org/10.1063/1.532307>

- [12] Cleary R.M. Scattering of Single-Particle Excitations by a Vortex in a Clean Type-II Superconductor. *Phys. Rev.*, 1968, **175**(2), P. 587–596. <http://dx.doi.org/10.1103/PhysRev.175.587>
- [13] Shore J.D., Huang M., Dorsey A.T., Sethna J.P. Density of states in a vortex core and the zero-bias tunneling peak. *Phys. Rev. Lett.*, 1989, **62**(26), P. 3089–3092. <http://dx.doi.org/10.1103/PhysRevLett.62.3089>
- [14] Gygi F., Schlüter M. Electronic tunneling into an isolated vortex in a clean type-II superconductor. *Phys. Rev. B*, 1990, **41**(1), P. 822–825. <http://dx.doi.org/10.1103/PhysRevB.41.822>
- [15] Doettinger S.G., Huebener R.P., Kittelberger S. Kramer-Pesch effect and damping of the vortex motion in the cuprate superconductors. *Phys. Rev. B*, 1997, **55**(9), P. 6044–6050. <http://dx.doi.org/10.1103/PhysRevB.55.6044>
- [16] Gygi F., Schlüter M. Self-consistent electronic structure of a vortex line in a type-II superconductor. *Phys. Rev. B*, 1991, **43**(10), P. 7609–7621. <http://dx.doi.org/10.1103/PhysRevB.43.7609>
- [17] Schmidt V.V., *The Physics of Superconductors: Introduction to Fundamentals and Applications*, Springer, 1997. <http://dx.doi.org/10.1007/978-3-662-03501-6>
- [18] Maggio-Aprile I., Renner C., Erb A., Walker E., Fischer O. Direct Vortex Lattice Imaging and Tunneling Spectroscopy of Flux Lines on  $\text{YBa}_2\text{Cu}_3\text{O}_{7-\delta}$ . *Phys. Rev. Lett.*, 1995, **75**(14), P. 2754–2757. <http://dx.doi.org/10.1103/PhysRevLett.75.2754>
- [19] Borg J.L., Pulé J.V. Pauli approximations to the self-adjoint extensions of the Aharonov-Bohm Hamiltonian. *Journal of Mathematical Physics*, 2003, **44**(10), P. 4385–4410. <http://dx.doi.org/10.1063/1.1601298>
- [20] Mel'nikov A.S., Samokhvalov A.V., Zubarev M.N. Electronic structure of vortices pinned by columnar defects. *Physical Review B (Condensed Matter and Materials Physics)*, 2009, **79**(13), P. 134529/1–8. <http://dx.doi.org/10.1103/PhysRevB.79.134529>

## Synthesis of copper nanoparticles for use in an optical initiation system

V. M. Pugachev<sup>1</sup>, K. A. Datiy<sup>2</sup>, A. S. Valnyukova<sup>1</sup>, M. V. Ananyeva<sup>1</sup>, A. V. Kalenskii<sup>1</sup>

<sup>1</sup> Kemerovo state University, Kemerovo, 650043, Russia

<sup>2</sup>Institute of Coal Chemistry and Material Science SB RAS, Kemerovo, 650000, Russia  
kriger@kemsu.ru

PACS 61.46.+w, 82.33.Vx

DOI 10.17586/2220-8054-2015-6-3-361-365

In this work, the modes of synthesizing copper nanoparticles for use in an optical initiation system were proposed. The optimal sizes of the copper particles in the pentaerythritol tetranitrate were estimated, for use as a cup of the optical detonator on the first and the second harmonics of the Nd:Yag laser. For the first harmonic of the Nd:Yag, laser the absorptivity maximum was 0.097 and the particle's radius was 98 nm, for the second harmonic, the absorptivity maximum rose more than in 34 times, and it was equal to 3.29 and the copper particle's radius was 30 nm. Comparison of the calculated critical energy densities shows that pentaerythritol tetranitrate, which contains the copper nanoparticles, must be significantly more sensitive ( $\sim 29$  times) to the second harmonic than to the first. The modes of synthesis for copper nanoparticles of the required size were determined and tested.

**Keywords:** Hot spot model, laser initiation, metal nanoparticles absorption, copper nanoparticles, synthesis of nanoparticles.

*Received: 19 January 2015*

### 1. Introduction

Metal nanoparticles with the definite sizes and shapes are currently found in wide use in optical and electronic equipment [1], chemical, biochemical sensors and catalysts [2-4]. In works [5-6] the potential for using gold and silver nanoparticles as a part of the composites with a transparent medium for an optical detonator's cup was shown. In contrast to the iron-group [7-8] and aluminium-group elements, for which the maximal absorptivities ( $Q_{abs}$ ) do not exceed 2.5, silver and gold nanoparticles  $Q_{abs}$  have values more than 6 [6]. One way to enhance the safety of using energetic materials-based equipment based is to develop optical initiation systems. Explosives in these systems must have selective sensitivity to irradiation and at the same time have low sensitivity to sound waves and impact [10]. In work [11], the initiation threshold values were determined for the pentaerythritol tetranitrate, containing aluminium nanoparticles. The composites were shown to have laser sensitivity about 1 J/cm<sup>2</sup>, this value is in 100 times smaller than that of pure pentaerythritol tetranitrate pressed pellet. That is why the main direction of optical detonators development is the doping of the existing explosives with the light sensitive impurities [5]. At the same time, one of the most important questions is the synthesis of the stable nanoparticles of the required size. The aim of this work is to define the optimal nanoparticle size for use in the cup of an optical detonator, and to determine the synthetic method for those nanoparticles. To achieve the object it is necessary:

1) to calculate the optical properties of the copper nanoparticles in the pentaerythritol tetranitrate pressed matrix for the first and the second harmonics of the Nd:Yag laser;

2) to calculate the minimal initiation energy density of explosive decomposition of the pentaerythritol tetranitrate containing copper nanoparticles taking into account the absorptivities obtained in step 1;

3) to determine and test methods for the synthesis of properly-sized copper nanoparticles.

## 2. Hot spot model

Experimental solution of the first and second point is a very laborious task, even for one wavelength [12-13]. That is why the absorptivities ( $Q_{abs}$ ) of the spherical nanoparticles with radii  $R$  were calculated in terms of Mie theory using the method described in [14].

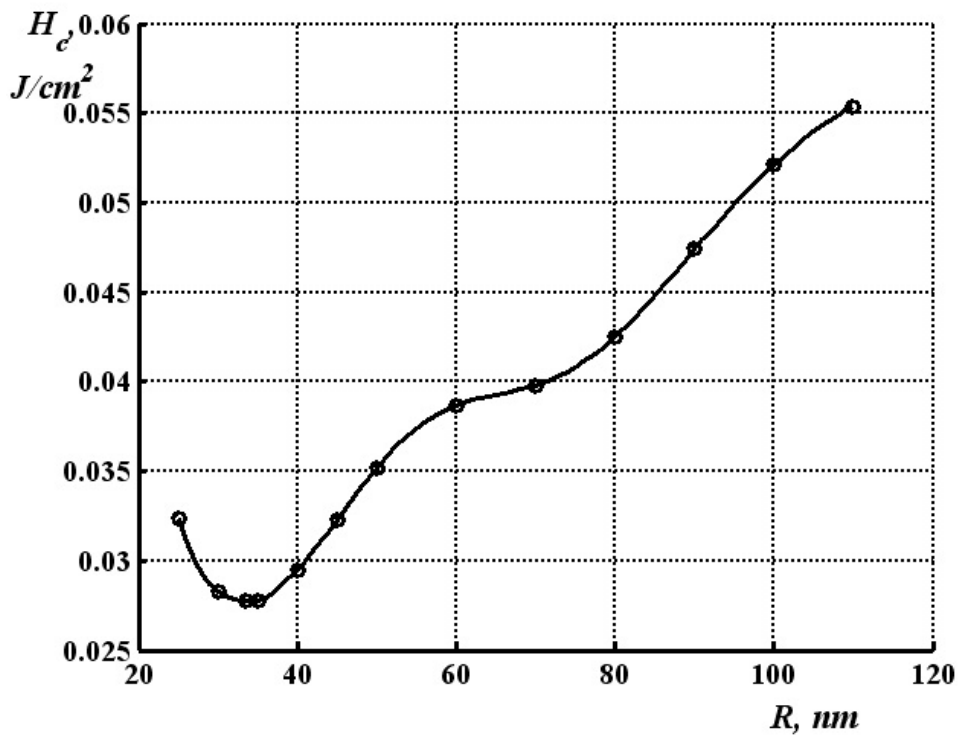


FIG. 1. Dependence of the critical initiation energy of the pentaerythritol tetranitrate on the copper nanoparticles' radii for the 532 nm wavelength

To calculate the absorptivity, it is necessary to use the complex refractive index ( $m_i$ ), which also depends on the wavelength of the incident irradiation [11]. In work [15], the  $m_i$  for copper was estimated to be 0.85–2.39  $i$  for the first harmonic (1064 nm) of the Nd:Yag laser and 0.21–7.0  $i$  for the second harmonic (532 nm). For each wavelength, the dependences  $Q_{abs}(R)$  were calculated. These dependences have maxima ( $Q_{abs \ max}$ ) whose positions ( $R_{abs \ max}$ ) depend on the wavelength. For the first harmonic of the Nd:Yag laser,  $Q_{abs \ max} = 0.097$  and  $R_{abs \ max} = 98$  nm, for the second harmonic,  $Q_{abs \ max}$  increases to 3.29 and  $R_{abs \ max}$  decreases to 30 nm.

The considerable (more than in 34-fold) increase of  $Q_{abs \ max}$  comparing two harmonics must give the corresponding decrease of the energy density ( $H_c$ ), required to initiate the explosive decomposition of the pentaerythritol tetranitrate – copper system. Model of initiation of the explosive decomposition in the vicinity of the absorbing particle and the method

of the calculation was presented in previous works [16–17]. The minimal value of the critical energy density ( $H_{c\ min}$ ) for the pentaerythritol tetranitrate – copper system, calculated in terms of the model for the first harmonic, was  $0.82\ \text{J}/\text{cm}^2$  while  $R_{min} = 96\ \text{nm}$ . Figure 1 shows the dependence  $H_c(R)$  calculated for copper nanoparticles at a wavelength of  $532\ \text{nm}$ . The dependence has a strongly marked minimum, which corresponds to the minimal energy density necessary to transition the reaction into a self-accelerated mode. The coordinates for the minimum are  $H_{c\ min} = 0.0278\ \text{J}/\text{cm}^2$  and  $R_{min} = 33.5\ \text{nm}$ .

Comparing the calculated critical energy densities shows that pentaerythritol tetranitrate, containing copper nanoparticles, acted upon by the second harmonic of Nd:Yag laser has a considerably smaller critical energy density (by 29 times) than that of the first harmonic. For the optical detonator cups using the first harmonic, the optimal size of copper particles is about  $200\ \text{nm}$ , for the second harmonic, the ideal size is  $60\text{--}70\ \text{nm}$ . The following stage of research is to work out the methods of synthesis of the copper with required sizes.

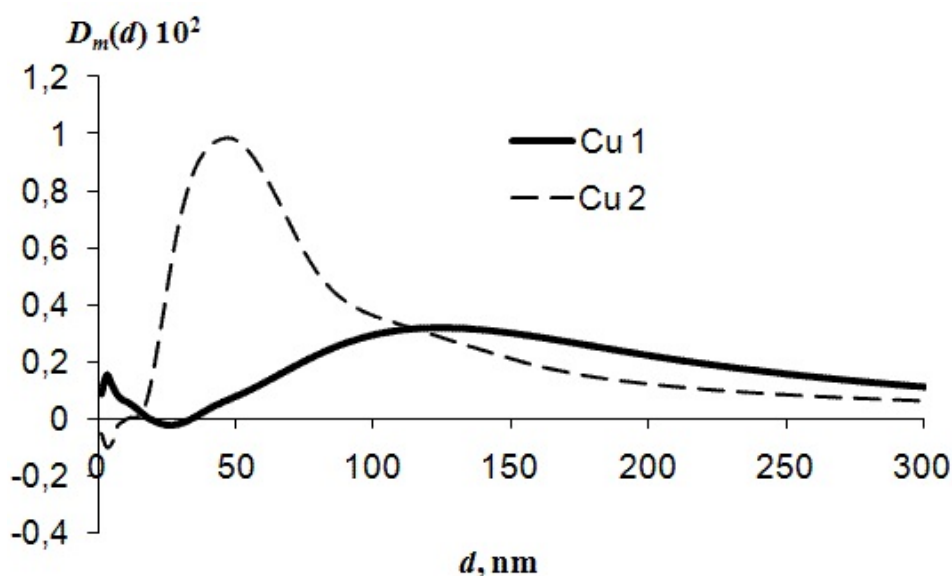


FIG. 2. Typical mass contribution function of the heterogeneity on size. The samples were got using regimes “A” (1) and “B” (2)

### 3. Synthesis of copper nanoparticles

Different methods of synthesizing the copper particles are known. In work [18] copper nanoparticles of different diameters (from  $3$  till  $22\ \text{nm}$ ) were obtained by the reduction of copper sulfate and ascorbic acid in an aqueous solution of ethylene glycol (sodium borohydride was used as a reducing agent), this caused the existence the copper(I) oxide impurity in the copper nanoparticles. The abundance of the copper(I) oxide varied from  $11.5\%$  to  $44.1\%$  depending on the conditions of the reaction. For optical detonators, it is necessary to use nanoparticles with considerably larger diameters which have oxidation-free surfaces.

In this work, the synthesis of Cu nanoparticles was performed in an “Anton Paar” reactor. The copper hydroxide, deposited by alkali ( $\text{NaOH}$ ,  $99\ \text{wt.}\%$ ) in an aqueous solution of the copper chloride (analytical grade), and then, the in situ-formed hydroxide was reduced by hydrazine hydrate. Conditions were optimized taking into account the methods for obtaining two-component powders Fe–Co, Fe–Ni and Cu–Ni [19–23]. We have also determined the optimal conditions for obtaining copper of one phase, which was proved by the results of

the radiographic analysis. Alkali 2–3 g ( $\sim 0.3$  mol/l) and reducing agent 15–20 ml ( $\sim 3$  mol/l) are added to 100 ml (assuming 1 gram of metal) of the reaction mixture, which temperature was 80–85°. Then, in mode A the mixture of alkali salt and hydrazine are added simultaneously, in mode B the alkali salt is added prior to the hydrazine. A compulsory condition for synthesis is intense agitation (mechanical stirrer of “squirrel cage” type). All steps of the process were performed using equipment that permitted the use of an inert atmosphere and excluded all contact of the reactants with air.

Immediately after synthesis and washing, the powder was placed in a weighing bottle and stored under glycerin. The main purpose of the synthesis under a nitrogen atmosphere is to obtain metal nanoparticles having a minimal percentage of the oxidized impurity phase.

Determination of the phase composition and structural parameters was performed using X-ray diffractometer Difreii-401 (Russia) and DRON-3. The average particle size was determined by the method of small-angle X-ray scattering in copper irradiation using PFC-1 apparatus. Copper nanoparticles, synthesized in mode A, had diameters ( $d$ ) from 100 to 300 nm (fig. 2 (1)); while mode B gave particles with diameters of about 60 nm (fig. 2 (2)). Data from the small-angle X-ray scattering agreed with the results of the diffraction peak broadening calculation, which gave the particles' sizes of about 50 nm. Thus, the analyzed powders might be considered nanopatterned.

The mass size contribution function has areas with the minima below zero (area of sizes up to 5 nm), this is because of a thin film of oxide on the particles' surfaces. The average thickness of the layer is 2.5 nm. When comparing the experimental data, one readily sees that when changing the synthetic method, the copper nanoparticles' average sizes decrease from 100–200 nm (mode A) to 60 nm (mode B).

#### 4. Conclusion

In this presented work, synthetic methods for copper nanoparticles for use in optical initiation system were proposed. Optimal sizes were estimated for copper particles in pentaerythritol tetranitrate, used as the cup of an optical detonator, for the first and the second harmonics of the Nd:Yag laser. For the first harmonic,  $Q_{abs\ max} = 0.097$  and  $R_{abs\ max} = 98$  nm, for the second harmonic  $Q_{abs\ max}$  rises to 3.29 and  $R_{abs\ max}$  decreases to 30 nm. Calculated for the first harmonic,  $H_{cmin}$  of the pentaerythritol tetranitrate – copper system is 0.82 J/cm<sup>2</sup> and the particle's radius  $R_{min} = 96$  nm. It was shown that pentaerythritol tetranitrate, containing the copper nanoparticles, must be significantly more sensitive ( $\sim 29$  times) to the second harmonic of the Nd:Yag laser than to the first. Methods for the synthesis of properly-sized copper nanoparticles were worked out and tested. The next step for the optimization of the optical detonator cup is to experimentally determine the critical initiation energy density for pentaerythritol tetranitrate, containing the copper nanoparticles of different diameters, for the first and the second harmonics of the Nd:Yag laser. This work was supported by Ministry of Education and Science of the Russian Federation (governmental project No. 2014/64) and Russian Foundation for Basic Research for the financial support (grant 14-03-31648).

#### References

- [1] Yang G., Zhang Z., et al. Synthesis and characterization of highly stable dispersions of copper nanoparticles by a novel one-pot method. *Materials Research Bulletin*, 2013, **48**, P. 1716.
- [2] Patolsky F., Zheng G., et al. Nanowire-based biosensors. *Analytical Chemistry*, 2006, **78**(13), P. 4260–4269.

- [3] Wang J. Carbon-nanotube based electrochemical biosensors: A review. *Electroanalysis*, 2005, **17**, P. 7–14.
- [4] Paxton W. F., Sen A., Mallouk T. E. Motility of catalytic nanoparticles through self-generated forces. *Chemistry - A European Journal*, 2005, **11**, P. 6462–6470.
- [5] Ananyeva M.V., Zvekov A.A., et al. Promising compounds for the cap of optical detonator. *Perspektivnye materialy*, 2014, **7**, P. 5–12.
- [6] Lukatova S.G. Calculation of the PETN-gold composites' absorptivity for the second harmonic of the ND:YAG laser. *Mezhdunarodnoe nauchnoe izdanie Sovremennye fundamental'nye i prikladnye issledovaniya*, 2014, **1**(12), P. 95–98.
- [7] Ananyeva M.V., Kalenskii A.V., et al. Kinetic regularities of explosive decomposition of PETN containing aluminium, cobalt and nickel nanoparticles. *Bulletin of Kemerovo state university*, 2014, **1-1**(57), P. 194–200.
- [8] Kalenskii A.V., Ananyeva M.V., et al. Spectrum dependence of the critical energy density of composites based on pentaerythritol tetranitrate with nickel nanoparticles. *Fundamental'nye problemy sovremennogo materialovedeniya*, 2014, **11**(3), P. 340–345.
- [9] Kalenskii A.V., Zvekov A.A., et al. Influence of the laser irradiation wavelength on the energetic materials' initiation critical energy. *Fizika goreniya i vzryva*, 2014, **50**(3), P. 98–104.
- [10] Kalenskii A.V., Kriger V.G., et al. The Microcenter Heat Explosion Model Modernization. *Izvestia Vuzov Fizika*, 2012, **55**(11-3), P. 62–66.
- [11] Aduiev B.P., Nurmukhametov D.R., et al. Vzryvchatoye razlozheniye TENa s nanodobavkami alyuminiya pri vozdeystvii impulsnogo lazernogo izlucheniya razlichnoy dliny volny. *Khimicheskaya fizika*, 2013, **32**(8), P. 39–42.
- [12] Aduiev B.P., Nurmukhametov D.R., et al. Integrating Sphere study of the optical properties of aluminum nanoparticles in tetranitropentaerythrite. *Zhurnal Tekhnicheskoi Fiziki*, 2014, **84**(9), P. 126–131.
- [13] Zvekov A.A., Ananyeva M.V., et al. Regularities of light diffusion in the composite material pentaerythritol tetranitrate – nickel. *Nanosystems: physics, chemistry, mathematics.*, 2014, **5**(5), P. 685–691.
- [14] Kriger V.G., Kalenskii A.V., et al. Vliyaniye effektivnosti pogloshcheniya lazernogo izlucheniya na temperaturu razogreva vklyucheniya v prozrachnykh sredakh. *Fizika goreniya i vzryva*, 2012, **48**(6), P. 54–58.
- [15] Gazenaur N.V., Zikov I.Yu., et al. The wavelength dependence of copper absorption. *Aspirant*, 2014, **5**, P. 94–98.
- [16] Aduiev B.P., Ananyeva M.V., et al. Miro-hotspot model for the laser initiation of explosive decomposition of energetic materials with melting taken into account. *Fizika goreniya i vzryva*, 2014, **50**(6), P. 92–99.
- [17] Kriger V.G., Kalenskii A.V., et al. Protsessy teploperenosa pri lazernom razogreve vklyucheny v inertnoy matritse. *Teplofizika i aeromekhanika*, 2013, **20**(3), P. 375–382.
- [18] Avchinnikova E.A., Vorob'eva S.A. Sintez i svoystva nanochastits medi, stabilizirovannykh polietilenglikolem. *Vestnik BGU*, 2013, **2**(3), P. 12–16.
- [19] Zaharov Yu.A., Pugachev V.M., et al. Nanosize powders of transition metals binary systems. *J. Phys.: Conf. Ser.*, 2012, **345**(1), P. 12024.
- [20] Pugachev V.M., Dativ K.A., et al. Study of products of nanoscale systems Fe–Co–Ni synthesis. *Bulletin of Kemerovo state university*, 2013, **55**(3), P. 77–80.
- [21] Zaharov Yu.A., Pugachev V.M., et al. Chemical synthesis, structure and magnetic properties of nanocrystalline Fe–Co alloys. *Materials Letters*, 2012, **74**, P. 173–175.
- [22] Pugachev V.M., Dodonov V.G., et al. Fazovyi sostav i nekotorye svoystva nanorazmernykh poroshkov Ni–Co i Ni–Cu. *Perspektivnye materialy*, 2011, **11**, P. 156–163.
- [23] Dativ K.A., Zakharov Yu.A., Khitsova L.M. Termostimilyryemye protsessy na poverkhnosti nanostryktirovannykh poroshkov Fe–Co–Ni. *Bulletin of Kemerovo state university*, 2014, **3-3**(59), P. 184–188.

## Statistical mechanics of transport processes of fluids under confined conditions

V. Rudyak, A. Belkin

Novosibirsk State University of Architecture and Civil Engineering, Novosibirsk, Russia  
valery.rudyak@mail.ru, a\_belkin@ngs.ru

PACS 47.61.-k, 47.10.-g

DOI 10.17586/2220-8054-2015-6-3-366-377

The problem of adequately describing transport processes of fluids in confined conditions is solved using methods of nonequilibrium statistical mechanics. The ‘fluid–channel wall’ system is regarded as a two–fluid medium, in which each phase has a particular velocity and temperature. The obtained results show that the transport equations in confined spaces should contain not only the stress tensor and the heat flux vector, but also the interfacial forces responsible for the transfer of momentum and heat due to the interaction with the wall surfaces. The stress tensor and the heat flux vector fluid can be expressed in terms of the effective viscosity and thermal conductivity. However, the constitutive relations contain additive terms that correspond to fluid–surface interactions. Thus, not only do the fluid transport coefficients in nanochannels differ from the bulk transport coefficients, but they are also not only determined by the parameters of the fluid.

**Keywords:** Micro flow, transport coefficients, nonequilibrium statistical mechanics, confined system.

*Received: 16 January 2015*

### 1. Introduction

The extensive study of liquid and gas microflows over the last two decades has been motivated by the emergence of a large number of microfluidics tools and systems. These flows are currently used in biochemistry, medicine, pharmacology, biology, thermal engineering, catalysis, etc. An important aspect of the active use of various micro and nanoflows is the development of a new generation of resource-saving technologies with low power consumption. The efficiency of micro and nanodevices is largely determined by the transport processes occurring in the fluid flows. Thus, for example, mixing in micromixers is due to diffusion processes, and the energy spent for fluid circulation depends on the fluid viscosity. Today, however, it is known that transport processes in confined geometries are significantly different from those in the bulk. Diffusion, for example, is anisotropic [1, 2], fluid viscosity is differed from the value in the bulk [3–5] and the fluid in nanochannel has a nonhomogeneous structure [6, 7].

Difficulties in measuring transport coefficients in small channels or pores are obvious. In fact, at present, there are no reliable experimental data. However, already today, we can argue with certainty, first, that the fluid viscosity in small channels is inhomogeneous over the channel cross-section and, second, that its average value is significantly different from the value in bulk. This, in particular, is suggested by the results of molecular dynamics simulations [2, 7]. Layers of structured fluid with characteristic scales on the order of nanometers are formed near the channel walls. In such channels, fluctuations in the number of molecules, momentum, and energy become important [8].

Existing experimental data on the pressure drop are very contradictory. Some authors argue that the pressure drop is described by the classical equations of fluid dynamics (see, e.g., [3]). However, there are indications that the pressure drop coefficient is much higher than the classical value (e.g., [3]) and less than it [9]. Often, these discrepancies are explained

by the slip boundary conditions on the micro or nanochannel walls (see for example [10] and referenced therein). However, in our opinion, the situation is more delicate. Transport processes are processes of relaxation of large-scale fluctuations, such as gradients of observed macroscopic variables: density, velocity, temperature, etc. Fluctuations can be maintained, in particular, by external forces with respect to the system. Transport processes in rarefied gases are easily interpreted: they are due to transfer of the corresponding microscopic characteristics on scales of the order of the mean free path of the molecules. In liquids, transport processes are much more complicated. For example, the viscosity is due not only to the momentum transfer in collisions of molecules, but also to the destruction of short-range order and diffusion processes of momentum transfer in the system. In the vicinity of the surface, an important factor in the equalization of momentum and energy in flow is the interaction of fluid molecules with the surface's molecules. In a nanochannel with a characteristic cross-sectional area on the order of 5 nm, almost half of all interactions of fluid molecules are their collisions with the molecules of the channel walls. Under such conditions, it becomes meaningless to speak about the viscosity of the fluid separately. The viscosity of the fluid becomes a property of the entire 'fluid–nanochannel wall' system. Of course, it is not easy to study this 'viscosity' experimentally. However, to develop an appropriate apparatus, it is first necessary to construct an adequate theory of transport processes, which should be used in interpreting experimental data. The aim of this work is to develop such a theory. It is constructed from the first principles using methods of nonequilibrium statistical mechanics.

## 2. The transport equations of the system

Since the states of the molecules of the fluid and the channel walls are significantly different (in particular, the walls are at rest and the fluid moves), the system is a peculiar two-fluid medium. The properties of this medium are described in this paper using the apparatus that we developed previously to describe dispersed media [11–14]. In this case, the 'fluid–channel wall' system is treated as a two-fluid medium, each of which phases consists of the same type of molecules and is characterized by their macroscopic variables: density, velocity, and temperature. The dynamics of the system is described by the  $N$ -particle distribution function  $F_N$  which satisfies the Liouville equation:

$$\partial F_N / \partial t + L_N F_N = 0, \quad (1)$$

in which the Liouville operator is defined as:

$$L_N = \sum_{\alpha, \varphi=1}^2 \sum_{i=1}^{N_\alpha} \left[ \frac{\mathbf{p}_i}{m_\alpha} \cdot \frac{\partial}{\partial \mathbf{r}_i} + \frac{1}{2} \sum_{j=1}^{N_\varphi} \mathbf{F}_{ij} \cdot \left( \frac{\partial}{\partial \mathbf{p}_i} - \frac{\partial}{\partial \mathbf{p}_j} \right) \right].$$

Here  $\mathbf{r}_i$ ,  $m_i$ , and  $\mathbf{p}_i$  are the coordinate of the center of mass, mass, and momentum of the  $i$ -th molecule of phase  $\alpha$ .

We will characterize the state of the system by partial values of the density  $n_\alpha$ , momentum  $\mathbf{p}_\alpha$ , and energy  $E_\alpha$ . These quantities are the averages of the corresponding dynamical variables:

$$\hat{n}_\alpha(\mathbf{r}) = \sum_{i=1}^{N_\alpha} \delta(\mathbf{r}_i - \mathbf{r}), \quad \hat{\mathbf{p}}_\alpha(\mathbf{r}) = \sum_{i=1}^{N_\alpha} \mathbf{p}_i \delta(\mathbf{r}_i - \mathbf{r}), \quad \hat{E}_\alpha(\mathbf{r}_i - \mathbf{r}) = \sum_{i=1}^{N_\alpha} E_i \delta(\mathbf{r}_i - \mathbf{r}), \quad (2)$$

where  $E_i$  is the energy of the  $i$ -th molecule. Applying the Liouville operator to the dynamic densities (2), we obtain the following transport equation for them:

$$\dot{\hat{n}}_\alpha = -\nabla \cdot \hat{\mathbf{J}}_{1\alpha}, \quad \dot{\hat{\mathbf{p}}}_\alpha = -\nabla \cdot \hat{\mathbf{J}}_{2\alpha} + \hat{\mathbf{j}}_{2\alpha}, \quad \dot{\hat{E}}_\alpha = -\nabla \cdot \hat{\mathbf{J}}_{3\alpha} + \hat{j}_{3\alpha}. \quad (3)$$

The operators of the number flux of molecules  $\hat{\mathbf{J}}_{1\alpha}$ , momentum flux  $\hat{\mathbf{J}}_{2\alpha}$ , the energy flux  $\hat{\mathbf{J}}_{3\alpha}$ , and the interfacial force operators  $\hat{\mathbf{j}}_{2\alpha}$  and  $\hat{j}_{3\alpha}$  are defined as follows:

$$\begin{aligned} \hat{\mathbf{J}}_{1\alpha} &= \sum_{i=1}^{N_\alpha} \frac{\mathbf{p}_i}{m_\alpha} \delta(\mathbf{r}_i - \mathbf{r}), & \hat{\mathbf{J}}_{2\alpha} &= \sum_{i=1}^{N_\alpha} \frac{\mathbf{p}_i \mathbf{p}_i}{m_\alpha} \delta(\mathbf{r}_i - \mathbf{r}) + \frac{1}{2} \sum_{i=1}^{N_\alpha} \sum_{\varphi=1}^{f,b} \sum_{j=1}^{N_\varphi} \mathbf{r}_{ij} \mathbf{F}_{ij} \int_0^1 d\eta \delta(\mathbf{r}_j - \mathbf{r} + \eta \mathbf{r}_{ij}), \\ \hat{\mathbf{j}}_{2\alpha} &= \frac{1}{2} \sum_{i=1}^{N_\alpha} \sum_{j=1}^{N_{\varphi \neq \alpha}} \mathbf{F}_{ij} [\delta(\mathbf{r}_i - \mathbf{r}) + \delta(\mathbf{r}_j - \mathbf{r})], \\ \hat{\mathbf{J}}_{3\alpha} &= \sum_{i=1}^{N_\alpha} \frac{\mathbf{p}_i E_i}{m_\alpha} \delta(\mathbf{r}_i - \mathbf{r}) + \frac{1}{4} \sum_{i=1}^{N_\alpha} \sum_{\varphi=1}^{f,b} \sum_{j=1}^{N_\varphi} \left( \frac{\mathbf{p}_i}{m_\alpha} + \frac{\mathbf{p}_j}{m_\varphi} \right) \cdot \mathbf{r}_{ij} \mathbf{F}_{ij} \int_0^1 d\eta \delta(\mathbf{r}_j - \mathbf{r} + \eta \mathbf{r}_{ij}), \\ \hat{j}_{3\alpha} &= \frac{1}{4} \sum_{i=1}^{N_\alpha} \sum_{j=1}^{N_{\varphi \neq \alpha}} \mathbf{F}_{ij} \cdot \left( \frac{\mathbf{p}_i}{m_\alpha} + \frac{\mathbf{p}_j}{m_\varphi} \right) [\delta(\mathbf{r}_i - \mathbf{r}) + \delta(\mathbf{r}_j - \mathbf{r})]. \end{aligned}$$

The hydrodynamic velocities of the fluid (hereinafter, we use the subscript  $f$ ) and the walls (subscript  $b$ ) are defined as follows:  $\mathbf{u}_f(\mathbf{r}, t) = \mathbf{p}_f(\mathbf{r}, t)/m_f n_f$ ,  $\mathbf{u}_b(\mathbf{r}, t) = 0$ . Transport equations of the hydrodynamic variables can be obtained by averaging the density transport equations (3) over the ensemble  $F_N$  and using a locally accompanying coordinate system for the fluid which moves relative to the laboratory system with velocity  $\mathbf{u}_f$ . It can be shown that these equations have the following form:

$$\begin{aligned} \frac{\partial n_f}{\partial t} + \nabla \cdot (n_f \mathbf{u}_f) &= 0, & \frac{\partial n_b}{\partial t} &= 0, \\ \rho_f \frac{\partial \mathbf{u}_f}{\partial t} + \rho_f \mathbf{u}_f \cdot \nabla \mathbf{u}_f &= -\nabla \cdot \mathbf{J}'_{2f} + \mathbf{j}_{2f}, & -\nabla \cdot \mathbf{J}'_{2b} + \mathbf{j}_{2b} &= 0, \\ \frac{\partial E'_f}{\partial t} + \nabla \cdot (\mathbf{u}_f E'_f) &= -\nabla \cdot \mathbf{J}'_{3f} - (\mathbf{J}'_{2f} + \mathbf{J}_{fb}) : \nabla \mathbf{u}_f - \mathbf{j}_{fb} \cdot \mathbf{u}_f + j'_{3f}, \\ \frac{\partial E'_b}{\partial t} &= -\nabla \cdot \mathbf{J}'_{3b} - j'_{3f} + \mathbf{J}_{fb} : \nabla \mathbf{u}_f. \end{aligned} \quad (4)$$

Here  $\mathbf{A} = \langle \hat{\mathbf{A}} \rangle$ , the angle brackets denote an average over the ensemble  $F_N$ , and all primed quantities were obtained from the corresponding unprimed ones by the momentum transformation:  $\mathbf{p}'_i = \mathbf{p}_i - m_\alpha \mathbf{u}_\alpha$ . Moreover, additional microscopic densities are introduced:

$$\hat{\mathbf{J}}_{fb} = -\frac{1}{4} \sum_{i=1}^{N_f} \sum_{j=1}^{N_b} \mathbf{r}_{ij} \mathbf{F}_{ij} \int_0^1 d\eta \delta(\mathbf{r}_j - \mathbf{r} + \eta \mathbf{r}_{ij}), \quad \hat{\mathbf{j}}_{fb} = \frac{1}{2} \sum_{i=1}^{N_f} \sum_{j=1}^{N_b} \mathbf{F}_{ij} \delta(\mathbf{r}_i - \mathbf{r}).$$

### 3. Nonequilibrium distribution function

The transport equations (4) are not closed; they contain the fluxes and interphases forces which should be connected with macroscopic variables. To calculate the fluxes  $\mathbf{J}'_{\alpha i}$  and forces  $\mathbf{j}'_{\alpha i}$  we need to determine the distribution function  $F_N$ . Thus the problem of deriving the transport equations and constitutive relations reduces to finding a solution of equation (1) for the macroscopic level of the system description. Due to the linearity of equation (1), its solution can be sought in the form of the sum of the quasi-equilibrium distribution function  $F_{N0}$  and the dissipation function  $F_{N1}$ :

$$F_N = F_{N0} + F_{N1}. \quad (5)$$

The function  $F_{N0}$  is obtained from the extremum condition for the information entropy  $S = -k \langle \ln F_{N0} \rangle$  ( $k$  is Boltzmann's constant) for the given average values of the number of particles, momentum, and energy of the particles of each medium (fluid and channel walls) (see [11, 15]). The distribution function obtained in this way corresponds to the two-fluid description of the system. In the derivation of  $F_{N0}$ , it should only be taken into account that the macroscopic velocity of the wall is equal to zero and that the temperatures of the walls and the fluid can be different. Thus the quasi-equilibrium distribution function has the following form:

$$F_{N0} = Q_0^{-1} \exp \left\{ - \int d\mathbf{r} \left[ \beta_f(\mathbf{r}, t) \hat{E}'_f(\mathbf{r}) - \nu_f(\mathbf{r}, t) \hat{n}_f(\mathbf{r}) + \beta_b(\mathbf{r}, t) \hat{E}_b(\mathbf{r}) - \nu_b(\mathbf{r}, t) \hat{n}_b(\mathbf{r}) \right] \right\}, \quad (6)$$

$$Q_0 = \left\langle \exp \left\{ - \sum_{\alpha=f}^b \sum_{k=1}^3 \int g_{k\alpha}(\mathbf{r}, t) \hat{G}_{k\alpha}(\mathbf{r}) \right\} \right\rangle,$$

$$\hat{G}_{1\alpha}(\mathbf{r}) = \hat{n}_\alpha(\mathbf{r}), \quad \hat{G}_{2\alpha}(\mathbf{r}) = \hat{\mathbf{p}}_\alpha(\mathbf{r}), \quad \hat{G}_{3\alpha}(\mathbf{r}) = \hat{E}_\alpha(\mathbf{r}).$$

Here  $g_{3\alpha} = \beta_\alpha = 1/kT_\alpha$  is the local inverse temperature of the component  $\alpha$ ,  $\nu_\alpha = -\beta_\alpha \mu_\alpha$ ,  $g_{1\alpha} = \beta_\alpha (-\mu_\alpha + m_\alpha \mathbf{u}_\alpha^2/2)$ ,  $g_{2\alpha} = -\beta_\alpha \mathbf{u}_\alpha$ , and  $\mu_\alpha$  is the local chemical potential. The average values of the particle number density of the component and its energy calculated for the quasi-equilibrium ensemble (6) are:

$$\langle \hat{n}_\alpha(\mathbf{r}) \rangle_0 = \frac{\delta \ln Q_0}{\delta \nu_\alpha(\mathbf{r})}, \quad \langle \hat{E}'_\alpha(\mathbf{r}) \rangle_0 = \frac{\delta \ln Q_0}{\delta \beta_\alpha(\mathbf{r})}.$$

Here, averaging over the ensemble (6) is denoted by the subscript 0 in the angle brackets. For the thermodynamics of the system to be defined by the function  $F_{N0}$ , it is necessary that the macroscopic variables coincide with their quasi-equilibrium values:  $n_\alpha(\mathbf{r}, t) = \langle \hat{n}_\alpha(\mathbf{r}) \rangle_0$ ,  $E'_f(\mathbf{r}, t) = \langle \hat{E}'_f(\mathbf{r}) \rangle_0$ .

Because  $F_{N0}$  is an even function of the momenta  $\mathbf{p}'_i$  and the coordinates  $\mathbf{r}_{ij}$ , the mean values of the nondiagonal elements of the stress tensor and the tensor  $\mathbf{J}_{fb}$  calculated from it are equal to zero:

$$\mathbf{J}'_{2f}{}^0(\mathbf{r}, t) = \frac{1}{3} \langle \hat{\mathbf{J}}'_{2f}(\mathbf{r}) : \mathbf{U} \rangle_0 = p_f(\mathbf{r}, t) \mathbf{U}, \quad \mathbf{J}'_{fb}{}^0(\mathbf{r}, t) = \frac{1}{3} \langle \hat{\mathbf{J}}_{fb}(\mathbf{r}) : \mathbf{U} \rangle_0 = p_{fb}(\mathbf{r}, t) \mathbf{U}.$$

Here,  $p_f$  is the partial pressure of the fluid, which we assume to be isotropic and  $\mathbf{U}$  is the unit tensor of second rank. For the same reason, the other fluxes and interfacial forces are equal to zero, and the equations of multifluid hydrodynamics for the quasi-equilibrium ensemble (6) are the Euler-type equations:

$$\begin{aligned} \frac{\partial n_f}{\partial t} + \nabla \cdot (n_f \mathbf{u}_f) &= 0, & \rho_f \frac{\partial \mathbf{u}_f}{\partial t} + \rho_f \mathbf{u}_f \cdot \nabla \mathbf{u}_f &= -\nabla p_f, \\ \frac{\partial E'_f}{\partial t} + \mathbf{u}_f \nabla \cdot E'_f &= - (E'_f + p_f + p_{fb}) \nabla \cdot \mathbf{u}_f, & \frac{\partial E'_b}{\partial t} &= p_{fb} \nabla \cdot \mathbf{u}_f. \end{aligned} \quad (7)$$

It is evident that these equations derived for the ensemble  $F_{N0}$  do not describe dissipative processes in the system. To construct the nonequilibrium distribution function, it is necessary to solve the linear inhomogeneous equation (see Eq. (5)):

$$\partial F_{N1}/\partial t + L_N F_{N1} = - (\partial F_{N0}/\partial t + L_N F_{N0}). \quad (8)$$

Applying the Liouville operator to the function  $F_{N0}$ , we obtain:

$$\begin{aligned} L_N F_{N0} = -F_{N0}(t_0) \int d\mathbf{r} \left[ \hat{\mathbf{J}}_{1f} \cdot \nabla \nu_f - \beta_f \left( \hat{\mathbf{J}}_{2f} - m_f \mathbf{u}_f \hat{\mathbf{J}}_{1f} \right) : \nabla \mathbf{u}_f + \right. \\ \left. \left( \hat{\mathbf{J}}_{3f} - \hat{\mathbf{J}}_{2f} \cdot \mathbf{u}_f + m_f \frac{\mathbf{u}_f^2}{2} \hat{\mathbf{J}}_{1f} \right) \cdot \nabla \beta_f + \right. \\ \left. \hat{\mathbf{J}}_{1b} \cdot \nabla \nu_b + \hat{\mathbf{J}}_{3b} \cdot \nabla \beta_b - \hat{\mathbf{j}}_{2f} \cdot \beta_f \nabla \mathbf{u}_f + \hat{j}_{3f} (\beta_f - \beta_b) \right]. \end{aligned}$$

The right side of equation (8) contains also time derivatives of hydrodynamic quantities which are determined from the transport equations (7) using the complete distribution function. The time derivative of the quasi-equilibrium distribution function can be written as follows:

$$\begin{aligned} \partial F_{N0}/\partial t &= T F_{N0} + T F_{N1}, \\ T F_{Nj} &= F_{N0} \sum_{\alpha=f}^b \sum_{k=1}^3 \int d\mathbf{r} \Delta \tilde{G}_{k\alpha}(\mathbf{r}) \frac{\partial_j \phi_{k\alpha}(\mathbf{r}, t)}{\partial t}, \quad j = 0, 1, \quad \phi_{1\alpha} = \nu_\alpha, \quad \phi_{2\alpha} = \mathbf{u}_\alpha, \quad \phi_{3\alpha} = -\beta_\alpha, \\ \Delta \tilde{G}_{k\alpha} &= \hat{G}_{k\alpha} - \tilde{G}_{k\alpha}, \quad \hat{G}_{1\alpha} = \hat{G}_{1\alpha}, \quad \hat{G}_{2\alpha} = \beta_\alpha \hat{G}'_{2\alpha}, \quad \hat{G}_{3\alpha} = \hat{G}'_{3\alpha}, \\ \frac{\partial_j \phi_{k\alpha}(\mathbf{r}, t)}{\partial t} &= \left\langle \frac{\partial \phi_{k\alpha}(\mathbf{r}, t)}{\partial t} \right\rangle_j. \end{aligned}$$

Then Eq. (8) becomes:

$$\partial F_{N1}/\partial t + (T + L_N) F_{N1} = - (T + L_N) F_{N0}.$$

A method for solving this equation was developed and described in detail previously [11–14]. Omitting cumbersome calculations, we give the explicit form of the nonequilibrium distribution function obtained using this method for the system considered:

$$\begin{aligned} F_{N1}(t) &= \pi(t, t_0) S_{(t-t_0)}^{(N)} F_{N1}(t_0) + \sum_{\alpha}^{f,b} \sum_{k=1}^5 \int_{t_0}^t dt_1 \int d\mathbf{r} \int d\mathbf{r}' \pi(t, t_1) S_{(t-t_1)}^{(N)} F_{N0}(t_1) \Delta \mathbf{I}_{k\alpha} \cdot \mathbf{Y}_{k\alpha}(\mathbf{r}', t_1), \\ \Delta \mathbf{I}_{k\alpha} &= \hat{\mathbf{I}}_{k\alpha}(\mathbf{r}, \mathbf{r}') - \mathbf{I}_{k\alpha}^0(\mathbf{r}, \mathbf{r}'), \quad \mathbf{I}_{ia}^0 = \left\langle \hat{\mathbf{I}}_{ia} \right\rangle_0. \end{aligned} \quad (9)$$

Here  $S_{(t-t_0)}^{(N)}$  is the displacement operator along the trajectory of  $N$  particles. The operator  $\pi(t, t_1)$  has the form of an infinite series in the thermodynamic forces [11, 16] :

$$\pi(t, t_1) = \sum_{n=0}^{\infty} \pi^n(t, t_1), \quad \pi^0(t, t_1) = 1,$$

$$\pi^n(t, t_1) = (-1)^n \int_{t_1}^t dt_2 \dots \int_{t_1}^t dt_{n+1} \prod_{i=2}^{n+1} S_{-(t-t_i)}^{(N)} T(t_i) S_{(t-t_i)}^{(N)},$$

where the product is formed starting from terms with the largest  $i$ . For weakly nonequilibrium systems (in ordinary hydrodynamics, this corresponds to the Navier-Stokes approximation), this series can be truncated to the first term. In this case the operator  $\pi(t, t_1)$  is equal to unity. The fluxes  $\hat{\mathbf{I}}_{k\alpha}$  and thermodynamic forces  $\hat{\mathbf{Y}}_{k\alpha}$  are given by:

$$\hat{\mathbf{I}}_{1f} = \hat{\mathbf{J}}'_{1f}(\mathbf{r}) \left( \delta(\mathbf{r} - \mathbf{r}') - \frac{\beta_f(\mathbf{r})}{n_f(\mathbf{r})} \left( \frac{\delta p_f(\mathbf{r})}{\delta \nu_f(\mathbf{r}')} \right)_{\beta_f} \right),$$

$$\hat{\mathbf{I}}_{1b} = \hat{\mathbf{J}}'_{1b}(\mathbf{r}) \delta(\mathbf{r} - \mathbf{r}'), \quad \mathbf{Y}_{1\alpha} = -\nabla' \nu_\alpha,$$

$$\hat{\mathbf{I}}_{2f} = \left( \hat{\mathbf{J}}'_{2f}(\mathbf{r}) + \hat{\mathbf{J}}_{fb}(\mathbf{r}) \right) \beta_f \delta(\mathbf{r} - \mathbf{r}') - [E'_f(\mathbf{r}) + p_f(\mathbf{r}) + p_{fb}(\mathbf{r})] \times$$

$$\left[ \hat{n}_f(\mathbf{r}) \left( \frac{\delta \nu_f(\mathbf{r})}{\delta E'_f(\mathbf{r}')} \right)_{n_f} - \hat{E}'_f(\mathbf{r}) \left( \frac{\delta \beta_f(\mathbf{r})}{\delta E'_f(\mathbf{r}')} \right)_{n_f} \right] \mathbf{U} -$$

$$n_f(\mathbf{r}) \left[ \hat{n}_f(\mathbf{r}) \left( \frac{\delta \nu_f(\mathbf{r})}{\delta n_f(\mathbf{r}')} \right)_{E'_f} - \hat{E}'_f(\mathbf{r}) \left( \frac{\delta \beta_f(\mathbf{r})}{\delta n_f(\mathbf{r}')} \right)_{E'_f} \right] \mathbf{U},$$

$$\hat{\mathbf{I}}_{2b} = p_{fb}(\mathbf{r}) \left[ \hat{n}_b(\mathbf{r}) \left( \frac{\delta \nu_b(\mathbf{r})}{\delta E'_b(\mathbf{r}')} \right)_{n_b} - \hat{E}'_b(\mathbf{r}) \left( \frac{\delta \beta_b(\mathbf{r})}{\delta E'_b(\mathbf{r}')} \right)_{n_b} \right] \mathbf{U}, \quad \mathbf{Y}_{2\alpha} = -\nabla' \cdot \mathbf{u}_f,$$

$$\hat{\mathbf{I}}_{3f} = \hat{\mathbf{J}}'_{3f}(\mathbf{r}) \delta(\mathbf{r} - \mathbf{r}') + \hat{\mathbf{p}}'_f(\mathbf{r}) \frac{\beta_f(\mathbf{r})}{m_f n_f(\mathbf{r})} \left( \frac{\delta p_f(\mathbf{r})}{\delta \beta_f(\mathbf{r}')} \right)_{\nu_f},$$

$$\hat{\mathbf{I}}_{3b} = \hat{\mathbf{J}}'_{3b}(\mathbf{r}) \delta(\mathbf{r} - \mathbf{r}'), \quad \mathbf{Y}_{3\alpha} = -\nabla' \beta_\alpha,$$

$$\hat{\mathbf{I}}_{4f} = -\hat{\mathbf{j}}'_{2f}(\mathbf{r}) \beta_f \delta(\mathbf{r} - \mathbf{r}'), \quad \mathbf{Y}_{4f} = \mathbf{u}_f, \quad \mathbf{Y}_{4b} = 0,$$

$$\hat{\mathbf{I}}_{5f} = \left( \hat{j}'_{3f}(\mathbf{r}) + \frac{1}{2} \hat{\mathbf{j}}'_{2f}(\mathbf{r}) \cdot \mathbf{u}_f \right) \delta(\mathbf{r} - \mathbf{r}'), \quad Y_{5f} = \beta_f - \beta_b, \quad \mathbf{Y}_{5b} = 0.$$

In these expressions, the subscript at a bracket indicates the expression in the bracket is calculated for the fixed variables specified in the subscript,  $\nabla' = \partial/\partial \mathbf{r}'$ .

The fluxes  $\hat{\mathbf{I}}_{k\alpha}$  are generally nonlocal. The characteristic scales of its nonlocality are about the size of the internal structural elements of the medium and the time of their interaction. For simple fluids, this type of nonlocality can be neglected. Therefore we can replace the functional derivatives with the partial derivatives, which will be done below.

#### 4. Constitutive relations and transport coefficients

Using the nonequilibrium distribution function (9), we obtain fluid transport equations in flows bounded by surfaces. The constitutive relations for the stress tensor, heat flux vector, and interfacial forces entering these equations are generally nonlocal and retarded:

$$\mathbf{f}_{ia}(\mathbf{r}, t) = \mathbf{f}_{ia}(\mathbf{r}, t_0) + \mathbf{f}_{ia}^0(\mathbf{r}, t) + \sum_{k=1}^5 \sum_{\beta, \varphi}^2 \int_{t_0}^t dt_1 \int d\mathbf{r}' \mathbf{M}_{ia}^{k\beta}(\mathbf{r}, \mathbf{r}', t - t_1) \cdot \mathbf{Y}_{k\beta}(\mathbf{r}', t_1), \quad (10)$$

$$\begin{aligned} \hat{\mathbf{f}}_{1a} &= \hat{\mathbf{J}}'_{1a}, & \hat{\mathbf{f}}_{2a} &= \hat{\mathbf{J}}'_{2a}, & \hat{\mathbf{f}}_{3a} &= \hat{\mathbf{J}}'_{3a}, & \hat{\mathbf{f}}_{4a} &= \hat{\mathbf{j}}_{2a}, \\ \hat{f}_{5a} &= \hat{j}'_{3a}, & \hat{\mathbf{f}}_{6f} &= \hat{\mathbf{J}}_{fb}, & \hat{\mathbf{f}}_{7f} &= \hat{\mathbf{j}}_{fb}, & \hat{\mathbf{f}}_{6b} &= \hat{\mathbf{f}}_{7b} = 0. \end{aligned}$$

The relaxation transport kernels included in these formulas are given by the relations:

$$\mathbf{M}_{ia}^{k\beta}(\mathbf{r}, \mathbf{r}', t - t_1) = \left\langle \hat{\mathbf{f}}_{ia}(\mathbf{r}) S_{(t-t_1)}^{(N)} \Delta \mathbf{I}_{k\beta}(\mathbf{r}') \right\rangle_0. \quad (11)$$

Given that the quasi-equilibrium distribution function is even in momenta and relative coordinates of the molecules, it can be shown that the uneven transport kernels (11) in these quantities are equal to zero. Moreover, in the constitutive relations (10), the stress tensor and the tensor  $\mathbf{J}_{fb}$  can be split into a symmetric nondivergent part (denoted below by superscript  $s$ ) and a divergent part (denoted by superscript  $0$ ). In this case, the constitutive relations for the fluid under confined conditions have the following form:

$$\begin{aligned} \mathbf{J}_{2f}^{\prime s}(\mathbf{r}, t) &= \int_{t_0}^t dt_1 \int d\mathbf{r}' \left\langle \hat{\mathbf{J}}_{2f}^{\prime s}(\mathbf{r}) S_{(t-t_1)}^{(N)} \Delta \left( \hat{\mathbf{J}}_{2f}^{\prime s}(\mathbf{r}') + \hat{\mathbf{J}}_{fb}^{\prime s}(\mathbf{r}') \right) \right\rangle_0 : \beta_f(\mathbf{r}') \nabla' \mathbf{u}_f(\mathbf{r}'), \\ \mathbf{J}_i^0(\mathbf{r}, t) &= \int_{t_0}^t dt_1 \int d\mathbf{r}' \left\langle \hat{\mathbf{J}}_i^0(\mathbf{r}) S_{(t-t_1)}^{(N)} \Delta \left( \hat{\mathbf{I}}_f^0(\mathbf{r}') + \hat{\mathbf{I}}_{fb}^0(\mathbf{r}') \right) \right\rangle_0 : \nabla' \cdot \mathbf{u}_f(\mathbf{r}') \mathbf{U}, \\ i = 1, 2, \quad \hat{\mathbf{J}}_1^0 &= \hat{\mathbf{J}}_{2f}^{\prime 0}, \quad \hat{\mathbf{J}}_2^0 = \hat{\mathbf{J}}_{fb}^{\prime 0}, \quad \hat{\mathbf{J}}_i^0 = \left\langle \hat{\mathbf{J}}_i^0 \right\rangle, \\ \hat{\mathbf{I}}_f^0(\mathbf{r}) &= \hat{\mathbf{J}}_{2f}^{\prime}(\mathbf{r}) \beta_f - (E_f'(\mathbf{r}) + p_f(\mathbf{r})) \mathbf{U} \times \\ &\left( \hat{n}_f(\mathbf{r}) \left( \frac{\partial \nu_f}{\partial E_f'} \right)_{n_f} - \hat{E}_f'(\mathbf{r}) \left( \frac{\partial \beta_f}{\partial E_f'} \right)_{n_f} \right) - n_f(\mathbf{r}) \left( \hat{n}_f(\mathbf{r}) \left( \frac{\partial \nu_f}{\partial n_f} \right)_{E_f'} - \hat{E}_f'(\mathbf{r}) \left( \frac{\partial \beta_f}{\partial n_f} \right)_{E_f'} \right) \mathbf{U}, \\ \hat{\mathbf{I}}_{fb}^0(\mathbf{r}) &= \hat{\mathbf{J}}_{fb}(\mathbf{r}) \beta_f - p_{fb}(\mathbf{r}) \mathbf{U} \times \\ &\left( \hat{n}_f(\mathbf{r}) \left( \frac{\partial \nu_f}{\partial E_f'} \right)_{n_f} - \hat{E}_f'(\mathbf{r}) \left( \frac{\partial \beta_f}{\partial E_f'} \right)_{n_f} \right) + p_{fb}(\mathbf{r}) \left( \hat{n}_b(\mathbf{r}) \left( \frac{\partial \nu_b}{\partial E_b'} \right)_{n_b} - \hat{E}_b'(\mathbf{r}) \left( \frac{\partial \beta_b}{\partial E_b'} \right)_{n_b} \right) \mathbf{U}, \\ \mathbf{j}_{2f}(\mathbf{r}, t) &= \frac{1}{2} \int_{t_0}^t dt_1 \int d\mathbf{r}' \left\langle \hat{\mathbf{j}}_{2f}(\mathbf{r}) S_{(t-t_1)}^{(N)} \hat{\mathbf{j}}_{2f}(\mathbf{r}') \right\rangle_0 (\beta_f(\mathbf{r}') + \beta_p(\mathbf{r}')) \mathbf{u}_f(\mathbf{r}'), \\ \mathbf{J}_{3f}'(\mathbf{r}, t) &= - \int_{t_0}^t dt_1 \int d\mathbf{r}' \left\langle \hat{\mathbf{J}}_{3f}'(\mathbf{r}) S_{(t-t_1)}^{(N)} \Delta \left( \hat{\mathbf{J}}_{3f}'(\mathbf{r}') + \hat{\mathbf{p}}_f(\mathbf{r}') \frac{\beta_f(\mathbf{r}')}{m_f n_f(\mathbf{r}')} \left( \frac{\partial p_f}{\partial \beta_f} \right)_{\nu_f} \right) \right\rangle_0 \cdot \nabla' \beta_f(\mathbf{r}'), \end{aligned}$$

$$\begin{aligned}
 j'_{3f}(\mathbf{r}, t) &= \int_{t_0}^t dt_1 \int d\mathbf{r}' \left\langle \hat{j}'_{3f}(\mathbf{r}) S_{(t-t_1)}^{(N)} \Delta \hat{j}'_{3f}(\mathbf{r}') \right\rangle_0 (\beta_f(\mathbf{r}') - \beta_b(\mathbf{r}')), \\
 \mathbf{J}_{fb}^s(\mathbf{r}, t) &= \int_{t_0}^t dt_1 \int d\mathbf{r}' \left\langle \hat{\mathbf{J}}_{fb}^s(\mathbf{r}) S_{(t-t_1)}^{(N)} \Delta \left( \hat{\mathbf{J}}_{2f}^s(\mathbf{r}') + \hat{\mathbf{J}}_{fb}^s(\mathbf{r}') \right) \right\rangle_0 : \beta_f(\mathbf{r}') \nabla' \mathbf{u}_f(\mathbf{r}'), \\
 \mathbf{j}_{fb}(\mathbf{r}, t) &= \frac{1}{2} \int_{t_0}^t dt_1 \int d\mathbf{r}' \left\langle \hat{\mathbf{j}}_{fb}(\mathbf{r}) S_{(t-t_1)}^{(N)} \hat{\mathbf{j}}'_{2f}(\mathbf{r}') \right\rangle_0 \cdot (\beta_f(\mathbf{r}') + \beta_b(\mathbf{r}')) \mathbf{u}_f(\mathbf{r}'). \quad (12)
 \end{aligned}$$

Equations (12) are nonlinear, nonlocal, and retarded constitutive relations. Its nonlocality is associated with the correlation between dissipative fluxes and thermodynamic forces and is due to the finite speed of propagation of disturbances in the medium. For weakly nonequilibrium systems for which the gradients of the observed macroscopic variables are relatively low (in classical fluid mechanics, this corresponds to Newton's constitutive equations for the stress tensor and Fourier's equations for the heat flux vector), this nonlocality and retardation can also be neglected. In addition, as noted above, the operator  $\pi(t, t_1) = 1$  in this case. If we neglect the initial values of the fluxes and interfacial forces, the constitutive equations in this case can be written as:

$$\begin{aligned}
 \mathbf{J}'_{2f}(\mathbf{r}, t) &= p_f(\mathbf{r}, t) \mathbf{U} - (\boldsymbol{\mu}_{ff}^s + \boldsymbol{\mu}_{fb}^s) : \nabla \mathbf{u}_f^s - (\boldsymbol{\mu}_{ff}^0 + \boldsymbol{\mu}_{fb}^0) : \nabla \cdot \mathbf{u}_f \mathbf{U}, \quad \mathbf{j}_{2f}(\mathbf{r}, t) = -\boldsymbol{\nu} \cdot \mathbf{u}_f, \\
 \mathbf{J}'_{3f}(\mathbf{r}, t) &= \boldsymbol{\lambda}_f \cdot \nabla \beta_f + \boldsymbol{\lambda}_b \cdot \nabla \beta_b, \quad j'_{3f}(\mathbf{r}, t) = \omega (\beta_f - \beta_b), \\
 \mathbf{J}_{fb}(\mathbf{r}, t) &= p_{fb}(\mathbf{r}, t) \mathbf{U} - (\boldsymbol{\mu}_{bf}^s + \boldsymbol{\mu}_{bb}^s) : \nabla \mathbf{u}_f^s - (\boldsymbol{\mu}_{bf}^0 + \boldsymbol{\mu}_{bb}^0) : \nabla \cdot \mathbf{u}_f \mathbf{U}, \quad (13) \\
 \mathbf{j}_{fb}(\mathbf{r}, t) &= -\boldsymbol{\sigma} \cdot \mathbf{u}_f.
 \end{aligned}$$

Here, transport coefficients  $\boldsymbol{\mu}_{ff}^s$ ,  $\boldsymbol{\mu}_{fb}^0$ ,  $\boldsymbol{\mu}_{fb}^s$ , and  $\boldsymbol{\mu}_{fb}^s$  are fourth-rank tensors,  $\boldsymbol{\nu}$ ,  $\boldsymbol{\lambda}_f$ ,  $\boldsymbol{\lambda}_b$  and  $\boldsymbol{\sigma}$  are second-rank tensors, and  $\varpi$  is a scalar. These quantities are given by the following relations:

$$\begin{aligned}
 \boldsymbol{\mu}_{if}^s &= \beta_f \int_{t_0}^t dt_1 \int d\mathbf{r}' \left\langle \hat{\mathbf{J}}_i^s(\mathbf{r}) S_{(t-t_1)}^{(N)} \hat{\mathbf{J}}_{2f}^s(\mathbf{r}') \right\rangle_0, \quad i = f, b, \quad \hat{\mathbf{J}}_f = \hat{\mathbf{J}}'_{2f}, \quad \hat{\mathbf{J}}_b = \hat{\mathbf{J}}'_{fb}, \\
 \boldsymbol{\mu}_{ib}^s &= \beta_f \int_{t_0}^t dt_1 \int d\mathbf{r}' \left\langle \hat{\mathbf{J}}_i^s(\mathbf{r}) S_{(t-t_1)}^{(N)} \hat{\mathbf{J}}_{fb}^s(\mathbf{r}') \right\rangle_0, \\
 \boldsymbol{\mu}_{if}^0 &= \int_{t_0}^t dt_1 \int d\mathbf{r}' \left\langle \hat{\mathbf{J}}_i^0(\mathbf{r}) S_{(t-t_1)}^{(N)} \hat{\mathbf{I}}_f^0(\mathbf{r}') \right\rangle_0, \\
 \boldsymbol{\mu}_{ib}^0 &= \int_{t_0}^t dt_1 \int d\mathbf{r}' \left\langle \hat{\mathbf{J}}_i^0(\mathbf{r}) S_{(t-t_1)}^{(N)} \hat{\mathbf{I}}_{fb}^0(\mathbf{r}') \right\rangle_0, \\
 \boldsymbol{\lambda}_f &= \int_{t_0}^t dt_1 \int d\mathbf{r}' \left\langle \hat{\mathbf{J}}'_{3f}(\mathbf{r}) S_{(t-t_1)}^{(N)} \Delta \left( \hat{\mathbf{J}}'_{3f}(\mathbf{r}') + \hat{\mathbf{p}}'_f(\mathbf{r}') \frac{\beta_f(\mathbf{r}')}{m_f n_f(\mathbf{r}')} \left( \frac{\partial p_f}{\partial \beta_f} \right)_{\nu_f} \right) \right\rangle_0,
 \end{aligned}$$

$$\begin{aligned}
\lambda_b &= \int_{t_0}^t dt_1 \int d\mathbf{r}' \left\langle \hat{\mathbf{J}}'_{3f}(\mathbf{r}) S_{(t-t_1)}^{(N)} \Delta \hat{\mathbf{J}}'_{3b}(\mathbf{r}') \right\rangle_0, \\
\varpi &= \int_{t_0}^t dt_1 \int d\mathbf{r}' \left\langle \hat{j}'_{3f}(\mathbf{r}) S_{(t-t_1)}^{(N)} \hat{j}'_{3f}(\mathbf{r}') \right\rangle_0, \\
\sigma &= \frac{1}{2} (\beta_f + \beta_b) \int_{t_0}^t dt_1 \int d\mathbf{r}' \left\langle \hat{\mathbf{j}}_{fb}(\mathbf{r}) S_{(t-t_1)}^{(N)} \hat{\mathbf{j}}_{2f}(\mathbf{r}') \right\rangle_0, \\
\nu &= \frac{1}{2} (\beta_f + \beta_b) \int_{t_0}^t dt_1 \int d\mathbf{r}' \left\langle \hat{\mathbf{j}}_{2f}(\mathbf{r}) S_{(t-t_1)}^{(N)} \hat{\mathbf{j}}_{2f}(\mathbf{r}') \right\rangle_0. \tag{14}
\end{aligned}$$

Note that in the case of incompressible channel walls, their hydrodynamic velocity equals zero,  $\mathbf{u}_b = 0$ . The condition that the magnitudes of the interfacial forces  $\mathbf{j}_{2f} = \mathbf{j}_{2b}$  and the momentum equation for the wall:

$$-\nabla \cdot \mathbf{J}'_{2b} + \mathbf{j}_{2b} = 0$$

imply that  $\mathbf{j}'_{2b} = -\nabla \cdot \mathbf{J}'_{2b}$ . If we neglect the bulk viscosity, the evolution equation of the fluid velocity can be written in simple form:

$$\rho_f \frac{d\mathbf{u}_f}{dt} = -\nabla p_f - \nabla \cdot (\boldsymbol{\mu}_{ff}^s + \boldsymbol{\mu}_{fb}^s + \boldsymbol{\mu}_b^s) : \nabla \mathbf{u}_f^s.$$

Thus, the viscosity of the fluid in confined geometry depends not only on the interaction between the fluid molecules (responsible tensor coefficient  $\boldsymbol{\mu}_{ff}^s$ ). The effective viscosity contains the contributions due to the interaction with the surface, the coefficient  $\boldsymbol{\mu}_b^s$  is given by the relation:

$$\boldsymbol{\mu}_b^s(\mathbf{r}) = \beta_b \int_{t_0}^t d\mathbf{r}' \int dt_1 \left\langle \hat{\mathbf{J}}'^s_{2b}(\mathbf{r}) S_{(t-t_1)}^{(N)} \Delta \hat{\mathbf{J}}'^s_{fb}(\mathbf{r}') \right\rangle_0.$$

Further simplification of the constitutive relations is possible in systems having symmetrical properties. For an isotropic medium, the transport kernel (11) and the corresponding transport coefficients (14) are scalars multiplied by the isotropic tensors. Thus, for an isotropic medium, the local constitutive relations reduce to:

$$\begin{aligned}
\mathbf{J}'_{2f}(\mathbf{r}, t) &= p_f \mathbf{U} - (\mu_{ff}^s + \mu_{fb}^s + \mu_b^s) \nabla \mathbf{u}_f^s - (\mu_{ff}^0 + \mu_{fb}^0 + \mu_b^0) \nabla \cdot \mathbf{u}_f \mathbf{U}, \quad \mathbf{j}_{2f}(\mathbf{r}, t) = 0, \\
\mathbf{J}'_{3f}(\mathbf{r}, t) &= \lambda_f \nabla \beta_f + \lambda_b \nabla \beta_b, \quad j'_{3f}(\mathbf{r}, t) = \omega (\beta_f - \beta_b), \\
\mathbf{J}_{fb}(\mathbf{r}, t) &= -(\mu_{bf}^s + \mu_{bb}^s) \nabla \mathbf{u}_f^s - (\mu_{bf}^0 + \mu_{bb}^0) \nabla \cdot \mathbf{u}_f \mathbf{U}, \quad \mathbf{j}_{fb}(\mathbf{r}, t) = -\sigma \mathbf{u}_f. \tag{15}
\end{aligned}$$

The scalar transport coefficients are obtained by convolution of the tensor coefficients:

$$\mu_{if}^s = \frac{\beta_f}{5} \int_{t_0}^t dt_1 \int d\mathbf{r}' \left\langle \hat{\mathbf{J}}'^s_i(\mathbf{r}) : S_{(t-t_1)}^{(N)} \hat{\mathbf{J}}'^s_{2f}(\mathbf{r}') \right\rangle, \quad \mu_{ib}^s = \frac{\beta_f}{5} \int_{t_0}^t dt_1 \int d\mathbf{r}' \left\langle \hat{\mathbf{J}}'^s_i(\mathbf{r}) : S_{(t-t_1)}^{(N)} \hat{\mathbf{J}}'^s_{fb}(\mathbf{r}') \right\rangle,$$

$$\begin{aligned}
 \mu_b^s &= \frac{\beta_b}{5} \int_{t_0}^t dt_1 \int d\mathbf{r}' \left\langle \hat{\mathbf{J}}'_{2b}(\mathbf{r}) : S_{(t-t_1)}^{(N)} \hat{\mathbf{J}}'_{fb}(\mathbf{r}') \right\rangle, \\
 \mu_{if}^0 &= \frac{\beta_f}{9} \int_{t_0}^t dt_1 \int d\mathbf{r}' \left\langle \hat{\mathbf{J}}'_i(\mathbf{r}) : S_{(t-t_1)}^{(N)} \hat{\mathbf{J}}'_{2f}(\mathbf{r}') \right\rangle, \quad \mu_{ib}^0 = \frac{\beta_f}{9} \int_{t_0}^t dt_1 \int d\mathbf{r}' \left\langle \hat{\mathbf{J}}'_i(\mathbf{r}) : S_{(t-t_1)}^{(N)} \hat{\mathbf{J}}'_{fb}(\mathbf{r}') \right\rangle, \\
 \mu_b^0 &= \frac{\beta_b}{9} \int_{t_0}^t dt_1 \int d\mathbf{r}' \left\langle \hat{\mathbf{J}}'_{2b}(\mathbf{r}) : S_{(t-t_1)}^{(N)} \hat{\mathbf{J}}'_{fb}(\mathbf{r}') \right\rangle, \\
 \lambda_f &= \frac{1}{3} \int_{t_0}^t dt_1 \int d\mathbf{r}' \left\langle \hat{\mathbf{J}}'_{3f}(\mathbf{r}) \cdot S_{(t-t_1)}^{(N)} \Delta \left( \hat{\mathbf{J}}'_{3f}(\mathbf{r}') + \hat{\mathbf{p}}'_f(\mathbf{r}') \frac{\beta_f(\mathbf{r}')}{m_f n_f(\mathbf{r}')} \left( \frac{\partial p_f}{\partial \beta_f} \right)_{\nu_f} \right) \right\rangle_0, \\
 \lambda_b &= \frac{1}{3} \int_{t_0}^t dt_1 \int d\mathbf{r}' \left\langle \hat{\mathbf{J}}'_{3f}(\mathbf{r}) \cdot S_{(t-t_1)}^{(N)} \Delta \hat{\mathbf{J}}'_{3b}(\mathbf{r}') \right\rangle_0, \\
 \sigma &= \frac{1}{6} (\beta_f + \beta_b) \int_{t_0}^t dt_1 \int d\mathbf{r}' \left\langle \hat{\mathbf{j}}_{fb}(\mathbf{r}) \cdot S_{(t-t_1)}^{(N)} \hat{\mathbf{J}}'_{2f}(\mathbf{r}') \right\rangle_0. \tag{16}
 \end{aligned}$$

## 5. Conclusion

The technique developed in this paper to describe transport processes in confined geometries allows one to derive closed transport equations based on first principles. It is important that the characteristics in these equations, such as the stress tensor or heat flux vector, are expressed in terms of the parameters of the fluid-fluid and fluid-surface interaction forces. Therefore, specifying real material parameters, we can predict how the processes of momentum and energy transfer will occur in a particular microsystem. In this sense, the constructed equations are fairly universal.

The main conclusion is that transport processes in fluids under confined conditions differ significantly from fluid transport processes in bulk. Therefore, the viscosity and thermal conductivity coefficients of fluids in bulk and in nanochannels will be different. It is impossible to use the Green – Kubo formula to simulate the transport coefficients of fluids under confined conditions (using, for example, molecular dynamics method). In this case the shear viscosity coefficient is given by the formula:

$$\mu = \mu_{ff}^s + \mu_{fb}^s + \mu_b^s. \tag{17}$$

The first two terms are typical of a two-fluid medium. The last term does not have a classical analog. As a rule, we can neglect the space nonlocality of the relations (16), i.e. the transport relaxation kernels are  $\delta$ -functions of the coordinates  $\mathbf{r}$  and  $\mathbf{r}'$ . In this case, the viscosity coefficients are determined by the following formulas:

$$\mu_{ff}^s = \frac{\beta_f}{5} \int_{t_0}^t dt_1 \left\langle \hat{\mathbf{J}}'_{is}(\mathbf{r}) : S_{(t-t_1)}^{(N)} \hat{\mathbf{J}}'_{2f}(\mathbf{r}') \right\rangle, \quad \mu_{fb}^s = \frac{\beta_f}{5} \int_{t_0}^t dt_1 \left\langle \hat{\mathbf{J}}'_{is}(\mathbf{r}) : S_{(t-t_1)}^{(N)} \hat{\mathbf{J}}'_{fb}(\mathbf{r}') \right\rangle,$$

$$\mu_b^s = \frac{\beta_b}{5} \int_{t_0}^t dt_1 \left\langle \hat{\mathbf{J}}'_{2b}(\mathbf{r}) : S_{(t-t_1)}^{(N)} \hat{\mathbf{J}}'_{fb}(\mathbf{r}) \right\rangle. \quad (18)$$

The thermal conductivity process is determined by the gradients of the fluid and wall temperature (see Eq. (15)). If the channel walls have the same temperature as the fluid, the thermal conductivity coefficient of the fluid under confined conditions is described by the formula:

$$\lambda = \lambda_f + \lambda_b, \quad (19)$$

where, in local approximation, the coefficients have the following form:

$$\lambda_f = \frac{1}{3} \int_{t_0}^t dt_1 \left\langle \hat{\mathbf{J}}'_{3f}(\mathbf{r}) \cdot S_{(t-t_1)}^{(N)} \Delta \left( \hat{\mathbf{J}}'_{3f}(\mathbf{r}) + \hat{\mathbf{p}}'_f(\mathbf{r}) \frac{\beta_f(\mathbf{r})}{m_f n_f(\mathbf{r})} \left( \frac{\partial p_f}{\partial \beta_f} \right)_{\nu_f} \right) \right\rangle_0,$$

$$\lambda_b = \frac{1}{3} \int_{t_0}^t dt_1 \left\langle \hat{\mathbf{J}}'_{3f}(\mathbf{r}) \cdot S_{(t-t_1)}^{(N)} \Delta \hat{\mathbf{J}}'_{3b}(\mathbf{r}') \right\rangle_0. \quad (20)$$

Equations (17) – (20) are the generalization of the known Green – Kubo relations. The formula for transport coefficients of fluids under confined conditions is rather complex. We can hope to derive simple relations only for rarefied gases. In this case, the gas evolution is described by the Boltzmann's equation. There is a single method for calculating the transport coefficients of dense gases or liquids. This is the molecular dynamics (MD) method. In this case, formulas (18), (20) should be used. However, in some MD simulations of nanoflows, attempts are made to use conventional fluid-dynamic equation and Green – Kubo formulas for transport coefficients. Clearly, this approach is inappropriate for such small systems.

Note, finally, that the possible elasticity and compliance of the walls can be taken into account using the formalism developed. For this, however, a different quasi-equilibrium ensemble is required.

## Acknowledgement

This work was supported in part by the Russian Scientific Foundation (Grant No. 14-19-00312).

## References

- [1] Andryushchenko V., Rudyak V. Self-diffusion coefficient of molecular fluid in porous media. *Defect and Diffusion Forum*, 2011, **312–315**, P. 417–422.
- [2] Rudyak V.Ya., Belkin A.A., Egorov V.V., Ivanov D.A. About fluids structure in microchannels. *Int. J. of Multiphysics*, 2011, **5** (2), P. 145–155.
- [3] Judy J., Maynes D., Webb B.W. Characterization of frictional pressure drop for liquid flows through microchannels. *Int. J. Heat Mass Transfer*, 2002, **45**, P. 3477–3489.
- [4] Liu Y., Wang Q. Transport behavior of water confined in carbon nanotubes. *Phys. Rev. B*, 2005, **72**, P. 085420.
- [5] Hanasaki I., Nakatani A. Hydrogen bond dynamics and microscopic structure of confined water inside carbon nanotubes. *J. Chem. Phys.*, 2006, **124**, P. 174714.
- [6] Karniadakis G., Beskok A., Aluru N. *Microflows and nanoflows: Fundamentals and Simulation*. Springer, 2005, 824 p.
- [7] Rudyak V.Ya., Belkin A.A., Egorov V.V., Ivanov D.A. Modeling fluid flows in nanochannels by molecular dynamics method. *Nanosystems: Physics, Chemistry, Mathematics*, 2011, **2** (4), P. 100–112.

- [8] Kharlamov G.V., Rudyak V.Ya. The equilibrium fluctuations in small open systems. *Physica A*, 2004, **340**, P. 257–264.
- [9] Pfahler J., Harley J., Bau H., Zemel J.N. Gas and liquid flow in small channels. *Micromech. Sensors, Actuators, Syst.*, 1991, **32**, P. 49–58.
- [10] Kobryn A.E., Kovalenko A. Molecular theory of hydrodynamic boundary conditions in nanofluidics. *J. Chem. Phys.*, 2008, **129**, P. 134701.
- [11] Rudyak V.Ya. *Statistical aerohydropneumatics of homogeneous and heterogeneous media. V.2. Hydromechanics*. NSUACE, Novosibirsk, 2005.
- [12] Rudyak V.Ya., Belkin A.A. Statistical hydromechanics of multiphase systems. *J. Aerosol Sci.*, 1994, **25**, P. 387–388.
- [13] Rudyak V.Ya., Belkin A.A. Equations of multifluid hydrodynamics. *Mathematical Modeling*, 1996, **8**, P. 33–37.
- [14] Rudyak V.Ya., Belkin A.A. Equations of multifluid hydrodynamics for heterogeneous systems with rotational degrees of freedom. *Siberian J. of Industrial Mathematics*, 2002, **1** (9), P. 145–156.
- [15] Zubarev D.N. *Nonequilibrium statistical thermodynamics*. Consultants Bureau, New York, 1974.
- [16] Rudyak V.Ya. *Statistical theory of dissipative processes in gases and liquids*. Nauka, Novosibirsk, 1987.

# Neutron scattering from graphene oxide paper and thermally exfoliated reduced graphene oxide

E. F. Sheka<sup>1</sup>, I. Natkaniec<sup>2</sup>, V. Mel'nikov<sup>3</sup>, K. Druzicki<sup>2,4</sup>

<sup>1</sup>Peoples' Friendship University of Russia, Miklukho-Maklaya Str. 6, 117198 Moscow, Russia

<sup>2</sup>Faculty of Physics, Adam Mickiewicz University, Umultowska Str. 85, 61-614 Poznań, Poland

<sup>3</sup>Semenov Institute of Chemical Physics RAS, Kosyguina str. 4, 119991 Moscow, Russia

<sup>4</sup>Frank Laboratory of Neutron Physics, Joint Institute for Nuclear Research,  
Joliot-Curie Str. 6, 141980 Dubna, Russia

sheka@icp.ac.ru, inat@amu.edu.pl, melnikov@center.chph.ras.ru

**PACS** 61.05.fg; 61.46.+w; 63.22.±m; 81.05.Uw

**DOI** 10.17586/2220-8054-2015-6-3-378-393

Synthetic graphene oxide, in the form of graphene oxide paper (GOpp), and its reduction product – thermally exfoliated reduced graphene oxide (TErGO) – were studied by elastic and inelastic neutron scattering at low and room temperature conditions. The neutron diffraction patterns were analyzed to confirm stacking structures of both species consisting of 4 – 6 and  $\sim 8$  layers of microsize lateral dimension and the interlayer distances of 7.21 Å and 3.36 Å, respectively. The one-phonon hydrogen amplitude-weighted density of vibrational states  $G(\omega)$  represents the inelastic incoherent neutron scattering spectra of the products. The study has revealed the retained water in the freshly made GOpp, corresponding to the lowest humidity. The analysis of the TErGO  $G(\omega)$  spectrum has disclosed the chemical composition of its circumference attributing the latter to sets of CH units with a minor presence of atomic oxygen.

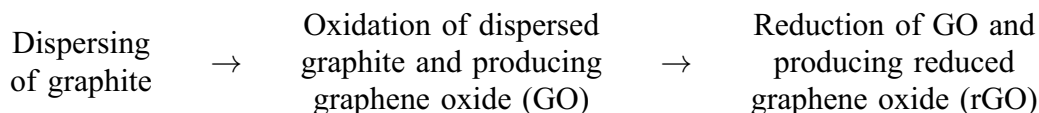
**Keywords:** Carbon nanostructures, graphene oxide, reduced graphene oxide, neutron diffraction, inelastic neutron scattering.

*Received: 18 March 2015*

## 1. Introduction

By the definition of K. Novoselov et al. graphene modern technology can be divided into two independent domains, namely: 'low performance' (LP) and 'high performance' (HP) [1]. The former includes a wide range of practical applications based on nanoscale graphene material. Typical products of this domain are touch screens, electronic paper, foldable organic light emitting diodes and others. Products of the second domain, based on a micro-size and larger single or multi-graphene sheets, concern electronic device such as a high-frequency, logic and thin-film field transistors. This separation of the graphene technology into two types, held *de facto*, is not just a tribute to simplify operating with complex technologies, but, in fact, is a consequence of the nature of the graphene molecule-crystal dualism and technical implementation of its unique chemical and physical properties [2], respectively. Both the successful implementation of any technology and the difficulties arising on this way depend primarily on the material in use. Serious problems associated with the development of processing methods aimed at the mass production of micro- and macro-dimension crystalline graphene sheet are objective reasons for postponing the implementation of the graphene HP technology up to 2030 [1, 3]. The latter is further exacerbated by the very high cost of this material [4]. Implementation of the LP technology has proved more successful. Active efforts of numerous teams of chemists

have resulted in solving the problem of mass production of the necessary technological material - technical (molecular) graphene. This material is the final product of a complicated chemical-technological cycle, a concise description of which is shown in Scheme 1. In numerous cases, structural analysis shows pronounced non-planarity for GO sheets and nearly complete recovery of the planarity for the basal plane of the carbon skeleton in reduced graphene oxide (rGO) sheets, in connection with which thus produced rGO is referred to as graphene.



SCHEME 1

Unlike hitherto used technological materials of strictly standardized chemical composition and structure, such a standardization of both GO and rGO products is not possible. The point is that the two terms refer to very wide ranges of substances, which actually represent various oxyhydride polyderivatives of graphene molecules of different chemical composition, size, and shape due to which the products can be characterized only by a restricted number of common features. Thus, in the GO case, there are two such characteristics that concern 1) interlayer distance between the GO sheets of  $\geq 7 \text{ \AA}$  and 2) an average chemical composition described by the C:O  $\sim 2:1$  ratio. The former exhibits the fact that both basal plane and the circumference area of the parent graphene molecules are involved in the oxidation while the latter points to the prepotency of epoxy units among the GO oxygen-containing groups (OCGs). A common feature of rGO is related to the interlayer distance of  $\sim 3.5 \text{ \AA}$  that points to the recovered planarity of the rGO carbon skeleton, on one hand, and to the location of residual OCGs in the circumference area [2, 5], on the other. Individual differences within the two communities are caused by the difference in size and shape of carbon skeletons of the parent graphene molecules and, consequently, by different numbers of attached OCGs, as well as by evidently individual combinations of these groups in each case. These circumstances result in that the structure and chemical composition of both GO and rGO may change on each stage of their chemical synthesis. The high-degree polyvariance of the chemical composition and structure of synthesized GO and rGO are widely discussed in the literature [6, 7]. Thus, such an important parameter of rGOs produced in the different laboratories of the world as the residual oxygen concentration can vary up to 20 times.

The lack of uniform properties deprives the obtained synthetic products the requested technological stability and stimulates studies aimed at both disclosing the sources of non-uniformity and finding the way to produce reliably standard products. Even now, the question of GO and rGO chemical composition is a major stumbling block toward technical progress. Empirical solution of the problem rests mainly in determination of C:O:H mass contents of the products. While the determination requires the application of a set of complementary techniques, e.g. XRF, TGA, Raman and FTIR spectroscopy, XRD, XPS, REELS, and so forth, it is mainly focused on the evaluation of carbon and oxygen contents, neglecting hydrogen and other small dopants. However, as was shown recently [8], elucidation of hydrogen's role permits one to come close to addressing the key question of chemical composition for both GO and rGO products. The quoted results were obtained by studying the scattering of thermal neutrons that is extremely sensitive to protium. Once stimulated by the results obtained, the authors (I. N. and E. Sh.) have suggested to extend the neutron scattering study to a set of synthetic GO and rGO products of different origins. The performed study not only revealed the retained water and hydrogen-enriched cores of the products as new facets of the product structure and chemical

composition, but also to show the way to link differences in the product behavior with the chemical protocols of their production as well as to shed light on the reasons of their instability over time. Recently, such a study has been performed for chemically produced GO/rGO pair (Ak-GO and Ak-rGO below) [9] provided by the Akkolab company [10]. The current paper presents the neutron scattering studies of chemically produced GO as GO paper and thermally exfoliated rGO (ppGO and TerGO below).

## 2. Methods in use

### 2.1. Sample preparation

**Graphite oxide (GrO) and GO paper.** The samples of oxidized graphite were prepared according to the Hummers technique [11]. In the standard procedure, 20 g of particulate pencil graphite (ash < 1 %) were charged into a solution of 10 g of  $\text{NaNO}_3$  in 460 ml of 94 %  $\text{H}_2\text{SO}_4$  and stirred for one hour at room temperature. Then the reactor was cooled to 0 °C and 60 g of  $\text{KMnO}_4$  were added to the suspension in small portions under stirring. After introduction of the permanganate, the reactor temperature was raised to  $35 \pm 3$  °C and has been maintained for one hour. Upon reaction completion, 920 ml of water were slowly added to the mixture and the temperature was raised to  $\sim 100$  °C. The temperature was maintained for 15 min, after which the mixture was diluted with 1400 ml of water and treated with hydrogen peroxide (3 %, 200 ml) to convert manganese dioxide to soluble and colorless manganese sulfate. GrO was allowed to settle and residual slightly yellow acidic solution was removed. The obtained GrO was repeatedly redispersed and centrifuged in HCl (1 %) solution at first until sulfate ions were removed and then in distilled water until the GO paste obtained displayed neutral pH. The paste was placed on a polytetrafluoroethylene plate and dried at room temperature to give free standing GO paper (ppGO below) (average thickness of 20 – 30 microns). Sheets of ppGO were cut into pieces of  $10 - 15 \times 40 - 50 \text{ mm}^2$ , dried at 60 °C overnight and stored in a sealed container. The general appearance of the ppGO is presented in Fig. 1a. Scanning electron microscopy was performed on a JSM7001F microscope. An accelerating voltage of 3 – 15 kV was used for observations. Images were obtained in the secondary electron mode.

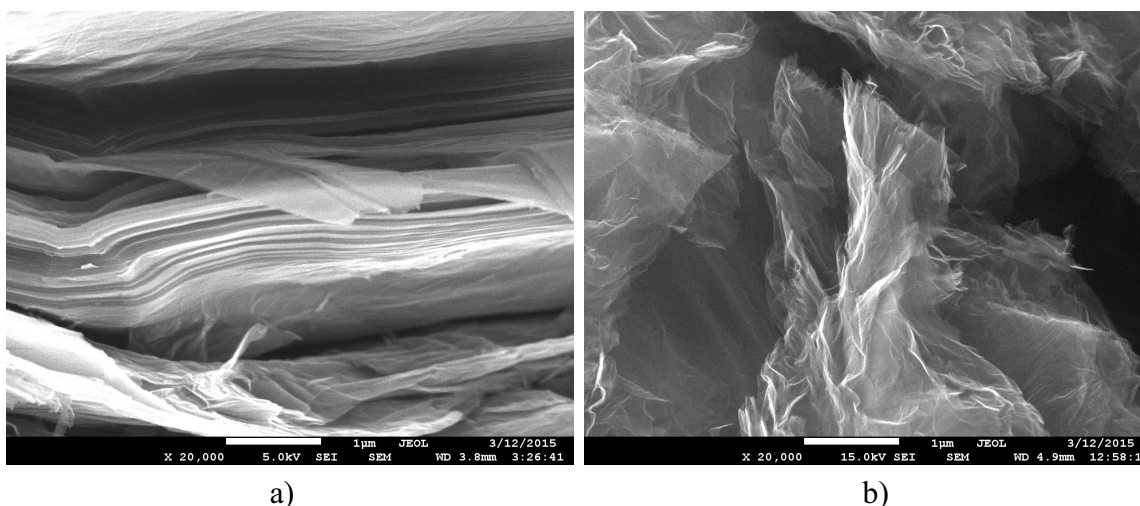


FIG. 1. SEM images of ppGO (a) and TerGO (b). White bars mark the image scaling of  $1\mu$  in both panels

TABLE 1. Mass content of ppGO and TErGO according to gaseous volumetry (gv) and elemental analysis (ea), wt %

Sample	C	H	O <sup>1</sup>
ppGO (gv)	56.2	0.7	40.5
TErGO (ea)	85.4	0.5	14.1 <sup>2</sup>
TErGO (gv)	87.1	0.5	12.1 <sup>2</sup>

<sup>1</sup> Oxygen content was obtained as the difference between total sample weight and the sum of weights related to other elements.

<sup>2</sup> Presumably, the contact of highly active TErGO with air is mainly responsible for the oxygen content as well as for water.

**Thermally exfoliated rGO.** Thermal shock is widely used to produce thermally expanded graphite, as well as exfoliation and/or reduction of GO [12]. This type of thermal treatment initiates the exothermic decomposition of oxygen containing groups (OCGs) that is accompanied by expansion due to gas evolution. In the current study, thermally reduced graphene oxide (TErGO) was obtained by introducing ppGO into a preheated 750 °C tubular furnace. As a result of the exothermic reduction reaction, which was accompanied by gas evolution and a rapid splitting of the layered ppGO structure, the TErGO sample obtained had a specific surface area of 500 – 600 m<sup>2</sup>/g. The freshly-prepared fluffy and voluminous TErGO was dispersed in water, compacted by vacuum filtration to reduce volume and dried at 100 °C. The general appearance of the TErGO is presented in Fig. 1b.

**Characterization methods.** The element content (C, H, and O) of both ppGO and TErGO was determined in due course of elemental analysis and gaseous volumetry. The former was performed with PE 2400 CHN Analyzer (Perkin Elmer, USA), which employs a combustion to convert the sample elements to CO<sub>2</sub>, H<sub>2</sub>O and N<sub>2</sub> gases. The gaseous volumetry monitors the yields of gaseous products (CO<sub>2</sub>, CO, H<sub>2</sub>O, and other) under stepwise annealing of the samples at different temperature. Typical temperature dependences of the measured yields for ppGO and TErGO samples are presented in Fig. 2. The accuracy of each element determination was about 0.30 wt % in both cases. Table 1 summarizes data on mass content of the studied samples.

Both ppGO and TErGO were analyzed by X-ray powder diffraction (XRD). Data collection was done with DRON-3M diffractometer (CuK $\alpha$  radiation). Diffraction patterns were collected between 8 ° and 50 ° of 2 $\theta$ . The XRD patterns of ppGO consisted of characteristic intense peaks positioned at 7.6 – 7.2 Å sometimes followed with peaks of unreacted graphite at 3.36 – 3.38 Å. The variation of the main peak positions is due to different content of retained water [13] the quantity of which is highly sensitive to details of the sample treatment. The XRD patterns of TErGO consisted of single peaks at 3.36 Å.

## 2.2. Neutron Scattering Experiments

The neutron scattering study was performed at the high flux pulsed IBR-2 reactor of the Frank Laboratory of Neutron Physics at the Joint Institute for Nuclear Research by using the inverted-geometry spectrometer NERA [14]. The investigated samples were illuminated by a white neutron beam analyzed by time-of-flight method on the 110 m flight path from the IBR-2 moderator to the sample. The NERA spectrometer allows for simultaneous recording of both neutron powder diffraction (NPD) and inelastic neutron scattering (INS) spectra. The NPD spectra were obtained for two scattering angles of diffraction detectors, the lowest and the highest of which allows one to measure the inter-planar distances up to 9 Å and 4 Å,

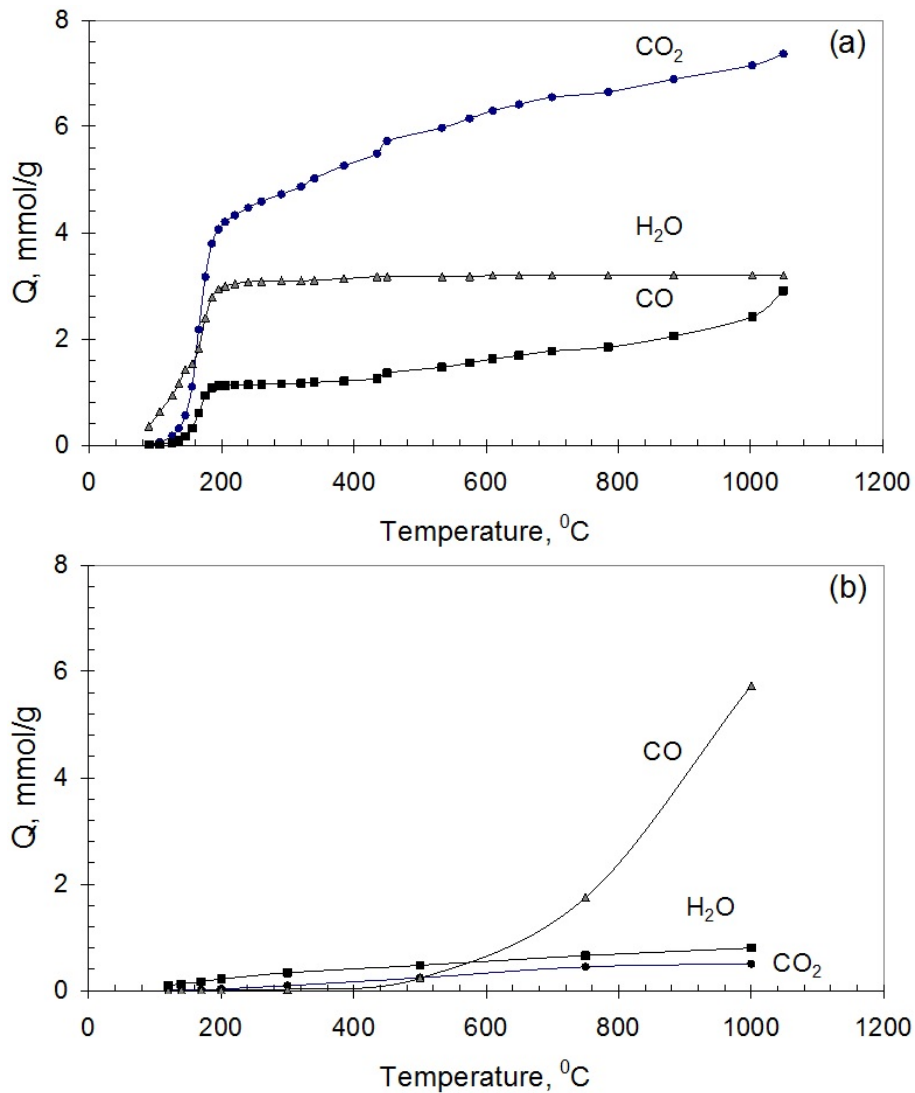


FIG. 2. Temperature dependence of the yields of the evolved gases  $Q$  at stepwise annealing of ppGO (a) and TErGO (b)

respectively. The INS spectra were collected at the final energy of the scattered neutrons, fixed by beryllium filters and crystal analyzers at  $E_f = 4.65$  meV, over fifteen scattering angles from  $20^{\circ}$  to  $160^{\circ}$  by step of  $10^{\circ}$ . The experiments were performed at temperatures 6 K and 295 K.

### 3. Experimental Results

#### 3.1. Neutron Diffraction

Figure 3 presents a set of the NPD plots, recorded at 6 K for ppGO and TErGO samples, alongside with the ones related to spectral graphite, which serves as the reference, collected at two different angles. As seen in Fig. 3a, the diffraction at  $2\Theta = 44.7^{\circ}$  provides a good vision of the structural features over  $3 \text{ \AA}$ , while the diffraction at  $2\Theta = 117.4^{\circ}$  (see Fig. 3b) allows tracking the sample structure in the region from  $1 \text{ \AA}$  to  $2.5 \text{ \AA}$ . The main feature of the ppGO found in Fig. 3a is described by a broad peak at  $7.21 \text{ \AA}$  that is equivalent to the Gr(001) reflex forbidden in graphite structure and gives an evidence for a stacked ppGO structure with the relevant interlayer distance. The peak is noticeably broadened (FWHM constitutes  $0.5 \text{ \AA}$ )

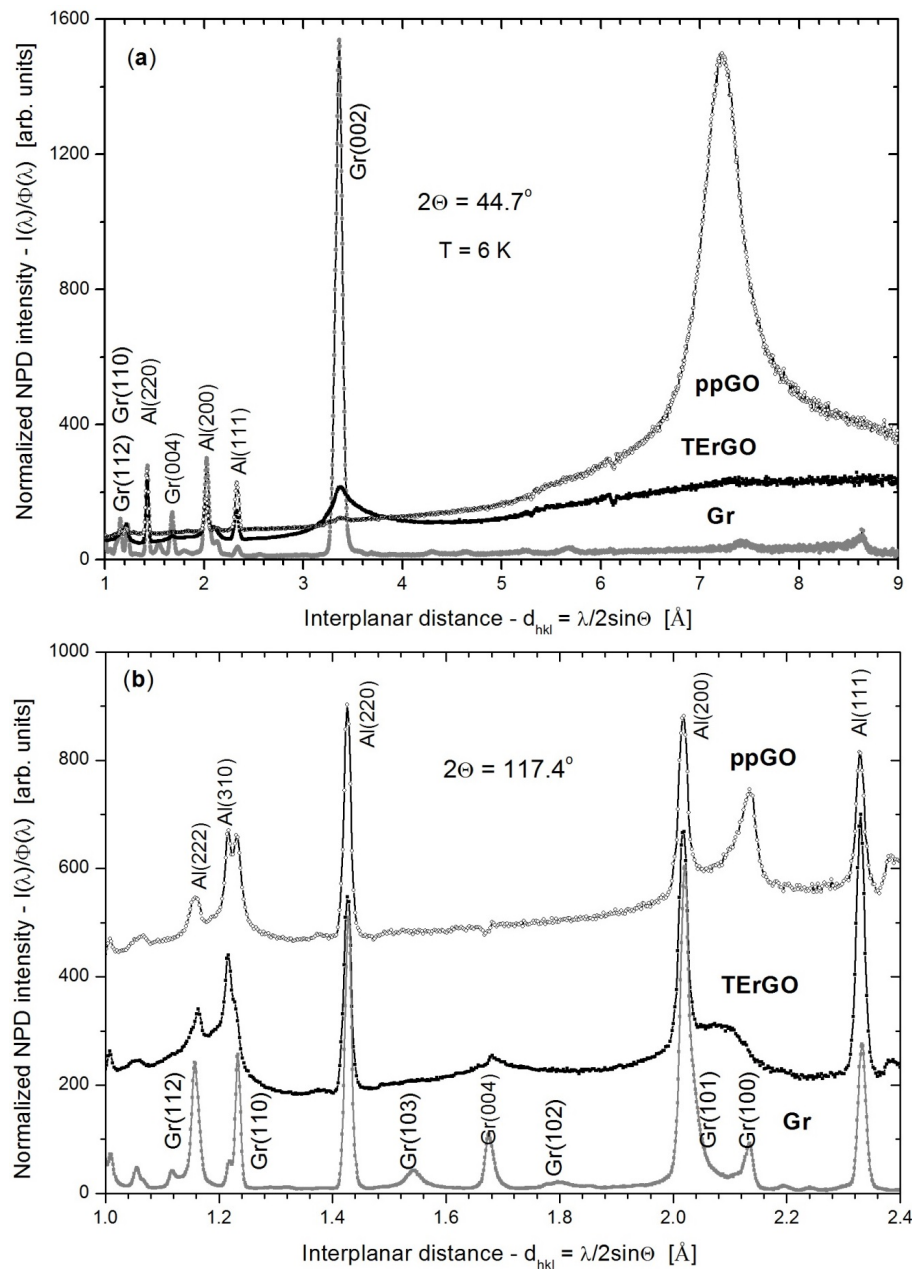


FIG. 3. NPD of spectral graphite (Gr), graphene oxide paper (ppGO) and thermally exfoliated reduced graphene oxide (TErGO) recorded at  $T = 6$  K at scattering angles  $2\Theta = 44.7^\circ$  (a) and  $2\Theta = 117.4^\circ$  (b). The data are normalized per neutron flux intensity  $\Phi(\lambda)$  at each neutron wavelength  $\lambda$ ; Gr(hkl) and Al(hkl) denote characteristic diffraction reflexes of spectral graphite and aluminum of cryostat and sample holder at different Miller indexes, respectively

with respect to the reference Gr(002) peak of graphite (FWHM of  $0.034 \text{ \AA}$ ), which exhibits a considerable size limiting of the stacks normal to the ppGO layers.

According to widely used Scherrer's equation, the FWHM of a diffraction peak  $B$  and the corresponding coherent scattering region (CSR) length  $L_{CSR}$  are inversely connected:  $B = k\lambda/L_{CSR} \sin \Theta$ , where  $k$  is a fitting factor,  $\lambda$  and  $\Theta$  are the neutron wavelength and scattering angle, respectively. When the diffraction study for a set of samples is performed

under the same conditions, it is possible to take one of the samples as the reference and to determine  $L_{CSR}$  of the remaining samples. In our study,  $L_{CSR}^{ref}$  is attributed to the crystalline graphite and constitutes  $\sim 20$  nm along the  $c$  direction [15]. Therefore,  $L_{CSR}$  of the studied GO can be determined as:

$$L_{CSR}^c = \left( B_{002}^{ref} / B \right) (\lambda / \lambda^{ref}) L_{CSR}^{ref}. \quad (1)$$

Substituting  $\lambda / \lambda^{ref}$  by the ratio of the relative peak positions and using  $B$  values given above, we obtain  $L_{CSR}^c = 2.9$  nm. Assuming that the thickness of a GO layer is  $\sim 0.6$  nm [16], the ppGO stacks may consist of 4 – 6 layers.

The lateral dimension of the stacks is described by peaks found below 2.5 Å. The Gr(110) peak is particularly characteristic for graphite-like structures [17]. As seen in Fig. 3b, there are no ppGO peaks broader than the reference graphite ones in the region. This means that the corresponding  $L_{CSR}^a$  values for graphite and ppGO are quite equivalent, which means the lateral dimensions of the GO stacks should evidently be larger than 20 nm.

Similar analysis of the Gr(002) peak of TErGO in Fig. 3a (positioned at 3.36 Å with FWHM of 0.26 Å) results in a  $L_{CSR}^c$  value of 2.6 nm, thus indicating  $\sim 8$  layer stacks for the studied TErGO sample. Similar to the ppGO, none of the diffraction peaks is broadened (see Fig. 3b) in the region below 2.5 Å, which points to large TErGO stacks in the lateral dimension. The obtained data for both ppGO and TErGO samples are in good agreement with results from XRD studies, indicating submicron-micron lateral size for both ppGO and TErGO. The described structures are typical for GO and rGO of different origins, which has been supported by both our study of Ak-GO/Ak-rGO pair [9] and by the recent neutron diffraction study of Pumera and co-workers [18]. Raising the temperature to 295 K influences the described diffraction patterns only slightly.

### 3.2. Inelastic Neutron Scattering

Figure 4 presents the time-of-flight (TOF) INS spectra of the studied samples, recorded at  $T = 6$  K and 295 K. The spectra are summed over 15 scattering angles, normalized per 10 hours of exposure time and for the 10 g mass. Previous studies [9] found that the INS intensity of the same mass of graphite is so weak that it cannot be distinguished at the level of the instrumental background. In the current study, the latter was extracted from the sample spectra, thereby excluding the contribution of the scattering from carbon atoms as well. Since the chemical content of the samples includes only oxygen and hydrogen atoms beside carbons, the scattering should be attributed to the hydrogens since the neutron scattering ability of oxygen is similar to that of carbon. As seen in the figure, the ppGO sample scatters quite intensely, thus indicating it is hydrogen-enriched, while scattering from TErGO sample is much weaker. As follows from Fig. 2a, freshly prepared ppGO contains a significant amount of retained water that is obviously responsible for the sample INS. In contrast, the quantity of the retained water in the freshly made TErGO is much smaller (see Fig. 2b). A considerable evolution of water from the sample at  $T > 600$  °C is evidently provided from the interaction of destructed TErGO with air. Since hydrogen atoms in retained water play the main role in the hydrophilic ppGO, its INS spectrum is, as expected, similar to that of oxygenated graphite (GrO) [13] and the previously studied Ak-GO [9]. The TErGO spectrum was quite different than that of retained water, thus the hydrogen atoms present are thought to be incorporated into the carbonaceous skeleton of the hydrophobic TErGO, similar to the chemically produced Ak-rGO [9] and natural rGO of shungite carbon (sh-rGO below) [8]. Altogether, the observed INS spectra of both samples are provided with incoherent inelastic neutron scattering (IINS) from hydrogen (protium) atoms. The temperature

dependence is typical for molecular solids [19,20] and is provided by considerable enhancement of multi-phonon scattering and a considerable smoothing of the total spectrum as a whole.

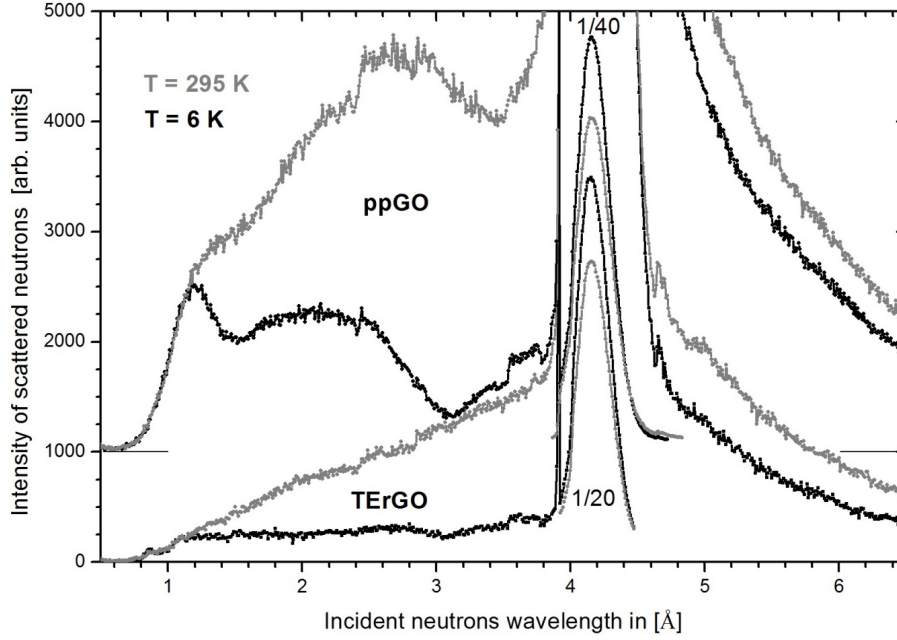


FIG. 4. Time-of-flight INS spectra of freshly made ppGO and TErGO samples, recorded at  $T = 6$  K (black) and 295 K (light gray) normalized by monitor counter to the same number of incident thermal neutrons flux for the wavelength region (0.8 – 6.8) Å, and exempted of background. The intensity of elastic peaks of the ppGO and TErGO spectra is 40- and 20-fold reduced, respectively

Within the confines of commonly used incoherent inelastic one-phonon scattering approximation, the IINS spectra intensity is determined by the scattering cross-section (see for example Ref. [19]) as:

$$\sigma_1^{inc}(E_i, E_f, \varphi, T) \approx \sqrt{\frac{E_f}{E_i}} \frac{\hbar |Q(E_i, E_f, \varphi)|^2}{\omega} \sum_n \frac{(b_n^{inc})^2}{M_n} \frac{\exp(-2W_n)}{1 - \exp\left(-\frac{\hbar\omega}{k_B T}\right)} G_n(\omega) \quad (2)$$

Here,  $Q(E_i, E_f, \varphi)$  is the neutron momentum transfer;  $\omega = (E_i - E_f)$  is the neutron energy transfer;  $b_n^{inc}$  and  $M_n$  are the incoherent scattering length and mass of the  $n$ -th atom;  $\exp(-2W_n)$  is the Debye-Waller factor;  $G_n(\omega)$  presents the  $n$ -th atom contribution into the amplitude-weighted density of vibrational states (AWDVS) expressed as:

$$G(\omega) = \sum_n G_n(\omega) = \sum_n \sum_j [A_j^n(\omega)]^2 \delta(\omega - \omega_j). \quad (3)$$

Here,  $A_j^n(\omega)$  is the  $n$ -th atom contribution into the eigenvector of the  $j$ -th phonon mode thus presenting the amplitude of the  $n$ -th atom displacement at the vibrational frequency  $\omega_j$ .

Figure 5 presents the one-phonon AWDVS  $G(\omega)$  spectra obtained in the course of a standard treatment procedure [20] and related to the TOF spectra shown in Fig. 4. All the spectra are normalized per 10 g of mass. When obtaining  $G(\omega)$  spectra, Debye-Waller factors were taken as unity, which meets the requirements at low temperature and rather narrow frequency region. The latter is met in the case of spectra at 6 K while spectra at room temperature

are burdened by the temperature dependence of the Debay-Waller factors as well as by highly considerable contribution of multi-phonon scattering [19]. Only low-temperature  $G(\omega)$  spectra will be considered later, since they present a suitable platform for testing  $G(\omega)$  delivered by computational modeling of the structure and dynamics of the studied ppGO and TErGO. Due to different origins of the hydrogen scattering, let us consider the  $G(\omega)$  spectra of the two samples separately.

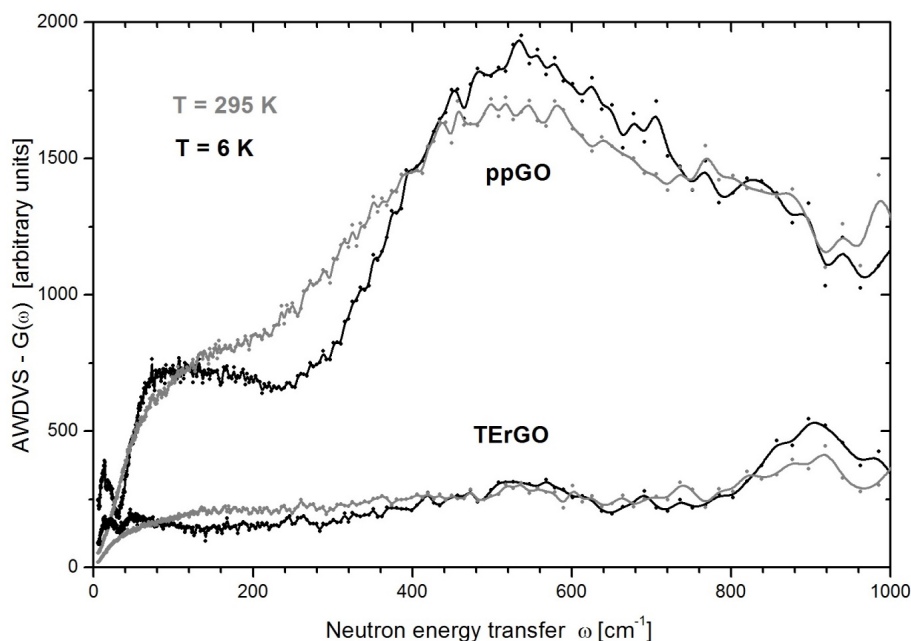


FIG. 5. Experimental amplitude-weighted density of vibrational states  $G(\omega)$  spectra of ppGO and TErGO at 6 K (black) and 295 K (light gray) extracted from the TOF spectra in Fig. 4 under one-phonon approximation

## 4. Discussion of Results

### 4.1. IINS Spectrum of the GO paper

The  $G(\omega)$  spectrum of ppGO at 6 K, along with its temperature dependence, is similar to that observed for GrO at the lowest humidity conditions [13]. In our case, a characteristic interlayer distance of 7.21 Å supports the conclusion. As was shown earlier, when the humidity becomes higher, the interlayer distance increases, but in a peculiar way. The four-fold lifting of the humidity from 20 % to 80 % stimulates a continuous growth of the interlayer spacing from 7.0 to 8.5 Å, while reaching 100 % humidity causes an abrupt growth of the spacing to 11 Å. This anomaly is thought to arise because water is retained in GrO in the interlayer space, once bound with the GrO layers in the form of incomplete monolayer coverage at lower humidities while completing the monolayer covering at interlayer distance 8.0 – 10 Å and forming additional water layer, which requires a sharp rise in the distance up to 11 Å [13]. This conclusion has been repeatedly confirmed subsequently (see Refs. [21, 22] and references therein), which gave a strong support in favor of the model suggested for calculations and received a strong support [9]. Let us consider the obtained results in the framework of the same model.

The left column of Fig. 6 presents  $G(\omega)$  spectra of two GO samples, where the spectrum of the ppGO sample studied in the current paper is given in panel (a) while the second in

panel (b) is related to the Ak-GO sample produced in [10] and previously studied in [9]. The model, which led the foundation for the description of the latter spectrum, is shown in Fig. 7. That involves two GO sheets separated by 7 Å in average and 48 water molecules located on both sides of the sheets. The relevant (5, 5) GO molecule (Fig. 7a) is based on the parent (5, 5) graphene molecule (a rectangular fragment with five benzenoid units along armchair and zigzag edges). As has been shown, a molecule of this size is large enough to reliably reveal the main idiosyncrasies of graphene's chemistry [5,23]. It is currently widely accepted that the atomic oxygens and hydroxyls (mainly) and carboxyls (in minority) take part in the graphene oxygenation, resulting in the formation of epoxy and hydroxy groups on the molecule basal planes, while carbonyls, hydroxyls, and carboxyls are spread over the circumferences (see a detailed analysis in [5]). The distribution of these OCGs over the carbon core is not standard and may vary widely, depending on the chemical protocol in use as well as on external conditions of the oxygenation. The (5, 5) GO molecule presented in Fig. 7a involves epoxy ( $\times 11$ ) and hydroxy ( $\times 8$ ) groups that are randomly spread over both sides of the basal plane (containing 44 carbon atoms), which corresponds to the average per-benzenoid-ring formula  $C_6O_{2.5}H_{1.2}$ . The relevant formula, which follows from the atomic-mass-content of ppGO in Table 1, is  $C_6O_3H_{0.85}$ , which is quite consistent with the model. Since the IINS cross-section of both carbon and oxygen atoms are about one order of magnitude less than that of protium, the contribution of the basal-plane atoms in the experimental spectrum is mainly provided due to the scattering from hydrogen atoms from hydroxyls.

In addition to the basal plane, the chemical composition of the GO periphery is of great importance. Usually, this area is presented by carbonyls, hydroxyls, and carboxyls, among which only two latter ones contribute to IINS. To make the periphery contribution more vivid, it was decided [9] to intentionally terminate the edge atoms with hydrogens. This termination gives one the potential to trace the changes of the IINS spectra of GOs after transformation into the rGOs, since the appearance of hydrogen atoms in the GO periphery always accompanies reduction (see detailed discussion in [8]).

Figure 7b shows the double-layer 'solvated sandwich' of two (5, 5) GO sheets surrounded by 48 water molecules. A detailed analysis has shown [9] that none of the water molecules is dissociated and each of them forms the hydrogen bonds (HBs) with the relevant GO layers (either  $H \cdots O$  with epoxy groups or  $O \cdots H$  with hydroxyls) that are supplemented with one-two HBs with neighboring water molecules. Evidently, the water molecules forming monolayers around (5, 5) GO substrates are differently coordinated in terms of the number of H-bonds,  $N_{HB}$ . As occurred in the current model,  $N_{HB}$  changes from 4 to 1, thus pointing to four-, three-, two-, and one-HB configured molecules and constitutes 7, 10, 25, and 6 (7:10:25:6 HB-composition below), respectively. It should be noted that none of the four- and three-HB molecules surrounded by other water molecules, which is a characteristic feature of bulk water, is observed. Apparently, the dynamics of differently configured water molecules is not the same.

The right column panels in Fig. 6 presents the  $N_{HB}$ -partitioned spectra of water for  $N_{HB} = 1, 2, 3,$  and 4 as normalized per 100 % molecular fraction of each. As seen in the figure, differently  $N_{HB}$ -configured molecules provide quite differently shaped spectra. Hence, when turning from  $N_{HB} = 1$  to  $N_{HB} = 4$ , the spectra undergo a continuous shifting toward higher wavenumbers. By comparing these spectra with the experimental  $G(\omega)$  spectra of ppGO and Ak-GO presented in the left column of Fig. 6, one can readily see that differently  $N_{HB}$ -configured molecules contribute to different parts of the experimental spectrum. The water IINS spectrum has a characteristic two-humped look and consists of two bands located at  $\sim 80 \text{ cm}^{-1}$  (A) and  $500 \text{ cm}^{-1}$  (B) that are bridged with a smooth linking L. The spectrum attribution to particular vibrational modes is widely discussed and will not be considered here (see [9] and

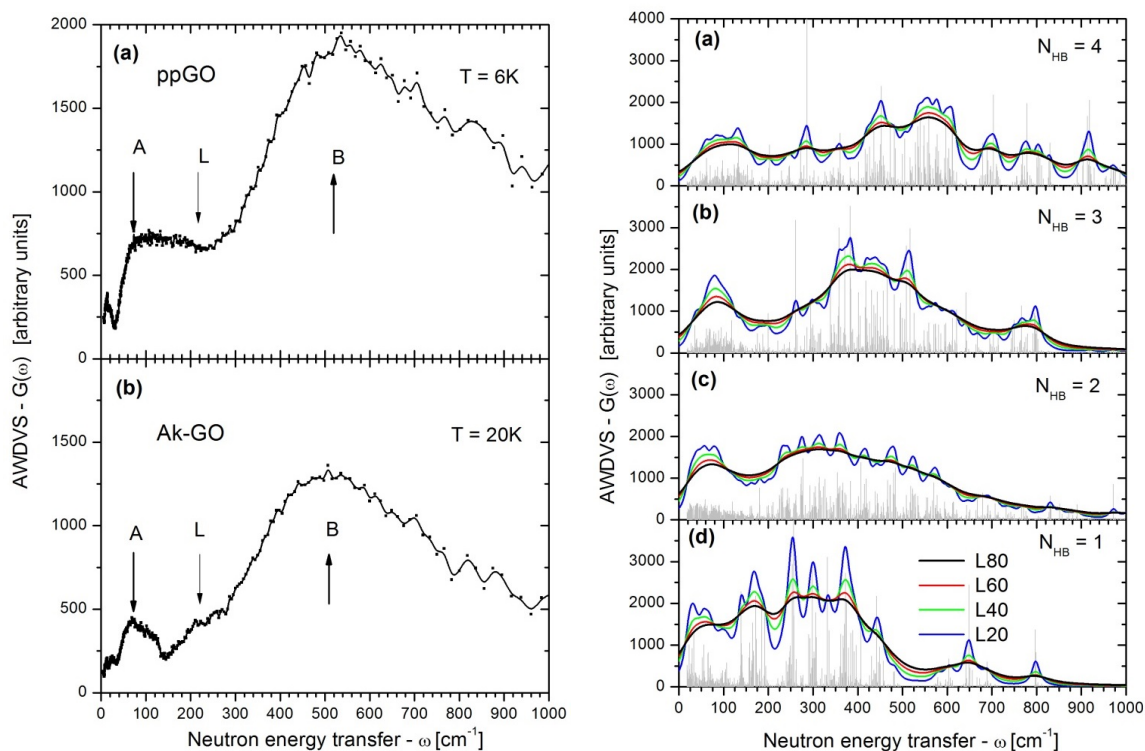


FIG. 6. AWDVS  $G(\omega)$  spectra. Left: (a) Experimental  $G(\omega)$  spectrum of ppGO at 6 K; (b). The same as in panel (a) but related to Ak-GO at 20 K [9]. Right:  $N_{HB}$ -partitioned spectra of water molecules related to  $N_{HB} = 4$  (a);  $N_{HB} = 3$  (b);  $N_{HB} = 2$  (c); and  $N_{HB} = 1$  (d) [9]. Bar spectra intensities are normalized per the same number of water molecules each. The 0-1 IINS vibrational mode intensities (light gray bars) were convoluted by using Lorentzians of 20, 40, 60, and 80  $\text{cm}^{-1}$  half width (black lines L20, L40, L60, and L80, respectively). The labeling is attributed to all panels

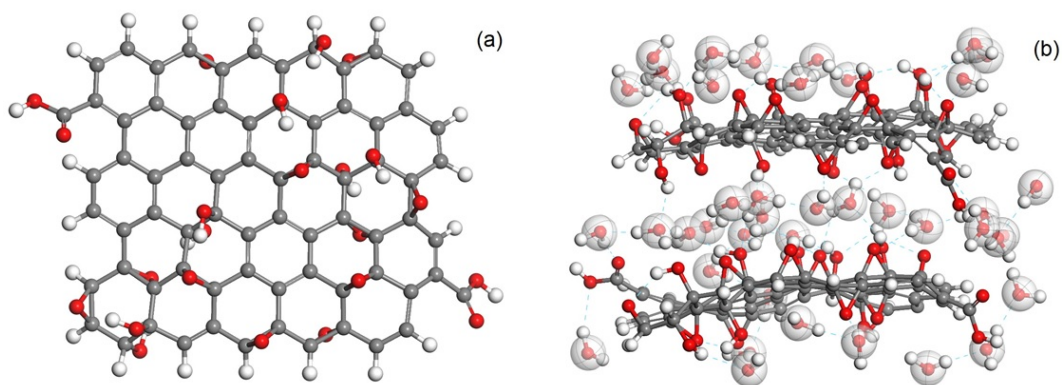


FIG. 7. Equilibrium structure of the  $\{\text{GO} + \text{water}\}$  model [9]. (a). (5, 5) GO molecule. (b). Two-layer solvated sandwich of (5, 5) GO molecules including 48 water molecules (see detail description in [9]). Gray, red and white balls present carbon, oxygen, and hydrogen atoms, respectively

references therein). As for calculated spectra, those related to  $N_{HB} = 1$  and  $N_{HB} = 2$  are mainly responsible for the A and L parts of the real spectrum while  $N_{HB} = 3$  and  $N_{HB} = 4$  spectra are consistent with the higher-wavenumber part B. Therefore, the experimental spectrum actually presents a convolution of the contributions provided with differently configured water molecules, which obviously depend on the relevant  $N_{HB}$ . In practice, the  $N_{HB}$  composition is not only difficult to be predicted, but should not be treated as fixed, since the water is quite dynamic. Consequently, it is not surprising that the calculated 7:10:25:6  $N_{HB}$  composition of the {GO + water} model [9] does not fit any of the presented experimental  $G(\omega)$  spectra in detail. However, when all the molecules are artificially substituted by the  $N_{HB} = 4$  – configured ones (panel (d)), fitting becomes much better, which might indicate the preferential presence of the  $N_{HB} = 4$  – configured molecules in the real case. The dependence of the total spectrum shape on the contribution of alternatively configured molecules may be the reason that the IINS spectra of the interlayer retained water are quite similar in different matrices with respect to the general character of the shape, while the position of B band – as well as intensity of the bridging linking L – are different due to a difference in the arrangement of water molecules in the two cases. The difference can be caused by both the varied chemical composition of the OCGs, which cover carbon skeletons, and size and shape of the skeletons themselves thus giving a topochemical character to the feature observed.

Particular attention should be given to the convolution series at each right panel of Fig. 6. According to Ex.(3), the originally calculated  $G(\omega)$  spectra present the extended sets of  $\delta$ -functions. Multiple different internal and external factors, such as finite lifetime and anharmonicity of vibrations as well as various structural and dynamic inhomogeneities, result in the broadening of the spectral shape. This is usually taken into account via convolution of the  $\delta$ -spectra with Lorentzians with a different half-width L. As seen in the figure, the broadening significantly affects the spectra shapes, thus, the spectra related to L20 and L100 look differently. While L20 curves may be considered as the ones of the highest level of anharmonicity and short lifetime for vibrations, L100 curves disclose the inhomogeneity effects. The latter are highly expected in systems similar to the studied GO and rGO samples. A comparison of the spectra of both columns of Fig. 6 shows that not questioned inhomogeneity of the studied GO samples is rather significant and may be characterized in terms of Lorentzian's parameters by L80.

## 4.2. IINS spectrum of TERGO

As was said in the Introduction, analogously to the GO case, the term rGO covers a large class of polyderivatives of empty-core-based graphene molecules, with the only indication on the disposition of the chemical addends in the sheet circumference (*ccf*). A chemical composition of the relevant rGO *ccf* oxyhydride derivatives, as in the case of the GO ones, greatly varies depending on the rGO production protocols [6]. However, due to the fact that oxygens scatter neutrons inefficiently, the main contribution to the IINS of any rGO sample is provided with the vibrations that involve displacements of hydrogen atoms only. The hydrogens contribute into the rGO structure by the formation of C-H bonds as well as of hydroxyls and carboxyls at the edge atoms. The presence of two latter addends depends on the rigidity of the performed reduction and can exist if only the reduction is not too hard [8]. In the case of hard reduction, the periphery of rGO molecules consists of C-H and C=O bonds only so that the IINS spectra of the samples are provided with hydrogens attached to the edge atoms. The reduction performed for the studied TERGO product is obviously hard, due to which, one can expect a pronounced similarity of the obtained  $G(\omega)$  spectrum with those related to hard-reduced rGOs of different origin.

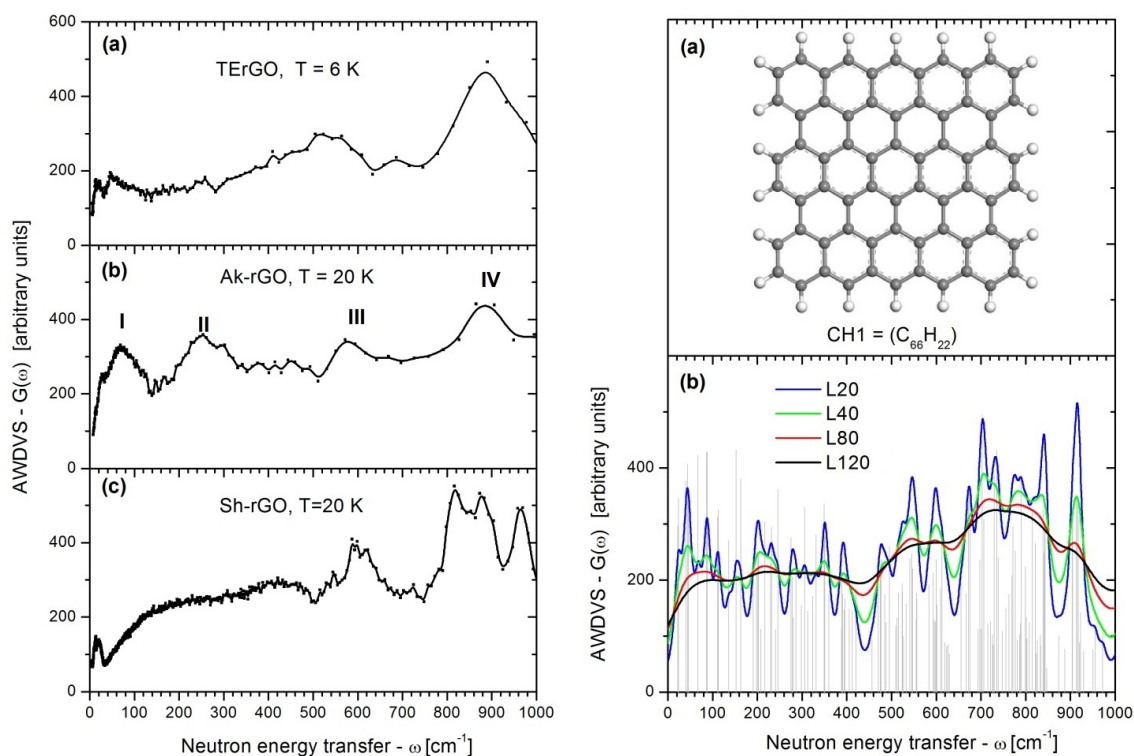


FIG. 8. AWDVS  $G(\omega)$  spectra. Left: Experimental  $G(\omega)$  spectra of TErGO at 6 K (a); Ak-rGO at 20 K (b) [9], and sh-rGO at 20 K (c) [8]. Right: (a) Equilibrium structure and (b) computed  $G(\omega)$  spectrum of  $\text{C}_{66}\text{H}_{22}$  hydride. The 0-1 IINS vibrational mode intensities (gray bars) were convoluted by using Lorentzians of 20, 40, 80, and 120  $\text{cm}^{-1}$  half width (blue, red, green, and black lines, respectively)

Two more such rGO samples have been studied by now: the first is synthetically produced Ak-rGO when using hydrogenolysis in supercritical isopropanol at the last stage on Scheme 1 [9]. The second sh-rGO presents shungite carbon of natural origin [8]. The obtained  $G(\omega)$  spectra of the two samples are presented in the b and c left column panels of Fig. 8. The spectrum of the TErGO studied in the current paper is presented in panel a. As seen in the figure, all the three spectra are evidently quite similar: all of them are spread over a large area from a few wavenumbers to more than thousand  $\text{cm}^{-1}$ ; there is a common feature of the spectra related to their most intensive part in the region of 800 – 1000  $\text{cm}^{-1}$  (part IV); the spectra below 800  $\text{cm}^{-1}$  look like a steady equal-intensity background, slightly structured: the amplitude of the structuring (parts I, II, and III) is comparable with the background intensity or less. The structuring is different for all the samples and presents that very mark that distinguish the latter. Therefore, contrary to the expectations of a close similarity, the spectra turned out rather different. This means that not only chemical composition of the *ccf* area, but other factors also influence the IINS spectra image. Thus, features I and III in the spectrum of TErGO should be partially attributed to small amount of water in the sample (see Fig. 2b).

When examining the  $G(\omega)$  spectrum of the Ak-GO [9], it was shown that the latter is fairly consistent with the calculated  $G(\omega)$  spectrum of *ccf* graphene hydrides. One such hydride, namely, *ccf* (5, 5) monohydride, is presented in the right a panel of Fig. 8 while its computed spectra is shown in panel b. As seen in the figure, the spectrum of vibrations, which involve displacements of hydrogen atoms, is very rich and spread over all the area

where experimental spectra are observed. This very large spectrum width, which is a specific peculiarity of the spectrum, is provided by a peculiar dynamics of hydrogen atoms of the *ccf* graphene hydrides due to participation of the atoms in all vibrational modes of the molecule. Part of these modes can be attributed to the vibrations related to framing C–H bonds. Thus, the above mentioned feature IV centered at  $900\text{ cm}^{-1}$  covers well characterized non-planar deformational vibrations of the bonds. This is the reason why it is observed in all the three experimental spectra. Vibrations below  $800\text{ cm}^{-1}$  are mainly attributed to different modes with the dominant participation of carbon atoms. However, the eigenvectors of these vibrations involve hydrogen atoms, the displacement of which causes a peculiar ‘riding effect’ [19] due to which the vibrations of carbon atoms become vivid under neutron scattering. Conversely, the community of such carbon-dominated vibrations is evidently dependent on the size and shape of the rGO molecule, on the interaction between the rGO sheets and their number in the rGO stacks, on packing of the rGO stacks in massive samples, and so forth. Since the latter motifs are obviously different in the studied samples, the observed difference in the structured part of the  $G(\omega)$  spectra below  $800\text{ cm}^{-1}$  should be expected just revealing a structural polyvariance of rGO products thus exhibiting their topochemical nature.

## 5. Concluding remarks

The current paper brings to a close an extended neutron scattering study of a set of GO and rGO products of different origin. The first part concerned the rGO of natural origin presented by shungite carbon [8], the second was related to synthetic GO and rGO with the latter produced in the course of chemical treatment [9], and the current study was devoted to another pair of synthetic GO/rGO products with the latter produced via thermal exfoliation of the parent GO. The study involved both the neutron diffraction (ND) and inelastic neutron scattering (INS). The obtained results gave convincing evidence for a significant polyvariance of both chemical composition and structural motifs that is the main peculiar characteristic of the products. Additionally, the results well demonstrated the ability of the neutron scattering to exhibit the polyvariance and provide means for its description at the microscopic level.

Briefly summarized, the obtained results for the studied GO and rGO may be presented as the following. For GOs, the neutron diffraction showed that the standardly pretreated fresh samples are characterized by an interlayer distance of  $\sim 7\text{ \AA}$ , which is characteristic for the product stored at ambient conditions under the lowest humidity. However, prolonged storage under more humid conditions causes an increase in the distance due to additional adsorption of water. INS from the samples is mainly provided by retained water and evidently shows the water interaction with the GO substrate resulting in the production of hydroxyls tightly bound with the carbon skeleton of the GO samples [9]. The water spectrum is noticeably different for the two samples indicating different arrangements of water molecules in the two cases. The latter is of the topochemical nature, once depending on both detail chemical composition of the GO surfaces as well as of size and shape of the GO sheets.

Neutron diffraction of the three rGO samples has exhibited a common feature related to the interlayer distance of  $3.36 - 3.51\text{ \AA}$ , thus indicating a flattening of the carbon skeletons of all the three samples. At the same time, the rGO layers form multi-fold stacks of different thicknesses: from 2 layers for Ak-rGO to 5 – 6 layers of sh-rGO and 4 – 6 layers in the case of the TErGO. The layer linear dimensions are different as well: from  $\sim 1.5\text{ nm}$  for sh-rGO to a submicron size for both synthetic rGOs. Thus, the structural studies have revealed a significant polyvariance.

The INS studies have convincingly shown that all the samples are significantly hydrogen-enriched and their IINS spectra are well reproduced by computational spectra related to graphene

hydrides with empty basal plane and monoatomic-hydrogen framing of the edge atoms. The monoatomic-hydrogen motif is well revealed as a number of C–H bonds with characteristic vibrational feature related to non-planar deformational vibrations in the region of 800 – 1000  $\text{cm}^{-1}$ . The feature has been observed in the spectra of all the three samples. However, the energy region shown in the IINS spectra is much larger due to the very large number of vibrations related mainly to the carbon skeleton. The manifestation of these vibrations in the observed IINS spectra below 800  $\text{cm}^{-1}$  is due to a specific ‘riding effect’ which is caused by the presence of hydrogen atoms with noticeable displacements in eigenvectors of the relevant vibrational modes. Obviously, this contribution should depend on the topology of the carbon skeletons due to which it is evidently different by shape and intensity in the observed IINS spectra.

Therefore, the performed study has convincingly shown that neutron scattering should be considered as a useful techniques for examining GO and rGO products. The technique has clearly distinguished GO and rGO products and well exhibited both common features and differences related to the members of both communities. If retained water in GOs and graphene-hydride nature of rGOs provide the commonality of dynamic properties within each of the community, the difference in the relevant sheet topology is responsible for a noticeable variability of the latter. The study has convincingly shown the topochemical nature of the variability, giving evidence for the topochemical nature of the discussed products.

### Acknowledgements

This research was supported in part by PL-Grid Infrastructure (Grant ID: phd2014, phd2013). The calculations with use of DMOL3 were performed within Polish National Accelerators License (Mars Supercomputer, CYFRONET, AGH, Cracow). The financial support of Polish Government Plenipotentiary for JINR in Dubna, Russia (Grant No. 44/27-01-2015/7/1121/5) is also gratefully acknowledged.

### References

- [1] Novoselov K.S., Fal'ko V.I., Colombo L., et al. A roadmap for graphene. *Nature*, 2012, **490**, P. 192–200.
- [2] Sheka E.F. The uniqueness of physical and chemical natures of graphene: their coherence and conflicts. *Int. J. Quantum Chem.*, 2014, **114**, P. 1079–1095.
- [3] Ferrari A.C., Bonaccorso F., Fal'ko V., et al. Science and technology roadmap for graphene, related two-dimensional crystals, and hybrid systems. *Nanoscale*, 2015, **7**, P. 4598–4810.
- [4] Peplow M. The quest for supercarbon. *Nature*, 2013, **503**, P. 327–329.
- [5] Sheka E.F., Popova N.A. Molecular theory of graphene oxide. *Phys. Chem. Chem. Phys.*, 2013, **15**, P. 13304–13322.
- [6] Chua C.K., Pumera M. Chemical reduction of graphene oxide: a synthetic chemistry viewpoint. *Chem. Soc. Rev.*, 2014, **43**, P. 291–312.
- [7] Zhao J., Liu L., Li F. *Graphene oxide: Physics and applications*. Springer, 2014, 154 p.
- [8] Sheka E.F., Rozhkova N.N., Holderna-Natkaniec K., Natkaniec I. Neutron scattering study of reduced graphene oxide of natural origin. *Nanosystems: Phys. Chem. Math.*, 2014, **5**, P. 659–676.
- [9] Natkaniec I., Sheka E.F., Druzicki K., et al. Computationally supported neutron scattering study of parent and chemically reduced graphene oxide (Submitted).
- [10] AkKoLab LLC, URL: [www.akkolab.ru](http://www.akkolab.ru).
- [11] Hummers W.S., Offeman R.E. Preparation of graphitic oxide. *J. Am. Chem. Soc.*, 1958, **80**, P. 1339–1339.
- [12] Krishnan D., Kim F., Luo J., et al. Energetic graphene oxide: Challenges and opportunities. *Nano Today*, 2012, **7**, P. 137–152.
- [13] Buchsteiner A., Lerf A., Pieper J. Water dynamics in graphite oxide investigated with neutron scattering. *J. Phys. Chem. B*, 2006, **110**, P. 22328–22338.
- [14] Natkaniec I., Chudoba D., Hetmańczyk L., et al. Parameters of the NERA spectrometer for cold and thermal moderators of the IBR-2 pulsed reactor. *J. Phys.: Conf. Series*, 2014, **554**, P. 012002.

- [15] Opalev S.V., Belenkov E.A. Experimental research of graphite structure transformation at mechanical milling. *Proceedings of Chelyabinsk Scientific Center*, **3**, P. 27–30 [in Russian].
- [16] Sheka E., Popova N. Molecular theory of graphene oxide. *Phys. Chem. Chem. Phys.*, 2013, **15**, P. 13304–13332.
- [17] Kovalevski V.V., Buseck P.R., Cowley J.M. Comparison of carbon in shungite rocks to other natural carbons: An X-ray and TEM study. *Carbon*, 2001, **39**, P. 243–56.
- [18] Sofer Z., Šimek P., Jankovský O., et al. Neutron diffraction as a precise and reliable method for obtaining structural properties of bulk quantities of graphene. *Nanoscale*, 2014, **6**, P. 13082–13089.
- [19] Bokhenkov E.L., Natkaniec I., Sheka E.F. Determination of density of phonon states in a naphthalene crystal on basis of inelastic incoherent neutron scattering. *Sov. Phys. JETP*, 1976, **43**, P. 536–545.
- [20] Johnson M.R., Parlinski K., Natkaniec I., et al. Ab initio calculations and INS measurements of phonons and molecular vibrations in a model peptide compound – urea. *Chem. Phys.*, 2003, **291**, P. 53–60.
- [21] Liao K.-H., Mittal A., Bose S., et al. Aqueous only route toward graphene from graphite oxide. *ACS Nano*, 2011, **5**, P. 1253–1258.
- [22] Dimiev A.M., Alemany L.B., Tour J.M. Graphene oxide. Origin of acidity, its instability in water, and a new dynamic structural model. *ACS Nano*, 2013, **7**, P. 576–588.
- [23] Sheka E., Popova N. Odd-electron molecular theory of graphene hydrogenation. *J. Mol. Mod.*, 2012, **18**, P. 3751–3768.

# Classical density functional approach to adsorption of hydrogen in carbon materials

V. V. Zubkov, V. M. Samsonov, I. V. Grinev, I. V. Popov

Tver State University, Tver, Russia

zvvictor@mail.ru

PACS 68.43.-h, 68.18.Fg, 68.43.De DOI 10.17586/2220-8054-2015-6-3-394-404

The adsorption of hydrogen in carbon adsorbents was investigated at low and high temperatures (20.33, 77, 200 and 300 K) over a wide range of pressures using the classical density functional theory. The adsorbent was simulated by a slit-like pore presented by the gap between two monocarbon (graphene) walls. In most cases, our results demonstrate a good agreement with the available experimental and theoretical results of other authors. A conclusion was made that, contrary to the low temperature region ( $T < 100$  K), at high temperatures (200 and 300 K), predicted values for the adsorption and of the gravimetric density of hydrogen are not sufficient for the practical design of a hydrogen accumulator.

**Keywords:** Adsorption, hydrogen, carbon adsorbents, density functional theory.

*Received:* 6 April 2015

*Revised:* 21 April 2015

## 1. Introduction

For the last decade, the interest in the adsorption of hydrogen in carbon porous materials has peaked from time to time, first of all, in view of its possible applications in the hydrogen energetics. This kind of energetics may be considered as a very clear way for the production and storage of energy. Hydrogen is the most abundant element not only on the Earth but also in the whole Universe. It has the highest combustion temperature, and the only product of the hydrogen combustion is water. In the framework of the previously-mentioned problem, a specific, and most importantly, still unsolved issue concerns hydrogen storage. Some estimations [1] predict that 3.1 kg of the molecular hydrogen is required for a car to travel 500 km car mileage. At the same time, in [1] it is noted that the existing approaches to hydrogen storage do not allow one to solve the problem under consideration. For instance, using the compressed gaseous hydrogen is usually treated as one of the main alternatives to the liquefied hydrogen. However, the first of the above alternatives requires extremely high pressures, which is very dangerous. The storage of the liquefied hydrogen requires prohibitively high pressures as well as at very low temperatures. Among other alternatives, the use of pure and mixed metal hydrides should also be mentioned; however, these metal materials also do not allow one to solve the problem under consideration.

At the same time, other authors [2–7] believe that physical adsorption is a promising means of hydrogen storage. In particular, fullerenes, single-walled carbon nanotubes (SWNTs), carbon nanofibers and metal-organic frameworks [8] have been treated as promising adsorbents [4, 7]. Monte Carlo simulations of hydrogen adsorption on SWNTs bunches at 77 and 293 K, and pressures up to 20 MPa [5, 6] revealed a high enough adsorption capacity of these structures. However, until recently, the results of adsorption simulation in microporous carbon adsorbents on, SWNTs and nanofibers has not allowed one to draw a final conclusion regarding the potential use of carbon adsorbents for practical hydrogen storage.

At the same time, there are experimental data for hydrogen adsorption in carbon materials at different temperatures and pressures [7]. As a rule, in theoretical estimations and computer simulations, the porous adsorbents under investigation are represented as a single slit-like pore of the width  $H$  corresponding to an average adequate value of the pore size in real carbon adsorbents.

Basic theoretical approaches to adsorption in porous materials are based on semi-empirical state equations of adsorption layers, in particular on the Langmuir isotherm, the Dubinin-Radushkevich and Dubinin-Astakhov equations [9, 10]. Among more modern approaches, the vacancy solution theory [11] and the classical density functional theory (DFT) [12–14] seem to be of special interest. Monte-Carlo simulations [15, 16] should also be also mentioned as one of the available approaches for investigating the adsorption of hydrogen in different types of carbon adsorbents. However, Monte Carlo results for slit-like micropores formed by graphene hexagonal planes do not give a clear answer on the potential of microporous carbon adsorbents for the hydrogen storage [16].

In our previous papers [17–20], DFT was used to calculate the adsorption of hydrogen on fullerene molecules and in the slit-like pore formed by graphene walls. The slit-like pore reproduces, to a greater or lesser extent, conventional industrial carbon adsorbents. In [20] two important conclusions were made:

- (i) at high temperatures ( $T > 200$  K) the adsorption  $a$  per 1 g of adsorbent and the gravimetric density  $wt$  for the cases of the available industrial carbon adsorbents and fullerene molecules are not sufficient for the practical design of the adsorption hydrogen accumulator (according our estimations,  $a \approx 20$  mmole/g and  $wt \approx 5\%$ );
- (ii) fullerenes and fullerene materials hardly have any advantages in comparison with conventional carbon adsorbents.

In spite of many opinions that an appropriate hydrogen accumulator, including adsorption one, cannot be designed, publications on this topic have not ceased. For instance, in [21] some electrospun composite nanofibers containing carbon nanotubes were fabricated and investigated. However, at high temperatures, the authors of [21] experimentally obtained approximately the same adsorption characteristics as our DFT calculation results for carbon modelling adsorbents and fullerene molecules [20]. So, additional more accurate experimental and theoretical investigations are needed to solve the problem or to show that it principally cannot be solved. In particular, we do not believe that the adsorption and gravimetric density at  $T = 77$  K and at  $T = 200$  K can be approximately equal as it is stated in [22].

## 2. Method of calculations

DFT theory may be regarded as a powerful modern method for the investigation of vapor-liquid interfaces, adsorption in pores, and calculations of pore size distributions from experimental isotherms. As the hydrogen molecule is nonpolar and has very low degree of asphericity, molecular hydrogen belongs, in a reasonable approximation, to the class of simple fluids. Respectively, theoretical results obtained in the framework of the simple fluid model can be correctly compared with corresponding experimental data. However, a detailed comparison of DFT results with experimental data is not straightforward. Structural and energetic heterogeneity of pores strongly influences on the adsorption in real materials [23, 24]. The ways of measurements are different and, therefore, some experimental results contradict to each other [25]. Hence, there are reasons to calculate average values of the adsorption for adequate modelling systems and to compare them with the available experimental data.

TABLE 1. Molecular parameters for H<sub>2</sub> and graphite.

	Linear parameter $\sigma$ , nm	Energy parameter $\varepsilon/k$ , K
Graphite	0.34 [27]	28 [27]
Hydrogen	0.296 [29]	36.7 [29]

The slit-like pore model seems to be quite adequate, as the formation of micropores in carbon adsorbents can be considered as a process of thermochemical elimination of atoms from hexagonal planes in carbon crystallites being activated by water vapor [22]. In our calculations, we used the model of an ideal pore, for which the distance between the surfaces presented by two graphene layers corresponds the 1-5 deleted (burnt out) layers of graphene. So, the neighboring micropores will be separated by single carbon grapheme monolayer. We assume that the distance  $H$  between hexagonal layers in graphite is equal to 0.335 nm and the side length  $b$  of hexagons, forming layers, is 0.142 nm [27].

An adsorbate molecule located in the pore undergoes adsorptive forces of two planes (below referred to as upper and lower). The effect of the finite wall length is small enough and, respectively, may be neglected [26]. The interaction potential between a fluid molecule and one graphene wall was described by the next potential [28]:

$$U_{sf}(z) = 2\pi\rho_s\varepsilon_{sf}\sigma_{sf}^2 \left( \frac{2}{5} \frac{\sigma_{sf}^{10}}{z^{10}} - \frac{\sigma_{sf}^4}{z^4} \right), \quad (1)$$

where  $\rho_s$  is the wall surface density equal to the number of atoms per unit area,  $\sigma_{sf}$  and  $\varepsilon_{sf}$  are the parameters of the wall-fluid potential. The adsorption (single particle) potential (1) was obtained integrating the Lennard-Jones (LJ) pair potential over the wall area. For this reason, it will be referred to as the integrated LJ-potential (ILJ). The wall-adsorbate parameters  $\sigma_{sf}$  and  $\varepsilon_{sf}$  were found using the Lorentz-Berthelot mixing rules, via the values of  $\sigma_s$ ,  $\varepsilon_s$  for the solid walls and  $\sigma_f$ ,  $\varepsilon_f$  for the fluid, respectively, i.e.  $\sigma_{sf} = (\sigma_s + \sigma_f)/2$  and  $\varepsilon_{sf} = \sqrt{\varepsilon_s\varepsilon_f}$ . The reduced surface density of atoms in the walls may be evaluated as follows:

$$n_s = \rho_s\sigma_s^2 = \frac{N_s}{S}\sigma_s^2 = \frac{4\sigma_s^2}{3\sqrt{3}b^2} = \frac{4\sqrt{3}}{9} \left( \frac{\sigma_s}{b} \right)^2 = 4.413. \quad (2)$$

So, the total potential of the pore walls

$$U(z) = U_{sf}(z) + U_{sf}(H - z) \quad (3)$$

is equal to the sum of two terms corresponding to two walls located at  $z = 0$  and  $z = H$ , respectively, where  $z$  is the distance between the fluid particle and the first wall. All the used parameters of the potential (1) are presented in Table 1 ( $k$  is the Boltzmann constant).

The main problem of DFT is the design of thermodynamic characteristic functions as some density functionals. For this purpose, expressions for the Helmholtz energy  $F[\rho(\mathbf{r})]$  and grand potential  $\Omega[\rho(\mathbf{r})]$  of the system under consideration are used as the density functionals. The expression for  $\Omega[\rho(\mathbf{r})]$  can be written as [14]

$$\Omega[\rho(\mathbf{r})] = F[\rho(\mathbf{r})] + \int [U(\mathbf{r}) - \mu]\rho(\mathbf{r})d^3\mathbf{r}, \quad (4)$$

where  $\mu$  is the chemical potential. The Helmholtz energy functional can be formally expressed as the ideal-gas term

$$F_{id}[\rho(\mathbf{r})] = kT \int [\ln \rho(\mathbf{r}) - 1]\rho(\mathbf{r})d^3\mathbf{r} \quad (5)$$

and an excess contribution which, in turn, can be decomposed into the hard sphere (subscript *hs*) and attractive (subscript *attr*) terms:

$$F_{ex}[\rho(\mathbf{r})] = F_{hs}[\rho(\mathbf{r})] + F_{attr}[\rho(\mathbf{r})]. \quad (6)$$

In Eq. (5), the cube of the thermal wavelength  $\Lambda$  is omitted because it gives no direct contribution to the density profiles or thermodynamic properties. The excess Helmholtz energy term, due to hard sphere repulsion, will be presented in accordance with the modified fundamental measure theory [30]:

$$F_{hs}[\rho(\mathbf{r})] = kT \int \Phi^{hs}[n_\alpha(\rho(\mathbf{r}))] d^3\mathbf{r}. \quad (7)$$

In Eq. (7), the reduced excess energy density  $\Phi^{hs}$  is interpreted as a function of six weighted densities  $n_\alpha(\mathbf{r}) = \int \omega^\alpha(|\mathbf{r}' - \mathbf{r}|) \rho(\mathbf{r}') d^3\mathbf{r}'$ . The expressions for  $n_\alpha$  and  $\omega^\alpha$  are presented in [30]. The attractive part of the excess Helmholtz energy can be written in terms of the mean-field approximation:

$$F_{attr} = \frac{1}{2} \iint u^{attr}(|\mathbf{r}' - \mathbf{r}|) \rho(\mathbf{r}') \rho(\mathbf{r}) d^3\mathbf{r}' d^3\mathbf{r}. \quad (8)$$

In Eq. (8)  $u^{attr}$  is the long-range attraction part of LJ potential represented according to the WCA potential model [31]. The minimization of the grand potential with respect to the density profiles yields the following Euler–Lagrange equation

$$\rho(\mathbf{r}) = \exp \left[ \frac{1}{kT} \left( \mu - U(\mathbf{r}) - \frac{\delta F[\rho(\mathbf{r})]}{\delta \rho(\mathbf{r})} \right) \right] \quad (9)$$

satisfied by the equilibrium density profile. Below we also use the reduced value of the local density  $\eta = \pi \rho d_f^3/6$ . Here,  $d_f$  is the hard sphere diameter of the hydrogen molecular which can be expressed through the  $\sigma_f$  parameter by the next expression [32]

$$d_f = \frac{1 + 0.2977 kT/\varepsilon_f}{1 + 0.33163 kT/\varepsilon_f + 1.0477 \times 10^{-3} (kT/\varepsilon_f)^2 \sigma_f} \sigma_f \quad (10)$$

Knowing the density profile  $\eta(z)$ , one can find the reduced absolute adsorption

$$\Gamma^* = \int_0^H \eta(z) dz \quad (11)$$

in the pore under consideration. Below, the next commonly used adsorption parameters will be calculated:

(i) the adsorption of hydrogen (volume density)

$$a = \frac{6}{\pi} \left( \frac{\sigma_s}{d} \right)^2 \frac{\Gamma^*}{M_s \rho_s \sigma_s^2} \quad (12)$$

in kg/m<sup>3</sup>;

(ii) the gravimetric density (mass ratio)

$$wt = \frac{m_s}{m_s + m_f} 100\% = \frac{1}{1 + 1/(aM_f)} 100\% \quad (13)$$

of H<sub>2</sub>(%). Here  $M_s$  and  $M_f$  are the molar masses of graphite and hydrogen respectively,  $m_f$  is the total mass of hydrogen in the pore and  $m_s$  is the mass of the adsorbent.

### 3. Calculation results

Previously, [17–20] we have calculated the density distributions in different modeling fluid layers in the slit-like pore, for different wall parameters, external pressures and temperatures (20.35, 77 and 200 K). In this work, our DFT results for hydrogen adsorption in porous carbon at 20.35, 77, 200 and 300 K, and various pressures are presented. So, all the former data have been recalculated for wider temperature and pressure ranges. Previously, we calculated the density distribution profiles corresponding to different wall parameter values, in particular for a wide range of the wall surface densities  $n_s$  (from 2.0 to 6.2). It is also worth mentioning that an intermediate value  $n_s = 4.4$  corresponds to real porous graphite adsorbents [22].

In [22], the adsorption of hydrogen was calculated using a semi-empirical approach based on the Dubinin-Radushkevich equation. Namely, standard data for the adsorption of benzene were recalculated for the hydrogen-AC35 system. The abbreviation AC35 taken from [22] corresponds to a model porous carbon adsorbent with 3 of 5 graphene layers deleted. In the present paper, the above-mentioned adsorption characteristics were calculated for different  $N$  values for deleted graphene monolayers and, in particular, for  $N = 3$  as the slit-like pore, corresponding to  $N = 3$  and  $n_s = 4.4$ , which reproduces the model adsorbent AC35 most adequately.

In figure 1(a) the density profile is presented for the hydrogen layer when  $N = 3$ ,  $n_s = 4.4$  and  $T = 20.35$  K, corresponding to the boiling point of hydrogen. The figure demonstrates two reasonably high maxima at the pore walls, symmetrical relative to the pore center and two additional lower but noticeable maxima in the central part of the pore.

In figures 1(b) and 1(c), density profiles are shown for higher (supercritical) temperatures. Figure 1(b) corresponds to a supercritical but low enough temperature  $T = 77$  K, i.e. to the nitrogen boiling temperature, and a wide range of the pressures: from 0.05 to 20 MPa. One can see that at the lowest pressure 0.05 MPa only two weak maxima at the pore walls are seen, i.e. the density profile corresponds to two density profiles at two separate graphene layers. At  $p = 0.625$  MPa, a slope central maximum is formed with a plateau, and only at high pressures of about 6 MPa are two pronounced central maxima formed. In figure 1(c) three density profiles are compared, corresponding to three different temperatures: 77, 200 and 300 K and a very high external pressure 20 MPa. One can see that, in spite of the high pressure, at temperatures 200 and 300 K, central maxima are not observed and two maxima at the pore walls are 5-10 times smaller than at  $T = 77$  K. The known density profiles make it readily possible to find the adsorption  $a$  and the gravimetric density  $wt$ . The dependences of the  $a$  and  $wt$  parameters upon the external pressure  $p$  are shown in figures 2 and 3 for a low (77 K) and high (200 K) temperatures, respectively.

Figures 2 and 3 demonstrate the dependence of  $a$  and  $wt$  on the pore width  $H$  or the corresponding number  $N$  of the deleted graphene layers. As one could expect, increasing the pressure  $p$  results in an increase of both  $a$  and  $wt$  parameters. At the same time, the variation of  $N$  affects  $a$  and  $wt$  parameters in opposite directions: increasing  $N$  results in a decreasing of the adsorption  $a$  and an increase in the gravimetric density  $wt$ .

### 4. Analysis of the results and discussion

According to [33], for 2010 U.S. Department of Energy (DOE) proclaimed goals are as follows:  $wt = 6.5\%$  mass ratio and  $a = 62$  kg/m<sup>3</sup> volume density. Obviously, these goals relate to the problem of the hydrogen accumulator design. Later, the above goals were deemed to be unrealistic and, therefore, to 2015 DOE established new goals as  $wt = 5.5\%$  and

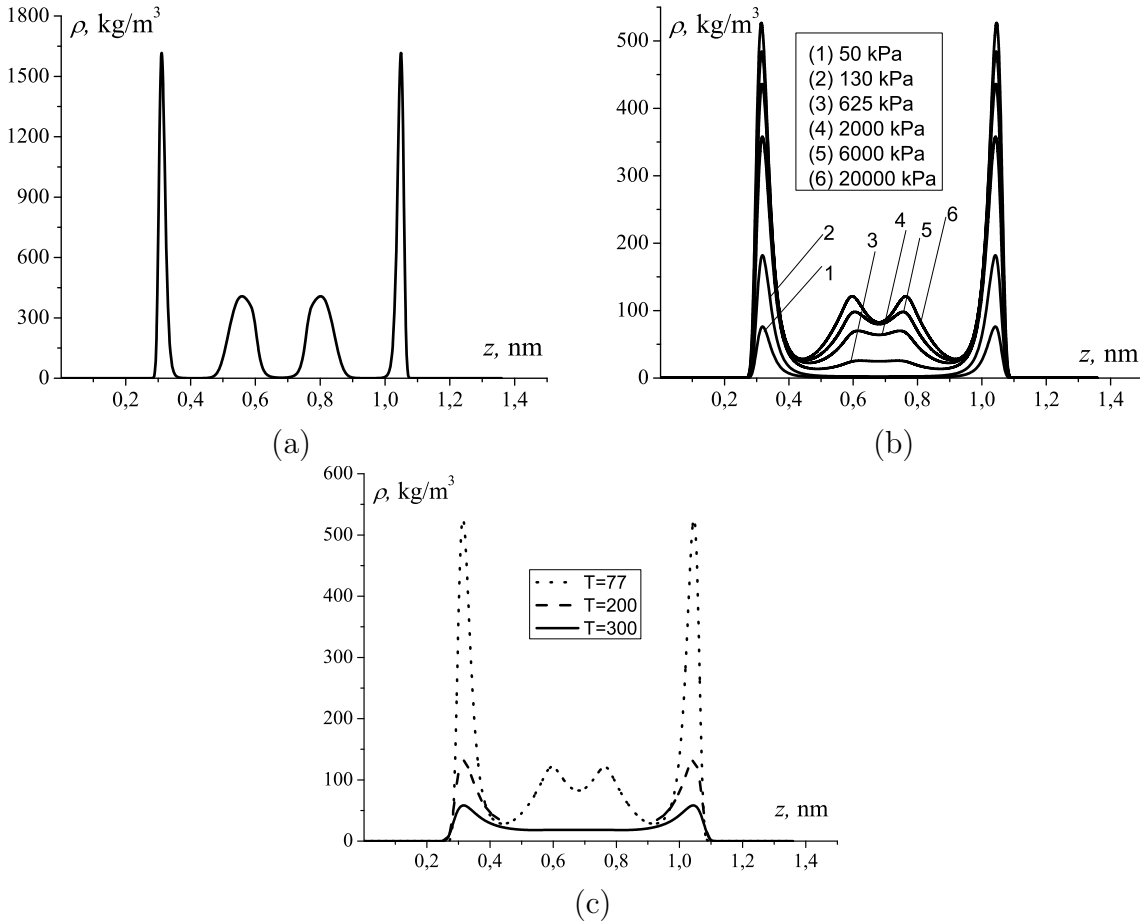


FIG. 1. Density profiles for the hydrogen layers in modeling slit-like pores representing the carbon adsorbent AC35 at different temperatures and pressures: (a)  $T = 20.35$  K,  $p = 85.5$  kPa; (b)  $T = 77$  K, values of the pressure are shown in the figure; (c) comparison of the density profiles at  $T = 77$  K, 200 K, 300 K and  $p = 20$  MPa

$a = 45$  kg/m<sup>3</sup> at ambient temperatures and practical pressures (usually less than 10 bar = 1 MPa). However, according to our calculation results presented in figure 3, at  $T = 200$  K and even enormous pressures up to 25 MPa these values of both  $wt$  and  $a$  parameters cannot be reached.

To confirm the reliability of our results, we compared them with the available experimental and theoretical results of other authors. In figure 4, our results for  $wt$  at  $T = 77$  K are compared to experimental results [34] where a redefined pore thickness  $\tilde{H} = H - \sigma_s$  was used as a pore parameter. The value  $\tilde{H} = 0.5$  nm corresponds to  $H = 0.84$  nm, i.e. to  $N = 1.235$ . Obviously, in [34] an average (effective) value of  $\tilde{H}$  was used corresponding to a real carbon adsorbent. As one can see, our calculation results satisfactorily agree with the experimental results [34]. For  $p = 0.02$  MPa our results and results of measurements [34] coincide almost identically.

In figure 5 our results for the adsorption  $a$  are compared to Monte-Carlo results [35]. As in [35], the value  $\varepsilon_f/k = 34.2$  K was used which differs a bit from the value presented in Table 1, we also used (in this case) the same value of the  $\varepsilon_f/k$  parameter. One can see that figure 5 demonstrates a good agreement between our calculation results and the results [35].

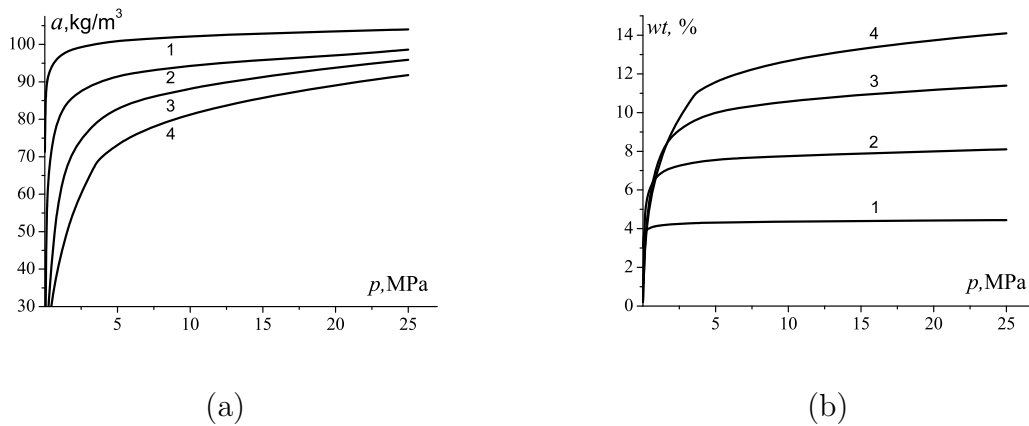


FIG. 2. The pressure dependences of the adsorption parameters  $a$  (a) and  $wt$  (b) at different values of  $N$  ( $T = 77$  K). Curves 1,2,3 and 4 correspond to  $N = 1$  ( $H = 0.68$  nm),  $N = 2$  ( $H = 1.02$  nm),  $N = 3$  ( $H = 1.36$  nm) and  $N = 4$  ( $H = 1.7$  nm), respectively

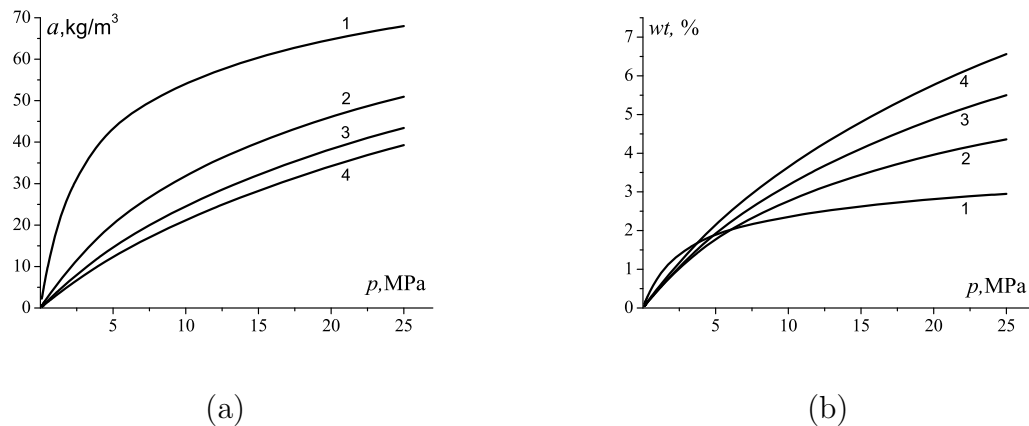


FIG. 3. The pressure dependences of the adsorption parameters  $a$  (a) and  $wt$  (b) at different values of  $N$  ( $T = 200$  K). The numeration of curves is the same as in figure 2

As was mentioned above, in [22], standard data for the adsorption of benzene in AC35 were recalculated to the adsorption of hydrogen using the Dubinin–Radushkevich equation [9]. In figure 6, our calculation results for the  $a$  parameter are compared to the results of [22]. One can see that at  $T = 77$  K, our results satisfactorily agree with the results of [22]. However, at higher temperatures (200 and 300 K), the divergence between our results and [22] becomes noticeable enough. Obviously, at 200 and 300 K, the results for [22] are overestimated. In particular, at high pressures (on the order of 25 MPa) the results [22] correspond very closely to seemingly improbable  $a$  values.

Another important problem which is worth discussing here is the choice of the single particle potential and its influence on the DFT calculation results. In the previous section, we used the integral form (1) of the LJ-pair potential with reliable parameters presented in Table 1. We also tried to use some *ab initio* data for the  $\text{H}_2$  - graphene interaction to obtain corresponding adsorption potential. However, as one can see in figure 7, different

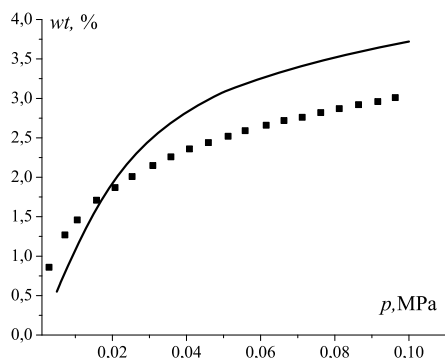


FIG. 4. Comparison of our results for the  $wt$  dependence with experimental results [34] presented by dots  $\blacksquare$  ( $T = 77$  K,  $H = 0.84$  nm).

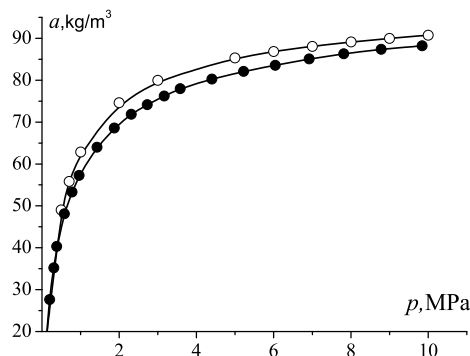


FIG. 5. Comparison of our calculation results (white circles  $\circ$ ) to the Monte-Carlo results [35] presented by black circles  $\bullet$  ( $T = 77$  K,  $H = 1.26$  nm, i.e.  $N = 2.7$ ).

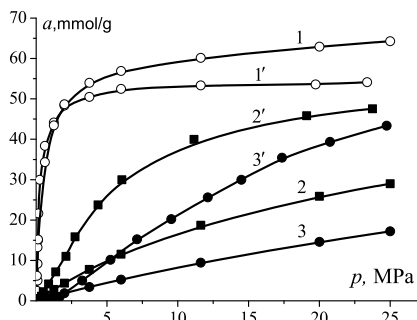


FIG. 6. Comparison of our DFT results (curves 1, 2 and 3) to the results [22] (curves 1', 2' and 3') for temperatures 77 K (white circles  $\circ$ ), 200 K (black squares  $\blacksquare$ ) and 300 K (black circles  $\bullet$ ).

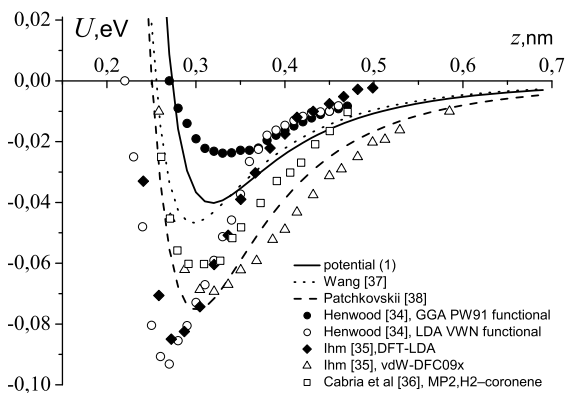


FIG. 7. Comparison of our adsorption potential (1), i.e. ILJ with ab initio data [36–38]. and semi-empirical potentials obtained via integration of  $H_2 - C$  pair potentials [39, 40].

approximations of the same *ab initio* method can give noticeably different results. Also, in the available papers on the  $H_2$  - graphene interaction, only separate values of the attractive part of  $U_{sf}(z)$  are presented, which makes it difficult to obtain an analytical form of  $U_{sf}(z)$  suitable for further classical DFT-calculations.

It is also noteworthy that ILJ potential (1) satisfactorily agrees with an integral form of the pair potential [39]. Among the available and formally approved, to a greater or lesser extent, semi-empirical pair potentials, proposed to describe the  $H_2 - C$  interactions, the pair

TABLE 2. Comparison of  $a$  and  $wt$  parameters calculated using ILJ and IP single particle potentials.

$N$	$T = 150 \text{ K}, P = 20 \text{ bar}$				$T = 298 \text{ K}, P = 450 \text{ bar}$			
	$a$		$wt$		$a$		$wt$	
	ILJ	IP	ILJ	IP	ILJ	IP	ILJ	IP
1	57.1	93.9	2.5	4.0	53.8	81.4	2.4	3.5
2	22.7	66.1	2.0	5.6	41.9	62.9	3.6	5.3
3	14.1	42.8	1.9	5.4	37.9	52.7	4.8	6.6
4	11.0	32.1	1.9	5.4	35.8	47.1	6.0	7.8
5	9.4	26.2	2.1	5.5	34.6	43.6	7.2	8.9

potential [40] seems to have the deepest potential well and, therefore, may be expected to give the highest adsorption characteristics. As one could expect, the potential [40] gives also the deepest single particle potential  $U_{sf}(z)$  (see figure 7).

So, we calculated the  $a$  and  $wt$  parameters for both ILJ and the integral form of Patchkovskii's potential (IP). The results of these calculations are presented in Table 2. As one would expect, IP really gives noticeably higher values for  $a$  and  $wt$  in comparison to ILJ. However, at high (room) temperature, 298 K, the deepest IP only gives practically suitable  $a$  and  $wt$  values at very high pressures, which are unlikely to be realized in vehicles.

There are no reasons to consider IP as the most exact and reliable adsorption potential. Moreover, according to the results of comparison of our DFT calculations of  $a$  and  $wt$  parameters with the results of other authors, a conclusion can be made that IP seems to give overestimated results for the adsorption of hydrogen in carbon adsorbents. But even this deepest potential does not demonstrate some realistic opportunities for high-temperature hydrogen storage in currently-available carbon adsorbents.

## 5. Conclusion

The above comparison with the available experimental and theoretical results of other authors confirms the adequacy of our DFT calculations for the adsorption of hydrogen in carbon adsorbents. At the same time, our results demonstrate that at high (room) temperatures the adsorption capacity of carbon adsorbents is not sufficient for the practical design of an appropriate hydrogen accumulator which can be, in particular, used in vehicles. Then, according to our former results [18–20] and the results of other authors [21, 41], neither conventional carbon adsorbents nor fullerenes and carbon nanotubes can help to solve this problem. This conclusion seems to be fulfilled not only for slit-like pores but also for pillared graphene [42]. At the same time, according to Monte-Carlo calculations presented in [42], the gravimetric density for Li-doped pillared materials can be several times higher than that of the analogous pure carbon materials. However, the very significant role of active sites in carbon adsorbents should be verified by further experimental and theoretical investigations, including classical DFT-calculations, which can be carried out, but are beyond the scope of this paper.

## Acknowledgements

The work was supported by Russian Foundation for Basic Research (grant No 13-03-00119) and by Ministry of Education and Science of Russian Federation, in frames of the

State Program in sphere of scientific activity. The authors are grateful for useful discussion to Prof. E.A. Ustinov.

## References

- [1] Dillon A. C., Jones K. M., Bekkedahl T. A., Kiang C. H., Bethune D. S., Heben M. J. Storage of hydrogen in single walled carbon nanotubes. *Nature*, 1997, **386**, P. 377–379. doi:10.1038/386377a0
- [2] Hynek S., Fuller W., Bendl J. Hydrogen storage by carbon sorption. *J. Int. J. Hydrogen Energy*, 1997, **22**, P. 601–610. DOI: 10.1016/S0360-3199(96)00185-1
- [3] Carpetis C., Peschka W. Study on hydrogen storage by use of cryoadsorbents. *Int. J. Hydrogen Energy*, 1980, **5**, P. 539–554. DOI: 10.1016/0360-3199(80)90061-0
- [4] Chambers A., Park C., Baker R. T., Rodriguez N. M. Hydrogen Storage in Graphite Nanofibers. *J. Phys. Chem. B.*, 1998, **102**, P. 4253–4256. DOI: 10.1021/jp980114l
- [5] Darkrim F., Levesque D. Monte Carlo simulations of hydrogen adsorption in single-walled carbon nanotubes. *J. Chem. Phys.*, 1998, **109**, P. 4981–4984. <http://dx.doi.org/10.1063/1.477109>
- [6] Yin Y. F., Mays T., McEnan B. Molecular Simulations of Hydrogen Storage in Carbon Nanotube Arrays. *Langmuir*, 2000, **16**, P. 10521–10527. DOI: 10.1021/la000900t
- [7] Anson A., Jagiello J., Parra J. B., Sanjuan M. L., Benito A. M., Maser W. K., Martinez M. T. Porosity, Surface Area, Surface Energy, and Hydrogen Adsorption in Nanostructured Carbons. *J. Phys. Chem. B.*, 2004, **108**, P. 15820–15826. DOI: 10.1021/jp047253p
- [8] Assfour B. Thaeer assaad, adnan odeh, Hydrogen adsorption properties of metal-organic frameworks within the density-functional based tight-binding approach. *Nanosystems: physics, chemistry, mathematics*, 2014, **5**, P. 820–828. <http://nanojournal.ifmo.ru/en/wp-content/uploads/2014/12/NPCM56P820.pdf>
- [9] Dubinin M. M. Physical Adsorption of Gases and Vapors in Micropores, in: D. A. Cadenhead (ed.), *Progress in Surface and Membrane Science*. City: New York Acad. Press, 1975, 1–70 p.
- [10] Ismadji S., Bhatia S. K. A Modified Pore-Filling Isotherm for Liquid-Phase Adsorption in Activated Carbon. *Langmuir*, 2001, **17**, P. 1488–1498. DOI: 10.1021/la0009339
- [11] Bhatia S. K., Ding L. P. Vacancy solution theory of adsorption revisited. *J. AIChE*, 2001, **47**, P. 2136–2138. DOI: 10.1002/aic.690470924
- [12] Neimark A. V., Ravikovitch P. I. Calibration of Pore Volume in Adsorption Experiments and Theoretical Models. *Langmuir*, 1997, **13**, P. 5148–5160. DOI: 10.1021/la970266s
- [13] Ravikovitch P. I., Vishnyakov A., Russo R., Neimark A. V. Unified Approach to Pore Size Characterization of Microporous Carbonaceous Materials from N<sub>2</sub>, Ar, and CO<sub>2</sub> Adsorption Isotherms. *Langmuir*, 2000, **16**, P. 2311–2320.
- [14] Wu J. Density functional theory for chemical engineering: from capillarity to soft materials. *J. AIChE*, 2006, **52**, P. 1169–1193. DOI: 10.1002/aic.10713
- [15] Vishnyakov A., Ravikovitch P. I., Neimark A. V. Molecular Level Models for CO<sub>2</sub> Sorption in Nanopores. *Langmuir*, 1999, **15**, P. 8736–8742. DOI: 10.1021/la990726c
- [16] Rzepka M., Lamp P., de la Casa-Lillo M. A. Physisorption of Hydrogen on Microporous Carbon and Carbon Nanotubes. *J. Phys. Chem. B.*, 1998, **102**, P. 10894–10898. DOI: 10.1021/jp9829602
- [17] Samsonov V. M., Zubkov V. V., Grinev I. V. Application of density functional method to problem of creating hydrogen adsorption fuel cell. *Technical Physics Letters*, 2011, **37**, P. 302–305. DOI: 10.1134/S1063785011040134
- [18] Zubkov V. V., Samsonov V. M., Grinev I. V. Study of structural and thermodynamic parameters of adsorption layers using density functional theory. Local density and adsorption isotherms on spherical surfaces. *Colloid Journal*, 2013, **75**, P. 524–531. DOI: 10.1134/S1061933X13040194
- [19] Zubkov V. V., Samsonov V. M., Grinev I. V. Hydrogen adsorption in slit-shaped pores on carbon adsorbents. *Bulletin of the Russian Academy of Sciences. Physics*, 2012, **76**, P. 814–818. DOI: 10.3103/S1062873812070398
- [20] Samsonov V. M., Zubkov V. V., Grinev I. V. Comparative study of hydrogen adsorption in slit like pore of carbon adsorbents and on fullerene molecules. Proceedings of the “International Conference Nanomaterials: Applications and Properties”, Alushta, the Crimea (Sumy State University, Sumy, 2013), Sep. 16–21, 2013, P. 01NTF14.

- [21] Haji A., Nasouri K., Shoushtari A. M., Kafrou A. Reversible Hydrogen Storage in Electrospun Composite Nanofibers. Proceedings of the “International Conference Nanomaterials: Applications and Properties”, Alushta, the Crimea (Sumy State University, Sumy, 2013), Sep. 16-21, 2013, P. 03NCNN05.
- [22] Fomkin A. A., Sinitsyn V. A. Hydrogen Adsorption on Model Nanoporous Carbon Adsorbents. *Protection of Metals*, 2008, **44**, P. 150–156. DOI:10.1134/S0033173208020070
- [23] Nguyen T. X., Bhatia S. K. Probing the Pore Wall Structure of Nanoporous Carbons Using Adsorption. *Langmuir*, 2004, **20**, P. 3532–3535. DOI: 10.1021/la036244p
- [24] Bhatia S. K. Density Functional Theory Analysis of the Influence of Pore Wall Heterogeneity on Adsorption in Carbons. *Langmuir*, 2002, **18**, P. 6845–6856. DOI: 10.1021/la0201927
- [25] Fenelonov B. V., Ustinov E. A., Yakovlev V. A., Barnakov Ch. N., Melgunov M. S. Carbon Adsorbents as Candidate Hydrogen Fuel Storage Media for Vehicular Applications. *Kinetics and Catalysis*, 2007, **48**, P. 599–602. DOI: 10.1134/S0023158407040192
- [26] Vanin A. A., Piotrowskaya E. M., Brodskaya E. N. Molecular and statistical modeling of adsorption of binary mixture of Lennard-Jones fluids in graphite mesopores square section. *Zhurnal fizicheskoi khimii*, 2004, **78**, P. 2064–2070.
- [27] Do D. D. *Adsorption analysis: equilibria and kinetics*. City: London Imperial College Press, 1998.
- [28] Zubkov V. V., Grinev I. V., Samsonov V. M. Single-particle potentials for adsorbents with spherical and cylindrical geometry. *Nanosystems: physics, chemistry, mathematics*, 2013, **3**, P. 52–68. <http://nanojournal.ifmo.ru/en/articles-2/volume3/3-3/physics/paper04/>
- [29] Matyushov D. V., Schmid R. Calculation of Lennard-Jones energies of molecular fluids. *J. Chem. Phys.*, 1996, **104**, P. 8627–8638. <http://dx.doi.org/10.1063/1.471551>
- [30] Yu Y.-X., Wu J. Structures of hard-sphere fluids from a modified fundamental-measure theory. *J. Chem. Phys.*, 2002, **117**, P. 10156–10164. <http://dx.doi.org/10.1063/1.1520530>
- [31] Weeks D. J., Chandler D., Andersen H. C. Role of Repulsive Forces in Determining the Equilibrium Structure of Simple Liquids. *J. Chem. Phys.*, 1971, **54**, P. 5237–5247. <http://dx.doi.org/10.1063/1.1674820>
- [32] Tang Y. Role of the Barker-Henderson diameter in thermodynamics. *J. Chem. Phys.*, 2002, **116**, P. 6694–6700. <http://dx.doi.org/10.1063/1.1461360>
- [33] Peng L., Morris J. R. Prediction of Hydrogen Adsorption Properties in Expanded Graphite Model and in Nanoporous Carbon. *J. Phys. Chem. C.*, 2010, **114**, P. 15522–15529. DOI: 10.1021/jp104595m
- [34] Gogotsi Yu., Dash R. K., Yushin G., Yildirim T., Laudisio G., Fischer J. E. Tailoring of Nanoscale Porosity in Carbide-Derived Carbons for Hydrogen Storage. *J. Am. Chem. Soc.*, 2005, **127**, P. 16006–16007. DOI: 10.1021/ja0550529
- [35] Tanaka H., Noguchi D., Yuzawa A., Kodaira T., Kanoh H., Kaneko K. Quantum Effects on Hydrogen Isotopes Adsorption in Nanopores. *J. Low Temp. Phys.*, 2009, **157**, P. 352–373. DOI 10.1007/s10909-009-9917-8
- [36] Henwood D., Carey D. J. Ab initio investigation of molecular hydrogen physisorption on graphene and carbon nanotubes. *Phys. Rev. B.*, 2007, **75**, P. 245413–245423. DOI: 10.1103/PhysRevB.75.245413
- [37] Ihm Y., Cooper V. R., Peng L., Morris J. R. The influence of dispersion interactions on the hydrogen adsorption properties of expanded graphite. *J. Phys.: Condens. Matter.*, 2012, **24**, P. 424205–424212. DOI:10.1088/0953-8984/24/42/424205
- [38] Cabria I., Lopez M. J., Alonso J. A. Hydrogen storage capacities of nanoporous carbon calculated by density functional and Moller-Plesset methods. *Phys. Rev. B.*, 2008, **78**, P. 075415–075424. DOI: 10.1103/PhysRevB.78.075415
- [39] Wang S. C., Senbetu L., Woo C. W. Superlattice of parahydrogen physisorbed on graphite surface. *J. Low Temp. Phys.*, 1980, **41**, P. 611–628. <http://link.springer.com/article/10.1007/BF00114368>
- [40] Patchkovskii S., Tse J. S., Yurchenko S. N., Zhechkov L., Heine T., Seifert G. Graphene nanostructures as tunable storage media for molecular hydrogen. *PNAS*, 2005, **102**, P. 10439–10444. [www.pnas.org/cgi/doi/10.1073/pnas.0501030102](http://www.pnas.org/cgi/doi/10.1073/pnas.0501030102)
- [41] Spyrou K., Gournis D., Rudolf P. Hydrogen Storage in Graphene-Based Materials: Efforts Towards Enhanced Hydrogen Adsorption. *ECS Journal of Solid State Science and Technology*, 2013, **2**, P. 3160–3169. DOI: 10.1149/2.018310jss
- [42] Dimitrakis G. K., Tyliaakis E., Froedakis G. E. Pillared Graphene: A New 3-D Network Nanostructure for Enhanced Hydrogen Storage. *Nano Letters*, 2008, **8**, P. 3166–3170. DOI: 10.1021/nl801417w

# Synthesis of silver nanoparticles in DMSO solutions of starch: a comparative investigation of native and soluble starches

N. E. Kochkina<sup>1</sup>, O. A. Skobeleva<sup>2</sup>, Yu. V. Khokhlova<sup>1</sup>

<sup>1</sup>G. A. Krestov Institute of Solution Chemistry of the Russian Academy of Sciences, Ivanovo, Russia

<sup>2</sup>Research Center for Nonlinear Wave Mechanics and Technology of the Russian Academy of Sciences, Moscow, Russia

nek@isc-ras.ru, hohjul@mail.ru

PACS 81.16.Be

DOI 10.17586/2220-8054-2015-6-3-405-411

Silver nanoparticles (AgNPs) were synthesized in solutions of native and soluble starches in DMSO for the first time. The starches acted as reducing and stabilizing agents simultaneously. The kinetics of the process and its activation energy were determined by using UV-vis spectroscopy. The DMSO solution of soluble starch was characterized by better reductive activity than the native starch solution. The morphology and dispersion characteristics of AgNPs sols were evaluated from transmission electron microscopy (TEM). Sols, including spherical particles with mean diameter ( $D_m$ ) 42.8 nm and metal rod-like particles, were obtained by using the native starch solution. Morphologically uniform sols of spherical AgNPs with  $D_m=37.2$  nm were formed in the soluble starch solution. On the basis of zeta potential measurements, it was shown that the stability of a AgNPs dispersion in the soluble starch solution was higher in comparison to the native starch solution.

**Keywords:** Silver nanoparicles synthesis, starch, DMSO, dispersion analysis, zeta potential.

*Received: 16 December 2014*

*Revised: 3 February 2015*

## 1. Introduction

AgNPs exhibit unique physical, chemical and biocidal properties that make them attractive for application in different engineering branches and medicine [1-6]. Chemical methods of AgNPs synthesis in aqueous solutions, using reductants such as sodium borohydride, quercetin, etc. are most frequently used [7-9]. Among the chemical techniques of AgNPs synthesis, it should be especially noted that ecologically safe biomineralization methods exist which are based on the use of saccharides (glucose, fructose, and so on) and polysaccharides (cellulose, cellulose ethers) as reducing agents [10-16]. Starch was also successfully utilized in the process of AgNPs generation as a reducing and stabilizing agent simultaneously [17-19]. The authors pointed out that starch solutions including AgNPs could have pharmaceutical and biomedical application, owing to combination of antibacterial properties of Ag and biocompatibility of starch. It should also be noted that all known methods of AgNPs synthesis with participation of starch were performed in an aqueous medium and based on the application of water soluble starch.

In the present study, we prepared silver nanoparticles by utilizing DMSO-based starch solutions as the reducing and stabilizing medium for the first time. DMSO is a solvent that is commonly used to achieve complete dissolution of starch. DMSO is inexpensive,

biodegradable and is categorized as a class 3 solvent, the lowest toxicity class to humans and the environment [20, 21]. DMSO can easily penetrate biological membranes and has anti-inflammatory, analgesic, cryoprotective, prophylactic and radioprotective properties, whereupon this solvent is widely used as component of medicines [22-24]. Thus, composite materials combining the properties of DMSO, AgNPs and starch could be used for the preparation of new medical drugs.

The objective of this paper is to evaluate the kinetics features of AgNPs synthesis realized in DMSO solutions of native corn and soluble starches. Also, the morphology, size, and stability of the resulting AgNPs were characterized.

## 2. Experimental section

### 2.1. Materials

Corn starch and soluble starch (starch indicator) were obtained from CHIMMED Company. The amylose content and reducing values of starches were determined according [25] and [26] respectively. The amylose content was 28 and 41 %, and reducing values were 0.03 and 0.63 respectively, for corn and soluble starches. AgNO<sub>3</sub> and DMSO were of analytical grade and were purchased from Sigma-Aldrich.

### 2.2. Synthesis of AgNPs

In this method, 0.025 g starch sample was placed in a 50 ml volumetric flask and dissolved in 20 ml DMSO under stirring over three days. Then, 0.02123 g of AgNO<sub>3</sub> was added to the starch solution, the mixture was stirred well and diluted with DMSO (total volume 50 ml). The final concentration of the solution was 0.5 g/l and  $2.5 \times 10^{-3}$ M for the starch and the salt, respectively. The sample was maintained at specific temperatures (45, 50, 55 or 65°C) for two hours.

### 2.3. UV-visible spectral analysis

The absorption spectra of DMSO starch solutions (native or soluble) and AgNO<sub>3</sub> mixtures were recorded on an Agilent 8453 UV-Vis spectrophotometer, from 300 to 600 nm. A solution containing 0.5 g/l starch in DMSO was used as the blank.

The rate ( $\gamma$ ) of AgNPs formation was estimated from spectrophotometric data according next expression:  $\gamma = A_\tau/A_0$ , where  $A_\tau$ ,  $A_0$  – absorbance of the sample in the resonance band maximum at time  $\tau$  and 0 min respectively.

### 2.4. Transmission electron microscopy

The morphology and dispersion of AgNPs prepared were investigated by transmission electron microscopy (EMV-100L instrument, operating voltage 50 kV) on the next day after synthesis. Before sample preparation for TEM analysis, the complement of the reduction of Ag ions to AgNPs was tested. For this purpose, NaCl was added in DMSO starch solutions containing AgNPs. There was no white precipitate and/ or turbidity of AgCl in the samples, thereby giving evidence for the complete reduction of Ag<sup>+</sup> ions to Ag<sup>0</sup>. Samples were deposited onto carbon-filmed grids, air-dried and examined under the microscope. Digital microscope photos were taken and analyzed using the software Matlab 7.0.

### 2.5. Zeta-potential analysis

The zeta potential of AgNPs samples was evaluated by Zetasizer Nano ZS analyzer (Malvern Instruments Ltd). The samples were equilibrated before measurements at 25°C for 300 seconds. Tests of each AgNPs sols under study were repeated 5 times.

### 3. Results and discussion

The formation of AgNPs in solution is qualitatively manifested as a change of the sample coloration from colorless to yellow or brown, because of the interaction between metal particles' surface electrons with light (plasmon resonance). The absorption spectrum of AgNPs sol have characteristic surface plasmon band (SPB) and this allows the identification of cluster formation from metal atoms spectrophotometrically.

At room temperature 23°C, there was no formation of Ag particles in all solution systems under study, which was due to the extremely low rate of Ag ion reduction under these conditions. Spectrophotometric registration of the metallic particle synthesis was possible at temperatures above 45°C. Fig. 1 illustrates the change in the UV/Vis spectra of the DMSO/starch and AgNO<sub>3</sub> mixtures observed at 65°C over different periods of time after sample preparation. It can be seen that the SPB with a maximum at 418 nm appeared in the spectra of the samples at 20 minutes after synthesis initiation. The spectral patterns were qualitatively the same for the both starch solutions. Variation of the reaction temperature over the 45-65°C range was not accompanied by any shift of the surface plasmon band (SPB). Observed data were in good agreement with the results of studies of the UV/Vis spectra of the water starch solutions containing AgNPs [16-18]. Therefore, it can be concluded that the spectral changes of the systems under study here were related to the synthesis of AgNPs from the Ag ions with participation of DMSO/starch solutions.

It is known, that saccharides may act as a reducing agent through its aldehyde group, which is able to be oxidized [11, 12, 27]. In case of starch, a polysaccharide, the reducing power is also believed to be the action of aldehyde terminals mainly [18]. Soluble starch, containing more reductive aldehyde termini than the native one, likely provides higher rate of AgNPs synthesis. To verify this assumption, process kinetics were estimated from spectrophotometric data. As shown in Fig. 2, the temperature dependence of the reaction rate ( $\gamma$ ) in both starch solutions was approximated by a straight line in the  $\ln \gamma$  vs.  $1/T$  coordinates and described by the Arrhenius equation [28]. The slopes of these lines gave activation energies of 64.9 and 54.2 kJ/mol for the native and soluble starches respectively. It should also be noted that the solvent DMSO can also participate in the reduction of the silver cations [29]. Meanwhile, input of DMSO in the process rate evidently was equal for the both systems. So, these data demonstrate higher synthesis rate of AgNPs in the soluble starch system.

An important characteristic of AgNPs which affects to a large extent their application properties is the size of the particles. In order to investigate the morphology and size of AgNPs under study, transmission electron microscopy (TEM) was applied. The results for the samples generated at 65°C are presented on Fig. 3. The soluble starch solution appears to promote the formation of spherical AgNPs with a mean diameter ( $D_m$ ) of 37.2 nm and a standard deviation ( $\sigma$ ) of 10.7 nm. Application of native starch solution leads to the formation of AgNPs with two different geometric shapes, namely spherical particles, characterized by  $D_m = 42.8$  nm and  $\sigma = 19.8$  nm and rodlike particles which had diameter ranging from 62 to 104 nm and length ranging from 375 to 1917 nm.

These data demonstrate the fact that higher nanoparticles sizes and a polydispersity of metal sols were produced in the native starch medium. It can be supposed that one of the reasons that this phenomenon arises is the various macromolecular compositions of these starch samples. The main components of starch are two different homopolymers of d-glucose: the mainly linear amylose and the heavily branched amylopectin. As it is known that only sufficiently long linear macromolecules can form protective shields around synthesized

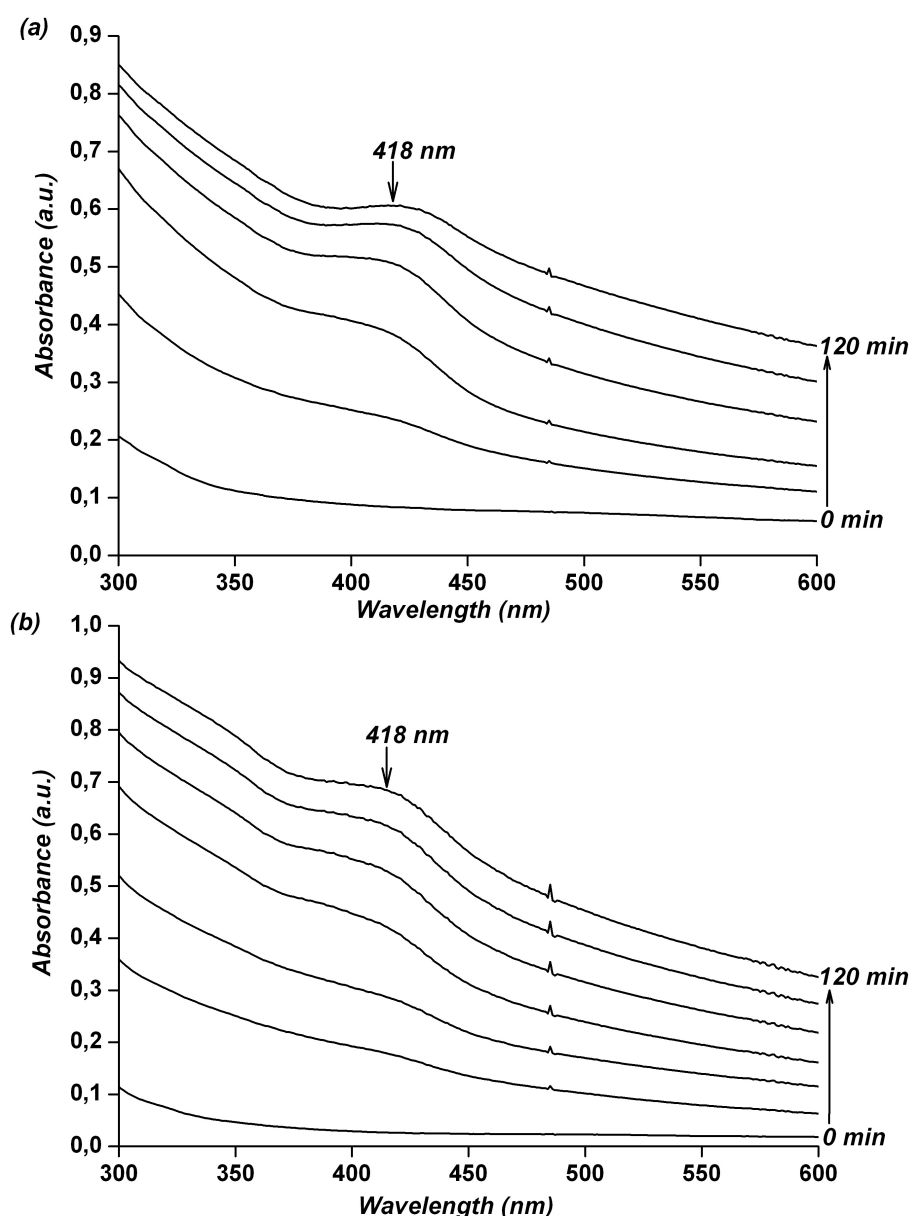


FIG. 1. UV-vis absorption spectra of the mixtures containing native (a) or soluble (b) starch solution in DMSO and  $\text{AgNO}_3$  within different time intervals after mixture's preparation. Reaction conditions:  $[\text{starch}] = 0.5 \text{ g/l}$ ,  $[\text{AgNO}_3] = 2.5 \times 10^{-3} \text{ M/l}$ , temperature =  $65^\circ\text{C}$

nanoparticles [30]. Amylopectin branched macromolecules with short side chains are not able to protect growing metal particles effectively. Thus, amylose chains are much more suitable for stabilizing the formation process than amylopectin. Therefore, soluble starch containing more amylose chains than the native starch provides formation of more morphologically uniform Ag nanoparticles with a narrower size distribution.

An essential factor for practical usage of colloidal systems is their stability, which can be evaluated by the measurement of the zeta potential of the dispersed particles. It is believed that systems including nanoparticles with zeta potential values greater than +25

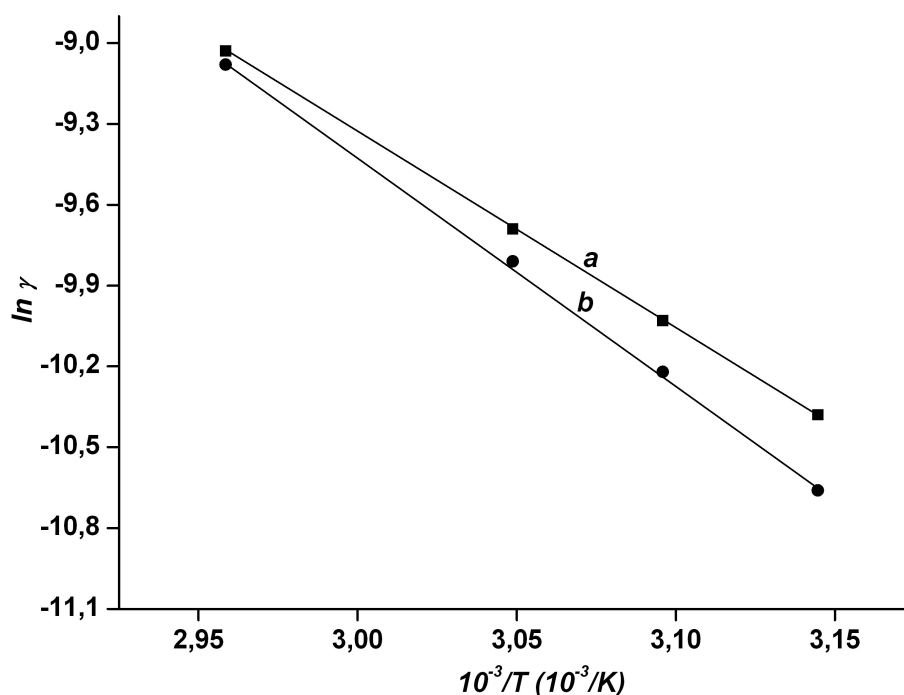


FIG. 2. Temperature dependence of the rate of AgNPs formation in the native (a) and soluble (b) starch solutions

mV or less than  $-25$  mV typically have high degrees of stability. In our study, it was revealed that the zeta potentials of AgNPs synthesized in solutions of soluble and native starches were  $+26 \pm 2$  mV and  $+12 \pm 3$  mV, respectively. The temperature of synthesis did not affect the values of AgNPs zeta potential. So these results demonstrated higher stability for AgNPs produced from DMSO solutions of soluble starch.

#### 4. Conclusions

DMSO solutions of native and soluble starches were utilized for AgNPs synthesis. The kinetic features of the AgNPs formation in these two starch solutions were monitored by UV-vis spectroscopy. The activation energy for the reduction of Ag ions was less in case of soluble starch solution. According to the TEM micrograph measurements, rodlike and spherical particles were synthesized in the native starch solution. Soluble starch provided formation of Ag nanospheres which were characterized by smaller sizes and a narrower size distribution. The stability of AgNPs sol was better in case of those fabricated using the soluble starch solution.

#### Acknowledgments

The authors thank the center for joint use of scientific equipment "The upper Volga region center of physico-chemical research" for the spectrophotometric analysis and zeta potential measurements.

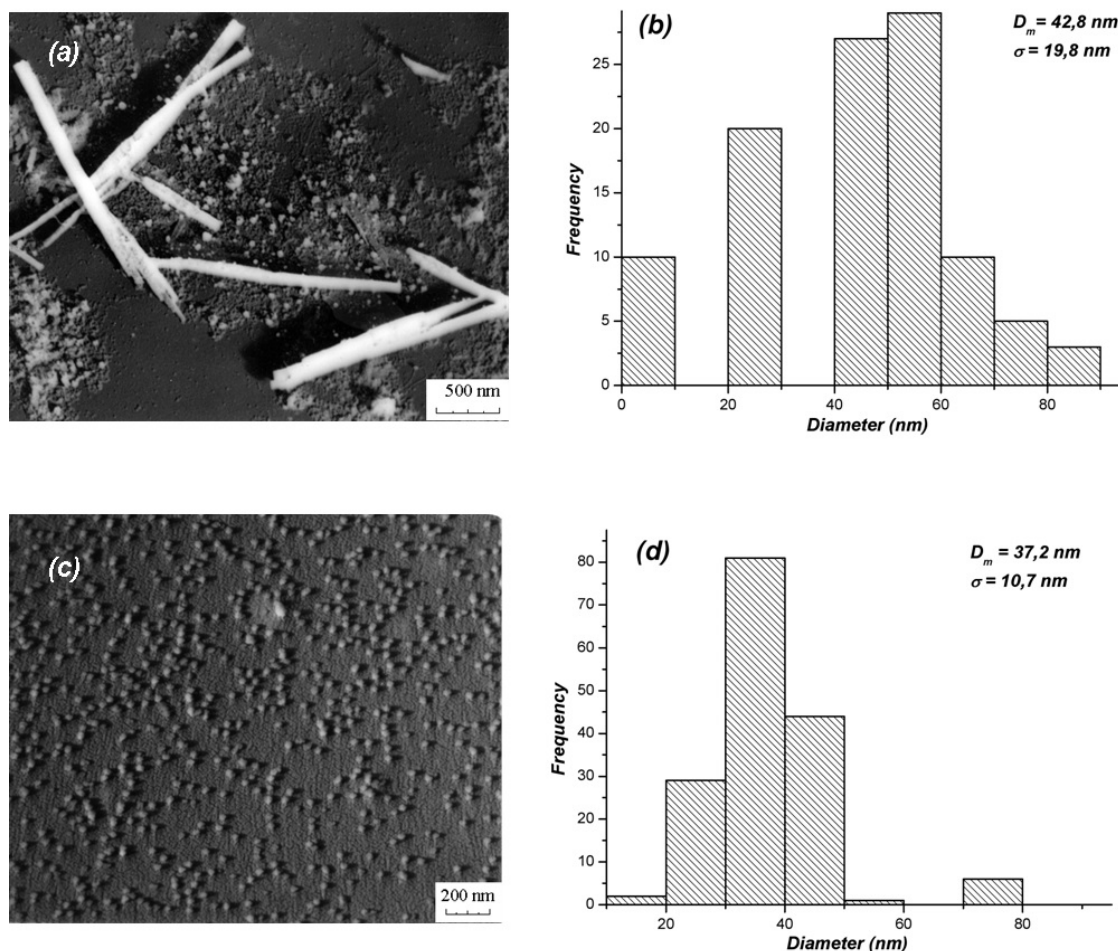


FIG. 3. TEM images (a, c) and particle size distribution histograms (b, d) of AgNPs prepared in the native (a, b) and soluble (c, d) starch solutions, synthesis temperature = 65°C

## References

- [1] Henglein A. Small-particle research: physicochemical properties of extremely small colloidal metal and semiconductor particles. *Chem. Rev.*, 1989, **89**(8), P. 1861–1873.
- [2] Welles A.E. (ed) *Silver nanoparticles: properties, characterization and applications*. Nova Science Publishers, StateplaceNew York, 2010, 397 p.
- [3] Krutyakov Yu.A., Kudrinskiy A.A., Olenin A.Yu., Lisichkin G.V. Synthesis and properties of silver nanoparticles: advances and prospects. *Russ. Chem. Rev.*, 2008, **77**(3), P. 233–257.
- [4] Silver S., Phung T., Silver G. Silver as biocides in burn and wound dressings and bacterial resistance to silver compounds. *J. Ind. Microbiol. Biotechnol.*, 2006, **33**(7), P. 627–634.
- [5] Sarycheva A.S., Parshina E.Yu., Baydjumanov A.A., Semenova A.A., Goodilin E.A., Maximov G.V. Influence of silver hydrosols on structural integrity of erythrocytes. *Nanosystems: Physics, Chemistry, Mathematics*, 2013, **4**(1), P. 66–71.
- [6] Moushummy N., Alameh K., Rajendran V., Yong Tak Lee. Silver-nanoparticle-based etch mask control for subwavelength structure development. *Nanosystems: Physics, Chemistry, Mathematics*, 2013, **4**(3), P. 387–394.
- [7] Caswell K.K., Bender C.B., Murphy C.J. Seedless, surfactantless wet chemical synthesis of silver nanowires. *Nano Letters*, 2003, **3**(5), P. 667–669.
- [8] Bois L., Chassagneux F., Battie Y., Bessueille F. Chemical growth and photochromism of silver nanoparticles into a mesoporous titania template. *Langmuir*, 2010, **26**(2), P. 1199–1206.

- [9] Egorova E.M., Revina A.A. Synthesis of metallic nanoparticles in reverse micelles in the presence of quercetin. *Colloids Surf. A*, 2000, **168**(1), P. 87–96.
- [10] Venediktov E.A., Ganiev R.F., Padokhin V.A. Mechanism of formation of silver nanoparticle ensembles in an aqueous solution of glucose. *Dokl. Chem.*, 2012, **442**(5), P. 34–36.
- [11] Hebeish A.A., El-Rafie M.H., Abdel-Mohdy F., Abdel-Halim E.A., et al. Carboxymethyl cellulose for green synthesis and stabilization of silver nanoparticles. *Carbohydr. Polym.*, 2010, **82**(3), P. 933–941.
- [12] Abdel-Halima E.S., Salem S.S. Utilization of hydroxypropyl cellulose for green and efficient synthesis of silver nanoparticles. *Carbohydr. Polym.*, 2011, **86**(4), P. 1615–1622.
- [13] Vysotsky V.V., Uryupina O.Ya., Roldughin V.I., Plachev Yu.A. Formation of silver nanoparticles in aqueous carboxymethyl cellulose solutions and the evolution of their sizes. *Colloid J.*, 2009, **71**(2), P. 156–162.
- [14] Raveendran P., Fu J., Wallen S. Completely “green” synthesis and stabilization of metal nanoparticles. *J. Am. Chem. Soc.*, 2003, **125**(46), P. 13940–13941.
- [15] Gao X., Wei L., Yan H., Xu B. Green synthesis and characteristic of core-shell structure silver/starch nanoparticles. *Materials Letters*, 2011, **65**(19-20), P. 2963–2965.
- [16] Vasileva P., Donkova B., SnplaceKaradjova SnI., Dushkin C. Synthesis of starch-stabilized silver nanoparticles and their application as a surface plasmon resonance-based sensor of hydrogen peroxide. *Colloid Surfaces A*, 2011, **382**(1-3), P. 203–210.
- [17] Ghaseminezhada S.M., Hamedib S., Shojaosadati placecountry-regionS.A. Green synthesis of silver nanoparticles by a novel method: Comparative study of their properties. *Carbohydr. Polym.*, 2012, **89**(2), P. 467–472.
- [18] Vigneshwaran N., Nachane R.P., Balasubramanya R.H., Varadarajan P.V. A novel one-pot ‘green’ synthesis of stable silver nanoparticles using soluble starch. *Carbohydr. Res.*, 2006, **341**(12), 2012–2008.
- [19] Venediktov E.A., Ganiev R.F., Padokhin V.A. Preparation and stabilization of silver nanoparticles in liquid water soluble starch matrix. *Dokl. Chem.*, 2012, **431**(1), P. 34–36.
- [20] ICH Topic Q3C (R4) – Impurities: Guideline for Residual Solvents. European Medicines Agency. Step 5, CityplaceLondon, 2011, 26 p.
- [21] Vignes R. Dimethyl sulfoxide (DMSO) - A “New” clean, unique, superior solvent. American chemical society. Annual meeting. Washington, August 20-24, 2000.
- [22] Santos N.C., Figueira-Coelho J., Martins-Silva J., Saldanha C. Multidisciplinary utilization of dimethyl sulfoxide: pharmacological, cellular, and molecular aspects. *Biochem Pharmacol.*, 2003. **65**(7), P. 1035–1041.
- [23] Jacob S.W., de la Torre J.C. la Torre J.C. Pharmacology of dimethyl sulfoxide in cardiac and CNS damage. *Pharmacological Reports*, 2009, **61**(2), P. 225–235.
- [24] Young V.L., Boswell C.B., Centeno R.F., Watson M.E. DMSO: Applications in plastic surgery. *Aesthet. Plast. Surg.*, 2005, **25**(2), P. 201–209.
- [25] Hoover R., Ratnayake W.S. Determination of total amylose content of starch. Current protocols in food analytical chemistry, 2001, E. 2.3.
- [26] Whistler R.L., Wolfrom M.L. (eds.) *Methods in Carbohydrate Chemistry*, Vol. 1, Academic Press, StateplaceNew York, 1962, P. 380–394.
- [27] Uryupina O.Ya., Vysotskii V.V., Matveev V.V., Gusel’nikova A.V., et al. Production of gold nanoparticles in aqueous solutions of cellulose derivatives. *Colloid J.*, 2011, **73**(4), P. 551–556.
- [28] Moelwyn Hughes E.A. *The chemical statics and kinetics of solutions*. Academic Press, New York, 530 pp.
- [29] Kuznetsova N.P., Ermakova T.G., Pozdnyakov A.S., Emel’yanov A.I., Prozorova G.F. Synthesis and characterization of silver polymer nanocomposites of 1-vinyl-1,2,4-triazole with acrylonitrile. *Russ. Chem. Bull.*, 2013, **62**(11), P. 2509–2513.
- [30] Papisov, I.M., Litmanovich A.A. On recognition phenomena in polymer–minute particle interactions and pseudo-matrix processes. *Colloids Surf. A.*, 1999, **151**(3), P. 399–408.

# Morphological memory of polymeric bodies

I. V. Melikhov<sup>1</sup>, O. V. Alekseeva<sup>2</sup>, V. N. Rudin<sup>1</sup>, E. D. Kozlovskaya<sup>1</sup>, A. V. Noskov<sup>2</sup>

<sup>1</sup>M. V. Lomonosov Moscow State University, Moscow, Russia

<sup>2</sup>G. A. Krestov Institute of Solution Chemistry RAS, Ivanovo, Russia

melikhov@radio.chem.msu.ru, ova@isc-ras.ru

PACS 81.05.Lg

DOI 10.17586/2220-8054-2015-6-3-412-423

The model of microrelief formation on the surface of polymers was formulated, describing the connection between the microrelief structural elements' distribution function on the states with the kinetics of macromolecule formation, aggregation and aggregates' integration into the polymer body. Methods for calculating the kinetics of these processes, using experimental data on the microrelief properties, were developed. The developed methods have proven effective in the study of microrelief on films obtained by the evaporation of *o*-xylene and toluene solutions of polystyrene, as well as polystyrene granules' microrelief. The hierarchical structures were found on the surface of these bodies, from which it was possible to "extract" information about the polymerization and aggregation of the polystyrene macromolecules. The obtained data are summarized in the form of a morphological memory representation of the polymer bodies, consisting in the long-term preservation of nonequilibrium structures available for study without destroying the body, as well as the possibility to use the results of the study to describe the kinetics of these structures' formation.

**Keywords:** polystyrene, microrelief, nanoparticles, subnanoparticles.

*Received: 9 April 2015*

## 1. Introduction

According to published results, electron and atomic force microscopy have been used to study polymeric bodies, many of which have surfaces with microrelief on their macromolecular structures. In [1], a microrelief on the surface of a film, formed by the evaporation of an *o*-xylene solution of polystyrene, was described. The microrelief of the film depended on the composition of the evaporating solution, and from this microrelief, the composition of the solution could be determined. In [2], this fact was interpreted as an indication that the film possessed a morphological memory that conferred the ability to gain the information about the conditions of its formation and the ability to use this information with the help of the data in the morphology of the microrelief. Such an interpretation requires detailed information about what was happening in the monomeric solution when the polymerization initiator was introduced. It is known that in such a solution, the nucleation and growth of the polymeric macromolecules occurs, which form the aggregates followed by their assembly into a polymeric body, and the macromolecules on the body's surface form the microrelief [3-6]. During the transition to the body structure, the condition of each macromolecule can change significantly, depending upon the relaxation time of its state [7,8]. As a result, if the body is formed quickly and the complete relaxation of the macromolecule state is not provided, the structure of the microrelief appears dependent on the kinetics of the body formation. All of this should be taken into account when considering the processes that lead to morphological memory.

## 2. Model of the body microrelief formation

In this model, body formation starts when the polymerization initiator is introduced into the monomeric solution ( $t=0$ ) and ends at the moment when the solvent is completely removed from the system by filtration or evaporation ( $t = t_F$ ). In the range of  $t = 0 \div t_F$  the solvent, the dissolved monomers and macromolecules ( $j=1$ ), macromolecular clusters ( $j=2$ ), and aggregates of clusters ( $j=3$ ) which comprise the system are uniformly distributed over the volume of the system. The state of each of these particles is characterized by parameters  $\vec{X} = \{v, n, \vec{P}\}$ , where  $v$  is the volume,  $n$  is the number of monomers included in the particle macromolecules;  $\vec{P} = \{P_1 \dots P_i \dots P_m\}$ ;  $P_i$  is one of the characteristics of the shape, composition and structure of the particle.

The states of the system are characterized by the parameters  $\vec{y} = \{V, C_A, C_B, N_1, N_2, N_3, W_V, T\}$ , where  $V$  is its volume,  $C_A$  and  $C_B$  are the concentrations of the monomer and initiator molecules in the solution;  $N_1, N_2, N_3$  are the quantities of the macromolecules, their clusters and aggregates in the system;  $W_V$  is the rate of the system volume change;  $T$  is the temperature. Wherein  $N_j = \sum_v N_j(v, t)$ , if the number of  $j^{\text{th}}$  type particles with volume  $v$  is equal to  $N_j(v, t)$ . Alternatively, in the continuum approximation,  $N_j = \int_v \phi_j(v, t) dv$  if the particles distribution function on volume is  $\phi_j(v, t)$ .

Distribution function  $\phi_j(v, t)$  is influenced by the events that can both increase and decrease the volume of each particle [9-12]. Therefore:

$$\frac{\partial \phi_j(v, t)}{\partial t} = \Omega_{jv} - \beta_{jv} \phi_j(v, t), \quad (1)$$

where  $\Omega_{jv}$  is the frequency function characterizing the frequency of events leading to the appearance of the particles of  $j^{\text{th}}$  type of size  $v$  in the system, that is, the frequency of particle transition in the state  $(j, v)$ ;  $\beta_{jv}$  is the probability of the exit from the state  $(j, v)$  per unit time.

The solution of the equation (1) with appropriate boundary conditions establishes a relationship between the frequency functions  $\Omega_{jv}$ ,  $\beta_{jv}$ , and the total volume  $V_j$  of the particles of each  $j^{\text{th}}$  type:

$$V_j = \int_{v_{nj}} v \phi_j(v, t) dv, \quad (2)$$

where  $v_{nj}$  is the minimum volume of the particle, to which the mentioned frequency functions (volume of the  $j^{\text{th}}$  type nucleus) can be ascribed.

Additionally, the condition of the conservation of the number of atoms introduced into the system is fulfilled:

$$C_{A0} V_0 = \left( V - \sum_j V_j \right) C_A + \sum_j v_{0j}^{-1} V_j, \quad (3)$$

where  $C_{A0}$  and  $V_0$  are the initial monomer concentration and the volume of the system;  $v_{0j}$  is the average volume per one monomer in the amount of the  $j^{\text{th}}$  type particles.

The volume of the system, decreased at rate  $W_v$ , due to solvent removal, is equal to  $V = V_0(1 - \Phi)$ , so that the condition (3) can be written in the form:

$$C_{A0} = \left( 1 - \sum_j \varepsilon_j - \Phi \right) C_A + \sum_j v_{0j}^{-1} \varepsilon_j, \quad (4)$$

where  $\varepsilon_j = V_j/V_0$ ;  $\Phi = \int_0^t (W_v/V_0)dt$ .

According to the equations (3) and (4), at  $t = t_F$ , when  $C_A = 0$  and  $\Phi = \int_0^{t_F} (W_v/V_0)dt = \frac{\bar{W}_v}{V_0}t_F$ , we have:

$$V_0 = (1 - P_F - v_{0S}C_{A0}) = \bar{W}_v t_F, \quad (5)$$

where  $P_F = V_P/V_0$  is the parameters of the body porosity at the volume of the space between the particles (pores) equal to  $V_P$ ;  $v_{0S}$  is the average volume per one monomer built into the body of macromolecule;  $\bar{W}_v$  is the average speed  $W_v$  in the interval  $(0 | t | t_F)$  dependent on  $\vec{y}$ .

Equation (5) defines the parameters  $\vec{y}$  of the system state, at which the time  $t_F$  remains within the range:

$$(\beta_{1v}^{-1} | t_F | \beta_{3v}^{-1}), \quad (6)$$

where  $\beta_{jv}^{-1}$  is the value that characterizes the time, suitable for the particle escape from the state  $(j, v)$ .

Relations (1)–(5) consider the possibility of implementing multiple routes of body formation, dependent on  $\vec{y}$ . The simplest of these is the route in which  $\beta_{1v} \gg \beta_{2v}, \beta_{3v}$ ,  $t_F \sim 1/\beta_{1v}$ , and the process comes down to the formation of the polymer molecules with the volume  $\varepsilon_1 = \varepsilon_1(t)$  increasing up to  $\varepsilon_1(t_F) = C_{A0}v_{01}$  at the time of their association in the body of randomly arranged macromolecules. In describing the simplest route, detailing the functions  $\Omega_{jv}$  and  $\beta_{jv}$  applied to the chained macromolecules as described in [13,14], the equation (1) can be reduced to the form:

$$\frac{\partial \phi_1(v, t)}{\partial t} = \frac{\partial^2 (D_{1v} \phi_{1v})}{\partial v^2} - \frac{\partial}{\partial v} (G_{1v} \phi_{1v}), \quad (7)$$

where  $D_{1v} = \frac{1}{2}(\alpha_{1v}C_A a_v^2 + \beta_{1v}b_v^2)$ ,  $G_{1v} = \alpha_{1v}C_A a_v - \beta_{1v}b_v$ ,  $\phi_{jv} = \phi_j(v, t)$ ,  $\alpha_{1v}$  and  $\beta_{1v}$  are frequency functions, characterizing the frequency of events leading to an increase and decrease in volume of the particle in the state  $(j = 1, v)$ ; and are the increase and decrease of  $v$  at a single event.

Due to the uniformity of the system, relations (1)–(7) characterize any of its areas, including the near-surface areas, where the microrelief of the body is formed. The parameters for the states of the surface and internal parts of the system may vary [15], but they develop according to the same rules. Therefore, we can assume that the above model describes the kinetics of microrelief formation on a mesokinetic level of detailing, that involves consideration of the distribution functions of the structural elements' microrelief on their volume.

### 3. Model of the microrelief change with body usage

When using the body its microrelief changes as a result of inevitable chemical, radiation and mechanical influence by the environment in which the body is moved. These influences can be imagined as a set of events, each of which leading to a specific increase or decrease in the volume of the particles of the near-surface areas of the body. As a result of thermal and chemical influences (e.g. collisions of the body with the molecules of the medium) or mechanical influences (e.g. contact with the bodies in the medium), the distribution function of the near-surface area particles is altered in accordance with equation (1). This equation, with reference to the microrelief, can be provided in the form:

$$-\frac{\partial \phi_j(v, \tau)}{\partial \tau} = \frac{\partial}{\partial v} (a_j \omega_j \phi_{jv}) + \nu_j \phi_{jv}, \quad (8)$$

where  $\phi_j(v, \tau) = \phi_{jv}$  is the distribution function of the particles in the near-surface area in the state  $(j, v)$  at the time  $\tau > t_F$  for the usage of the body;  $\omega_j$  is the frequency of events leading to the change in volume  $v$ ;  $a_j$  is the average volume change at a single event;  $\nu_j$  is the frequency of acts of escape of  $j^{\text{th}}$  type particles from the near-surface areas to the medium.

Also, if the transfer of the body from the medium where it was obtained to the medium of usage takes place without violating its integrity, it is reasonable to put the solution for equation (8) in the form:

$$\varphi_j(v, \tau) = \varphi_j(v, t_F) \exp\left(-\frac{\nu_j \tau}{\omega_j \tau_{Ri}} F_{ji}\right), \quad (9)$$

where  $\tau_{Ri}$  is the characteristic response time of the microrelief on this  $i$  impact;  $F_{ji} = F_{ji}(v, \tau)$  is the function that is determined by the solution of the equation (8) at known frequency functions and.

Equation (9) indicates the method of accounting for the influence of the medium of usage on the microrelief of the body. When frequency functions are defined experimentally, formula (9) enables one to calculate the distribution before the exposure from the data on the distribution after the exposure. With unknown frequency functions, it is possible to determine them by comparing the experimental data on the functions before and after exposure, followed by prediction of the behavior of the body with prolonged use [4,16]. It is possible that the frequency functions may be useful in solving practical problems.

#### 4. Characterization of the morphological memory

The complete characteristic of the body surface is the set of the state parameters of all the macromolecules that make up its microrelief. These state parameters are included in the distribution functions  $\{\phi_j(\vec{X}, \tau)\}$ , each of which can be represented as

$$\phi_j(\vec{X}, \tau) = \phi_j(v, \tau) f_j(\vec{P}, \tau)_v, \quad (10)$$

where  $f_j(\vec{P}, \tau)_v$  is the distribution density of the particle macromolecules in the state  $(j, v)$  on the properties  $\vec{P}$ .

Given this, it is advisable to carry out a characterization of microrelief by a consistent definition of functions  $\phi_j(v, \tau)$  and  $f_j(\vec{P}, \tau)_v$  by measuring the volume of all the particles of microrelief, followed by the study of the bodies that have similar volume. And if the determination of the particle volumes is considered as the beginning of the study of the microrelief morphology, the value

$$\phi(v, \tau) = \sum_j \phi_j(v, \tau) \quad (11)$$

can be taken as the basic morphological characteristics of the microrelief.

According to equations (8) and (9), using experimental data on the distributions  $\phi_j(v, t)$  at the known frequency functions  $\omega_j(\vec{y})$  and  $\nu_j(\vec{y})$ , the distributions  $\phi_j(v, t_F)$  can be calculated. According to the equations (1)–(7), in the known frequency functions  $\Omega_{jv}(\vec{y})$  and  $\beta_{jv}(\vec{y})$  one can go from  $\phi_j(v, t_F)$  to the distributions  $\phi_j(v, t)$  at any time  $t < t_F$ . The given frequency function can be determined from the special experiments by comparison of the experimental data with functions  $\phi_j(v, t)$ , measured at different moments of time. After these experiments, it is possible for a computer to use the experimental data on the morphology of the body's surface to calculate the change in the distribution of its macromolecules

on states in the formation process and new uses will arise. The possibility of creating such methods can be regarded as a manifestation of morphological memory of the body consisting in the long-term preservation of its nonequilibrium macromolecular structures, with the opportunity to study these structures without having to destroy the body. The formation of such structures can be considered as an accumulation of body information about the processes that lead to these structures' formation. The experimental determination of the functions  $\phi_j(v, \tau)$  can be considered as an extraction of information from the morphological memory with data capacity  $\varphi(v, \tau)$ .

## 5. Approaches to the use of morphological memory

Apparently, morphological memory can be used to study the fast polymerization, the effects of short intense influences on the polymeric body and their slow degradation, i.e. where it is difficult to measure the speed of processes *in situ*. However, to realize this possibility, it is necessary to experimentally determine the frequency functions, participating in the equations (1), (7) and (8). Therefore, it is necessary to study the elementary processes that determine the function  $\phi(v, \tau)$  on model bodies and to make sure that they leave a significant imprint on the microrelief. The obtained data on the frequency functions, supplemented by the boundary conditions of the solution of these equations, will lead to the formulation of a number of the boundary value problems on the morphological memory of the model bodies. Solution of these boundary value problems over a wide range of  $\vec{y}$  will allow one to identify the main relations of the microrelief with the speeds of the elementary processes as well as to describe the response of the function  $\phi(v, \tau)$  to the change of  $\vec{y}$  and to develop algorithms for calculating the parameters of elementary processes from the experimental data about the function  $\phi(v, \tau)$  at different  $\vec{y}$ . Currently, methods for solving such problems and the models of elementary processes are developed, and experimental data, allowing one to judge the main features of the microrelief and to make a phenomenological model of its formation, is accumulated [1-20]. For the quantitative study of the relation between the parameters of microrelief and the elementary processes, it is advisable to start with the simplest system, one in which the initiator molecules are rapidly converted into the nuclei of chain macromolecules, their number in the system reaching the value  $N_1 = C_B V_0$ . The nuclei become larger, merging individual monomer molecules, while the elimination of the molecules joined by chains is unlikely ( $\alpha_{1v} C_A \gg \beta_{1v}$ ) and the merging frequency is independent of the size of the macromolecule [ $\alpha_{1v} \neq \alpha_{1v}(v)$ ], due to the constant number of merge sites. At the same time,  $\Omega_{1v} \gg \Omega_{2v}, \Omega_{3v}$ , so that the aggregation during the time of the complete solvent removal  $t_F$  does not occur, and equation (7) is applicable, its solution at the boundary conditions  $\phi(v, t) = 0$  and  $(G_{1v}\phi_{1v} - D_{1v}\frac{\partial\phi_{1v}}{\partial v})_{v \rightarrow v_{n1}} = N_1\delta(t)$  has the form:

$$\phi_1(v, \tau) = N_1 \left[ (\pi A p)^{-1/2} \exp(-X_-^2) - \frac{1}{2p} \exp\left(\frac{v - v_{n1}}{p}\right) \operatorname{erfc}(X_+) \right]. \quad (12)$$

Here,  $\delta(t)$  is the Dirac delta function;  $A = \int_0^t G_{1v} dt$ ;  $p = D_{1v}/G_{1v}$ ;  $X_{\pm} = \frac{v - v_{n1} \pm A}{(4\pi A)^{1/2}}$ ;  $v_{n1}$  is the volume of the macromolecule nucleus;  $\operatorname{erfc}(X_+) = \frac{2}{\sqrt{\pi}} \int_{X_+}^{\infty} e^{-X^2} dX$ .

Distribution (12) corresponds to the following molecular weight distribution of the macromolecules in a given system

$$\Psi_1(m, t) \equiv \frac{1}{N_1} \frac{\partial N_{1m}}{\partial m} = B_1 \exp[-\gamma(M - A_1)^2] - B_2 \exp(Mv_0/p), \quad (13)$$

where  $m = (m_0/v_0)v$  is the mass of the macromolecule with the volume  $v$  if the mass of one link of the chain is  $m_0$ ;  $N_{1m}$  is the number of macromolecules with the mass less than  $m$ ;  $M = (m - m_n)/m_0$ ;  $m_n$  is the mass of the nucleus of the macromolecule;  $A_1 = A/v_0$ ;  $B_1 = \frac{v_0}{m_0}/(\pi Ap)^{1/2}$ ;  $B_2 = \frac{v_0}{2m_0p} \text{erf} [\gamma^{1/2}(M + A)]$ ;  $\gamma = v_0/(4\pi A_1)$ .

Equations (12) and (13) were obtained according to the kinetic models which are used in polymerization description [10,12,18-20], but using the function  $\varphi_1(v, t)$ . Similar relationships can be obtained to describe the aggregates, therefore one should detail the functions  $\Omega_{jv}$  and  $\beta_{jV}$  in accordance with the state parameters  $\vec{X}$  of these particles. The sequence of work on creation and use of the morphological memory is shown in Fig. 1.

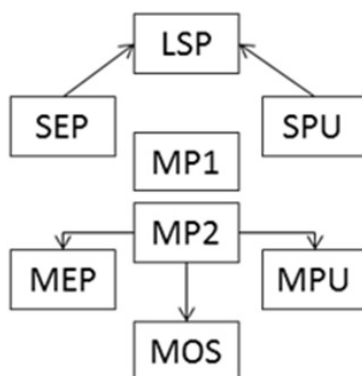


FIG. 1. Scheme of the work associated with the morphological memory. The complexes to resolve the following problems are shown. SEP – the study of elementary processes. LSP – laboratory synthesis of the product. SPU – study of the changes in the product properties when it is used. MM1 – the accumulation of the information about the regularities of the product obtaining and use in the morphological memory. MM2 – development of models of product creation. MEP – models of the elementary processes. MOS – the model of optimal production synthesis. MPU – the model of the product behavior when it is used

## 6. Morphological memory of the polystyrene bodies

In Fig. 2, an electron microscopic image of the microrelief one of the polystyrene granules purchased from “Aldrich” is shown. Macromolecules of these granules were once formed in the devices of the company, and then became larger and aggregated in the body, which remained for a long time in the environment of use, and was then transferred to a microscope, where the surface of the body has taken the shape shown in Fig. 2. The same figure shows the image of the film obtained by dissolving these granules in *o*-xylene, followed by solvent evaporation, resulting in the formation of a film [1,2]. Other films and granules, randomly taken from commercial products, had a similar appearance.

All the examined bodies had the hierarchical microrelief available for the morphological characterization, wherein this microrelief was similar to that presented in the publications on polystyrene (e.g., in [21-23]) and other polymers (e.g., [24-26]).

The primary subnanoparticles of the size of 1–2 nm ( $j=1$ ), integrated in the chains and ring-shaped clusters, nanoparticles in the form of aggregates of these clusters ( $j=2$ ) and microparticles composed of these aggregates ( $j=3$ ) were the structural elements of the microrelief.

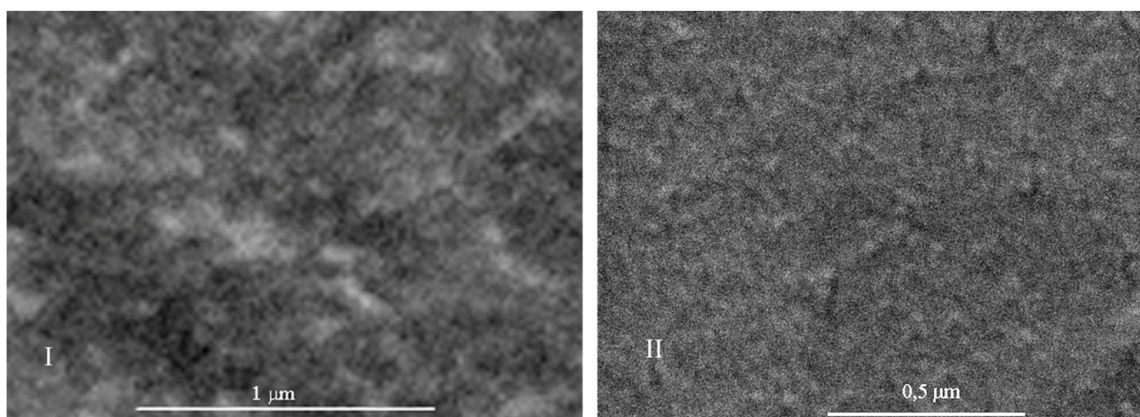


FIG. 2. The electron microscopic images of one of the areas of the surface of the granule and the film obtained by the method [1]. SamScan microscope (England) with a standard preparation of the samples and coating of the Au layer with the thickness of 5Å. I – granule; II –film

TABLE 1. Limit volumes of the particles

Volume, nm <sup>3</sup>	Film	Granule	Granule after the contact
$v_{10}$	2,2±0,3	470±40	19,7±4,2
$v_{1M} \cdot 10^4$	0,75±0,2	3,4±0,4	6,4±0,7
$v_{20} \cdot 10^5$	0,09±0,02	2,4±0,3	3,6±0,5
$v_{2M} \cdot 10^6$	1,3±0,1	13,1±0,4	36,6±0,4

These particles were sufficiently ordered, allowing us to delineate the image of each of them to measure the area  $S$  and to find the parameter  $v = S^{3/2}$  assigned as the volume of the particle. The average  $j^{th}$  type particle sizes within the composition of different  $(j + 1)^{th}$  type particles did not differ remarkably, so that all the particles of each type were characterized by a single function:

$$\theta_j(v) = \frac{1}{N_j} \int_{v_{0j}}^v \phi_j(v, \tau) dv = B_{jv}/B_{j0}, \quad (14)$$

where  $B_{jv}$  is the number of measured particles of  $j^{th}$  type with the volume less than  $v$ ;  $B_{j0}$  is the total number of measured particles of  $j^{th}$  type;  $v_{j0}$  is the volume of the smallest of the detected particles.

Several functions  $\theta_j(v)$  are shown in Figs. 3 and 4, where it is seen that the size of each particle type remained within a certain range of volumes  $v_{j0} < v < v_{Mj}$ , in which the value  $\theta_j(v)$  increased from 0 to 1 (Table 1). The measurements showed that the interval  $\Delta v_j = v_{Mj} - v_{0j}$  depended on the formation conditions and usage of the body. As it turned out, the interval  $\Delta v_j$  for the nanoparticles of the film obtained by evaporation of a fullerene( $C_{60}$ )-containing solution, was dependent on the concentration of fullerene according to the relationship:

$$\Delta v_2 = \Delta v_{20} (1 + \chi_F M_F / M_M), \quad (15)$$

where  $\Delta v_{20}$  is an interval without fullerene;  $M_F$  and  $M_M$  are masses of fullerene and polystyrene introduced in the original solution at  $M_F/M_M = (3 \cdot 10^{-4} \div 1 \cdot 10^{-3})$ ;  $\chi_F = (1552 \pm 42)$  is an empirical coefficient.

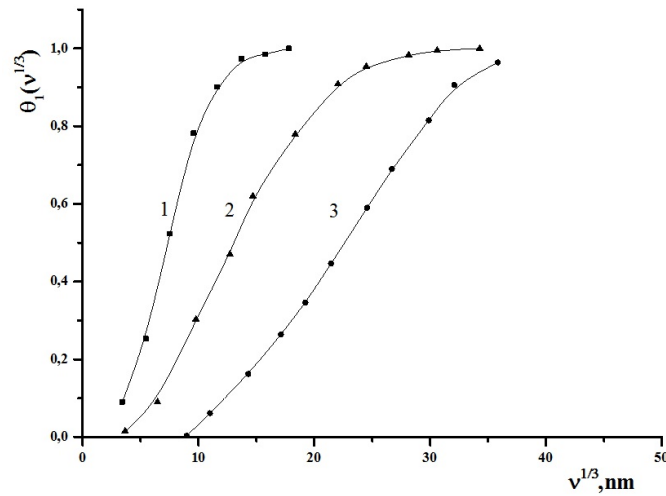


FIG. 3. Distribution functions  $\theta_1(v)$  of subnanoparticles of the film and granule microrelief on the volume before and after a short introduction in toluene. 1 – film, 2 – granule before to the contact with toluene, 3 – granule after the contact with toluene

TABLE 2. Limit volumes of the nanoparticles of the film with different content of the fullerene

$M_F/M_M$	$v_{0j} \cdot 10^5 \text{ nm}^3$	$v_{Mj} \cdot 10^6 \text{ nm}^3$
0	0,09	1,3
$3 \cdot 10^{-4}$	0,15	1,5
$10^{-3}$	0,22	1,7

The concentration of fullerene also affected the maximum volume of the nanoparticles:

$$v_{M2} = v_{M0}[(1 + \chi_v(M_F/M_M)^k)], \quad (16)$$

where  $v_{M0}$  is the maximum volume at  $M_F=0$ ;  $\chi_v=20,5 \pm 0,1$  and  $k=0.61 \pm 0.02$  are empirical coefficients (Table 2).

Equations (15) and (16) indicate that the microrelief of the film memorized the quantity of the fullerene in the solution in which the film was formed, whereas the granule subjected to the partial dissolution remembered what happened to it at dissolution. This is indicated by the data in Figs. 3 and 4, which show that the granule placement into the stream of toluene at a temperature of 300 °K for  $\tau = 60$  s resulted in a significant change of the distribution functions  $\theta_j(v)$ . This change can be characterized by the parameter  $P_j$ :

$$\theta_j(v)_{t_F} = \theta_j(v + P_j)_\tau, \quad (17)$$

where  $\theta_j(v)_{t_F}$  and  $\theta_j(v + P_j)_\tau$  are the functions  $\theta_j(v)$  before and after the contact with toluene when the volume of the particles was equal to  $v$  and  $v + P_j$ , respectively.

According to the data in Figs. 3-5, the parameter  $P_j$  was equal to:

$$P_j = v_{j\tau} - v = P_{0j}(v/v_{0j})^{q_j}, \quad (18)$$

where  $v_{j\tau}$  is the volume of the particle of  $j^{th}$  type, which volume equaled to  $v$  before the contact at the moment  $\tau$ ;  $P_{0j} = v_{j\tau} - v_{0j}$  and  $q_j$  are empirical parameters (Fig. 5). The

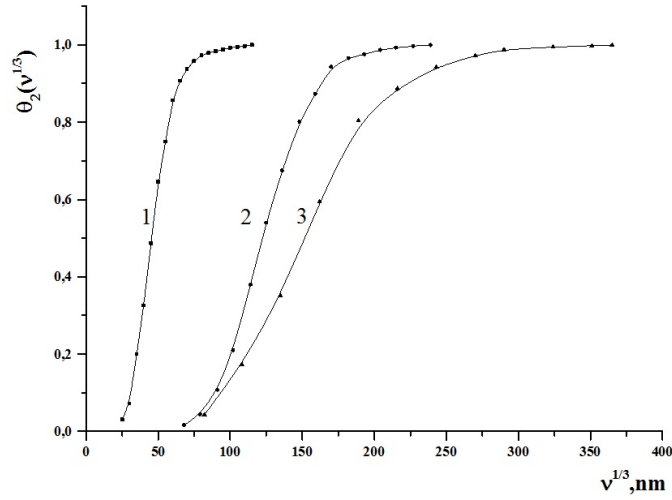


FIG. 4. Distribution functions  $\theta_2(v)$  on volume of nanoparticles of the film and granule. 1 – film, 2 – granule before to the contact with toluene, 3 – granule after the contact with toluene

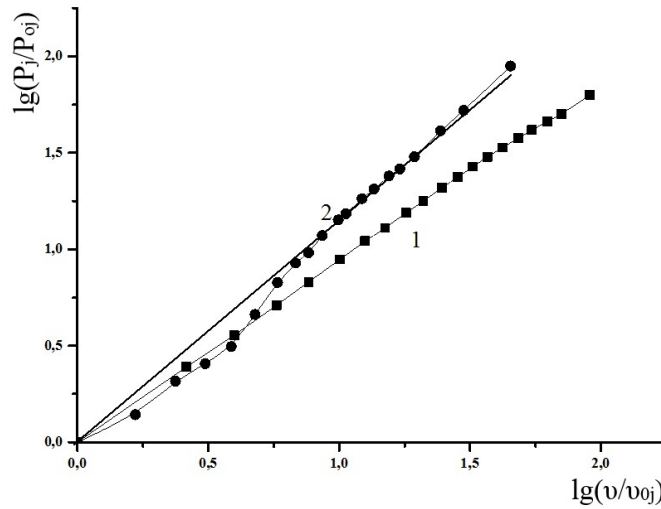


FIG. 5. Parameter  $P_j$  of the subnano- and nanoparticles of the granules microrelief. 1 – subnanoparticles at  $P_{01} q=0.98$ ; 2 – nanoparticles at  $P_{02} q=1,27$

volume  $v_{j\tau}$  could increase due to the capture of toluene molecules by the particles and decrease due to the release of macromolecules. Therefore:

$$P_j = \int_0^\tau (\omega_j a_j - \nu_j b_j) d\tau^*, \tag{19}$$

where  $\omega_j$  and  $\nu_j$  are the frequencies of events leading to the increase and decrease of  $v_{j\tau}$ ;  $a_j$  and  $b_j$  are the changes of  $v_{j\tau}$  at a single event at  $0 < \tau^* < \tau$ .

From equations (16) and (17), it follows that during contact with toluene and its subsequent removal from the granules, the following conditions were fulfilled:

$$\omega_j = \omega_j(\tau^*) (v/v_{0j})^{q_j}, \tag{20}$$

$$\nu_j = \nu_j(\tau^*) N_{j-1}^{q_i}, \tag{21}$$

where  $N_{j-1} = v/\bar{a}_{j-1}$  is the number of the particles of  $(j-1)^{th}$  type in the particle of  $j^{th}$  type with the volume  $v$ ;  $\bar{a}_{j-1}$  is the average volume per  $j^{th}$  type particle in the volume  $v$ ;  $\omega_j(\tau^*)$  and  $\nu_j(\tau^*)$  are the frequency functions, characterizing the probability of the participation of a single particle of the  $j^{th}$  type in the change of  $v$  per unit time.

States (18)–(21) can be considered as an indication of the fact that the capture of the toluene molecules by the granule causes their penetration in the volume of nano- and subnanoparticles with solvation of macromolecules, causing the weakening of the bond between the macromolecules and providing their removal from the subnanoparticles with a similar probability ( $q_1 \rightarrow 1$ ).

Toluene molecules, which penetrated into the subnanoparticles during contact, were removed from the subnanoparticles after contact, so when in the microscope, their parameter  $P_j$  is similar to:

$$P_1 = -N_0(v) \int_0^\tau \nu_1(\tau^*) b_1 d\tau^*, \quad (22)$$

where  $N_0(v)$  is the quantity of the macromolecules in the subnanoparticle of the volume  $v$  before the contact.

The parameter  $P_j$  of the nanoparticles in the microscope is equal to:

$$P_2 = (v/v_{0j})^{q_2} \int_0^\tau \omega_2(\tau^*) a_2 d\tau^*. \quad (23)$$

Their frequency function  $\omega_2(\tau^*)$  increased at the contact due to the capture of toluene, and decreased after the contact due to toluene removal from the granules. Additionally, if the structure of nanoparticles changed reversibly during toluene capture, the condition  $P_2 = 0$  would be fulfilled. However, solvation of the macromolecules lead to irreversible changes in the location of subnanoparticles in the volume of nanoparticles, so  $P_2 > 0$ .

Equations (18)–(23) make it possible to determine the frequency functions  $\omega_j(\tau^*)$  and  $\nu_j(\tau^*)$ , information on which is stored in the function  $P_j = P_j(v)$ . One can try to simulate the frequency functions using equations (7)–(11).

Considering the above, it can be argued that the studied films and granules of polystyrene possessed the morphological memory. These granules maintained their nonequilibrium hierarchical structures, formed on their surface, for the long time in such a state, thus allowing an approach for the identification of kinetic equations for the hierarchies' formation.

## 7. Conclusion

Experiments with polystyrene showed the concept of the morphological memory of the polymeric bodies as the ability of their surface microrelief to maintain long-term nonequilibrium macromolecular structures that can be effectively used in the study of polymerization and in the search for the optimal conditions for polymer synthesis. It was found that the proposed models for the formation of polymers, devoid of arbitrary assumptions, could be the basis for creating a computer system for the application of morphological memory to determine the rates of elementary processes and to predict the behavior of polymers during their prolonged use.

## Acknowledgment

The work was supported by Russia Foundation for Basic Research (grant N 15-43-03034-a).

## References

- [1] Alekseeva O.V., Bagrovskaya N.A., Kuzmin S.M., Noskov A.V., Melikhov I.V., Rudin V.N. Influence of fullerene additives on the structure of the polystyrene films. *Russ. J. Phys. Chem.*, 2009, **83**(7), P. 1320–1326.
- [2] Alekseeva O.V., Bagrovskaya N.A., Kuzmin S.M., Noskov A.V., Melikhov I.V., Rudin V.N. Effect of C<sub>60</sub> Doping on the Structure and Properties of Polystyrene. In Handbook on Fullerene: Synthesis, Properties and Applications ISBN 978-1-62100-429-5. Editor: R.F. Verner, C. Benvenuto, P. 439–456. 2012 Nova Science Publishers, Inc. New York, 558 p.
- [3] Brinker C.J., Scherer G.W. *Sol-Gel Science. The Physics and Chemistry of Sol-Gel Processing*. San Diego, CA: Academic Press, 1990, 908 p.
- [4] Salamone C. (Ed). *Polymeric Material Encyclopedia*. Boca Raton FL: CRC Press, 1996.
- [5] Korolev G.V., Mogilevich M.M. *Three-dimensional radical polymerization. Mesh and hyperbranched polymers*. Khimia. St. Petersburg, 2006.
- [6] Kabanov V.A. *Selected Works*. Nauka, Moscow, 2010, 603 p.
- [7] Ferreira, V., Douglas, J. F., Warren, J., and Karim, A. Non-Equilibrium Pattern Formation in the Crystallization of Polymer Blend Films. *Physical Review E*, 2002, **65**(4), P. 042802:1-4.
- [8] Irzhak V.I., Mezhevikov S.M. Kinetics of oligomer curing. *Russ. Chem. Rev.*, 2008, **77**(1), P. 78–104.
- [9] Emanuel N.M., Buchachenko A.L. *Chemical physics of molecular degradation and stabilization of polymers*. Moscow, Nauka, 1988, 368 p.
- [10] Grosberg A.Yu., Khokhlov A.R. *Polymers and biopolymers from the point of view of physics*. Dolgoprudny: Publishing House “Intellect”, 2010, 304 p.
- [11] Palmer R.E., Pratontier S., Boyen H.-G. Nanostructured Surfaces from size-selected clusters. *Nature Materials*, 2003, **2**(7), P. 443–448.
- [12] Askadskii A.A., Khokhlov A.R. *Introduction to physical chemistry of polymers*. Moscow, Nauchny Mir, 2009, 384 p.
- [13] Melikhov I.V. An evolutionary approach to the creation of nanostructures. *Nanosystems: physics, chemistry, mathematics*, 2010, **1**(1), P. 148–155.
- [14] Melikhov I.V., *Physico-chemical evolution of solid*. Moscow, Binom, 2006, 309 p.
- [15] Yampolsky Yu.P. Methods of studying the free volume in polymers. *Russ. Chem. Rev.*, 2007, **76**(1), P. 66–87.
- [16] Nalwes H.S. (Ed). *Handbook of Nanostructured Materials and Nanotechnology*, v 5. Organics, Polymer and Biological Compounds. Boston: Acad. Press, 2000.
- [17] Tant M.R., Connell J.W., McManus H.L.N. (Eds). *High Temperature Properties and Applications of Polymeric Materials. ACS Symposium Series*. V 603. American Chemical Society, Washington Dc, 1995.
- [18] Mozhikovskiy S.M., Arinshtein A.E., Deberdeev R.Ya. *Oligomeric state of matter*. Moscow, Nauka, 2005, 252 p.
- [19] Volfson S.A., Enikolopyan I.S. *The calculation of high-performance polymerization processes*. Moscow, Khimia, 1980, 312 p.
- [20] Fredrickson G.H. *The Equilibrium Theory of Inhomogeneous Polymers*. Oxford: University Press, 2006.
- [21] Simon P., Huhle R., Lehmann M., Lichte H., Monter D., Bieber T., Reschetilowski V., et al. Electron Holography on Beam Sensitive Materials: Organic Polymers and Mesoporous Silica. *Chem.Mater.*, 2002, **14**, P. 1505–1514.
- [22] Vang D., Zhu J., Yao Q., Wilkie C.A. A Comparison of Various Methods for the Preparation of Polystyrene and Poly(methyl methacrylate) clay Nanocomposites. *Chem.Mater.*, 2002, **14**(9), P. 3837–3843.
- [23] Dutschke A., Diegelmann C., Lobmann P. Nucleation and Growth of TiO<sub>2</sub> Thin Films on Modified Polystyrene Surfaces. *Chem.Mater.*, 2003, **15**(18), P. 3501–3506.
- [24] Seeman N.C. DNA in a material world. *Nature*, 2003, **421**(6921), P. 427–431.

- [25] Egen M., Voss R., Griesebock B., Zentel R. Heterostructures of Polymer Photonic Crystal Films. *Chem.Mater.*, 2003, **15**(20), P. 3786–3790.
- [26] Donald A.M. The use of environmental scanning electron microscopy for imaging wet and insulating materials. *Nature Materials*, 2003, **2**(8), P. 511–516.

# Chemostimulating effect of mixture and separate evaporation of manganese (IV) oxide compositions with lead (II) oxide and vanadium (V) oxide on GaAs thermal oxidation

I. Ya. Mittova, V. F. Kostryukov

Voronezh State University, Universitetskaya pl.1, Voronezh, 394893 Russia

imittova@mail.ru, vc@chem.vsu.ru

PACS 81.05.Ea

DOI 10.17586/2220-8054-2015-6-3-424-434

The effects of variable compositions of manganese (IV) oxide - lead (II) oxide and manganese (IV) oxide - vanadium (V) oxide on the GaAs thermal oxidation process have been studied. The spatial separation of the oxides in  $\text{MnO}_2 + \text{PbO}$  and  $\text{MnO}_2 + \text{V}_2\text{O}_5$  binary compositions activating the thermal oxidation of GaAs has made it possible to locate the interactions between these oxides that are responsible for the non-linear effects observed in their coaction. Solid-phase interactions enhance the chemostimulating activities of both oxides (a positive nonlinear effect takes place). Gas-phase interactions cause a marked negative deviation from the additive chemical stimulation effect.

**Keywords:** semiconductors, gallium arsenide, thin films, thermal oxidation, nonlinear effects.

*Received: 13 February 2015*

*Revised: 19 February 2015*

## 1. Introduction

The study of the GaAs thermal oxidation process stimulated by the p-block oxide compositions has revealed the nonlinear effects for various compositions of chemostimulators on the oxide film thickness on the semiconductor surface [1, 2]. These effects result from additional feedback channels between the chemostimulators, which influence the kinetic blocks of conjugations between various stages of the GaAs oxidation process.

Prior studies [3–5] have demonstrated that in some systems ( $\text{Sb}_2\text{O}_3 + \text{Bi}_2\text{O}_3$ ,  $\text{Sb}_2\text{O}_3 + \text{PbO}$ ,  $\text{PbO} + \text{Bi}_2\text{O}_3$ ), such feedback channels are localized with comparable impacts in solid and gas phases. It is, thus, of great interest to examine the revealed dependencies using d-block oxides together with p-block oxide and with any other d-block oxide as well. Manganese is taken as a model element, as its oxidation degrees vary greatly. As it is practically impossible to use the higher oxide  $\text{Mn}_2\text{O}_7$  for the experiment due to its extremely fast decomposition, the study is based on compositions of  $\text{MnO}_2$  with p-block oxides ( $\text{PbO}$ ) and d-block oxides ( $\text{V}_2\text{O}_5$ ). The individual chemostimulating effects of these oxides have already been studied [6, 7].

Thus, the aim of this work is to study the process of gallium arsenide thermal oxidation under the coaction of manganese (IV) oxide – lead (II) oxide, and manganese (IV) oxide – vanadium (V) oxide compositions, and to determine the nature and localization of the nonlinear effects of various compositions of chemostimulators on the oxide film thickness.

## 2. Experimental

The oxide films were grown on polished single-crystal (111) GaAs wafers (AGChTs-1, gallium face). To determine the gallium face and the arsenic face, the substrate had been chemically milled in 49 % HF for 20 min. Powdered  $\text{MnO}_2$  (AR grade, GOST 4470-79),  $\text{PbO}$  (AR grade, GOST 9199-68), and  $\text{V}_2\text{O}_5$  (AR grade, TS CM-4566-55) compositions with 20 mole % steps were used as chemostimulators. The oxygen flow into the reactor was a constant 30 L/h.

The GaAs oxidation was carried out in a quartz reactor in a horizontal resistor furnace with automated temperature regulation (BPRT-1, with accuracy of  $\pm 2^\circ\text{C}$ ). The chemostimulator compositions came out of the quartz container and were introduced through the gas phase under conditions isothermal with respect to the substrate being oxidized. The distance from the oxides surface to the working side of the substrate was 10 cm. The sample size was a constant 0.3000 g. The oxidation was carried out at 530 and 560°C using the final oxidation method (from 10 to 60) with 10-minute intervals. Using a temperature of 530°C allowed comparison of the obtained data with previous results, while 560°C was the maximum temperature used to determine the temperature effects on the process. The thicknesses of the oxide films were measured using an LEF-3M ellipsometer with an accuracy of  $\pm 1$  nm.

To identify the processes and reactions occurring during the chemostimulator binary composition-activated GaAs thermal oxidation, the following methods were used: X-ray powder diffraction (EMPYREAN), IR spectroscopy (Infralyum FT-02, UR-10), X-ray fluorescence analysis (VRA-30, Carl Zeiss Yena), electron probe X-ray microanalysis (EPXMA, CamScan), and high-temperature mass spectrometry (MS-1301).

## 3. Results and discussion

The dependencies of the oxide films thickness on the chemostimulator compositions ( $\text{MnO}_2+\text{PbO}$  and  $\text{MnO}_2+\text{V}_2\text{O}_5$ ) at both temperatures are presented in Fig.1. The figure shows marked nonlinear effects present in both cases: the actual oxide film thickness is different from the additive value, which is highly dependent upon the temperature, especially for compositions with vanadium oxide.

Dependencies of the oxide films' relative integrated thickness [1] on the composition are shown in Fig.2. The GaAs thermal oxidation activated by  $\text{MnO}_2+\text{PbO}$  compositions show overall negative deviation from additivity. Both at 530°C and 560°C the deviation increases with the longer oxidation times. Similar results were obtained when activating the GaAs thermal oxidation with p-block chemostimulator compositions [2]. When a higher temperature is used, however, the results are completely different: the negative deviation from additivity decreases with time, which becomes clear at latter stages of the process.

When GaAs thermal oxidation is activated by  $\text{MnO}_2+\text{V}_2\text{O}_5$  at 530°C for a short period of time, a variable sign deviation from additivity appears with the overall insignificant change in  $d^R$ . With time, the variable sign deviation becomes an increasingly negative deviation in all compositions with a minimum of 60% for vanadium oxide (time interval – 60 min). At 560°C the results are completely different. The variable sign deviation is present regardless of the process duration, and the positive deviation from additivity also increases with time. At the same time, however, the negative deviation also increases (with minimum of 80% for  $\text{V}_2\text{O}_5$ ).

Table 1 shows the chemostimulator compositions' X-ray powder diffraction data (presented as interplanar distance) [8]. The chemostimulator compositions studied had been annealed under an oxygen atmosphere at 560°C, for 30 min. Table 1 shows, that the vanadium oxide system contained vanadium and manganese oxides. In the 80% MnO<sub>2</sub> + 20% V<sub>2</sub>O<sub>5</sub> composition, Mn<sub>2</sub>O<sub>3</sub> appeared as well as MnO<sub>2</sub>; in the 20% MnO<sub>2</sub> + 80% V<sub>2</sub>O<sub>5</sub> composition – MnO<sub>2</sub> and Mn<sub>3</sub>O<sub>4</sub> were present. Thus, the lower reduction of manganese (IV) after its partial conversion enhances the transit activeness of the chemostimulator and results in positive deviation from additivity (Fig.2).

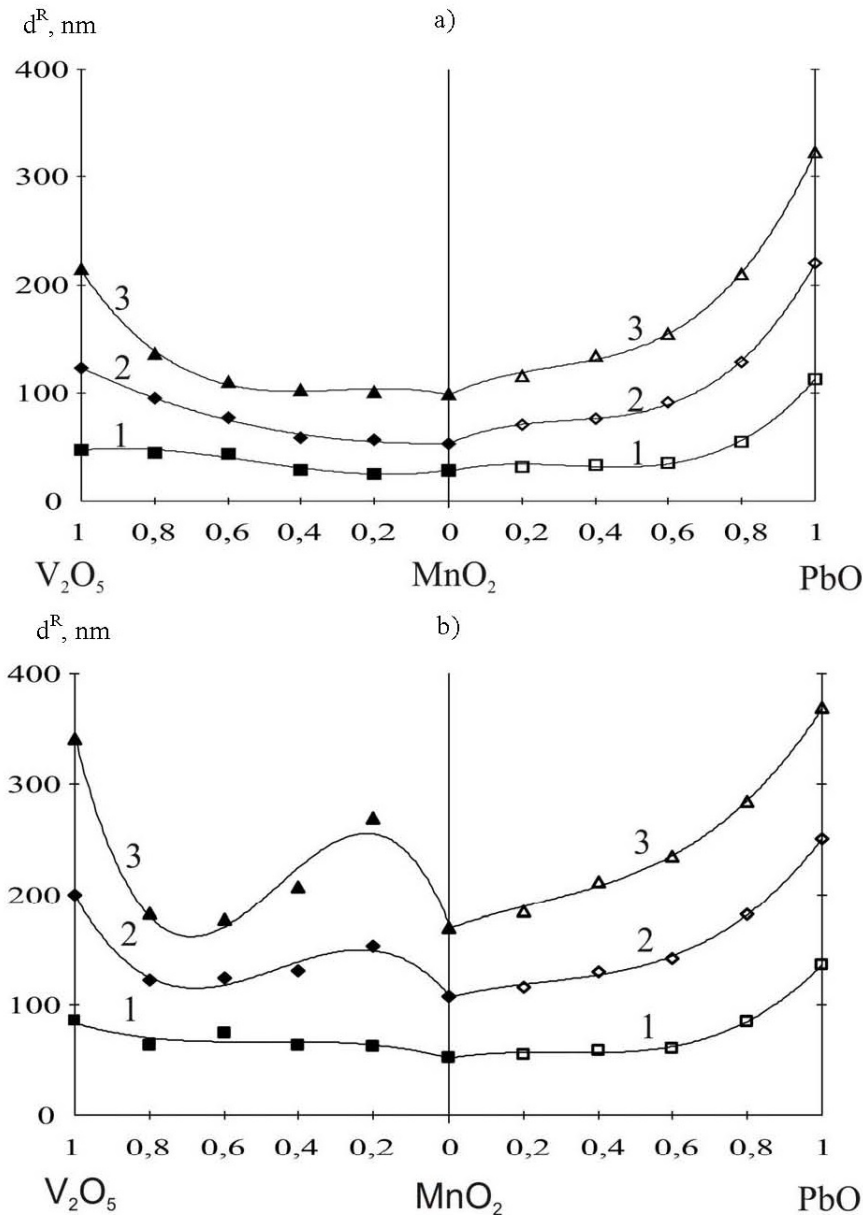


FIG. 1. Concentration dependence of the oxide film thickness on GaAs surface at 530°C (a) and at 560°C (b) over time intervals: 1 – 10 min., 2 – 30 min., 3 – 60 min

All the powdered compositions of the lead oxide system contained PbO, Pb<sub>3</sub>O<sub>4</sub>, PbO<sub>2</sub>, MnO<sub>2</sub>, Mn<sub>3</sub>O<sub>4</sub>. Manganese and lead did not act together (similarly to the system described

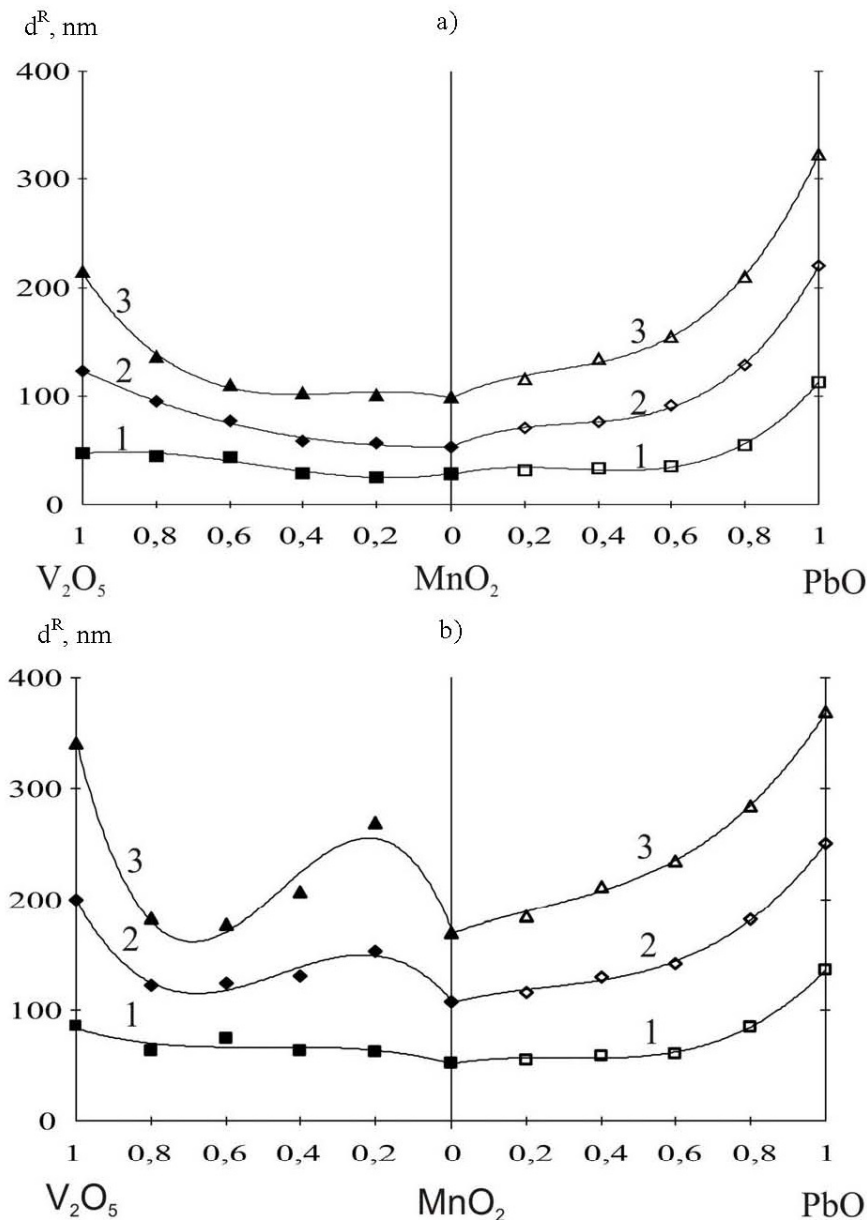


FIG. 2. Relative integrated thickness of the films grown presented as a dependency of chemostimulator composition elements at 530°C (a) and at 560°C (b) over time intervals 1 – 10 min., 2 – 30 min., 3 – 60 min

above), but the radiography showed spikes of high intensity that we did not manage to identify. The system showed the same patterns:  $MnO_2$  transforms into  $Mn_3O_4$  better than in  $V_2O_5$  system (due to the additional lead oxide oxidation), which results in overall negative deviation from additivity. Thus, manganese (IV) oxide and lead (II) oxide used together, as well as manganese (IV) oxide and vanadium (V) oxide, affect each other while still being in the container. This results in mixed phases (for  $MnO_2+V_2O_5$ ), and in conversion of the initial chemostimulators into compositions with different oxidation degrees (for  $MnO_2+PbO$ ), which changes the evaporation rate and can lead to a joint nonlinear effect for the GaAs thermal oxidation.

TABLE 1. Interplanar distance ( $d_{hkl}$ ) defined by the X-ray powder diffraction method for chemostimulator compositions ( $\text{MnO}_2+\text{V}_2\text{O}_5$ ) and ( $\text{MnO}_2+\text{PbO}$ )

Phases revealed	$\text{MnO}_2+\text{V}_2\text{O}_5$	
	20 $\text{MnO}_2$	80 $\text{MnO}_2$
$\text{V}_2\text{O}_5$	4.374, 4.077	4.374, 4.077
$\text{MnO}_2$	1.445, 1.570	3.058, 2.186
$\text{Mn}_2\text{O}_3$	–	1.848, 1.361
$\text{Mn}_3\text{O}_4$	2.495, 1.499	–
Phases revealed	$\text{MnO}_2+\text{PbO}$	
	20 $\text{MnO}_2$	40 $\text{MnO}_2$
$\text{PbO}$	5,906, 1,722	1.918
$\text{Mn}_3\text{O}_4$	1.639	2.876
$\text{PbO}_2$	1.208	1.514
$\text{MnO}_2$	3.069	1.993
$\text{Mn}_3\text{O}_4$	2.006	1.488
<b>Intermediate phase</b>	5.574	5.754, 3.401

The X-ray powder diffraction and IR spectroscopy methods are complementary. The first method allows us to determine the presence of a certain element in the film, while the second is used to obtain information about the state of the element. The samples used for analysis were determined according to the extreme points of the dependencies of relative integrated oxide film thickness of on the chemostimulator composition at the maximal temperature and duration, i.e. 40%  $\text{MnO}_2$  – 60%  $\text{V}_2\text{O}_5$ , 80%  $\text{MnO}_2$  – 20%  $\text{V}_2\text{O}_5$ , 40%  $\text{MnO}_2$  – 60%  $\text{PbO}$  at 560°C for 60 min. X-ray powder diffraction data showed manganese in oxide films in all cases studied. The films obtained using compositions with vanadium oxide contain vanadium. There were, however, no traces of lead [9].

The IR spectra of the samples show several minima. According to [10], absorption bands at 420-440  $\text{cm}^{-1}$  and 670  $\text{cm}^{-1}$  correspond to Ga-O. The same bands appeared when the samples were oxidized without chemostimulators, which means that gallium oxide appears. The absorption band at 900  $\text{cm}^{-1}$  usually corresponds to As-O, while the absorption band of 850  $\text{cm}^{-1}$  corresponds to Pb-O. The second absorption band corresponding to As-O is 480  $\text{cm}^{-1}$  and is similar to the second absorption band corresponding to V-O. As the X-ray powder diffraction showed vanadium in oxide films, it is highly possible that the frequency corresponds both to As-O and V-O. The minimum absorption at 840  $\text{cm}^{-1}$  corresponds to the fluctuations of Mn-O. Of particular interest are the absorption bands of 540  $\text{cm}^{-1}$ , which can be explained by the substrate's GaAs bond.

Our experiment, has thus demonstrated, that according to the X-ray powder diffraction and IR spectroscopic data, the chemostimulators become part of the oxide film grown on the GaAs surface. Moreover, the oxidized substrate elements are also present in the film (which is particularly important for arsenic).

Spatial separation of the chemostimulators [3–5] can be used to determine the localization of their interactions resulting in deviations from additivity (Fig.2). Figures 3 and 4 illustrate effects of  $\text{MnO}_2$  interacting with  $\text{PbO}$  and  $\text{V}_2\text{O}_5$  in mixures and spatially separated (for oxide film thickness and relative integrated thickness respectively). Clearly, the overall effect of the chemostimulators in the thermal oxidation of GaAs is nonlinear for separate

evaporation techniques. The nonlinearity is more pronounced in the separate evaporation experiments than in the mixture evaporation experiments.

Since the nonlinear effects arise from both solid- and gas-phase reactions in the case of mixture evaporation and only from gas-phase reactions in the case of separate evaporation, it is possible to separate the effective contribution from the solid-phase reactions to the overall effect.

At 530°C the nonlinear effects in the mixture evaporation and separate evaporation experiments are of the same sign and the corresponding relative integrated thicknesses are similar (Fig. 3, 4). Consequently, the contribution from the solid-phase reactions between the chemostimulators is of small positive value, and the negative overall deviation from additivity is due to the interaction between the oxides in the gas phase.

At 560°C the nonlinear effects in the mixture evaporation and separate evaporation experiments for both chemostimulator systems differ greatly both in magnitude and in the way they vary with composition.

The contribution from the solid-phase interaction is again positive throughout the chemostimulator composition range, but is larger. The fact that the contribution from the solid-phase interactions increases markedly with increasing temperature suggests that these interactions are chemical in nature. This inference is supported by X-ray powder diffraction data (which indicate the formation of  $\text{Mn}_2\text{O}_3$ ,  $\text{Mn}_3\text{O}_4$ ; and conversions  $\text{PbO} \rightarrow \text{Pb}_3\text{O}_4 \rightarrow \text{PbO}_2$ ).

The contribution from the gas-phase interaction between the chemostimulators increases negatively with increasing temperature and exceeds the positive contribution from the solid-phase interaction. As a result, the relative integrated thickness is negative and varies nonlinearly with the composition of the chemostimulator system.

The composition of the vapor over  $\text{PbO} + \text{MnO}_2$  mixtures in the composition range from 20%  $\text{PbO} + 80\%$   $\text{MnO}_2$  to 80%  $\text{PbO} + 20\%$   $\text{MnO}_2$  was studied using high-temperature mass spectrometry (MS-1301) [11]. The mass spectra of the vapor over the samples from 920 to 980 K showed  $\text{Pb}^+$ ,  $\text{PbO}^+$ ,  $\text{Pb}_2\text{O}_2^+$  and  $\text{Pb}_4\text{O}_4^+$  ion peaks, indicating the presence of lead atoms and  $\text{PbO}$ ,  $\text{Pb}_2\text{O}_2$  and  $\text{Pb}_4\text{O}_4$  molecules in the vapor phase. The spectra do not indicate the presence of mixed molecular ions, such as  $\text{PbMnO}_2^+$ ,  $\text{PbMnO}_3^+$ ,  $\text{PbMnO}_4^+$ ; therefore, there is no interaction between lead and manganese oxides in the condensed or gas phase. The most important result of the mass spectrometric study is that the relative lead atom concentration in the gas phase is higher for the mixtures used in the experiment than for pure  $\text{PbO}$ . The  $\text{Pb}/\text{PbO}$  ratio changes from 1.67 and 0.84 for  $\text{PbO}$ -rich compositions to 0.80 and 0.73 for  $\text{MnO}_2$ -rich compositions. The vapor over the mixtures contains all molecular species typical of the evaporation of pure  $\text{PbO}$ ; however, the  $\text{Pb}/\text{PbO}$  partial pressure ratio indicates the domination of lead atoms. The  $\text{Pb}$  atom concentration in the gas phase is approximately twice higher in the evaporation of a  $\text{PbO} + \text{MnO}_2$  mixture than in the evaporation of pure  $\text{PbO}$  [12]. In the presence of  $\text{MnO}_2$ , the vapor contains polymerized lead oxide species; nevertheless,  $\text{PbO}$  definitely tends to decompose. It is due to this process that the oxide compositions show a lower chemostimulating activity in GaAs oxidation than pure  $\text{PbO}$  or  $\text{MnO}_2$  and, accordingly, a negative nonlinear effect is observed in the coaction of  $\text{PbO}$  and  $\text{MnO}_2$ .

According to electron probe X-ray microanalysis (EPXMA) [13] (Table. 2, 3) data for  $(\text{PbO})_{0,8}(\text{MnO}_2)_{0,2}$  compositions, the  $\text{Mn}:\text{Pb}$  ratio of the film in the mixture, evaporation is 0.21 (0.089% : 0.425%), while in a separate evaporation experiment, the ratio is 0.66, i.e. the manganese, content of the film is about 3 times higher. For the manganese dioxide-rich composition  $(\text{PbO})_{0,2}(\text{MnO}_2)_{0,8}$ , the  $\text{Mn} : \text{Pb}$  ratio in the film is 0.42 for the mixture evaporation experiment and 0.84 for the separate evaporation experiment; that is, the separate

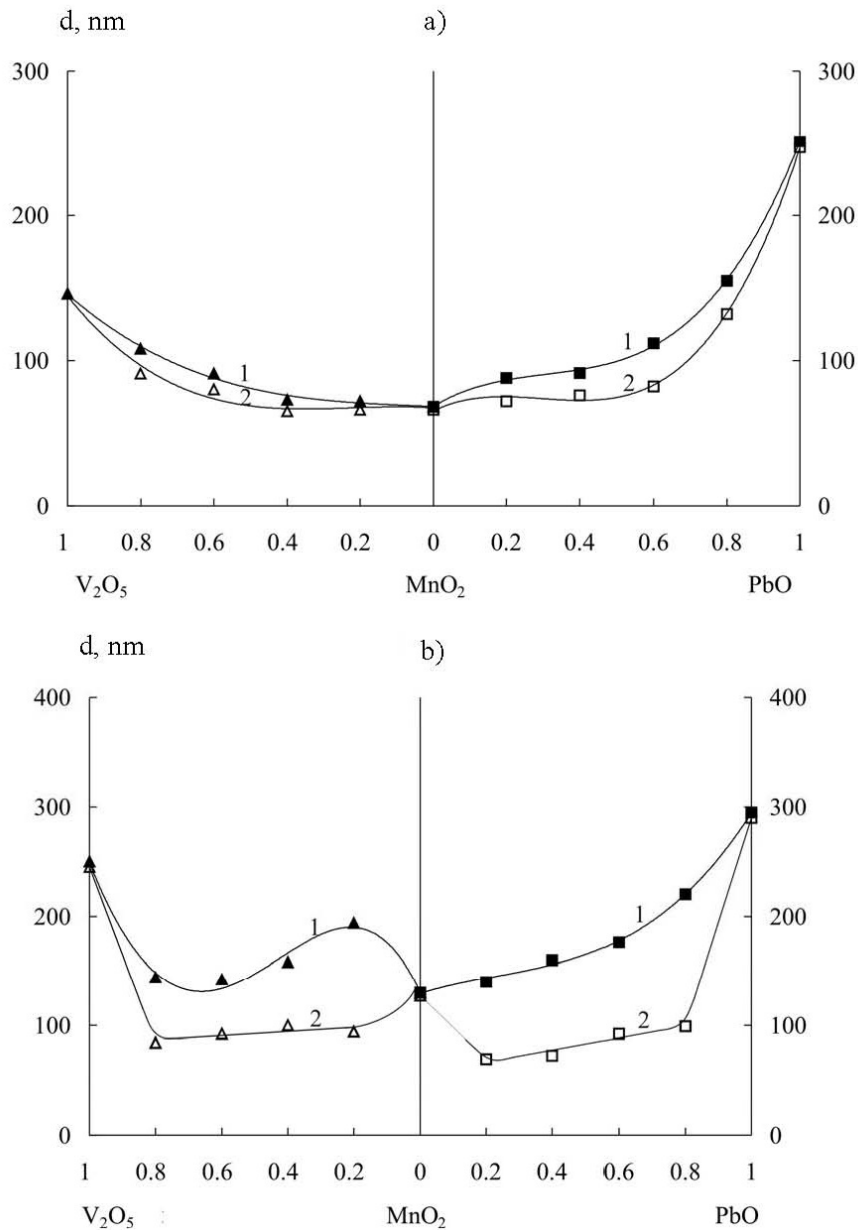


FIG. 3. The dependencies of the oxide films' thickness on the chemostimulator compositions  $\text{MnO}_2+\text{PbO}$  and  $\text{MnO}_2+\text{V}_2\text{O}_5$  at  $530^\circ\text{C}$  (a) and  $560^\circ\text{C}$  (b), for 40 min.: 1 – mixture evaporation experiment; 2 – separate evaporation experiment

evaporation of the chemostimulators increases the manganese content of the film by a factor of 2.

For the chemostimulator with  $(\text{PbO})_{0,8}(\text{MnO}_2)_{0,2}$  composition, the ratio  $\text{Mn}_{\text{mixture}}/\text{Mn}_{\text{separate}}$  is about 2 (0.089/0.046), i.e. in the case of separate evaporation, the manganese content of the film is about 2 times lower, while the lead content of the film is more than 6 times lower –  $\text{Pb}_{\text{mixture}}/\text{Pb}_{\text{separate}} = 0.425/0.068 = 6.25$ . A similar pattern was observed for the  $(\text{PbO})_{0,2}(\text{MnO}_2)_{0,8}$  composition: the manganese content ratio  $\text{Mn}_{\text{mixture}}/\text{Mn}_{\text{separate}}$  was 2.6 (0.136/0.052), and the lead content ratio  $\text{Pb}_{\text{mixture}}/\text{Pb}_{\text{separate}}$  was 5.2 (0.324/0.062).

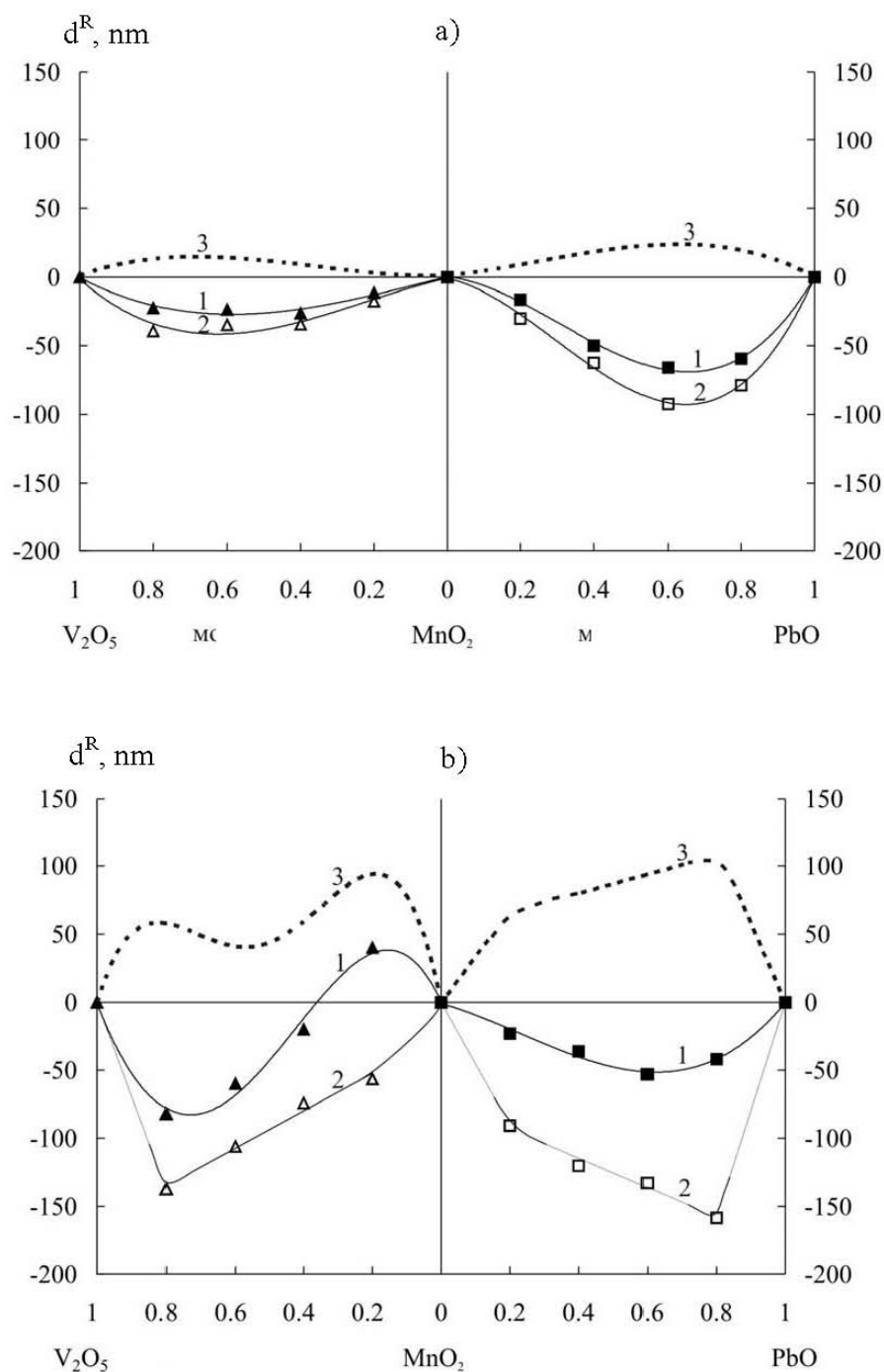


FIG. 4. The dependencies of the relative integrated films thickness on the chemostimulator compositions MnO<sub>2</sub>+PbO and MnO<sub>2</sub>+V<sub>2</sub>O<sub>5</sub> at 530°C (a) and 560°C (b), for 40 min.: 1 – mixture evaporation experiment; 2 – separate evaporations experiment; 3 – calculated contribution from the gas-phase interaction between the chemostimulators

TABLE 2. EPXMA data for the samples obtained by the thermal oxidation of GaAs at 560°C for 40 min in the presence of MnO<sub>2</sub>+PbO compositions introduced by the mixture evaporation and separate evaporation techniques

<b>Elemental composition of the films, at %</b>				
Ga	As	Mn	Pb	O
<b>Separate evaporation</b>				
20 mole % MnO <sub>2</sub> + 80 mole % PbO				
29.439	4.383	0.046	0.068	66.028
Activating composition – Mn : Pb = 1 : 4				
Film – Mn : Pb = 1 : 1.47				
80 mole % MnO <sub>2</sub> + 20 mole % PbO				
33.570	4.882	0.052	0.062	61.415
Activating composition - Mn : Pb = 4 : 1				
Film – Mn : Pb = 1 : 1.35				
<b>Mixture evaporation</b>				
20 mole % MnO <sub>2</sub> + 80 mole % PbO				
28.548	3.421	0.089	0.425	67.517
Activating composition – Mn : Pb = 1 : 4				
Film – Mn : Pb = 1 : 4				
80 mole % MnO <sub>2</sub> + 20 mole % PbO				
31.124	4.156	0.136	0.324	64.260
Activating composition – Mn : Pb = 4 : 1				
Film – Mn : Pb = 1 : 2.4				

Thus, the apparently higher manganese content of the films obtained by the separate evaporation of the chemostimulators is due to the decreased percentage of lead, which is a more effective chemical stimulator. It is this circumstance that enhances the negative nonlinear effect in the case of the separate evaporation of the chemostimulators.

This marked decrease in the chemical stimulation activity of lead oxide is caused by the enhancement of dissociation processes in the gas phase, as in the case of p-element-containing mixtures [2]. Due to these processes, the concentration of lead atoms, which are not chemical stimulators, is up to 2 times higher in the vapor over PbO + MnO<sub>2</sub> than in the vapor over pure PbO [12]. Although chemically stimulated oxidation is carried out under flowing oxygen, which can oxidize lead atoms, the efficiency of the oxygen transit transfer to the substrate components is much lower in this case. The nature of the precursor is significant here: the lead atom resulting from a transit transfer event is in an active, excited state, unlike the lead atoms present in the gas phase. If solid-phase interactions take place (PbO oxidation by manganese dioxide into higher lead oxides), the dissociation processes in the gas phase will be suppressed to some extent, particularly in the case of manganese dioxide-rich compositions. Thus, the solid-phase interactions in the PbO+MnO<sub>2</sub> mixtures somewhat hamper the dissociation processes in the gas phase, thereby making a positive contribution to the observed nonlinear effect. The fact that this contribution increases with increasing temperature is obviously explained by the rate enhancement of redox addition reactions in the solid phase.

TABLE 3. EPXMA data for the samples obtained by the thermal oxidation of GaAs at 560°C for 40 min in the presence of MnO<sub>2</sub>+V<sub>2</sub>O<sub>5</sub> compositions introduced by the mixture evaporation and separate evaporation techniques

Elemental composition of the films, at %				
Ga	As	Mn	V	O
<b>Separate evaporation</b>				
20 mole % MnO <sub>2</sub> + 80 mole % V <sub>2</sub> O <sub>5</sub>				
30.524	4.821	0.052	0.255	64.348
Activating composition - Mn : V = 1 : 4				
Film - Mn : V = 1 : 5				
80 mole % MnO <sub>2</sub> + 20 mole % V <sub>2</sub> O <sub>5</sub>				
30.718	4.654	0.301	0.076	64.248
Activating composition - Mn : V = 4 : 1				
Film - Mn : V = 4 : 1				
<b>Mixture evaporation</b>				
20 mole % MnO <sub>2</sub> + 80 mole % V <sub>2</sub> O <sub>5</sub>				
29.486	3.583	0.164	0.648	66.119
Activating composition - Mn : V = 1 : 4				
Film - 1 : 4				
80 mole % MnO <sub>2</sub> + 20 mole % V <sub>2</sub> O <sub>5</sub>				
28.843	3.871	0.643	0.254	66.389
Activating composition - Mn : V = 4 : 1				
Film - Mn : V = 2.53 : 1				

For a given activator composition, the films obtained using the mixture evaporation and separate evaporation techniques are comparable in terms of their Mn : V ratio (Table 3). For example, for (MnO<sub>2</sub>)<sub>0,2</sub>(V<sub>2</sub>O<sub>5</sub>)<sub>0,8</sub>, Mn:V=0.052:0.255=1:5 for the separate evaporation technique, and Mn:V=0.164:0.648=1:4 for the mixture evaporation technique; that is, for an activating mixture containing excess vanadium oxide, the manganese content of the film and, therefore, that of the gas phase are somewhat higher for mixture evaporation than for separate evaporation. By contrast, for (MnO<sub>2</sub>)<sub>0,8</sub>(V<sub>2</sub>O<sub>5</sub>)<sub>0,2</sub>, Mn:V=4:1 for separate evaporation, and Mn:V=2.6:1 for mixture evaporation; that is, the manganese content of the film is lower for mixture evaporation than for separate evaporation. At the same time, the relative amounts of the elements in the film change in the same way in passing from one evaporation technique to the other: both manganese and vanadium contents are 2-3 times higher for mixture evaporation than for separate evaporation. For the (MnO<sub>2</sub>)<sub>0,2</sub>(V<sub>2</sub>O<sub>5</sub>)<sub>0,8</sub> composition the Mn<sub>mixture</sub>/Mn<sub>separate</sub> ratio is 3.15 (0.164/0.052), and the V<sub>mixture</sub>/V<sub>separate</sub> ratio is 2.54 (0.648/0.255). For the (MnO<sub>2</sub>)<sub>0,8</sub>(V<sub>2</sub>O<sub>5</sub>)<sub>0,2</sub> composition, the Mn<sub>mixture</sub>/Mn<sub>separate</sub> ratio is 2.14 (0.643/0.301), and the V<sub>mixture</sub>/V<sub>separate</sub> ratio is 3.34 (0.254/0.076). Thus, due to the solid-phase interactions, the manganese and vanadium contents of the film and, therefore, the manganese and vanadium oxide contents of the vapor are higher in the case of mixture evaporation (according to IR spectroscopic data, the chemostimulators in the film are in their oxidized states); i.e., the dissociation processes in oxide evaporation are somewhat hampered by the solid-phase interactions.

#### 4. Conclusions

The observed nonlinear effects appearing during GaAs thermal oxidation under the coaction of manganese (IV) oxide – lead (II) oxide and manganese (IV) oxide - vanadium(V) oxide compositions can be attributed to their interaction in the initial powder mixture under the conditions corresponding to the process studied. These effects result in differences in their oxide film contents grown on GaAs surfaces and hence, differences in their chemostimulation capacities. The solid-phase interactions between the chemostimulators (during the evaporation of their mixtures) extend the lifetime of molecular oxide species in the vapor, giving rise to a positive thermal oxidation effect. The gas-phase interactions between the chemostimulators are mainly dissociative. They reduce somewhat the chemostimulating effect and make a negative contribution to the nonlinear effects.

#### Acknowledgements

The reported study was supported by the Ministry of Education and Science of the Russian Federation as a project part of the State Task for higher education institutions in the sphere of scientific research for years 2014–2016 (project N 225), and funded by the Russian Foundation for Basic Research (grant N 13-03-00705-a).

#### References

- [1] Mittova I.Ya., Pshestanchik V.R., Kostryukov V.F. Thermal Oxidation of Gallium Arsenide in oxygen: combined effect of Antimony and Bismuth oxides. *Russian Journal of Inorganic Chemistry*, 1997, **42**(2), P. 182–187.
- [2] Mittova I.Ya., Pshestanchik V.R., Kostryukov V.F. Alternating Alternating nonlinearity of the joint activating effect of binary mixtures of p-element oxides on the chemically activated thermal GaAs oxidation. *Doklady Chemistry*, 2001, **378**(4-6), P. 165–167.
- [3] Mittova I.Ya., Kostryukov V.F. GaAs Thermal oxidation activated by the coaction of p-block oxides. *Nanosystems: physics, chemistry, mathematics*, 2014, **5**(3), P. 417–426.
- [4] Mittova I.Ya., Pshestanchik V.R., Kostryukov V.F., Donkareva I.A. Spatial Localization of Interactions between Activating Additives during Chemostimulated Thermal Oxidation of GaAs. *Doklady Chemistry*, 2002, **386**(4-6), P. 258–260.
- [5] Mittova I.Ya., Pshestanchik V.R., Kostryukov V.F., Donkareva I.A. Mutual Effect of Activators on Chemostimulated GaAs Thermal Oxidation with Spatially Separated Coupling Stages. *Russian Journal of Inorganic Chemistry*, 2003, **48**(4), P. 480–483.
- [6] Mittova I.Ya., Pshestanchik V.R. The chemistry of processes which create dielectric layers with functional group substituents on semiconductors by impurity thermo-oxidation. *Russian Chemical Reviews*, 1991, **60**(9), P. 967–980.
- [7] Sladkopevtsev B.V., Tretyakov N.N., Dontsov A.I., Tomina E.V., Mittova I.Ya. Effect of oxide composition ( $V_2O_5 + Al_2O_3$ ) via gas phase on the thermal oxidation of InP. *Nanosystems: physics, chemistry, mathematics*, 2013, **4**(2), P. 260–268.
- [8] Diffraction Data. Catalog. International centre for diffraction data.
- [9] Hufner S. *Photoelectron Spectroscopy. Principles and Applications*. Heidelberg, Springer Verlag, 1995, 515 p.
- [10] Nakamoto K. *Infrared and Raman Spectra of Inorganic and Coordination Compounds*. World, Moscow, 1991, 441 p.
- [11] Balicheva T.G., et al. *Physical methods of inorganic substances*. Academia, Moscow, 2006, 442 p.
- [12] Kazenas E.K., Tsvetkov Yu.V. *Evaporation of oxides*. Science, Moscow, 1997, 543 p.
- [13] Goldstein J.I., Newbury D.E., Echlin P. *Scanning Electron Microscopy and X-Ray Microanalysis*, 1992, 829 p.

## Mass transport properties of water soluble light fullerene tris-malonate – $C_{60} [= C(COOH)_2]_3$ in aqueous solutions

K. N. Semenov<sup>1</sup>, N. A. Charykov<sup>2,3</sup>, O. S. Manyakina<sup>2</sup>, A. V. Fedorov<sup>2</sup>,  
V. A. Keskinov<sup>2</sup>, K. V. Ivanova<sup>2</sup>, O. V. Rakhimova<sup>3</sup>, D. G. Letenko<sup>4</sup>,  
V. A. Nikitin<sup>5</sup>, N. A. Kulenova<sup>6</sup>, Z. Akhmetvalieva<sup>6</sup>, M. S. Gutenev<sup>5</sup>

<sup>1</sup>St. Petersburg State University, Saint-Petersburg, Russia

<sup>2</sup>St. Petersburg State Technological Institute (Technical University), Saint-Petersburg, Russia

<sup>3</sup>St. Petersburg State Electro-Technical University (LETI), Saint-Petersburg, Russia

<sup>4</sup>St. Petersburg State University of Architecture and Civil Engineering, Saint-Petersburg, Russia

<sup>5</sup>Peter the Great St. Petersburg Polytechnic University, Saint-Petersburg, Russia

<sup>6</sup>D. Serikbayev East Kazakhstan state technical university, Ust-Kamenogorsk, Kazakhstan

keskinov@mail.ru

PACS 61.48.+c

DOI 10.17586/2220-8054-2015-6-3-435-441

The investigation of concentration dependence of mass transport properties (diffusion coefficients and viscosity) of the water soluble light fullerene tris-malonate –  $C_{60} [= C(COOH)_2]_3$  in aqueous solutions was provided. Activation energies for the diffusion and viscous current were calculated.

**Keywords:** tris-malonate of light fullerene, mass transport properties.

*Received: 12 July 2014*

### 1. Introduction

This article furthers the investigations which were initiated previously [1–5], devoted to describing the synthesis and identification of the  $C_{60} [= C(COOH)_2]_3$  tris-malonate [1] (the original synthesis of this water soluble derivative was described earlier in [5]), the investigation of volume and refraction properties of its aqueous solutions at 25 °C [2], poly-thermal solubility and complex thermal analysis [3], the concentration dependence of electric conductivity and pH for aqueous solutions [4], and concentration dependence of the last-mentioned properties for  $C_{60} [= C(COOH)_2]_3$  aggregates [5].

This article is devoted to investigating the concentration dependence of mass transport properties (diffusion coefficients and viscosity) of water soluble light fullerene tris-malonate –  $C_{60} [= C(COOH)_2]_3$  in aqueous solutions and calculation of activation energies for the diffusion and viscous current over a wide range of concentrations – up to 40 g/dm<sup>3</sup>.

### 2. Diffusion of $C_{60} [= C(COOH)_2]_3$ in water solutions at 20 and 50 °C

The diffusion of  $C_{60} [= C(COOH)_2]_3$  in the  $C_{60} [= C(COOH)_2]_3$  – H<sub>2</sub>O system was investigated with the help of an original diffusometer, which allowed the determination of the  $C_{60} [= C(COOH)_2]_3$  concentration  $C_{C60-tris-malonate}$  – mg/dm<sup>3</sup> (and the gradient of concentration – grad  $C_{C60-tris-malonate} = \partial C_{C60-tris-malonate} / \partial x$ , where  $x$  is coordinate of the direction of uni-dimensional diffusion) by light absorption in the near UV spectral range – at  $\lambda = 330$  nm [1], according to the first diffusion Fick's law (see, for example [6]):

$$dm_{\text{C}_{60}\text{-tris-malonate}}/dt = D \cdot S \cdot \partial C_{\text{C}_{60}\text{-tris-malonate}}/\partial x, \quad (1)$$

where:  $m$  is mass of  $\text{C}_{60}$ -tris-malonate, which crosses through the surface  $S$  per time  $t$  under concentration gradient  $\partial C_{\text{C}_{60}\text{-tris-malonate}}/\partial x$ .

Data were provided over a wide concentration range ( $5 \text{ g/dm}^3 \leq C_{\text{C}_{60}\text{-tris-malonate}} \leq 40 \text{ g/dm}^3$ ) for comparatively concentrated solutions at two temperatures  $20 \text{ }^\circ\text{C}$  and  $50 \text{ }^\circ\text{C}$  ( $293 \text{ K}$  and  $323 \text{ K}$ ).

The results of the determination are represented in Table 1 and in Fig. 1.

TABLE 1. Diffusion coefficient of  $\text{C}_{60}$ -tris-malonate of in water –  $D$  and diffusion activation energy –  $E_D$

Number of solution No.	Concentration of $\text{C}_{60}$ tris-malonate in water – $C$ (mass.%)	Diffusion coefficient of $\text{C}_{60}$ tris-malonate in water at $293 \text{ K}$ – $D_{293} 10^8$ ( $\text{cm}^2/\text{s}$ )	Diffusion coefficient of $\text{C}_{60}$ tris-malonate in water at $323 \text{ K}$ – $D_{323} 10^8$ ( $\text{cm}^2/\text{s}$ )	Energy of the diffusion activation according to the Arrhenius equation – $E_D$ (kJ/mole)
1*	0	5.5	11.0	18.2
2	0.5	4.6	9.1	17.6
3	1.0	4.1	7.9	17.2
4	2.0	3.8	7.5	17.8
5	4.0	3.7	7.5	18.5

\* – Extrapolation to infinite diluted solution  $C \rightarrow 0 \text{ g/dm}^3$ .

$$E_D = 17.9 \pm 0.4 \text{ kJ/mole}, \quad \gamma_D = 1.31 \pm 0.05 \text{ rel. un.}$$

Temperature dependence of diffusion coefficient of  $\text{C}_{60}$ -tris-malonate in water was described with the help of both methods:

Arrhenius equation:

$$D_T = D_0 \exp(-E_D/RT), \quad (2)$$

where:  $D_T$  is the diffusion coefficient at temperature  $T(\text{K})$ ,  $D_0$  is the diffusion pre-exponent,  $E_D$  is the diffusion activation energy,

and Vant-Hoff rule multiplication:

$$\gamma_D = D_{T+10}/D_T. \quad (3)$$

One can see from the data following:

1. It seems the diffusion coefficients ( $D$ ) of  $\text{C}_{60}$ -tris-malonate in water solutions have much lower values ( $D$  on the order of  $10^{-8} \text{ cm}^2/\text{s}$ ). Than those for their analogs – non-modified light fullerenes –  $\text{C}_{60}$  and  $\text{C}_{70}$  in organic (mainly aromatic) solvents [7] ( $D$  on the order of  $10^{-7}$  –  $10^{-6} \text{ cm}^2/\text{s}$ ).

2. Additionally, the authors of [7] tried to crudely estimate the radius of the particles in the diffusion processes ( $r_D$ ) according to the Smolukhovskiy – Stokes – Einstein law (spherical approximation):

$$D = \frac{kT}{6\pi\eta r_D}, \quad (4)$$

where:  $D$  – diffusion coefficient,  $T$  – temperature (K),  $k$  – Boltzmann constant,  $\eta$  – dynamic viscosity of the solvent,  $r_D$  – radius of spherical particle.

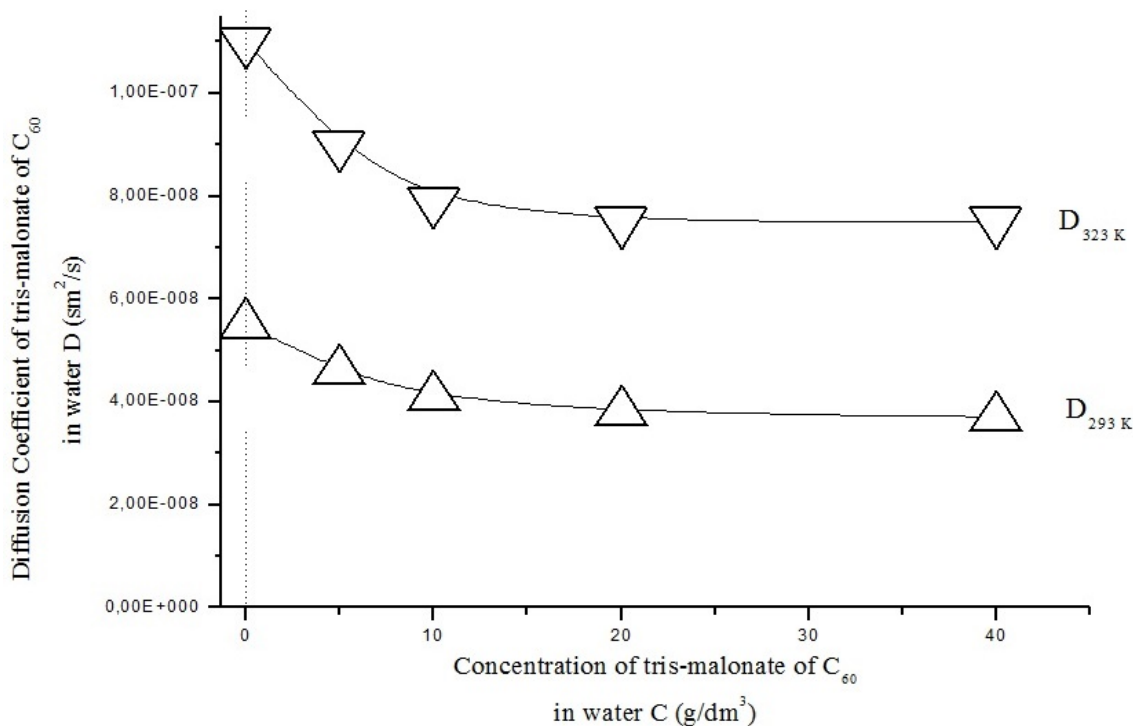


FIG. 1. Diffusion coefficient of C<sub>60</sub>-tris-malonate in water

In different solvents they obtained values for  $r_D$  ranging from 0.4 – 3 nm; the considerable growth of  $r_D$  when comparing non-associated and non-solvated light fullerenes ( $r_D \approx 0.35$  nm [8]) may be the result of light fullerene association in clusters and perhaps simultaneous intensive interaction of fullerenes with solvent molecules.

In the case of our water soluble light fullerene derivatives, one can expect a higher degree of association and hydration, which was proven earlier by light scattering experiments [5]. In that work, the formation of three types of aggregates was observed with the following characteristic radii:  $r_D \approx 20 - 40$  nm (for type 1 aggregates),  $r_D \approx 150 - 250$  nm (for type 2 aggregates),  $r_D \approx 2000 - 3000$  nm (for type 3 aggregates). Simultaneously, non-aggregated forms were not found at all [5]. Such a stepwise hierarchical association model was proven earlier in analog binary C<sub>60</sub>(OH)<sub>n</sub> fulleranol – H<sub>2</sub>O – systems see, for example [9, 10].

3. So, also according to the Smolukhovskiy – Stokes – Einstein law (using the temperature dependence of the dynamic viscosity of the solvent – water – see Fig. 2), one can obtain the following radius values for the particles in the diffusion processes in the C<sub>60</sub>[=C(COOH)<sub>2</sub>]<sub>3</sub> – H<sub>2</sub>O system:  $r_D = 30 - 60$  nm. From these data, we can confirm that practically, only type 1 C<sub>60</sub>-tris-malonate aggregates participate in mass transport diffusion processes. Other type aggregates are not realized in solution (monomers of C<sub>60</sub>-tris-malonate [5]), or are not labile enough for effective mass transport (type 2 and -3 aggregates – [5]). The fact that diffusion coefficients decrease while the concentration of C<sub>60</sub>-tris-malonate increases may be explained by the proposition that the relative mass fraction of main transport particles (type 1 aggregates of C<sub>60</sub>[=C(COOH)<sub>2</sub>]<sub>3</sub>) decreases with concentration growth, while the concentration of larger, non-mobile particles increases.

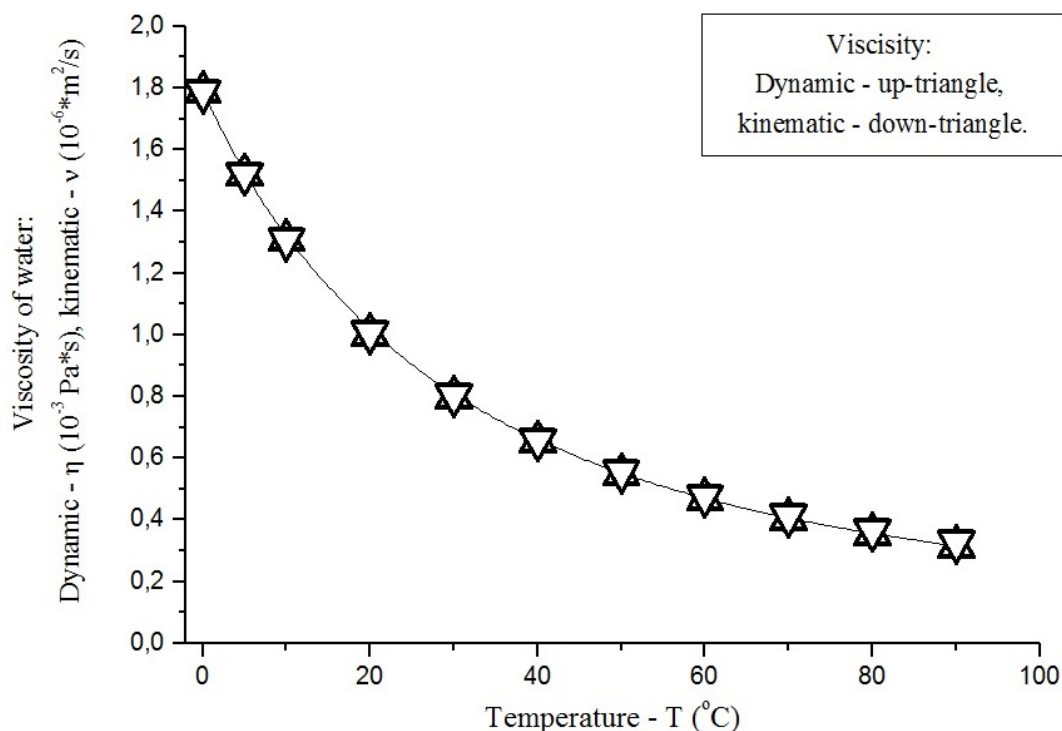


FIG. 2. Temperature dependence of the dynamic and kinematic viscosity of the water

### 3. Viscosity of $C_{60}[C(COOH)_2]_3$ water solutions at 20 and 50 °C

The dynamic viscosity of  $C_{60}$ -tris-malonate in aqueous solutions was derived using the capillary viscosity-meter method by the determining the liquid flow times of the solutions through the vertical capillary (the glass viscosity-meter is of the type 'VNJ' (Ecochim. Rus. – Ukr.))

The determined kinetic viscosity of  $C_{60}$ -tris-malonate in aqueous solutions was additionally used to derive the densities at constant temperature with the help of quartz pycnometer [2].

Air thermostats were used, with an accuracy of temperature fixation of  $\Delta T = \pm 0.5$  K.

According to Newton's law of viscosity (internal friction), the dynamic viscosity for 'Newtonian liquids' ( $\eta$ ) is defined as:

$$F_{l-f} = \eta \Delta V S, \quad (5)$$

where:  $F_{l-f}$  – is the force of the internal friction,  $\Delta V = \text{grad } V = \partial V / \partial x$  ( $x$  – is the direction, perpendicular to the vector of the velocity of liquid layer –  $V$ ),  $S$  – surface of contact layers.

Kinematic viscosity ( $\nu$ ) is defined as:

$$\nu = \eta / \rho, \quad (6)$$

where:  $\rho$  – is the density of liquid.

Values for  $\eta$ , as a rule, are measured in (Pa·s) or in (P (Poise – lat.) = Пз (Пяз – rus.) = Pa·s/10), values  $\nu$  – in (m<sup>2</sup>/s, cm<sup>2</sup>/s) or in non-systematic units (°E – Engler degree):

$$\nu = 0.073 \text{ } ^\circ\text{E} - 0.063 \text{ } ^\circ\text{E}. \quad (7)$$

Temperature dependence of the dynamic viscosity of  $C_{60}$ -tris-malonate in aqueous solutions was described with both methods.

The analog of Arrhenius equation for the viscous current (also named as equation of Frencl – Andrade [12]):

$$\eta_T = \eta_0 \exp(+E_\eta/RT), \tag{8}$$

where:  $\eta_T$  is dynamic viscosity at temperature  $T(K)$ ,  $\eta_0$  is dynamic viscosity pre-exponent,  $E_\eta$  is energy of activation of the viscous current, and analog of Vant-Hoff rule multiplication for the viscous current –  $\gamma_\eta$ :

$$\gamma_\eta = \eta_{T-10}/\eta_T. \tag{9}$$

Viscosity data are represented in the Table 2 and Fig. 3.

TABLE 2. Concentration dependence of the dynamic and kinematic of C<sub>60</sub>-tris-malonate in aqueous solutions at 298 and 323 K

Number of solution No.	Concentration of C <sub>60</sub> tris-malonate C (mass.%)	Dynamic viscosity $\eta_{298}$ (Pa · s · 10 <sup>-3</sup> )	Kinematic viscosity $\nu_{298}$ (m <sup>2</sup> /s · 10 <sup>-6</sup> )	Dynamic viscosity $\eta_{323}$ (Pa · s · 10 <sup>-3</sup> )	Viscosity activation energy according to the Arrhenius equation – $E_\eta$ (kJ/mole)
1	0.0	0.894	0.893	0.548	15.7
2	0.00001	0.886	0.885	0.544	15.6
3	0.0001	0.872	0.872	0.536	15.6
4	0.001	0.849	0.849	0.523	15.5
5	0.01	0.777	0.777	0.480	15.4
6	0.1	0.641	0.641	0.398	15.2
7	0.5	0.643	0.642	0.401	15.1
8	1.0	0.645	0.643	0.404	14.9

$$E_\eta = 15.3 \pm 0.3 \text{ kJ/mole}, \quad \gamma_\eta = 1.21 \pm 0.05 \text{ rel. un.}$$

From the data in Fig. 3 and Table 2 one can see the following:

1. Values for  $\eta(C)$  decrease while the concentration increases in dilute solutions and becomes nearly constant in more concentrated ( $C > 0.1$  mass.% of C<sub>60</sub>-tris-malonate in water) at both temperatures.

2. To describe the dependence of the dynamic viscosity on the concentration of C<sub>60</sub>-tris-malonate in aqueous solutions ( $C$ ) at a constant temperature –  $\eta(C)$  (in the initial region of the function ( $C \rightarrow 0$ )), one can use the empirical Bachinskiy equation:

$$\eta = \frac{c_B}{V_m - b_B}, \tag{10}$$

where:  $V_m$  is average molar volume of water solution of C<sub>60</sub>-tris-malonate (can be determined from the density measurements – [2]);  $c_B$  and  $b_B$  are constants of the Bachinskiy equation and may be dependent on temperature and the type of the system only. So, using Taylor decomposition of the function  $\eta(C)$  in the region  $C > 0$ , one can easily obtain the following equations for the calculation of the constants of Bachinskiy equation:

$$b_B = \frac{V_m^0(\eta^0 - \eta^x) - \eta^x(\partial V_m/\partial x)^0 x}{\eta^0 - \eta^x}, \tag{11}$$

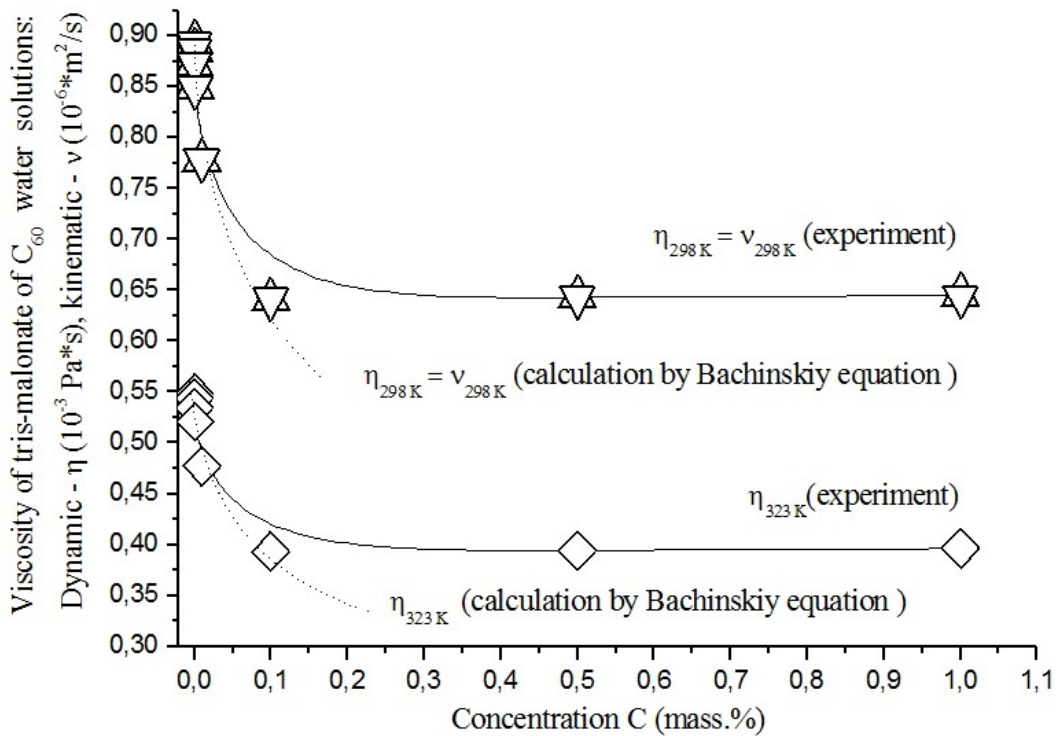


FIG. 3. Dynamic and kinematic viscosity of  $C_{60}$ -tris-malonate in aqueous solutions at 298 K and 323 K

$$c_B = \frac{\eta^0 \eta^x (\partial V_m / \partial x)^0 x}{\eta^0 - \eta^x}, \quad (12)$$

where:  $V_m^0$  – average molar volume of pure solvent – water,  $\eta^0$  – the dynamic viscosity of the solvent,  $C$  – concentration in mass.% and  $x$  – molar fraction of  $C_{60}$ -tris-malonate in aqueous solutions:

$$x = \frac{C}{1026[C/1026 + (100 - C)/18]}, \quad (13)$$

$\eta^x$  – the dynamic viscosity of solution with molar fraction  $x$ ,  $(\partial V_m / \partial x)^0 = \lim_{x \rightarrow 0} (\partial V_m / \partial x) \approx \text{const} \approx 1002 \text{ cm}^3/\text{mole}$  [2].

Calculation of the dependence  $\eta(C)$  using equations (10) – (12) is represented in Fig. 3. One can see more or less good agreement between the experimental and calculated data in comparatively dilute aqueous  $C_{60}$ -tris-malonate solutions – quick drop of  $\eta$  while  $C$  is increasing from  $C \approx 0 \rightarrow C \approx 0.1$  mass.%. Such decrease of the function  $\eta(C)$ , even in dilute solutions is atypical enough for the solutions with high molecular weight compounds. In more concentrated solutions,  $C \approx 0.1 \rightarrow C \approx 1.0$  mass.%, the results between the experimental and the calculated differed considerably, and according to our point of view, naturally increases (see Fig. 3) – the function  $\eta(C)$  continues to decrease and becomes nearly constant. These facts may be explained by the following: there two influences, which cause the change of  $\eta(C)$  in different directions. First – the destruction of hydrogen bonds structure between solvent molecules, can decrease  $\eta$  (this influence is stronger in dilute solutions), second – increasing the concentration of the main mass transport species (in the direction perpendicular to the velocity vector of the liquid layers), can only increase  $\eta$  (this influence becomes more pronounced at higher concentrations). In the  $1.0 \geq C \geq 0.1$  mass.% concentration range these two factors have approximately equal weight, and as a result,  $\eta(C)$  crosses through a ‘soft minimum’.

3. Dependencies of dynamic and kinematic viscosity  $\eta(C)$  and  $\nu(C)$  are naturally approximately equal at 298 K, because densities of aqueous C<sub>60</sub>-tris-malonate are very close to  $\rho \approx 1 \text{ g/cm}^3$ .

4. Values for  $\eta(C)$  decrease at higher temperatures over the entire concentration range ( $0.0 < C < 1 \text{ mass.}\%$ ).

#### 4. Conclusions

The investigation of concentration dependence of mass transport properties (diffusion coefficients and viscosity) of water soluble light fullerene tris-malonate – C<sub>60</sub>[=C(COOH)<sub>2</sub>]<sub>3</sub> in aqueous solutions in concentration range (0 – 1 mass.%) and at 298 and 323 K was performed and the results obtained were provided. The diffusion and viscous current activation energies were calculated. It was shown, that the type 1 aggregates of C<sub>60</sub>[=C(COOH)<sub>2</sub>]<sub>3</sub> with the linear dimensions on the order of tens of nm determine the mass transport properties in aqueous solutions over the entire concentration range tested.

#### Acknowledgement

Investigations were supported by Russian Foundation for Basic Research - RFBR (Project No. 15-08-08438).

#### References

- [1] K.N. Semenov, N.A. Charykov, A.S. Kritchenkov et al. Synthesis and identification water-soluble tris-malonate of light fullerene – C<sub>60</sub>[=C(COOH)<sub>2</sub>]<sub>3</sub>. *Nanosystems: Physics, Chemistry, Mathematics*, 2014, **5** (2), P. 315–319.
- [2] K.N. Semenov, N.A. Charykov, A.S. Kritchenkov et al. Volume properties of water solutions and refraction at 25 °C water soluble tris-malonate of light fullerene – C<sub>60</sub>[=C(COOH)<sub>2</sub>]<sub>3</sub>. *Nanosystems: Physics, Chemistry, Mathematics*, 2014, **5** (3), P. 427–434.
- [3] K.N. Semenov, N.A. Charykov, A.S. Kritchenkov et al. Poly-thermal solubility and complex thermal analysis of water soluble tris-malonate of light fullerene – C<sub>60</sub>[=C(COOH)<sub>2</sub>]<sub>3</sub>. *Nanosystems: Physics, Chemistry, Mathematics*, 2014, **5** (3), P. 435–440.
- [4] K.N. Semenov, N.A. Charykov, A.S. Kritchenkov et al. Concentration dependence of electric conductivity and hydrogen indicator for water solutions of water soluble tris-malonate of light fullerene –C<sub>60</sub>[=C(COOH)<sub>2</sub>]<sub>3</sub>. *Nanosystems: Physics, Chemistry, Mathematics*, 2014, **5** (5), P. 709–717.
- [5] K.N. Semenov, N.A. Charykov, A.S. Kritchenkov et al. Concentration dependence of the dimension of the associates of water soluble tris-malonate of light fullerene –C<sub>60</sub>[=C(COOH)<sub>2</sub>]<sub>3</sub> in water solutions at 25 °C. *Nanosystems: Physics, Chemistry, Mathematics*, 2015, **6** (2), P. 294–298.
- [6] B.S. Bokshstein, M.I. Mendeleev, D.J. Srolovitz. *Thermodynamics and Kinetics in Materials Science. A Short Course*. Oxford University Press, Oxford, 2005, P. 167–171.
- [7] V.N. Bezmel'nitsin, A.V. Eletskiy, M.V. Okun'. Fullerenes in solutions. *Uspekhi Physicheskikh Nauk*, 1998, **168** (11), P. 1195-1220 [in Russian].
- [8] L.N. Sidorov, M.A. Yurovskaya. *Fullerenes*. Examen, Moscow, 2005, 608 p. [in Russian].
- [9] K.N. Semenov, N.A. Charykov, V.A. Keskinov. Fullerenol Synthesis and Identification. Properties of Fullerenol Water Solutions. *J. Chem. Eng. Data*, 2011, **56**, P. 230–239.
- [10] K.N. Semenov, V.A. Keskinov, N.A. Charykov, et al. The fullerenol-d solubility in the fullerenol-d-inorganic salt-water ternary systems at 25 °C. *Industrial and Engineering Chemical Research*, 2013, **52**, P. 16095–16100.
- [11] J. Kestin, M. Sokolov, W.A. Wakeham. Viscosity of liquid water in the range from –8 to 150 °C. *J. Phys. Chem. Ref. Data*, 1978, **7** (3), P. 941–949.
- [12] A.V. Zakharov. Effect of a bounding surface on the rotational viscosity of liquid crystals. *Physics of the Solid State*, 1998, **40** (10), P. 1765.

## Atomic order and metallic nanoclusters in $\text{Na}_4\text{Ir}_3\text{O}_8$

M. V. Talanov<sup>1,\*</sup>, V. B. Shirokov<sup>2</sup>, V. M. Talanov<sup>3</sup>

<sup>1</sup>Research Institute of Physics, Southern Federal University, Rostov-on-Don, Russia

<sup>2</sup>Southern Scientific Center of Russian Academy of Sciences, Rostov-on-Don, Russia

<sup>3</sup>South-Russian State Polytechnical University, Novocherkassk, Russia

tmikle-man@mail.ru, shirokov-vb@rambler.ru, \*valtalanov@mail.ru

PACS 61.50.Ks; 36.40.-c

DOI 10.17586/2220-8054-2015-6-3-442-450

A theory for forming Ir-atomic nanoclusters in a dielectric matrix of  $\text{Na}_4\text{Ir}_3\text{O}_8$  structure and spinel-like structures is suggested. The atomic order in the  $\text{Na}_4\text{Ir}_3\text{O}_8$  structure is investigated by group-theoretical methods of phase transition theory. The critical irreducible representation  $\tau$ , generating appearance of enantiomorphic  $P4_132$  ( $P4_332$ )-phases from high symmetry spinel-like phase with space group  $\text{Fd}\bar{3}\text{m}$ , is six dimensional irreducible representation  $k_{10}(\tau_1)$  (in Kovalev designation). Ir and Na atoms form an intriguing atom ordering, giving rise to a network of corner shared Ir triangles, called a hyperkagome lattice. It is shown that inside the hyperkagome lattice, there are closed metal contours of chemical bonds formed by Ir-clusters – decagons. Unusual physical properties of solid solutions on the basis of  $\text{Na}_4\text{Ir}_3\text{O}_8$  are expected. The existence of hyperkagome lattices in six types in ordered spinel structures is theoretically predicted.

**Keywords:** hyper-kagome order, ordered spinels, decagons, nanoclusters.

*Received: 7 January 2015*

*Revised: 24 February 2015*

### 1. Introduction

Oxides with the  $\text{A}[\text{B}_2]\text{O}_4$  spinel structure containing atoms of transition elements in octahedral positions (atoms B), are characterized by a large variety of physical properties, among which are superconductivity, charging ordering, heavy fermion behavior, unusual magnetic properties in strong magnetic fields and others. In many cases, these important physical properties are connected with a structural feature of spinels – a three-dimensional network of the tetrahedra formed by octahedral B-cations. A network of these tetrahedra is called a pyrochlore lattice, for B-cations are formed in pyrochlore structure such a sublattice as B-cations in spinel structure. P.W. Anderson was the first who showed that B- sublattice in spinel structures was geometrically frustrated and caused unusual physical properties of this class of materials [1]. The term “geometrical frustration” describes structures with local order generated by lattice geometry. Frustration arises when the geometry of a system allows for a set of degenerate ground states. Such highly degenerate systems are extremely sensitive to thermal and quantum fluctuations, and thereby intriguing classical and quantum ground states may emerge via “order by disorder”.

One of compounds in which it is possible to expect the manifestation of unusual physical properties is  $\text{Na}_4\text{Ir}_3\text{O}_8$ , which has spinel-like structure. The geometrical frustration of spins in this substance causes the existence of exotic electronic and structural state – spin liquid. The crystals of  $\text{Na}_4\text{Ir}_3\text{O}_8$  are the only substances in which an electronic subsystem is 3D spin liquid [2].

The purpose of this work is the theoretical research of the symmetry and structural conditions for the appearance of atomic hyperkagome order in structures of ordered low symmetric modifications of spinels and spinel-like substances.

## 2. Atomic hyperkagome order in $\text{Na}_4\text{Ir}_3\text{O}_8$ structures

The atomic order in  $\text{Na}_4\text{Ir}_3\text{O}_8$  was investigated by group-theoretical methods of phase transition theory. Structural studies allowed the authors [2] to establish space group  $P4_132$  or  $P4_332$  and some features of the  $\text{Na}_4\text{Ir}_3\text{O}_8$  structure. It was shown that in this structure there is hyperkagome sublattice in positions of which there are  $\text{Ir}^{4+}$  ions in a low-spin state ( $t_{2g}^5$ ) with  $S=1/2$ .

In this paper, we theoretically describe the formation of atom hyperkagome lattice in  $\text{Na}_4\text{Ir}_3\text{O}_8$  on the basis of hypothetical parent phase conception. This parent phase has a spinel-like structure (space group  $\text{Fd}3\text{m}$ ) and a  $[\text{Na}_{1/2}\text{Ir}_{3/2}]^{16(d)}[\text{Na}_{3/2}]^{16(c)}\text{O}_4^{32(e)}$  composition.

This structure differs from spinel one by the following:

- positions 8 (a) are vacant;
- positions 16 (c), occupied by 75%  $\text{Na}^{1+}$  ions in  $\text{Na}_4\text{Ir}_3\text{O}_8$  structure [2, 3], are vacant in spinel structure.

The critical order parameter which induces hypothetical phase transition has been stated. The critical irreducible representation (IR)  $\tau$ , generating appearance of enantiomorphic  $P4_132$  ( $P4_332$ )-phases from high symmetry spinel-like phase with space group  $\text{Fd}3\text{m}$ , is six dimensional irreducible representation  $\mathbf{k}_{10}(\tau_1)$  (table 1). IR designations are given according to Kovalev [4]:  $\mathbf{k}_{10}(\tau_i)$  – is the star of wave vector;  $\tau_{i,-}$  is a number of corresponding IR.

Stratification of Wyckoff positions in spinel-like structure with space group  $\text{Fd}3\text{m}$  occurs as the result of a hypothetical phase transformation that takes place.

The 16(d) position in the parent structure was stratified into positions 4(b) and 12(d) in  $P4_132$  ( $P4_332$ )-structure, 16(c) position was stratified into positions 4(a) and 12(d), the 32(e) position was stratified into positions 8(c) and 24(e). Taking into account the occupation of 16(c) positions equal to 75% [2, 3], structural formula  $\text{Na}_4\text{Ir}_3\text{O}_8$  in  $P4_132$  ( $P4_332$ )-phase can be presented as  $[\text{Na}_{1/2}^{4(b)}\text{Ir}_{3/2}^{12(d)}][\text{Na}_{3/8}^{4(a)}\text{Na}_{9/8}^{12(d)}]\text{O}_8^{8(c)}\text{O}_3^{24(e)}$ .

It should be noted that in  $\text{Na}_4\text{Ir}_3\text{O}_8$ , there cannot be charge ordering of iridium atoms in principle, for this atom takes only one position 12(d) with site symmetry  $2(C_2)$  in  $P4_132$  ( $P4_332$ )-phase. This means that all the Ir sites and Ir-Ir bonds are equivalent.

The analysis of mechanical, permutation and orbital representations of parent structure allowed us to establish that that the structure of  $\text{Na}_4\text{Ir}_3\text{O}_8$  is formed as a result of atoms displacements of sodium, iridium and oxygen, and also atoms ordering of sodium, iridium and oxygen [5-8]. Ordering of all atoms occurs according to the type 1:3. (Fig. 1). Enantiomorphic forms of  $\text{Na}_4\text{Ir}_3\text{O}_8$  are mirror antipodes. Their structures coincide with each other only in the reflection in the mirror (Fig. 1). Chemical and physical properties of the enantiomorphic modifications of  $\text{Na}_4\text{Ir}_3\text{O}_8$  are the same (except optical activity) [9-15].

In the structure of this substance there is a pyrochlore sublattice in which each tetrahedron is occupied by three Ir and one  $\text{Na}^{12(d)}$ . These Ir and Na atoms form an intriguing atom ordering, giving rise to a network of corner shared Ir triangles, called a hyperkagome lattice [14].

Metal atoms in  $\text{Na}_4\text{Ir}_3\text{O}_8$  structure form two different networks of tetrahedra:  $[\text{Na}_3^{12(d)}\text{Na}^{4(a)}]$  and  $[\text{Ir}_3^{12(d)}\text{Na}^{4(b)}]$  (Fig. 2). Each of these networks forms its own hyperkagome sublattice. The hyperkagome sublattice in the network of  $[\text{Na}_3^{12(d)}\text{Na}^{4(a)}]$  tetrahedra is formed

TABLE 1. Symmetrically structural identification of the phase states in low-symmetry phases ( $G_D$ ) induced by the IR  $k_{10}(\tau_1)$  of the space group Fd3m

$\vec{\varphi}$	$G_D$	Splitting of Wyckoff position of spinel-like structure of parent phase		
		8(a)	16(c), 16(d)	32(e)
$0\varphi 0\varphi 0-\varphi$	P4 <sub>1</sub> 32 (P4 <sub>3</sub> 32)	1(8):3(C <sub>3</sub> )	1(4):32(D <sub>3</sub> )+1(12):2(C <sub>2</sub> )	1(8):3(C <sub>3</sub> )+1(24):1(C <sub>1</sub> )
$\varphi\varphi\varphi\varphi\varphi\varphi$	R $\bar{3}$ m	1(4):3m(C <sub>3v</sub> )+ +1(12):m(C <sub>s</sub> )	1(2): $\bar{3}$ m(D <sub>3d</sub> )+1(6):2/m(C <sub>2h</sub> )+ +1(12):m(C <sub>s</sub> )+1(12):2(C <sub>2</sub> )	1(4):3m(C <sub>3v</sub> )+3(12): :m(C <sub>s</sub> )+1(24):1(C <sub>1</sub> )
00000 $\varphi$	P4 <sub>1</sub> 22 (P4 <sub>3</sub> 22)	1(16):2(C <sub>2</sub> )	2(16):2(C <sub>2</sub> )	2(32):1(C <sub>1</sub> )
$0\varphi 00\varphi 0$	P $\bar{4}$ 2 <sub>1</sub> m	1(4):mm2(C <sub>2v</sub> )+1(4): : $\bar{4}$ (S <sub>4</sub> ) +1(8):m(C <sub>s</sub> )	2(8):m(C <sub>s</sub> )+1(16):1(C <sub>1</sub> )	4(8):m(C <sub>s</sub> )+2(16):1(C <sub>1</sub> )
00 $\varphi\varphi$ 00	Pbmn	1(16):m(C <sub>s</sub> )	2(8):2/m(C <sub>2h</sub> )+1(16):2(C <sub>2</sub> )	2(16):m(C <sub>s</sub> )+1(32):1(C <sub>1</sub> )
$\varphi_1\varphi_2\varphi_1\varphi_2\varphi_1\varphi_2$	R32	1(4):3(C <sub>3</sub> )+ +1(12):1(C <sub>1</sub> )	1(2):32(D <sub>3</sub> )+3(6):2(C <sub>2</sub> )+ +1(12):1(C <sub>1</sub> )	1(4):3(C <sub>3</sub> )+5(12):1(C <sub>1</sub> )
$\varphi_1 00\varphi_2 00$	P2 <sub>1</sub> 2 <sub>1</sub> 2	2(4):2(C <sub>2</sub> )+ +1(8):1(C <sub>1</sub> )	4(8):1(C <sub>1</sub> )	8(8):1(C <sub>1</sub> )
0000 $\varphi_1\varphi_2$	P222 <sub>1</sub>	1(16):1(C <sub>1</sub> )	4(8):2(C <sub>2</sub> )	4(16):1(C <sub>1</sub> )
$0\varphi_1 0\varphi_2 0-\varphi_1$	P4 <sub>1</sub> 2 <sub>1</sub> 2 (P4 <sub>3</sub> 2 <sub>1</sub> 2)	1(16):1(C <sub>1</sub> )	2(8):2(C <sub>2</sub> )+1(16):1(C <sub>1</sub> )	4(16):1(C <sub>1</sub> )
$\varphi_1\varphi_1\varphi_2\varphi_2-\varphi_1-\varphi_1$	C2/m	2(4):m(C <sub>s</sub> )+ +1(8):1(C <sub>1</sub> )	2(2):2/m(C <sub>2h</sub> )+1(4): $\bar{1}$ (C <sub>i</sub> )+ +1(4):m(C <sub>s</sub> )+1(4):2(C <sub>2</sub> )+ +2(8):1(C <sub>1</sub> )	4(4):m(C <sub>s</sub> )+6(8):1(C <sub>1</sub> )
$\varphi_1 0\varphi_2 0\varphi_3 0$	P2 <sub>1</sub> 2 <sub>1</sub> 2 <sub>1</sub>	2(8):1(C <sub>1</sub> )	4(8):1(C <sub>1</sub> )	8(8):1(C <sub>1</sub> )
$\varphi_1 0\varphi_2\varphi_3-\varphi_1 0$	C222 <sub>1</sub>	2(8):1(C <sub>1</sub> )	4(4):2(C <sub>2</sub> )+2(8):1(C <sub>1</sub> )	8(8):1(C <sub>1</sub> )
$\varphi_1\varphi_1\varphi_2\varphi_2\varphi_3\varphi_3$	P $\bar{1}$	4(4):1(C <sub>1</sub> )	v4(2): $\bar{1}$ (C <sub>i</sub> )+6(4):1(C <sub>1</sub> )	16(4):1(C <sub>1</sub> )
$\varphi_1\varphi_1\varphi_2\varphi_3\varphi_3\varphi_2$	Cm	4(2):m(C <sub>s</sub> )+ +2(4):1(C <sub>1</sub> )	4(2):m(C <sub>s</sub> )+6(4):1(C <sub>1</sub> )	8(2):m(C <sub>s</sub> )+12(4):1(C <sub>1</sub> )
$\varphi_1\varphi_2\varphi_3\varphi_4\varphi_3\varphi_4$	C2	4(4):1(C <sub>1</sub> )	4(2):2(C <sub>2</sub> )+6(4):1(C <sub>1</sub> )	16(4):1(C <sub>1</sub> )
$0\varphi_1 0\varphi_2\varphi_3\varphi_4$	P2 <sub>1</sub>	4(4):1(C <sub>1</sub> )	8(4):1(C <sub>1</sub> )	16(4):1(C <sub>1</sub> )
$\varphi_1\varphi_2\varphi_3\varphi_4\varphi_5\varphi_6$	P1	8(2):1(C <sub>1</sub> )	16(2):1(C <sub>1</sub> )	32(2):1(C <sub>1</sub> )

Notes. Designation for order parameters  $k_{10} - \varphi$ . One of the enantiomorphic space groups is recorded in parentheses in the second column. The number and multiplicity (in parentheses) of the Wyckoff position are indicated. After the colon, the local symmetry of the Wyckoff position is given. For example, the record of 1(8):3(C<sub>3</sub>)+1(24):1(C<sub>1</sub>) means that Wyckoff position 32e of group Fd3m in the low-symmetry phase  $G_D$  with space group P4<sub>1</sub>32 stratified into one eightfold Wyckoff position with local symmetry 3(C<sub>3</sub>) and one 24-fold Wyckoff position with local symmetry 1(C<sub>1</sub>).

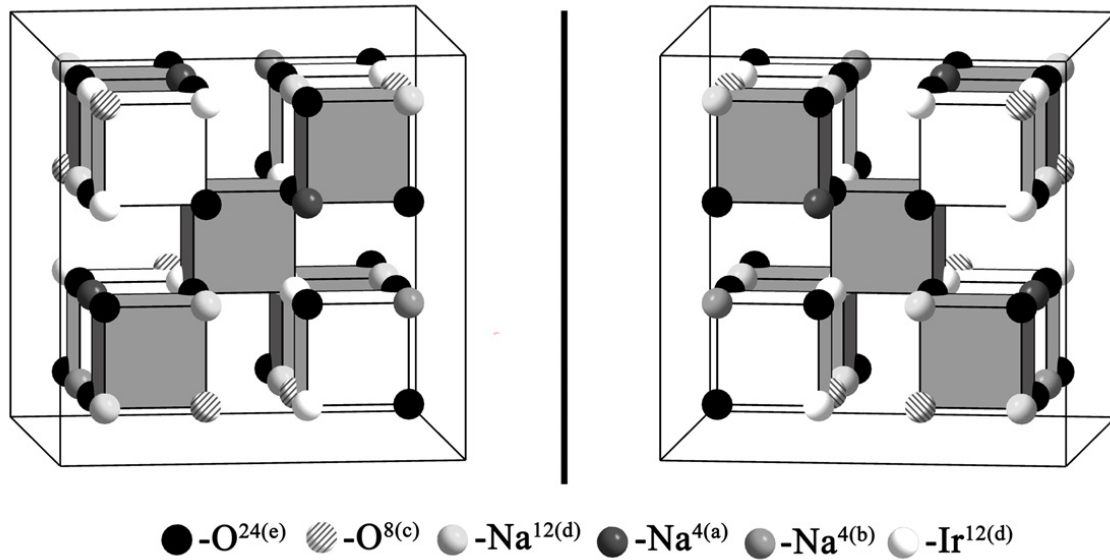


FIG. 1. Ordered cation and anion distributions in enantiomorphous structures  $P4_332$ - and  $P4_131$ - $\text{Na}_4\text{Ir}_3\text{O}_8$  modifications (without atoms displacements). The line between the structures means mirror

by  $[\text{Na}_3^{12(d)}]_n$  triangles. This hyperkagome sublattice has an artificial character from the point of view of physics because there is no principal difference in properties of  $\text{Na}^{12(d)}$  and  $\text{Na}^{4(a)}$  ions. The  $[\text{Ir}_3^{12(d)}]_n$  – hyperkagome sublattice in  $\text{Na}_4\text{Ir}_3\text{O}_8$  structure has significant physical importance. In this hyperkagome sublattice, in each tetrahedron, three vertices occupy magnetic iridium ions  $\text{Ir}^{12(d)}$  and one vertex is occupied by a sodium ion  $\text{Na}^{4(b)}$ .

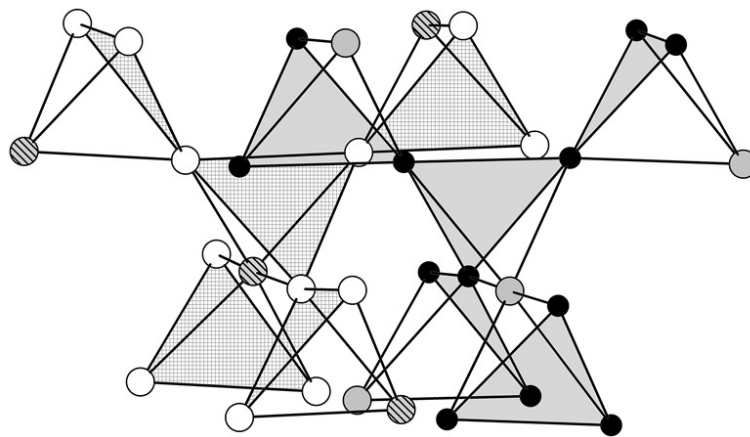


FIG. 2. Two networks of tetrahedra  $[\text{Na}_3^{12(d)}\text{Na}^{4(a)}]$  and  $[\text{Ir}_3^{12(d)}\text{Na}^{4(b)}]$  forming two hyper-kagome sublattices. One sublattice atoms formed Ir atoms (this sublattice is painted in gray), the second sublattice formed by atoms  $\text{Na}^{12(d)}$  (this sublattice is hatched pattern)

Four tetrahedra form hypertetrahedra  $[\text{Ir}_3^{12(d)}\text{Na}^{4(b)}]_4$  (Fig. 3). A hyperkagome-lattice is formed from a network of corner shared  $[\text{Ir}_3^{12(d)}\text{Na}^{4(b)}]_4$  tetrahedra as follows: in every tetrahedron a right triangle  $[\text{Ir}_3^{12(d)}]$  is formed from iridium atoms.

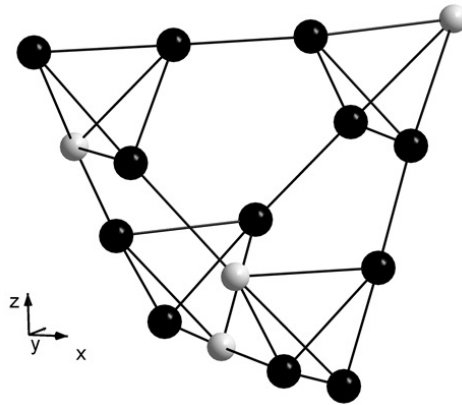


FIG. 3. Hypertetrahedron  $[\text{Ir}_3^{12(d)}\text{Na}^{4(b)}]_4$  in structure  $\text{Na}_4\text{Ir}_3\text{O}_8$

As all Ir positions in structure of  $\text{Na}_4\text{Ir}_3\text{O}_8$  are equivalent, all distances of Ir-Ir are identical and equal to  $3.112\text{\AA}$ . These right triangles form a network  $[\text{Ir}_3^{12(d)}]_n$ . (Fig. 4). This network of connected triangles forms unique atom hyperkagome order [2] (Fig. 5, 6).

In a hyperkagome lattice, it is possible to allocate the module from three crossed minimum closed contours (Fig.7). These contours are formed by Ir-Ir chemical bonds. The module consists of 14 iridium triangles. Two of these triangles are general for all three minimum contours. The minimum (or shortest) closed contour includes ten Ir-Ir bonds. These ten Ir atoms form a crown-like cluster – so-called decagon [8] (Fig. 8). The perimeter of all minimum contours is identical and equal to  $31.12\text{ \AA}$ . The greatest distance between opposite Ir atoms in decagon is equal to  $10.775\text{ \AA}$ , and its maximum width –  $5.659\text{ \AA}$ .

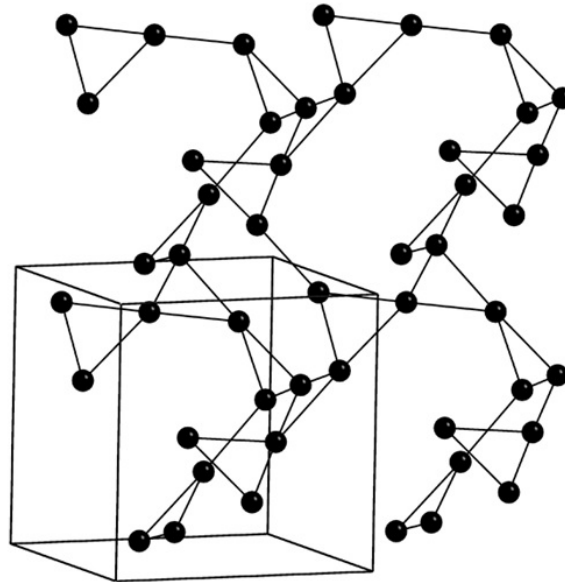


FIG. 4. A hyperkagome sublattice. A hyperkagome sublattice is a cubic lattice with 12 sites in a unit cell, it is a network of corner-sharing Ir-triangles

$P4_132$  ( $P4_332$ )-spinel phases are widely spread types of low-symmetry ordered enantiomorphic modifications of spinel structures. They are formed as a result of phase transitions from spinel structures. These phases are generated by critical irrep  $\mathbf{k}_{10}(\tau_1)$  [5, 6, 14]. Irrep

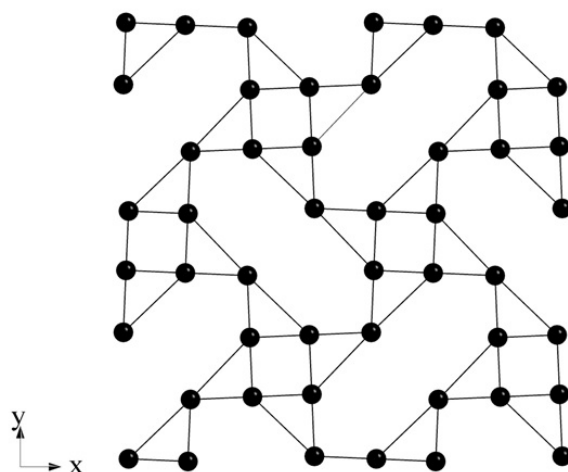


FIG. 5. A hyperkagome sublattice. View of hyperkagome sublattice along the  $[001]$  axes

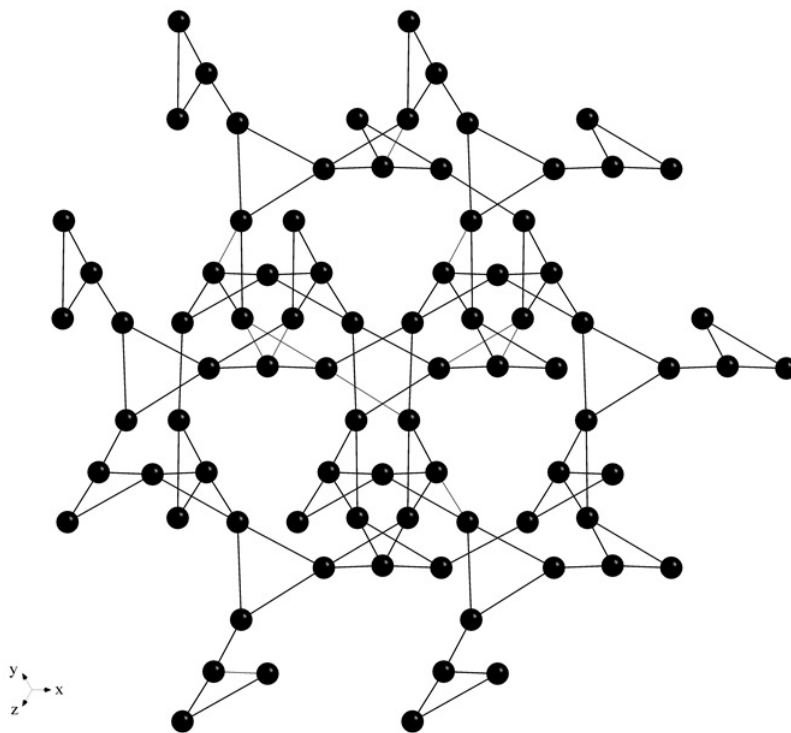


FIG. 6. A hyperkagome sublattice: general picture

TABLE 2. The types of binary cation ordering of 1:3 types in Wyckoff position 16(d) of spinel structure

N	Order parameters	Symbol of space group	$V_0/V$	Structural formula
1	$(\xi, -\xi, \xi)^7$	$R\bar{3}2/m$ (N166)	1	$A^{(c)}\underline{B_{1/2}^{(b)}}\underline{B_{3/2}^{(e)}}\underline{X^{(c)}}\underline{X_3^{(h)}}$
2	$(\varphi, 0, \varphi, 0, \varphi, 0)^3$	$P\bar{4}3m$ (N215)	4	$A_{1/8}^{(a)}A_{3/8}^{(c)}A_{1/2}^{(e)}\underline{B_{1/2}^{(e)}}\underline{B_{3/2}^{(i)}}\underline{X_{1/2}^{(e)}}\underline{X_{1/2}^{(e)}}\underline{X_{3/2}^{(i)}}\underline{X_{3/2}^{(i)}}$
3	$(0, \varphi, 0, \varphi, 0, -\varphi)^1$	$P4_332$ (N212) $P4_132$ (N213)	4	$A^{(c)}\underline{B_{1/2}^{(a)}}\underline{B_{3/2}^{(d)}}\underline{X^{(c)}}\underline{X_3^{(e)}}$
4	$(0, \varphi, 0, \varphi, 0, -\varphi)^3(\xi)^4\text{sec.}$	$P\bar{4}3m$ (N215)	4	$A_{1/8}^{(a)}A_{3/8}^{(c)}A_{1/2}^{(e)}\underline{B_{1/2}^{(e)}}\underline{B_{3/2}^{(i)}}\underline{X_{1/2}^{(e)}}\underline{X_{1/2}^{(e)}}\underline{X_{3/2}^{(i)}}\underline{X_{3/2}^{(i)}}$
5	$(\xi)^{4,A}(\xi, -\xi, \xi)^7$	$R3m$ (N160)	1	$\underline{A_{1/2}^{(a)}}\underline{A_{1/2}^{(a)}}\underline{B_{1/2}^{(a)}}\underline{B_{3/2}^{(b)}}\underline{X_{1/2}^{(a)}}\underline{X_{1/2}^{(a)}}\underline{X_{3/2}^{(b)}}\underline{X_{3/2}^{(b)}}$
6	$(\xi)^4(0, \varphi, 0, \varphi, 0, -\varphi)^1$	$P2_13$ (N198)	4	$\underline{A_{1/2}^{(a)}}\underline{A_{1/2}^{(a)}}\underline{B_{1/2}^{(a)}}\underline{B_{3/2}^{(b)}}\underline{X_{1/2}^{(a)}}\underline{X_{1/2}^{(a)}}\underline{X_{3/2}^{(b)}}\underline{X_{3/2}^{(b)}}$

$\mathbf{k}_{10}(\tau_1)$  enters into both permutation (on Wyckoff position 16(d) and 32(e)) and mechanical (on Wyckoff position 8(a), 16(d), 32(e)) representations of spinel structure. Therefore, the lowering of crystal symmetry is due to displacements of all atom types and ordering of octahedral cations and anions (in both cases the type of order is 1:3). Calculated results show that atoms  $A^{8(c)}$  are located in weakly distorted tetrahedra, atoms  $B^{12(d)}$  are in distorted octahedra, atoms  $B^{4(b)}$  are present in regular octahedra (Fig. 11 a, b). Structure formula of low-symmetry phases has the following view:  $A_2^{8(c)}B_3^{4(b)}B_3^{12(d)}X_2^{8(c)}X_6^{24(e)}$  [5,6]. The existence of 6 new types of hyperkagome lattice in spinel ordered structures has been theoretically predicted on the basis of group-theoretical analysis results (table 2).

The hyperkagome sublattice in  $P4_132$  ( $P4_332$ )-phase structure is formed by triangles  $[B_3^{12(d)}]_n$ . Each of these sublattices is topologically the same as hyperkagome sublattice in  $Na_4Ir_3O_8$  structure. However the surroundings of hyperkagome sublattices in  $P4_132$  ( $P4_332$ )-phase structures and in  $Na_4Ir_3O_8$  structure are different.

Designations for order parameters:  $k_{10} - \varphi$ ,  $k_{11} - \xi$ . The superscript index after the closing parenthesis is the representation number according to [5, 6] and  $V_0/V$  is the multiplication of primitive cell volume as a result of the structural phase transition. The superscript index in the structural formula means the type of Wyckoff position according to International Tables for Crystallography. In the structural formulas, ordered cations are underlined.

Note that the hyperkagome atomic order was first predicted theoretically in our paper [16], in which aspects of the cation ordering (type 1: 3) in the spinel structure was studied. Atomic order, shown in Fig.1c and 2 [16], is a hyperkagome order. It is exactly the same as in Fig. 4-6 of this work. The name of the hyperkagome order (sublattice) was proposed in [2].

Antiferromagnets with spin  $S = 1/2$  on kagome- and hyperkagome lattices are rare substances, exotic structure-electronic states of matter. Scientists hope that these materials will find important applications. The theory proposed is in accordance with experimental results [2]. Unusual physical properties are expected to appear when doping  $Na_4Ir_3O_8$  crystals. It is known that crystals with broken mirror symmetry show macroscopic effects which were prohibited in centrosymmetric crystals [17, 18]. The theory predicted three types

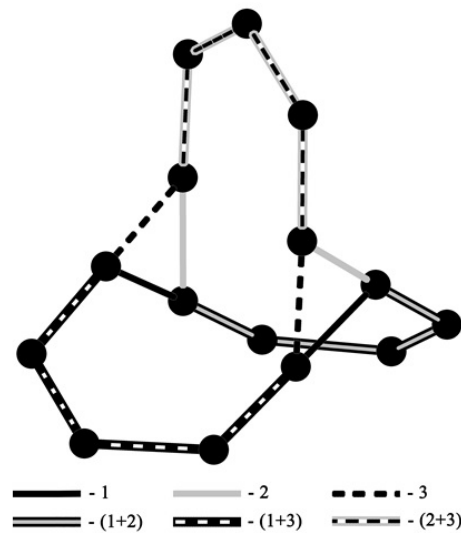


FIG. 7. Structure module of  $\text{Na}_4\text{Ir}_3\text{O}_8$ , consisting of three minimal intercrossing contours (loops) of Ir-Ir bonds. Each type of contours is designated by one number. If the Ir-Ir bond included in the two contours, they designated as the sum of two numbers

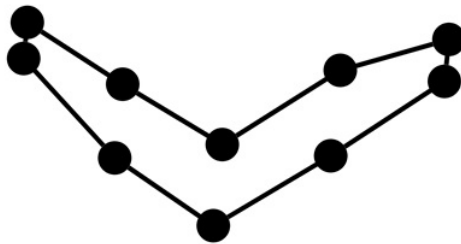


FIG. 8. Nanocluster “decagon” in  $\text{Na}_4\text{Ir}_3\text{O}_8$  structure

of structures that can realize a network of corner-sharing tetrahedral (atom hyperkagome order): spinels  $\text{AB}_2\text{O}_4$ , pyrochlores  $\text{A}_2\text{B}_2\text{O}_7$  and C15 Laves phases  $\text{AB}_2$ .

The results of this work have been obtained with the support of the Ministry of Education and Science of the Russian Federation in the framework of the State tasks (Talanov V.M., project N 2983(9.14), (Talanov M.V., Federal program: state contract N 14.575.21.0007; theme Nos. 213.01-11/2014-21, 3.1246.2014/K, 213.01-2014/012-BГ).

## References

- [1] Anderson P. Ordering and Antiferromagnetism in Ferrites. *Phys. Rev.*, 1956, **102**, P. 1008–1013.
- [2] Okamoto Y., Nohara M., Aruga-Katori H., Takagi H. Spin-Liquid State in the  $S=1/2$  Hyperkagome Antiferromagnet  $\text{Na}_4\text{Ir}_3\text{O}_8$ . *Phys. Rev. Lett.*, 2007, **99**, P. 137207(4)
- [3] Iwasaki M., Takizawa H., Uheda K., Endo T. Synthesis and crystal structure of  $\text{Na}_4\text{Sn}_3\text{O}_8$ . *J. Mater. Chem.*, 2002, **12**, P. 1068–1070.
- [4] Kovalev O.V. Representations of Crystallographic Space Groups. Irreducible Representations, Induced Representations and Co-representations London: Taylor and Francis Ltd., 1993, 390 p.
- [5] Talanov V.M., Shirokov V.B. Tilting structures in spinels. *Acta Crystallographica A*, 2012, **A68**, P. 595–606.
- [6] Talanov V.M., Shirokov V.B. Atomic order in spinel structure – a group-theoretical analysis. *Acta Cryst.*, 2014, **A70**, P. 49–63.

- [7] Talanov V.M. Structural mechanism of tetragonal Jahn-Teller distortion of spinels. *Izv. Akad. Nauk SSSR. Inorganic materials.*, 1989, **6**, P. 1001–1005.
- [8] Talanov V.M. Structural mechanism of the ordering of ions in tetrahedral holes in spinels. *Journal of Structural Chemistry*, 1986, **2**, P. 172–176.
- [9] Talanov V.M. Enantiomorphic modifications of spinels. *Izv. Akad. Nauk SSSR. Inorganic materials.*, 1990, **26**(11), P. 2428–2430.
- [10] Pashchenko N.V., V.M. Talanov. Classification and properties of structural states of crystals. 1. Crystallographic conditions of appearance of extraordinary and irrational structural states *Kristallographiya*, 1995, **40**(6), P. 973–981. *Crystallography Reports*, 1995, **40**(6), P. 900–907.
- [11] Pashchenko N.V., V.M. Talanov. Classification and properties of structural states of crystals. 2. Crystallographic conditions of the appearance of isosymmetric, enantiomorphous, and antisostructural states. *Kristallographiya*, 1995, **40**(6), P. 982–988; *Crystallography Reports*, 1995, **6**, P. 908–914.
- [12] Talanov V.M.; Fedorova N.V. Classification and properties of the structural states of crystals: III. Adjacency graphs for the structural states characterized by different numbers of parameters *Kristallographiya*, 1997, **42**(3), P. 394–398; *Crystallography Reports*, 1997, **3**, P. 350–353.
- [13] Talanov V.M.; Fedorova N.V. Application of crystallogometrical theory of structural states of matter to the description of structural transformations in point group 32. *Kristallographiya*, 1997, **42**(3), P. 389–393; *Crystallography Reports*, 1997, **3**, P. 345–349.
- [14] Talanov V.M. Theoretical grounds of the natural classification of structure types *Kristallographiya*, 1996, **44**(6), P. 979–997; *Crystallography Reports*, 1996, **6**, P. 929–946.
- [15] Ivanov V.V., Talanov V.M. The principle of the modular structure of the nanostructures: information codes and combinatorial design. *Nanosystems: physics, chemistry, mathematics*, 2010, **1**(1), P. 72–107.
- [16] Talanov V.M. Structural Modelling of Low-Symmetry Phases of Spinels. II. Phases with 1: 3 Octahedral Order. *Phys. Stat. Sol. (b)*, 1990, **162**, P. 339–346.
- [17] Ramirez A.P. *Handbook on Magnetic Materials*. Amsterdam: Elsevier Science, 2001, **13**, 423 p.
- [18] Bergholtz E.J., Läuchli A. M., Moessner R. Symmetry Breaking on the Three-Dimensional Hyperkagome Lattice of  $\text{Na}_4\text{Ir}_3\text{O}_8$ . *Phys. Rev. Lett.*, 2010, **105**, P. 237202(4).



# ***NANOSYSTEMS:***

## ***PHYSICS, CHEMISTRY, MATHEMATICS***

### **INFORMATION FOR AUTHORS**

The journal publishes research articles and reviews, and also short scientific papers (letters) which are unpublished and have not been accepted for publication in other magazines. Articles should be submitted in English. All articles are reviewed, then if necessary come back to the author to completion.

The journal is indexed in Chemical Abstract Service of the American Chemical Society and in Russian Scientific Citation Index.

#### **Author should submit the following materials:**

1. Article file in English, containing article title, the initials and the surname of the authors, Institute (University), postal address, the electronic address, the summary, keywords, MSC or PACS index, article text, the list of references.
2. Files with illustrations, files with tables.
3. The covering letter in English containing the article information (article name, MSC or PACS index, keywords, the summary, the literature) and about all authors (the surname, names, the full name of places of work, the mailing address with the postal code, contact phone number with a city code, the electronic address).
4. The expert judgement on possibility of publication of the article in open press (for authors from Russia).

Authors can submit a paper and the corresponding files to the following addresses: nanojournal.ifmo@gmail.com, popov1955@gmail.com.

#### **Text requirements**

Articles should be prepared with using of text editors MS Word or LaTeX (preferable). It is necessary to submit a pdf copy. In the name of files the English alphabet is used. The recommended size of short communications (letters) is 4-6 pages, research articles – 6-15 pages, reviews – 30 pages.

##### Recommendations for text in MS Word:

Formulas should be written using Math Type. Figures and tables with captions should be inserted in the text. Additionally, authors present separate files for all figures and Word files of tables.

### Recommendations for text in LaTeX:

Please, use standard LaTeX without macros and additional style files. The list of references should be included in the main LaTeX file. Single LaTeX file of the paper with the corresponding pdf file should be submitted.

### **References**

References in the article text are given in square brackets. The list of references should be prepared in accordance with the following samples:

- [1] N. Surname. *Book Title*. Nauka Publishing House, Saint Petersburg, 2000, 281 pp.
- [2] N. Surname, N. Surname. Paper title. *Journal Name*, 2000, **1** (5), P. 17–23.
- [3] N. Surname, N. Surname. Lecture title. In: Abstracts/Proceedings of the Conference, Place and Date, P. 17–23, 2000.
- [4] N. Surname, N. Surname. Paper title. 2010, URL: <http://books.ifmo.ru/ntv>.
- [5] N. Surname, N. Surname. Patent Name. Patent No. 11111, Bul. No. 33, 5 pp., 2010.
- [6] N. Surname, N. Surname. Thesis Title. Thesis for full doctor degree in math. and physics, Saint Petersburg, 105 pp., 2000.

### **Requirements to illustrations**

Illustrations should be submitted as separate black-and-white files. Formats of files – jpeg, eps, tiff with resolution no less than 150 dpi. For electronic version it is better to use color figures.



# ***NANOSYSTEMS:***

***PHYSICS, CHEMISTRY, MATHEMATICS***

## **Журнал зарегистрирован**

Федеральной службой по надзору в сфере связи, информационных технологий и массовых коммуникаций

(свидетельство ПИ № ФС 77 - 49048 от 22.03.2012 г.)

ISSN 2220-8054

**Учредитель:** федеральное государственное автономное образовательное учреждение высшего образования

«Санкт-Петербургский национальный исследовательский университет информационных технологий, механики и оптики»

**Издатель:** федеральное государственное автономное образовательное учреждение высшего образования

«Санкт-Петербургский национальный исследовательский университет информационных технологий, механики и оптики»

**Отпечатано** в Учреждении «Университетские телекоммуникации»

Адрес: 197101, Санкт-Петербург, Кронверкский пр., 49

## **Подписка на журнал НФХМ**

На первое полугодие 2016 года подписка осуществляется через

ОАО Агентство «Роспечать»

Подписной индекс 57385 в каталоге «Издания органов научно-технической информации»